Dissertation
submitted to the
Combined Faculties for the Natural Sciences and for Mathematics
of the Ruperto–Carola University of Heidelberg, Germany
for the degree of
Doctor of Natural Sciences

presented by
Diplom-Physicist: Oliver Sebastián Müller–de Vries
born in: Gehrden (Hannover)

Oral examination: 19.05.2004

The relative contribution of free radicals to the oxidation chain of Dimethylsulphide in the marine boundary layer.

Referees: Prof. Dr. Ulrich Platt
Prof. Dr. Ulrich Schurath

Der relative Beitrag von freien Radikalen zum Abbaumechanismus von Dimethylsulfid in der marinen Grenzschicht.

Hydroxylradikale (OH) sind die dominierende photochemische Senke von Dimethylsulfid (DMS) in der reinen marinen Atmosphäre und beherrschen den globalen Abbau von DMS. In Gebieten mit starker Luftverschmutzung kann das Oxidationsvermögen von nächtlich gebildetem NO_3 jenes von OH am Tage bei Weitem übertreffen. Während so genannter "Bromexplosionen" kann Bromoxid (BrO) auf lokaler Ebene eine dominerende Senke für DMS darstellen. Der Abbau von DMS steht am Anfang eines komplexen Oxidationsmechanismus dessen Ablauf wesentlich durch die Mischungsverhältnisse von Sticktoffoxiden (NO,NO_2,NO_3), Ozon, OH und Peroxyradikalen bestimmt wird.
Im Verlauf dieser Arbeit wurden drei Messkampagnen in der marinen Grenzschicht durchgeführt. Das Ziel war der Vergleich der Konzentration von Halogen- und Stickstoffoxiden sowie weiterer Radikale mit denen von DMS und dessen Oxidationsprodukten DMSO und MSA. Die Ergebnisse der ersten Messstudie im östlichen Mittelmeer (Kreta) ermöglichen eine ausgiebige Untersuchung der Wechselwirkung von DMS und NO_3. Darauf folgende Messungen in der Hudson Bay (Kanada) stellen den ersten bodengestützen Nachweis von BrO in der subarktischen Grenzschicht dar. Die Ergebnisse weisen auf einen erheblichen Einfluss von Bromoxid auf den Oxidationsprozess von DMS in diesem Gebiet hin. Die gemessenen Mischungsverhältnisse von Halogen und Stickstoffradikalen während der dritten Messkampagne im südlichen Indischen Ozean sind zu gering um direkte Bezüge zum Abbauprozess von DMS zu erkennen. Die gemessen Iodoxid-Konzentrationen können jedoch einen zusätzlichen Beitrag zum Ozonabbau leisten und durch die Proportionalität der OH-Produktionsrate zur Ozonkonzentration zu einer verringerten OH Bildung führen.

The relative contribution of free radicals to the oxidation chain of Dimethylsulphide in the marine boundary layer.

Hydroxyl radicals (OH) are the major photochemical sink of Dimethylsulphide (DMS) in the clean marine boundary layer and may have the largest contribution to DMS depletion on a global scale. In polluted areas the oxidation capacity of nightly produced NO_3 can exceed by far those reached by OH during daytime. During bromine explosion events, bromine oxide (BrO) can represent a dominant sink for DMS on a local scale. The depletion of DMS is the initial step of a complex reaction chain whose course is defined mainly by the mixing rates of Nitrogen oxides, ozone, OH and peroxy radicals which control the relative yields of methane sulphonic acid (MSA), Dimethylsulphoxide (DMSO) and SO_2.
Within this thesis three field campaigns have been carried out. The aim was the comparison of concentrations of halogen and nitrogen oxide species among other radicals to those of DMS and its oxidation products MSA and DMSO. The results of the first study carried out in the Eastern Mediterranean (Crete), allow an extensive analysis of the DMS-NO_3 interaction. Subsequent measurements at the Hudson Bay (Canada) represent the southernmost and first direct detection of abundant BrO formation in the subarctic boundary layer. The results reveal severe implications of BrO in the DMS oxidation process in this area. The third measurement campaign performed in the remote Southern Indian Ocean delivered mixing rates of halogen and nitrate radical species too low to establish direct links to the DMS depletion process. Nevertheless, Iodine Oxide at concentration levels observed on Kerguelen may enhance ozone depletion and, due to the dependence of OH formation rates on O_3 amounts, inhibit OH radical formation.

Contents

Chapter 1

Introduction

1.1 Scientific context

The change in climate is of great public concern and of enormous global importance. Due to the progress in environmental research, the importance of aerosols for the global change has become increasingly evident. Aerosols in general, more than affecting climate, play a role in the chemistry of the stratosphere and troposphere through heterogeneous reactions. They are involved in the formation and development of clouds and influence the radiative transfer properties of the atmosphere. Acid deposition, visibility degradation, damage to plants and human health, are all phenomena which are related to the presence of aerosols.
Evidence has been presented that sulphate aerosol climate forcing is sufficiently large to reduce considerably the positive forcing by anthropogenic greenhouse gases regionally, especially in the Northern Hemisphere [Baker 1997]. Natural sources contribute significantly to the European sulphate budget and short radiative forcing [Langmann et al. 1998]. Global models predict that about 30% of the sulphate burden and its short wave radiative forcing over Europe is caused by sulphate from natural sources. Different predictions of the amount of clouds by regional and global models modify the forcing significantly, emphasizing the role of clouds in estimating the direct short wave forcing of sulphate aerosols.
Biogenic reduced sulphur compounds, including dimethyl sulphide (DMS), hydrogen sulphide (H_2S) and carbon disulphide (CS_2) are the major source of sulphur in the marine atmosphere [Gershenzon et al. 2001]. Their sum is estimated to contribute 15 to 25% of global sulphur emissions [Lelieveld et al. 1997; Watts 2000]. Of the biogenically produced species, DMS is the most abundant and widespread in its distribution. The predominant oceanic source of DMS is the bacterial induced enzymatic cleavage of dimethylsulphoniopropionate (DMSp), a compatible solute synthesized mostly by phytoplankton for osmoregulation and/or cryoprotection [Simò 2001]. A fraction of the produced DMS crosses the sea surface and enters the atmosphere where it is readily oxidized by radicals to produce a series of sulphur compounds including methane sulphonic acid MSA, dimethylsulphoxide DMSO, $DMSO_2$ and non-sea salt sulphate (NSSS) particles [Liss et al. 1997]. These particles further degrade to sulphate and sulphonate aerosols and are the main source of cloud condensation nuclei (CCN) over oceanic areas remote from land.
Thank to the effort of the scientific community in the last decade, the main oxidation path-

ways of DMS and its oxidation products are mostly understood. However, a large number of topics concerning DMS still demand further investigation. Although the hydroxyl (OH) and the nitrate radicals (NO_3) have been identified as the main oxidants of atmospheric DMS, additional sink processes must be taken into account to explain observed DMS oxidation rates. Among the gas phase reactions the relative contribution of halogen radicals is still under scrutiny as the rate constants and global distributions of halogen monoxide radicals are not well defined yet.

The investigation of heterogeneous reactions involved the DMS oxidation cycle is still in the fledgling stages. According to Lee and Zhou [1994, Gershenzon et al. [2001] the heterogenous reaction of DMS with ozone in cloud droplets is much faster than the gas–phase reaction and may be fast enough to contribute to the overall oxidation rate of DMS. Only recently multiphase reactions of OH, H_2O_2 and some halogen radicals with DMS and it's oxidation products DMSO, MSA and MSIA have been investigated [Bardouki et al. 2002; Barnes 2003; Barcellos da Rosa et al. 2003]. Some of these reactions may have notable atmospheric implications particulary inside clouds; although the current understanding of the microphysics of particle formation in the atmosphere is not sufficiently developed to estimate the rates of heterogeneous and multiphase reactions with an accuracy comparable with those calculated for gas-phase reactions.

Given the spatial and temporal variability of aerosol particles in the troposphere, it has not been feasible so far to develop an observational network to map global distributions at the resolution needed for climate models. Therefore, accurate assessments of current radiative forcing due to aerosols presently rely on chemical transport models to generate the needed global aerosol distributions. While anthropogenic emissions have uncertainty ranges of about 30%, global estimates of natural emissions are associated with uncertainties up to a factor of 2. [Lelieveld et al. 1997]. Due to this uncertainties, current atmospheric models fail to agree with field observations [James et al. 2000].

Therefore, to generate accurate global distribution, the models must incorporate the physical and chemical processes that transform natural and anthropogenically induced emissions of aerosols and their precursors into the heterogeneously dispersed aerosol distributions that exist in the atmosphere. Natural emissions and the resulting background aerosol are essential components of both chemical transport models and radiative forcing calculations. Without a knowledge of the background aerosol properties, it is not possible to accurately quantify the direct and indirect forcing resulting from anthropogenically derived emissions.

The project EL CID (Evaluation of the Climatic Impact of Dimethyl Sulphide) was directed at understanding the processes in the DMS oxidation which lead to the formation of CCN which can modify the radiative budget of the troposphere and consequently climate. This project will help to quantify the role played by DMS oxidation chemistry in regulating global climate, which can be seriously perturbed by the release of pollutants. The major benefit of the investigation should be a clearer understanding of the processes leading to H_2SO_4 and MSA in the oxidation of DMS and their variation with meteorological conditions (specially temperature) and geographical location (latitude, remote marine regions(unpolluted) and coastal regions (often polluted)). The results may contribute to a better assessment of the

natural DMS versus anthropogenic SO_2 proportion of sulphur to climatic forcing by sulphate aerosols not only within the European context but also globally. Some benefit may arise in judging the relative negative forcing effects of greenhouse gases.
The technique of (D)ifferential (o)ptical (a)bsorption (s)pectroscopy (DOAS) [Platt 1994] delivered a significant contribution to the EL CID project monitoring the concentration of a large number of trace gases, including the nitrate radical NO_3 and halogen oxides, throughout three intensive field campaigns performed at coastal sites of the Mediterranean Sea, the Hudson Bay and the Southern Indian Ocean.

1.2 Outline of this thesis

A general introduction to the Chemistry involved in the oxidation of DMS in the marine boundary layer is given in Chapter 2. After a brief description of the global distribution and relevance of existing sulphur sources, special emphasis is given to the production of atmospheric DMS, the main source of marine sulphur emissions. Later on, the oxidation pathways of DMS are described in detail. Focus is on the Nitrate radical NO_3 and halogen oxides, trace gases measurable with the differential optical absorption spectroscopy (DOAS). The principles and further details of the DOAS–technique are described in Chapter 3, as well as some fundamentals about the other techniques employed to obtain the presented data are presented. Chapter 4 will give an overview of the field campaigns performed for the EL CID–Project in the eastern Mediterranean at Crete, in the Canadian Hudson Bay and in the remote Indian Ocean at Kerguelen. General conditions and data from the field measurements are shown. An Analysis and Discussion of the Data is presented in Chapter 5. The main results of this work are summarised and an outlook to future research is given in the final chapter 6.

Chapter 2

Chemistry of the DMS initiated sulphur cycle.

2.1 Global sulphur emissions and the impact on climate

The cycling of sulphur in the form of numerous compounds plays many important environmental roles, particularly with respect to the atmosphere. In the biosphere sulphur compounds are important as nutrients and electron carriers in metabolic pathways. A small fraction of the biogenic sulphur (0.04% yr^{-1}) volatilizes to the atmosphere [Crutzen et al. 1985; Charlson et al. 1992].
Over the oceans the release of sea salt sulphate into the atmosphere from sea spray may amount to several hundred Teragrammes Sulphur per year($Tg\,S\,yr^{-1}$) [Erickson 1989]. However, most of it occurs in coarse particles that are removed rapidly by gravitational settling and therefore are not spread into the atmosphere higher than a few decameters [Lelieveld et al. 1997].
The principal volatile sulphur species found in seawater are Dimethylsulphide (DMS), carbonyl sulphide (OCS), carbon disulphide (CS_2) and hydrogen sulphide (H_2S) (see Table 2.1). All these gases are oxidized to sulphur dioxide (SO_2) in the stratosphere and/or troposphere. Except for OCS, these gases are efficiently oxidized by OH radicals, which limits their lifetimes to few days (Table 2.1).

OCS is the most abundant, relatively long–living sulphur gas in the atmosphere. The chemical lifetime is about 20 years because of slow conversion by OH and photodissociation in the stratosphere, which is a main source of sulphur at about 20 km altitude [Crutzen 1976]. However, uptake by vegetation and the oceans (Table 2.1) limits the overall lifetime to a few years [Goldan et al. 1988; Weiss et al. 1995]. Oceanic OCS concentrations are a result of photochemical and non–photochemical production from organosulphur species, hydrolysis of dissolved OCS and air–sea exchange [Watts 2000]. The concentrations display a diurnal and seasonal cycle with a daylight and summer/autumn maximum [Ulshofer et al. 1996]. In general tropical and subpolar waters are richer in OCS and coastal waters display higher concentrations than open oceans.
There are very few oceanic measurements of CS_2, but such as there are seem to follow the

Table 2.1: Mean lifetime and observed mixing ratios of sulphur species in the lower atmosphere in ppt (Lelieveld et al. 1997).

Species	average lifetime	Concentration range [ppt] marine air	clean continental	polluted continental	free troposphere
H_2S	2 days	0–110	15–340	0–800	1–13
OCS	3 years	530 ± 20	510 ± 80	520 ± 80	510 ± 60
CS_2	1 week	30–45	15–45	80–300	≤ 5
DMS	0.5 day	5–400	7–100	2–400	≤ 2
SO_2	2 days	10–200	70–200	10^2–10^4	30–260
SO_4^{2-}	5 days	5–300 *	10–120	10^2–10^4	5–70

* refers to non–sea salt sulphate(NSSS)

pattern of OCS with higher concentrations in coastal waters, and less high in open ocean situations [Xie et al. 1998](see Table 2.1). The main sources of CS_2 are thought to be rotting organic matter and possibly an ocean photosynthetic source [Watts 2000; Xie et al. 1998]. In the atmosphere CS_2 is converted into SO_2 and OCS.
Estimates for oceanic H_2S emissions are the most tenuous, due to the scarce data available. The main source of H_2S in the oceans appears to be the hydrolysis of OCS and possibly direct emission by marine algae [Watts 2000]. The main sink reaction of H_2S in the lower troposphere is the reaction with OH to form SO_2.
From all reduced sulphur compounds emitted from oceanic sources, Dimethylsulphide has probably largest atmospheric implications as it has the shortest atmospheric lifetime (12 hours, see Table 2.1) and sulphate aerosols, derived by atmospheric oxidation of marine-derived DMS, are the main source of cloud condensation nuclei(CCN) in the marine troposphere remote from land [Liss et al. 1997].
Terrestrial sources of reduced sulphur are comparatively small (Table 2.3). H_2S release from swamps, marshes and estuaries is the most important example for emissions from the continents, though part of the emissions occurs as DMS and other reduced sulphur compounds. The dominant source is bacterial decay of organic matter under anoxic conditions below the water table. Due to the high variability, emissions from volcanoes constitute a very high but unpredictable source of sulphur. SO_2 emitted from hot magna is the main sulphur product, while a small fraction is released as H_2S and even OCS and CS_2. Roughly half the emissions occur from non-eruptive volcanoes such as Mount Etna (Italy) and from other more or less continuous fumaroles. In addition several dozens of eruptions take place annually all over the globe. During this nearly unpredictable explosive events large amounts of sulphur are shot into the free troposphere, where lifetime of sulphur is significantly larger. Therefore volcanoes play an important role in the global atmospheric sulphur budget.

Since the beginning of the industrial era, anthropogenic sulphur emissions have increased continuously. In the 1970s, anthropogenic SO_2 emissions from fossil fuel combustion (mainly coal and, to a lesser extent oil) had grown so strongly, that deposition of the oxidation product, sulphate, reached alarming levels, causing widespread ecosystem acidification (acid rain). In

Table 2.2: *Sources and sinks of sulphur compounds in Teragrammes sulphur per year [[Lelieveld et al. 1997; Watts 2000],[Rasch et al. 2000; Boucher et al. 2003]].*

	CS_2	DMS	H_2S	OCS	SO_2	SO_4^{2-}
Sources[Tg S/year]	0.66±0.19$^{(a)}$	24.5±5.3$^{(a)}$	7.7±1.3$^{(a)}$	1.3±0.3$^{(a)}$	79$^{(b)}$	55$^{(b)}$
Anthropogenic	0.34±0.17 (51.5%)	0.13±0.04 (0.5%)	3.30±0.33(42.7%)	0.12±0.06(9.2%)	75$^{(d)}$	–
Biomass burning	–	–	–	0.07±0.05(5.3%)		
Oceans $^{1)}$	0.18±0.04 (27.3%)	20.77±5.20 (84.8%)	1.80±0.61(23.3%)	0.30±0.18(22.9%)	biogenic	
Terrestrial	0.09±0.08 (13.6%)	3.59±1.01 (14.7%)	1.49±0.43(19.3%)	0.05±0.03(3.8%)	14$^{(d)}$	
Volcanism	0.05±0.04 (7.6%)	–	1.05±0.94(13.6%)	0.05±0.04(3.8%)	6–20$^{(d)}$	
Precipitation	–	–	–	0.13±0.08(9.9%)		
DMS oxidation	–	–	–	0.17±0.04(13.0%)		
CS_2 oxidation	–	–	–	0.42±0.12(32.1%)		
Gas phase prod.	–	–	–	–	–	14$^{(d)}$
In cloud prod.	–	–	–	–	–	22.5$^{(d)}$
Sinks						
Gas phase oxidation					12%	
Reaction with OH	0.57±0.25 (56.4%)	11.4–19.4 (42–71%)$^{(c)}$	8.50±2.80	0.13±0.10 (7.8%)		
Reaction with NO3	0.57±0.25 (56.4%)	6.2–15.7 (22–58%)$^{(c)}$	8.50±2.80	0.13±0.10 (7.8%)		
Reaction with BrO	0.57±0.25 (56.4%)	7.8$^{(c,2)}$	8.50±2.80	0.13±0.10 (7.8%)		
Reaction with O	–		–	0.02±0.01 (1.2%)		
In cloud oxidation		1.7 (DMS+O3(aq))$^{(c)}$			56%	
Dry deposition		–			42$^{(d)}$ (31%)$^{(b)}$	5$^{(d)}$ (7%)$^{(b)}$
Oxic soils	0.44±0.38 (43.6%)	–	–	0.92±0.78 (55.4%)		
Vegetation	–	–	–	0.56±0.10 (33.7%)		
Wet deposition		–			10$^{(d)}$ (2%)$^{(b)}$	35$^{(d)}$ (93%)$^{(b)}$
Photolysis	–	–	–	0.03±0.01 (1.8%)		
Total	1.01±0.45	24–27 $^{(c)}$	8.50±2.80	1.66±0.79	52$^{(d)}$	40$^{(d)}$

(a) [Watts 2000], (b) [Rasch et al. 2000], (c) [Boucher et al. 2003]
(d) [Chin et al. 2000]
1) including salt marshes and estuaries, (2)at 1 ppt BrO during daytime up to 1.3km height

Table 2.3: *Estimates of global sulphur sources [Lelieveld et al. 1997].*

Source	$Tg\ Sulphur/year$	Range of estimations
Volcanic	7.8	3–20
Terrestrial	1.1	0.1–7
Oceanic(NSS)	15.5	12–58
Total natural	24.4	15-72
Biomass burning	2.3	1–4
Fossil fuel use	67	67-103
Total manmade	69.3	69–103
TOTAL	93.7	86–154

our days, human emissions clearly surpass natural emissions [Albritton and Meira Filho 2001] on a global scale and dominate the atmospheric sulphur cycle(Table 2.2), in particular in the northern hemisphere (Figure 2.1). About 90% of the man-made emissions occur in northern latitudes, i.e. from the Eurasian and North American continents. On the other hand, the 10% contribution from southern latitudes accounts for roughly half the atmospheric sulphur budget in the Southern Hemisphere [Rasch et al. 2000]. Obviously the regional emission rates

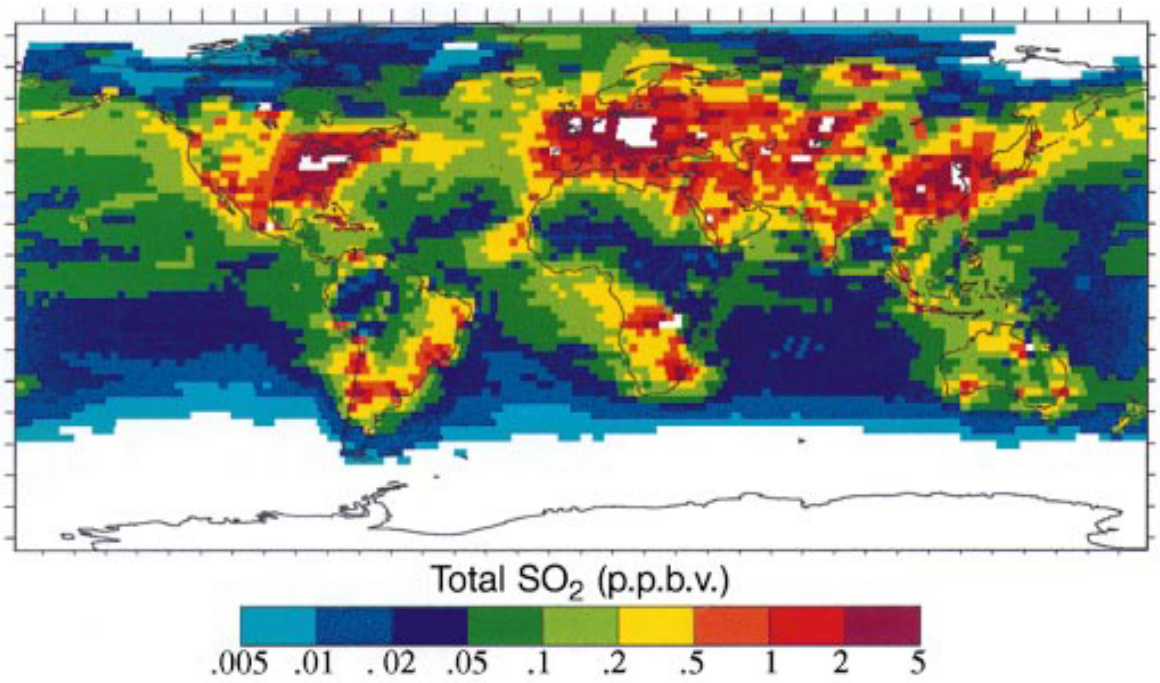

Figure 2.1: Total predicted surface SO_2 concentrations (Capaldo 1999)

are correlated to the extent of human activity. As depicted in Figure 2.1 the main worldwide emissions SO_2 correspond to the densely populated regions of Northern America, Europe and Asia. The emissivity of the remaining continents is low and particulary over the oceans in the southern hemisphere tiniest SO_2 mixing rates are predicted. It is important to remark though, that the contribution to the global sulphate burden is not directly proportional to the emissions budgets. Meteorology plays a crucial role in the removal of sulphur from the atmosphere. As the most effective sink of SO_2 is the rapid in–cloud oxidation to form SO_4^{2-}

(Table 2.2), wet deposition(rain) of sulphate is the main removal mechanism of sulfur from the atmosphere. Another important sink of SO_2 is dry deposition on ground, which largely depends on transport patterns controlled by local wind fields. Recent analysis of [Rasch et al. 2000] suggests a significant regional dependence in the destiny of SO_2 molecules. A tagging of the sulphur by emission region (Europe, Asia, North America and rest of the world[ROW]), chemical pathway(gaseous versus in-cloud) and type of emissions (anthropogenic vs. biogenic) was used to differentiate the balance of processes controlling the production and loading of this material. It was found that SO_2 molecules emitted from the ROW region have the greatest potential worldwide to form sulphate, and once formed, the sulphate aerosol has a longer residence time (it is less readily scavenged). The yield of sulfate from ROW sources of SO_2 is apparently 4 times higher than that of Europe, a region where a substantially higher fraction of the emitted SO_2 is oxidized to sulphate through the ozone pathway(gas phase oxidation). The analysis also suggests regional differences in the vertical distribution and horizontal extent of sulphate propagation, pointing out that Asian emissions reach the farthest from its point of origin.

Indirect effect Global models [Bopp et al. 2003; Boucher et al. 2003] estimate a small negative feedback of sulphur aerosols on global warming due to the *indirect radiative effect*, which is the result of the two–stage process by which (i) increased aerosol concentrations modify cloud properties and (ii) the modifications in cloud properties result in increased cloud albedo (the direct radiative effect of aerosol particles is modification of the optical properties of clear air) [Baker 1997].
However several studies show that the influence of sulphur on climate forcing is still poorly understood (Figure 2.2 taken fromAlbritton and Meira Filho [2001]). Most modelling studies of the indirect radiative effect have concentrated on anthropogenic sulphate aerosols. Results of Global Chemical Model calculations [Boucher and Lohmann 1995] suggest that changes in sulphate aerosol distributions accompanying the Industrial Revolution have increased the concentration of cloud particles by ≈ 0 to 20% over the Southern Hemisphere and by $\approx 100\%$ over the Northern Hemisphere continents. The calculated associated indirect effect to the short–wave cloud radiative forcing was $\Delta CRF_{sw} = -1 \pm 1\, W/m^2$. In general, however, it is difficult to isolate and quantify the aerosol indirect effect on the basis of measurements. One reason for this difficulty lies in measurement limitations. Cloud microphysical parameters are estimated from in situ (aircraft based) and remote (surface and satellite based) sensors; in general, the former are extremely limited in time and space but provide information with spatial resolution on the order of meters, whereas the spaceborne sensors can have near global coverage but resolutions typically in the order of kilometers. Due to fast deposition and therefore limited carrying distance of anthropogenic SO_2, biogenic emissions will become the most important source of sulphur in pristine marine environments.

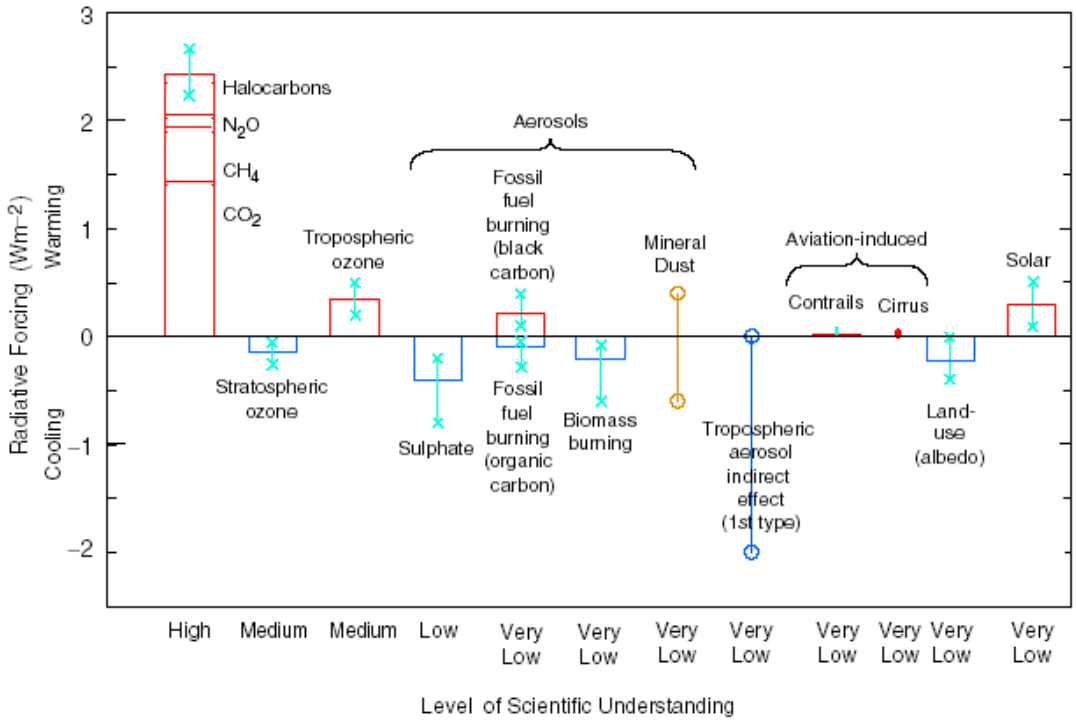

Figure 2.2: Global, annual–mean radiative forcings (Wm^{-2}). The height of the rectangular bar denotes a central or best estimate value, while its absence denotes no best estimate is possible. The vertical line about the rectangular bar with "x" delimiters indicates an estimate of the uncertainty range, for the most part guided by the spread in the published values of the forcing. A vertical line without a rectangular bar and with "o" delimiters denotes a forcing for which no central estimate can be given owing to large uncertainties. The uncertainty range specified here has no statistical basis and therefore differs from the use of the term elsewhere in this document. A "level of scientific understanding" index is accorded to each forcing, with high, medium, low and very low levels, respectively. This represents the subjective judgement about the reliability of the forcing estimate. The well-mixed greenhouse gases are grouped together into a single rectangular bar with the individual mean contributions due to CO_2, CH_4, N_2O and halocarbons shown. Fossil fuel burning is separated into the "black carbon" and "organic carbon" components with its separate best estimate and range. The sign of the effects due to mineral dust is itself an uncertainty. All the forcings shown have distinct spatial and seasonal features such that the global, annual means appearing on this plot do not yield a complete picture of the radiative perturbation.

2.2 Free radicals in the marine boundary layer

2.2.1 Hydrogen and peroxy radicals(OH,HO_2,RO_2)

The hydroxyl radical (OH) is the major tropospheric oxidant and is responsible for the chemical degradation of many atmospheric trace gases and pollutants [Levy 1971; Logan et al. 1981; Ehhalt 1999]. Peroxy radicals (HO_2 and RO_2, where R represents an organic group) are produced by reactions of OH with CO and volatile organic compounds (VOC) and play a central role in the photochemical formation of ozone in the troposphere [Chameides and Walker 1973; Fishman and Crutzen 1978; Trainer et al. 1987].

2.2.1.1 Formation of OH

The most important source of OH–radicals is the photolysis of ozone by UV–light at wavelengths below 320 nm and 420 nm:

$$\begin{aligned} O_3 + h\nu &\rightarrow O(^1D) + O_2(a^1\Delta_g) \qquad (\lambda \leq 310\,\text{nm}) && (2.1)\\ &\rightarrow O(^1D) + O_2(3\Sigma_g^-) \qquad (\lambda \leq 411\,\text{nm}) && (2.2)\\ &\rightarrow O(^3P) + O_2(3\Sigma_g^-) \qquad (\lambda \leq 1180\,\text{nm}) && (2.3) \end{aligned}$$

where the quantum yield of the spin-forbidden process (2.2) is very low [Moortgat 2001]. The excited $O(^1D)$ atoms can get quenched to ground state and rebuild ozone:

$$O(^1D) \xrightarrow{M} O(^3P) \qquad (M = N_2, O_2, H_2O) \qquad (2.4)$$

$$O(^3P) + O_2 \xrightarrow{M} O_3 \qquad (2.5)$$

A certain fraction F of the excited oxygen atoms will react with water vapour forming two OH molecules [Sander et al. 2003; Atkinson et al. 2003]

$$O(^1D) + H_2O \rightarrow 2\,OH \qquad (2.6)$$

Assuming that $k_{2.4A}$ and $k_{2.4B}$ are the rate constants for the reaction of $O(^1D)$ with N_2 and O_2 and $k_{2.6}$ the rate for reaction (2.6), the fraction F of OH forming oxygen atoms is:

$$F = \frac{k_{2.6}\cdot[H_2O]}{k_{2.4A}\cdot[N_2]+k_{2.4B}\cdot[O_2]+k_{2.6}\cdot[H_2O]} \qquad (2.7)$$

Typical values for F are in the range of 5–10%, reaching up to 20% at very high ambient humidity. The production rate of OH radicals can be derived correspondingly from the ozone concentration and the photolysis frequency of process (2.1):

$$\begin{aligned} \frac{d}{dt}[O(^1D)] &= [O_3]\cdot J(O^1D) && (2.8)\\ \frac{d}{dt}[OH] &= 2\cdot F\cdot[O_3]\cdot J(O^1D) && (2.9) \end{aligned}$$

As a consequence, the concentration of OH radicals exhibits a distinct diurnal cycle coupled to solar irradiation and depends largely on ambient ozone levels.
The relation of OH concentrations to $J(O^1D)$ rates appears to be linear in all environments studied so far, reaching from clean marine to moderately polluted rural (Ehhalt and Rohrer

[2000] and references therein). Although ozone photolysis is the primary source of OH, the apparent linearity to ozone photolysis is not self–evident. The atmospheric OH concentration depends on other production terms as well, most of them photolytic, such as photodissociation of H_2O_2, nitrous acid (HONO) [Alicke et al. 2003; Zhou et al. 2002; Platt and Janssen 1995] and carbonyls (mainly HCHO) in the presence of NO [Winer and Biermann 1994]. Because these molecules absorb UV at higher wavelengths [Kraus and Hofzumahaus 1998], their photolysis frequencies do not vary linearly with JO^1D. In addition to photolytic sources, dark reactions of NO_3 and O_3 with alkenes may be an important source at nighttime [Geyer et al. 2001; Paulson et al. 1999; Platt et al. 1990].
Global OH model estimations are frequently based on "accidental tracers", i.e. budgets of chemicals that react with OH (e.g. methyl chloroform). Until now the variability of estimations is large [Jöckel et al. 2003]. However, several measurements of OH and peroxy radicals performed at site locations ranging from remote marine to urban polluted ([Mihelcic et al. 2003] and references therein) give a survey of the global radical distribution. The largest concentrations of OH are calculated for the industrialized regions in the norther hemisphere in summer near to the ground (about 5×10^6 $molec/cm^3$). Very low concentrations ($< 10^5$ $molec/cm^3$) are calculated poleward of about 50° in the winter hemisphere [von Kuhlmann 2001; Spivakovsky et al. 2000]. For ambient conditions of the three field campaigns described in chapter 4, averaged 24–hour OH radical concentration estimations range from 15–26$\times 10^5$ in the Mediterranean summer down to 5–8$\times 10^5$ $molec/cm^3$ for the low arctic in spring. Recent measurements of [Berresheim et al. 2003] in the Mediterranean boundary layer in August 2001 (based on selected ion chemical ionization mass spectrometry (SI/CIMS)) reported daily average OH concentrations of 3.6–6.7$\times 10^6$ cm^{-3} reaching peak daytime OH mixing ratios between 11–19$\times 10^6$ cm^{-3}.

2.2.1.2 Sinks of OH and production of peroxy radicals

Due to fast reactions with a large number of natural and anthropogenic compounds the average tropospheric lifetime of OH is less than one second. Carbon monoxide provides the most important sink for OH, accounting for about 40% of the OH loss in the troposphere [von Kuhlmann 2001]. The remaining OH is mostly consumed by reactions with methane (CH_4) and the sum of non-methane-hydrocarbons (NMHC's) and other volatile organic compounds(VOC's). Other important sinks of OH are formaldehyde(HCHO or CH_2O), ozone, molecular hydrogen H_2 as well as other compounds given in Table 2.4.

A simplified tropospheric reaction scheme of the OH radical in the troposphere is given in Figure 2.3. Most OH oxidation reactions lead to the formation of peroxy radicals HO_2 (hydroperoxy) and RO_2 (organic peroxy). Organic peroxy radicals RO_2 further react with NO, NO_3 or other peroxy radicals forming alkoxy radicals (RO, OH, or RH-OH-O). To a major amount alloy radicals react back to peroxy radicals, however with a reduced alkyl group. This cycle will continue until HO_x radicals are formed at last [Gölz 1996].
Much attention has been driven to atmospheric chemistry surrounding Peroxy radicals ($RO_x = HO_2 + RO_2$) as they can give important information about the oxidation capacity of the troposphere and play a central role in the only known photochemical production

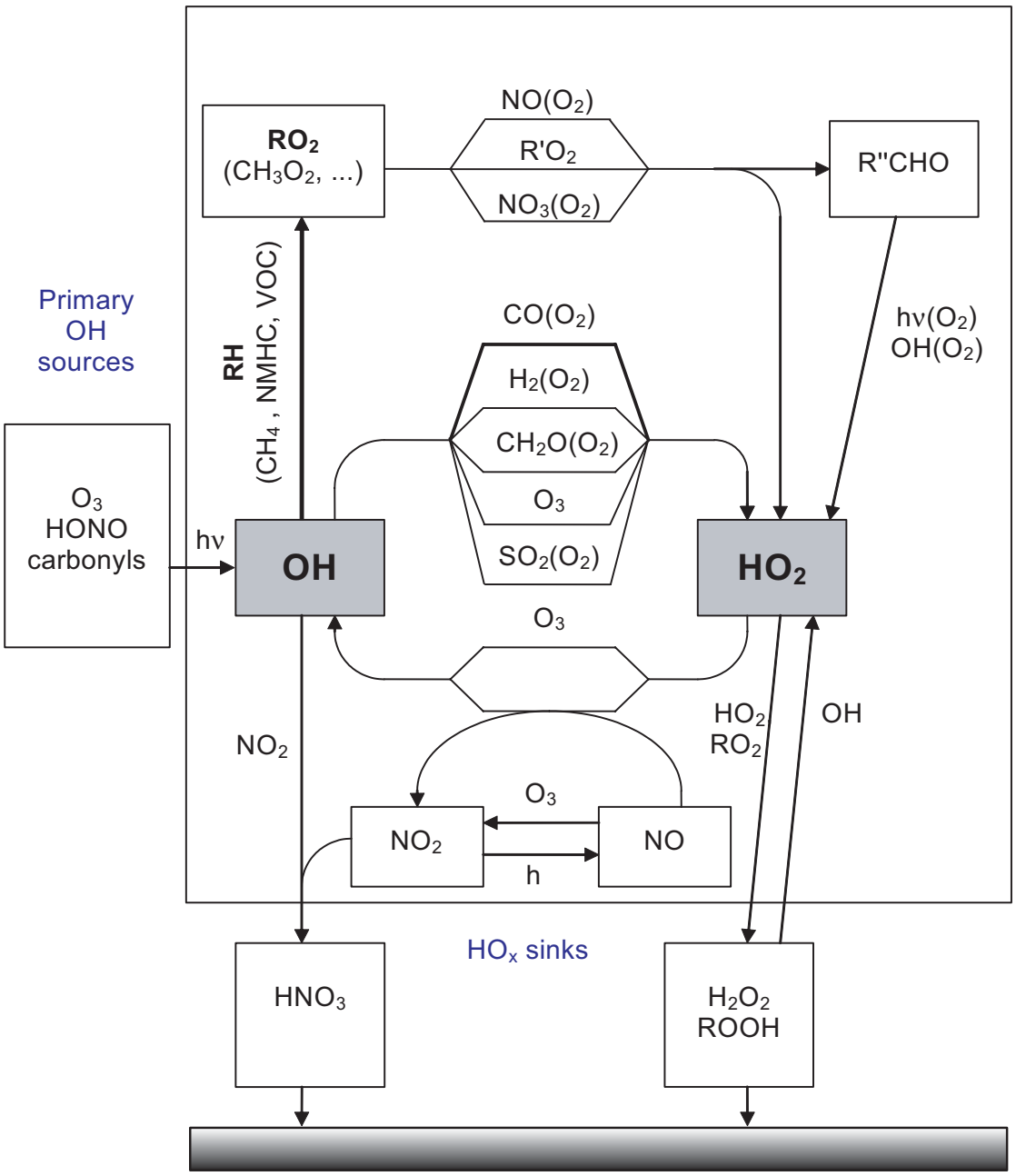

Figure 2.3: Simplified tropospheric reaction scheme of the OH initiated oxidation cycle.

Table 2.4: Main loss reactions of OH

	Reaction		k(298)$^{(a)}$ [cm^3 molec.$^{-1}$ s^{-1}]	Global $^{(b)}$ Contribution
2.10	$CO+OH$	$\rightarrow CO_2+HO_2$	$2.1e^{-13}$	41.2%
2.11	CH_4+OH	$\rightarrow CH_3+H_2O$	$6.4e^{-15}$	14.2%
2.12		$\rightarrow CH_3+O_2+M\rightarrow CH_3O_2+M$	$1.8e^{-12}$	
2.13	$HCHO+OH$	$\rightarrow HCO+H_2O$	$9.4e^{-12}$	6.6%
		$\rightarrow HCO+O_2\rightarrow CO+HO_2$	$5.2e^{-12}$	
2.14	O_3+OH	$\rightarrow HO_2+O_2$	$7.3e^{-14}$	4.9%
2.15	HO_2+OH	$\rightarrow H_2O+O_2$	$1.1e^{-10}$	4.9%
2.16	H_2O_2+OH	$\rightarrow HO_2+O_2$	$1.7e^{-12}$	4.5%
2.17	H_2+OH	$\rightarrow HO_2+H$	$6.7e^{-15}$	4.4%
	Isoprene+OH	$\rightarrow$products	$1.0e^{-10}$	2.4
2.18	NO_2+OH+M	$\rightarrow HONO_2+M$	$1.2e^{-11}$	2.4%
2.19	SO_2+OH+M	$\rightarrow HOSO_2+M$	$2.0e^{-12}$	
		$\rightarrow HOSO_2+O_2\rightarrow SO_3+HO_2$	$4.3e^{-13}$	

$^{(a)}$ Atkinson2003 , $^{(b)}$ vonKuhlmann2001

process of ozone in the lower troposphere [Crutzen 1979; Trainer et al. 1987]. In the remote troposphere, under low NO_x conditions, the main loss processes for RO_2 (mainly CH_3O_2 and HO_2) are their recombination reactions (2.20), (2.21) and the reaction with ozone (2.22) [Lelieveld et al. 2002]. Reaction (2.22) coupled to O_3 photolysis (2.1) may lead to net photochemical O_3 destruction. In more polluted, NO_x–rich atmospheres, peroxy radical oxidation of NO competes with reactions (2.20)–(2.22), resulting in the formation of ozone via photolysis of the NO_2 product (reactions (2.23)–(2.26) in table 2.5). Under this conditions the reaction of OH with NO_2 is a very effective loss process for the sum of HO_x (=OH and HO_2) radicals as nitric acid HNO_3 is readily removed from the gas phase by deposition on ground or the sea surface [Platt et al. 2002].
The balance between ozone destruction and production is defined in terms of the so–called "ozone–nitric compensation point". The equilibrium is dependent on ambient conditions. Within the study of [Cox 1999] the compensation point was found to be 20 ± 5 ppt NO at Cape Grim(Tasmania), slightly below the 60 ± 30 ppt established for Mace Head(Ireland) [Carpenter et al. 1997].

2.2.2 The Nitrate Radical

Following its first detection in the troposphere [Platt et al. 1980; Noxon et al. 1980], several measurements of the NO_3 concentration have been carried out in polluted and clean background air under both continental and marine conditions [Platt et al. 1981; Heintz et al. 1996; Allan et al. 2000; Geyer et al. 2001; Geyer et al. 2001; Geyer and Platt 2002].
These measurements and consecutive analysis agree that NO_3 plays a crucial role in the nighttime troposphere as it acts as main oxidizing agent for a number of volatile organic compounds (VOCs), in particular biogenic monoterpenes and dimethylsulphide (DMS). Although rate constants of reactions of VOCs with NO_3 are generally several orders mag-

Table 2.5: Main HO_2 reactions under low and high NOx conditions [Atkinson et al. 2002]

	Reaction	k(298)[cm^3 molec.$^{-1}$ s^{-1}]
low NOx		
2.20	$HO_2+HO_2 \rightarrow H_2O_2+O_2$	$1.6e^{-12}$
2.21	$CH_3O_2+HO_2 \rightarrow CH_3OOH+O_2$	$5.2e^{-12}$
2.22	$HO_2+O_3 \rightarrow OH+2\ O_2$	$2.0e^{-15}$
high NOx		
2.23	$HO_2+NO \rightarrow OH+NO_2$	$8.8e^{-12}$
2.24	$CH_3O_2+NO \rightarrow CH_3O+NO_2$	$7.7e^{-12}$
2.25	$NO_2+h\nu \rightarrow O(^3P)+NO$	
2.26	$O(^3P)+O_2+M \rightarrow O_3+M$	

nitude below those involving OH, the nitrate radical is frequently the main oxidizing agent in the continental boundary layer since typical nighttime concentrations are about 10-100 times higher than daytime OH levels. In addition NO_3 is an important intermediate in the conversion of nitrogen oxides to HNO_3 or nitrates and thus in the removal of NO_x from the atmosphere. The contribution of NO_3 to VOC and NO_x degradation strongly depends on the local chemical and meteorological conditions and can vary on a short timescale [Heintz et al. 1996; Geyer et al. 2001].

2.2.2.1 Sources of NO_3

The chemistry of the nitrate radical in the atmosphere has been discussed in detail before [Platt et al. 1981; Wayne et al. 1991]. The only relevant NO_3 production mechanism in the atmosphere is the relatively slow [Sander et al. 2003] oxidation of NO_2 by O_3:

$$NO_2 + O_3 \ \rightarrow \ NO_3 + O_2 \tag{2.27}$$

Therefore the production rate of NO_3 can easily be determined from known concentrations of NO_2 and ozone:

$$P_{NO_3} \ = \ [NO_2][O_3]k_{2.27}(T) \tag{2.28}$$

In the following sections the most important processes involved in the production and destruction of the nitrate radical NO_3 are listed. The loss mechanisms of NO_3 can be divided into three categories;i.e. photolysis, direct sinks of NO_3 , including homogeneous and heterogeneous reactions, and indirect sinks via loss mechanisms of N_2O_5 different from thermal decomposition, which result in a net loss of NO_3.

2.2.2.2 Sinks of NO_3

The major direct gas phase loss mechanisms of NO_3 tend to be the reactions of the radical with a number of Non–methane hydrocarbons(NMHC's). The reactions of NO_3 with a large number of organic compounds including a number of alkanes, aldehydes and aromatic compounds have been studied in detail by [Geyer et al. 2001; Gölz et al. 2001; Heintz et al. 1996].

They proceed dominantly via hydrogen abstraction and lead to the formation of HNO_3 and peroxy radicals. Of particular importance in the marine boundary layer(MBL) is the reaction with DMS described in section 2.3.2.2. During daytime the lifetime of NO_3 is limited to few seconds due to rapid photolysis [Orlando et al. 1993] and reaction with NO. The preferred photolysis path ($\approx 90\%$) is reaction (2.29)

$$NO_3 + h\nu \;\rightarrow\; NO_2 + O \tag{2.29}$$

$$NO_3 + h\nu \;\rightarrow\; NO + O_2 \tag{2.30}$$

The homogeneous gas phase reaction (2.31) will contribute to rapid loss of NO_3 by reconversion to NO_2

$$NO_3 + NO \;\rightarrow\; 2\,NO_2 \tag{2.31}$$

Unless fresh local emissions exist, the importance of this sink reaction decreases steadily after sunset as NO will be rapidly titrated away by O_3 . For conditions in the eastern Mediterranean (50 ppb O_3 at 301 K) the NO lifetime at night is limited to some ten seconds,

$$NO + O_3 \;\rightarrow\; NO_2 + O_2 \tag{2.32}$$

Due to the absence of photolysis and NO the lifetime of NO_3, and thus concentrations are likely to increase significantly at night. Other homogeneous loss processes like decomposition of NO_3 due to reactions with NO_2 (2.33), its self–reaction (2.34) and its thermal decay (2.35) are supposed to be of minor relevance (Table 2.6). Heterogeneous loss processes of NO_3

Table 2.6: Rate constants of gas phase reactions involved in NO_3 chemistry($T = 301\,K$)

	Reaction		A	B	k(301 K) [cm^3/(mol. s)]	Ref.
2.27	NO_2+O_3	→NO_3+O_2	$1.4e^{-13}$	-2470	$3.8e^{-17}$	a
2.33	NO_3+NO_2	→NO+NO_2+O_2	$4.5e^{14}$	1260	$6.8e^{-16}$	b
2.34	NO_3+NO_3	→2 NO_2+O_2	$8.5e^{13}$	2450	$2.3e^{-16}$	b
2.35	NO_3+M	→NO+O_2+M			$1.4e^{-4}$ cm^3	c
2.31	NO_3+NO	→2 NO_2	$1.8e^{-11}$	110	$2.6e^{-11}$	a
2.32	NO+O_3	→NO_2+O_2	$1.4e^{-12}$	-1310	$1.8e^{-14}$	a
2.37	NO_3+NO_2+M	→N_2O_5+M	$1.9e^{-12}(T/300)^{0.2}$		$1.9e^{-12}$	a
2.36	N_2O_5+M	→NO_3+NO_2+M	$9.7e^{14}(T/300)^{0.1}exp(-11080/T)$		$1.0e^{-1}$	a
2.39	N_2O_5+H_2O	→2 HNO_3			$2.5e^{-22}$	a*

Rate constants given in Arrhenius form: $k(T) = A\ exp(B/T)$.
[a)] Atkinson2003, [b)] Sander2003(288 K), [c)] Mentel1996(293 K)
[d)]Waengberg1997,[e)]Sander2000,[f)]Gershenzon2001
* at 298 K; $M = N_2, O_2$

proceed via deposition on ground or at the surface of aerosol or cloud particles. Although hydrolysis of NO_3 is slow [Rudich et al. 1996], it might react however with anions like Cl^- in solutions [Thomas et al. 1998]. The frequency of heterogeneous NO_3 loss is determined by chemical composition of aerosols and ambient temperature. Following estimations in [Geyer et al. 2001; Geyer and Platt 2002] the direct loss of nitrate radicals on aerosol surfaces seems

to be of minor importance unless foggy conditions dominate.
NO_3 removal by dry deposition on ground can be estimated using the wind profile, surface roughness and thickness of laminar boundary layer as described in [Heintz et al. 1996].

Indirect loss of NO_3: Another major scavenging process is based on the combination of NO_3 with NO_2 to produce N_2O_5

$$NO_3 + NO_2 \underset{\longleftrightarrow}{M} N_2O_5 \tag{2.37}$$

Owing to the thermal decay of N_2O_5, a temperature dependent equilibrium (Table 2.6) of this gas phase reaction is established within few minutes at ambient temperatures [Heintz et al. 1996], unless the NO_2 concentration is very low [Carslaw et al. 1997]. Due to this property any sink process for N_2O_5 will affect the NO_3 concentration and lifetime.
Presently, very few techniques allow direct measurements of the N_2O_5 concentration in the troposphere [Brown et al. 2003]. However, knowing the concentration of the precursors, the N_2O_5 equilibrium concentration can be determined from

$$[N_2O_5] \; = \; [NO_2]\,[NO_3] \times K_{eq} \tag{2.38}$$

The equilibrium constant is strongly temperature dependent $K_{eq} = 5.5e^{-27} \times \; exp(10724/T)$ [Wängberg et al. 1997]. Due to the inverse exponential proportionality, indirect sinks are expected to gain influence at continental winter conditions [Geyer and Platt 2002] as the equilibrium of (2.38) is shifted towards nitrous pentoxide. For the relatively high temperatures about 301 K as encountered in the Mediterranean summer, K_{eq} is by a factor of 5 lower than for continental conditions with 288 K on average as investigated by [Geyer and Platt 2002] and [Heintz et al. 1996] which estimated an important loss of NO_3 via N_2O_5 depletion.
Possible sinks of N_2O_5 are its hydrolysis producing HNO_3 either in the gas phase or heterogeneously on aerosol surfaces:

$$N_2O_5 + H_2O \; \rightarrow \; 2HNO_3 \tag{2.39}$$

For further detail read [Geyer et al. 2001; Geyer and Platt 2002].
In addition to the first–order reaction (2.39), a second–order process has been observed [Mentel et al. 1996; Wahner et al. 1998]

$$N_2O_5 + 2H_2O \; \rightarrow \; 2HNO_3 + H_2O \tag{2.40}$$

The rate constant of reaction (2.39) shows a strong increase with temperature [Dimitropoulou and Marsh 1997].

2.2.3 Tropospheric Halogen Chemistry

Reactive **H**alogen **S**pecies (RHS) comprise the halogen atoms X, their monoxides XO, higher oxides X_nO_m, the hypohalous acids HOX, the halogen molecules X_2 and interhalogen compounds XY (X,Y = F, Cl, Br, I). In contrast to RHS the reactivity of reservoir species like halogen-NO_x compounds (XNO_x) or hydrogen halides (HX) are comparably slow. As will be described in this section, there are two main catalytic reaction cycles involving halogens which can destroy ozone in the troposphere, particularly in the marine boundary layer: Cycle (I) is based on the XO-self or XO-YO cross reaction, cycle (II) on the reaction of XO with HO_x radicals.

Over the past decade significant amounts of XO have been detected in the marine boundary layer (MBL) at various coastal areas. Several ground-based measurements in the Arctic [Hausmann and Platt 1994; Tuckermann et al. 1997; Martínez et al. 1999; Hönninger and Platt 2002] and in the Antarctic [Kreher et al. 1997; Friess 1997; Friess 2001] boundary layer have shown that strong and sudden release of BrO is a common feature at polar regions in springtime. The observed Bromine explosion events showed levels up to 30 ppt of BrO and were always coincident with the destruction of ozone in the boundary layer, indicating that reactive bromine is responsible for catalytic ozone destruction. Observations from satellite instruments confirm the presence of huge clouds with highly elevated BrO amounts over the polar sea ice of both hemispheres, with areas spanning several thousand square kilometers [Wagner and Platt 1998; Richter et al. 1998; Hegels et al. 1998; Hollwedel et al. 2003]. It has been proposed that these boundary layer BrO clouds may also contribute to BrO in the free troposphere [Mc Elroy et al. 1999; Roscoe et al. 2001].

Observations of BrO are scarce at mid and low latitudes, however significant concentrations correlated with ozone depletion have been observed over regions with high salt accumulation as for the Caspian Sea [Wagner et al. 2001], the Dead Sea basin[Hebestreit et al. 1999; Zingler and Platt 2004] and the Salar de Unuji(Bolivia)[Hönninger et al. 2002]. Measurements of Leser et al. [2003] suggest a background of 1-2 ppt BrO in the marine boundary layer. Quite amazing amounts of BrO, reaching up to 1 ppb have been detected recently in volcanic plumes on Montserrat Island and in Italy [Bobrowski et al. 2003; Bobrowski and Lowe 2003].

Iodine oxide (IO) was first observed at Mace Head(Ireland) by Alicke et al. [1999] at levels up to 6 ppt. Recently IO as well as OIO were found at various coastal sites with mixing ratios of few ppt on Tenerife(Canary Islands,Spain) and Cape Grim(Tasmania) [Allan et al. 2000; Allan et al. 2001], at Mace Head [Allan et al. 2000; Hebestreit 2001], at Brittany(France) [Peters and Lotter 2003], in the European Arctic [Wittrock et al. 2000] and in Antarctica [Friess et al. 2001; Friess 2001].

Elevated chlorine oxide (ClO) mixing ratios have been reported mostly for the stratosphere. First direct spectroscopic observations of up to 15 ppt chlorine oxide (ClO) in the mid-latitude boundary layer have been reported by [Stutz et al. 2002] from measurements at the Great Salt Lake(Utah). Due to fast reactions with water and hydrocarbons, fluorine atoms are rapidly converted to HF, a stable compound which is rapidly removed from the atmosphere by deposition processes.

Besides DOAS measurements of halogen oxides, photolysable bromine species (mostly HOBr,

BrO) have been detected by Impey et al. [1999] using a Photolysable Halogen Detector (PHD, conversion of reactive halogens to chloroacetone and bromoacetone and subsequent GC analysis). Hydrocarbon Clock measurements to derive chlorine and bromine atom concentrations have been reported from various locations [Jobson et al. 1994; Ramacher et al. 1999; Solberg et al. 1996; Ariya et al. 1999]. Chemical amplifier measurements by Perner et al. [1999] suggest that ClO is present in the Arctic boundary layer during ozone depletion periods. The same study suggests a tropospheric background of ClO in the order of 1 ppt. Indirect estimates of chlorine atom concentrations are in the range of 10^4–10^5 Cl atoms cm^{-3} in the Arctic, and below 10^3 Cl atoms cm^{-3} on a global scale [Rudolph et al. 1997].

2.2.3.1 Reaction Pathways of Reactive Halogen Species in the Troposphere

The main reaction schemes of the halogens Cl, Br and I are very similar regarding tropospheric chemistry. As will be discussed at the end of this section, the atmospheric relevance of fluorine is negligible due to fast reactions of fluorine atoms with H_2O or hydrocarbons to HF, and subsequent removal from the gas–phase via deposition processes. Due to the frequent similarity of reactions involving halogens, X and Y will be used instead of the chemical symbols Cl, Br or I to summarize reactions pathways if applicable.
The tropospheric lifetime of Halogen atoms is commonly reduced to few milliseconds (lifetime τ=0.08 s, 0.8 s, 0.8 s for Cl, Br, I) due to fast reactions with ozone leading to the formation of halogen oxides. The key role of halogen atoms (X, Y) and their monoxides (XO, YO) in ozone destruction has been described via two ozone destruction cycles described below [Hausmann and Platt 1994; Le Bras and Platt 1995; Platt and Janssen 1995]. The corresponding kinetic parameters are listed in table 2.7.

Cycle I:

$$X + O_3 \longrightarrow XO + O_2 \tag{2.41a}$$
$$Y + O_3 \longrightarrow YO + O_2 \tag{2.41b}$$
$$XO + YO \longrightarrow X + Y + O_2 \tag{2.41c}$$
$$\longrightarrow XY + O_2 \tag{2.41d}$$
$$\longrightarrow OXO + Y \tag{2.41e}$$
$$2\,O_3 \longrightarrow 3\,O_2$$

where X and Y denote the halogen atoms (Cl, Br, or I). An overview of the possible reaction products and the respective branching ratios for the halogen oxide self- and cross reactions is given in Table 2.8.
The halogen or interhalogen molecules XY (e.g. Br_2 or BrCl) formed in reaction (2.41d) are rapidly photolyzed during daytime:

$$XY + h\nu \longrightarrow X + Y \tag{2.42}$$

Reaction (2.41e) does not lead to a net destruction of ozone, since photolysis of OXO leads

Table 2.7: List of rate constants and photolysis frequencies for reactions and compounds in both ozone destruction cycles. Photolysis frequencies are calculated for a solar zenith angle of 70° at 80°N and surface albedo of 0.9 .

Reaction	Rate constant k $[\frac{cm^3}{molec \cdot s}]$ Photolysis frequency j $[s^{-1}]$	Reference
ClO + ClO →Products[a]	k=$1.2 \cdot 10^{-14}$	[Atkinson et al. 2003]
BrO + ClO →Products	k=$1.3 \cdot 10^{-11}$	
IO + ClO →Products	k=$1.3 \cdot 10^{-11}$	
BrO + BrO→Products	k=$3.2 \cdot 10^{-12}$	
BrO + IO →Products	k=$6.9 \cdot 10^{-11}$	
IO + IO →Products	k=$8.0 \cdot 10^{-11}$	
$Cl + O_3$ →ClO + O_2	k=$1.2 \cdot 10^{-11}$	
$Br + O_3$ →BrO + O_2	k=$1.2 \cdot 10^{-12}$	
$I + O_3$ →IO + O_2	k=$1.2 \cdot 10^{-12}$	
ClO + HO_2→HOCl + O_2	k=$5.6 \cdot 10^{-12}$	
BrO + HO_2→HOBr + O_2	k=$2.1 \cdot 10^{-11}$	
IO + HO_2 →HOI + O_2	k=$8.4 \cdot 10^{-11}$	
$Cl_2 + h\nu$ →2Cl	j=0.0021	[Röth et al. 1996]
BrCl+$h\nu$ →Br+Cl	j=0.012	[Röth et al. 1996]
$Br_2 + h\nu$ →2Br	j=0.044	[Röth et al. 1996]
$I_2 + h\nu$ →2I	j=0.26	[Tellinghuisen 1973]
ClO+$h\nu$ →Cl+O	j=$4.2 \cdot 10^{-6}$	[Röth et al. 1996]
BrO+$h\nu$ →Br+O	j=0.035	[Röth et al. 1996]
IO+$h\nu$ →I+O	j=0.35	[Lazlo et al. 1995]
HOCl+$h\nu$ →Cl + OH	j=$1.8 \cdot 10^{-4}$	[Röth et al. 1996]
HOBr+$h\nu$ →Br + OH	j=$7.6 \cdot 10^{-4}$	[Röth et al. 1996]
HOI+$h\nu$ →I + OH	j=$5.9 \cdot 10^{-3}$	[Bauer et al. 1998]

[a] See reactions 2.41c, 2.41d, 2.41e and table 2.8 for the possible products.

Table 2.8: Rate constants and branching ratios of halogen oxide self- and cross-reactions (T=298 K) [Atkinson et al. 2003]

	ClO	k_{XO+YO} $[10^{-12}\frac{cm^3}{molec\cdot s}]$	BrO	k_{XO+YO} $[10^{-12}\frac{cm^3}{molec\cdot s}]$	IO	k_{XO+YO} $[10^{-12}\frac{cm^3}{molec\cdot s}]$
ClO	$\xleftrightarrow{M}$ $Cl_2O_2^{(a)}$ $\xrightarrow{39\%}$ Cl_2+O_2 $\xrightarrow{41\%}$ $Cl+ClOO$ $\xrightarrow{20\%}$ $Cl+OClO$	1.6×10^{-2}	$\xrightarrow{49\%}$ $Br+OClO$ $\xrightarrow{44\%}$ $Br+ClOO_2$ $\xrightarrow{7\%}$ $BrCl+O_2$	13.9	$\xrightarrow{55\%}$ $I+OClO$ $\xrightarrow{25\%}$ $I+Cl+O_2$ $\xrightarrow{20\%}$ $ICl+O_2$	12.0
BrO	———		$\xrightarrow{85\%}$ $Br+Br+O_2$ $\xrightarrow{15\%}$ Br_2+O_2	3.2	$\xrightarrow{\leq30\%}$ $I+Br+O_2$ $\xrightarrow{\leq5\%}$ $IBr+O_2$ $\xrightarrow{65-93\%}$ $OIO+Br$ $\xrightarrow{\leq15\%}$ $OBrO+I$ $\xrightarrow{\sim0\%}$ $IBrO_2+M$	$83^{(b)}$
IO	———		———		$\xrightarrow{\sim0\%}$ $2I+O_2$ $\xrightarrow{\sim0\%}$ I_2+O_2 $\xrightarrow{40\%}$ $OIO+I$ $\xrightarrow{60\%}$ I_2O_2+M	$91.5^{(b,c)}$
$\frac{k_{XO+YO}}{k_{BrO+BrO}}$	$\frac{k_{ClO+ClO}}{k_{BrO+BrO}}=5.1\times10^{-3}$		$\frac{k_{ClO+BrO}}{k_{BrO+BrO}} = 4.3$ $\frac{k_{BrO+BrO}}{k_{BrO+BrO}} = 1.0$		$\frac{k_{ClO+IO}}{k_{BrO+BrO}} = 3.8$ $\frac{k_{BrO+IO}}{k_{BrO+BrO}} = 26.1$ $\frac{k_{IO+IO}}{k_{BrO+BrO}} = 28.7$	

[a] not stable in the troposphere due to thermal decomposition
[b] [Sander et al. 2003] [c] [Crowley 2004]

to the formation of oxygen atoms which recombine quickly with O_2 to form ozone:

$$OXO + h\nu \longrightarrow XO + O \tag{2.43a}$$
$$O + O_2 + M \longrightarrow O_3 + M \tag{2.43b}$$

In case of X=I, however, the photo-dissociation of OIO possibly yields I and O_2, leading to a net ozone destruction [Plane et al. 2001; Hebestreit 2001].
The reaction of XO with YO ((2.41c) and (2.41d)) is the rate limiting step of the reaction cycle. The self reactions (X=Y=Br, X=Y=Cl) are usually slower than the cross reactions (X=Br, Y=Cl). Particularly reactions involving iodine (X=I, Y=Br or Cl) are very efficient in destroying ozone.
The second catalytic cycle involves HO_x radicals:

Cycle II:

$$X + O_3 \longrightarrow XO + O_2 \tag{2.44a}$$
$$OH + O_3 \longrightarrow HO_2 + O_2 \tag{2.44b}$$
$$XO + HO_2 \longrightarrow HOX + O_2 \tag{2.44c}$$
$$HOX + h\nu \longrightarrow OH + X \tag{2.44d}$$
$$2\ O_3 + h\nu \longrightarrow 3\ O_2$$

Reactive bromine is the most important species regarding catalytic ozone destruction in the troposphere. The branching ratio of both cycles is quite sensitive to mixing ratio of halogen oxides as the efficiency of cycle II is linearly dependent on the XO concentration, being quadratic for cycle I. Thus at high XO levels cycle I will dominate, at low XO cycle II.
In the case of bromine, at 15 ppt BrO the net effect of the HO_x cycle (cycle II) is comparable to that of cycle I (assuming a typical level of 1 ppt HO_2). At 30 ppt BrO, which are frequently observed during ozone depletion in the Arctic boundary layer, 66% of the ozone destruction will take place by cycle I.
The efficiency of both cycles can be enhanced by the presence of other halogen oxide species (i.e. IO, ClO) due to cross reactions (e.g. reaction 2.41c for BrO + IO) when reaction 2.41b occurs with IO or ClO instead of BrO.
An important loss channel for the halogen oxide formed in reaction (2.41a) is its photolysis and the reaction with NO:

$$XO + h\nu \longrightarrow X + O \tag{2.45}$$
$$XO + NO \longrightarrow X + NO_2 \tag{2.46}$$

The photolysis of halogen oxides 2.45 leads to a null cycle with respect to ozone destruction, since the oxygen atom formed quickly recombines with O_2 to yield ozone (reaction 2.43b).
Stutz et al. [1999] calculated the importance of the different cycles for the ozone destruction rate $d[O_3]/dt$ as a function of the NO_x mixing ratio (Figure 2.4) for given 6 ppt iodine oxide. Assuming no loss of reactive halogens and all self and cross reactions leading to O_3 destruction

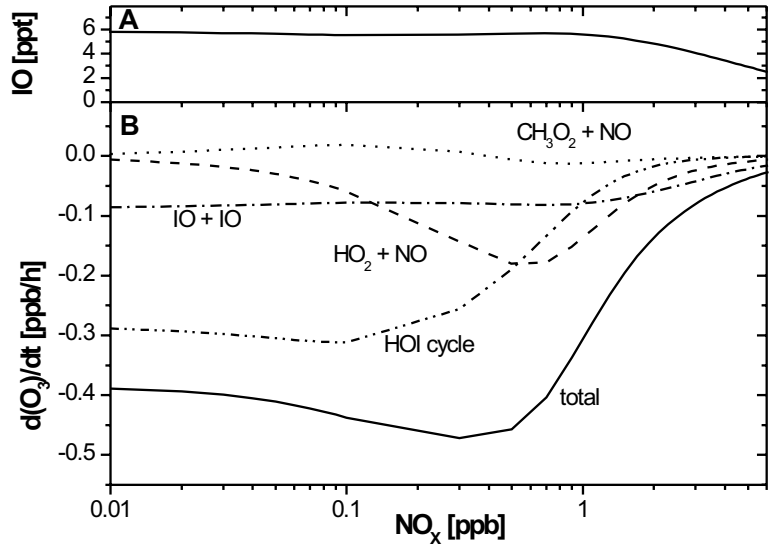

Figure 2.4: Ozone destruction rates of the different catalytic reaction cycles for the case of iodine, as a function of the NO_x concentration. Adapted from Stutz et al. [1999].

channels, an upper limit of the ozone loss rate as a function of XO concentration can be expressed as:

$$-\frac{d[O_3]}{dt} = 2 \cdot \sum_{i,j} k_{X_iO+Y_jO}[X_iO][Y_jO] + \sum_i k_{X_iO+HO_2}[X_iO][HO_2] \tag{2.47}$$

where the combined effects of the cycles I (including all self and cross reactions) and cycle II are taken into account.

At high NO_x concentrations, e.g. in the polluted marine boundary layer the exchange reactions with the reservoir species XNO_3 can significantly alter the partitioning of reactive halogen species.

$$XO + NO_2 \longrightarrow XNO_3 \tag{2.48a}$$

$$XNO_3 + h\nu \longrightarrow XO + NO_2 \tag{2.48b}$$

However, these reactions represent a null cycle with no net chemistry unless the photolysis of XNO_3 takes place in the XO + NO_2 channel. If X + NO_3 were formed instead, additional O_3 loss would result.

Apart from its importance for the destruction of ozone the reaction of halogen oxides with hydroperoxy radicals (2.44c) followed by the photolysis of the product from this reaction, the hypohalous acids HOX (2.44d), also have a strong influence on the ratio of OH/HO_2 [Stutz et al. 1999; Hebestreit 2001]. In analogy to reaction 2.44c, XO can also react with organic peroxy radicals (RO_2, R = organic group), e.g. the methyl peroxy radical, CH_3O_2, instead of HO_2. It has been shown in laboratory experiments that this reaction is very efficient for X=Br, yielding HOBr in about 80% of the reactions. [Aranda et al. 1997].

The efficiency of the catalytic ozone destruction cycles involving halogen radicals strongly depends on the number of cycles that the reactive compounds X and XO can pass before

being lost to a reservoir species. Regarding the halogen group from fluorine over chlorine and bromine to iodine, the reactivity of the halogen atoms decreases strongly. To assess the role of a halogen species in ozone destruction the branching ratio for the reaction of X with ozone (2.41a) and the reactions with hydrocarbons RH has to be considered. For bromine and iodine the reactions with HO_x are also important branching reactions:

$$X + RH \longrightarrow HX + R \tag{2.49}$$

$$X + HO_2 \longrightarrow HX + O_2 \tag{2.50}$$

$$XO + HO_2 \longrightarrow HOX + O_2 \tag{2.51}$$

- *Fluorine* atoms released in the troposphere react very quickly with atmospheric water vapor, which is much more abundant than hydrocarbons (e.g. CH_4). HF is stable against photolysis or reaction with OH. Therefore fluorine will always remain in this passive form and has no effect on ozone chemistry [Wayne et al. 1995].
- *Chlorine* atoms react rapidly with CH_4 and other hydrocarbons to form HCl. However, Cl can be reactivated in principle by reaction of HCl with OH and under certain circumstances it is released as a byproduct of the autocatalytic bromine release (see section 2.2.3.2).
- *Bromine* atoms only react with unsaturated hydrocarbons and already oxidized compounds like aldehydes.
- *Iodine* atoms almost exclusively react with ozone or other radicals.

The relative reaction rate $R_{O_3}/(R_{O_3} + \sum R_{RH} + R_{HO_2})$ is a measure of the probability of the reaction of a halogen atom with ozone. Table 2.9 gives a survey of the situation for all 4 halogens.

Table 2.9 shows, that fluorine is of no importance in the atmosphere since conversion to HF is very fast. Therefore, as reactive halogen species in the troposphere only chlorine, bromine and iodine are considered. In the case of chlorine about half of it is consumed by reactions with hydrocarbons. For bromine, however, the probability for reaction with ozone is 98% and reaching almost unity for iodine.

Assuming that all XO radicals formed in the reaction of X with O_3 are 100% reconverted to X atoms by self and cross reactions, the fraction of the rates R_{O_3} of reaction 2.41a and the sum of the rates $R_{RH} + R_{HO_2}$ of reactions 2.49 and 2.50 is an approximation of the mean number of catalytic ozone destruction cycles that a halogen atom can pass. This relation is shown in the last column in Table 2.9. As one can see, the ozone destruction efficiency of Bromine and especially Iodine outgoes largely that of Cl.

To describe the partitioning between the main RHS X and XO the ratio of the halogen oxide concentration [XO] and the corresponding halogen atom [X] is determined by the relative rates of the reactions which convert X into XO (the halogen reaction with ozone 2.41a and the reaction with hydrocarbons RH and HO_x (2.49, 2.50) and the reactions transforming XO to X (NO reaction, self- or cross-reaction and photolysis (2.46, 2.41c, 2.45)):

$$\frac{[XO]}{[X]} = \frac{k_{X+O_3}[O_3] + k_{X+RH}[RH]}{k_{XO+NO}[NO] + 2 \cdot k_{XO+XO}[XO] + k_{XO+YO}[YO] + J(XO)} \tag{2.52}$$

Table 2.9: Comparison of the branching between reaction 2.49, 2.50 and 2.41a. The 6^{th} column is a measure of the probability of the reaction with ozone, the last column can be seen as a zero order approximation for the number of ozone destruction cycles a halogen atom can pass before being lost to the reservoir.

X	RH	k^*_{X+RH} (k_{X+O_3}) $[cm^3 s^{-1}]$	$typ[RH]$ ($typ[O_3]$) $[cm^{-3}]$	$R_{RH} = k_{X+RH}[RH]$ ($R_{O_3} = k_{X+0_3}[O_3]$) $[s^{-1}]$	$\frac{R_{O_3}}{R_{O_3}+\sum R_{RH}+R_{HO_2}}$	$\frac{R_{O_3}}{\sum R_{RH}+R_{HO_2}}$
F	H_2O	$1.4 \cdot 10^{-11}$	$7 \cdot 10^{16}$	$2.8 \cdot 10^6$	$3.5 \cdot 10^{-6}$	$3.5 \cdot 10^{-6}$
	CH_4	$6.3 \cdot 10^{-11}$	$4.0 \cdot 10^{13}$	$2.6 \cdot 10^3$		
				$\sum R_{RH} = 2.8 \cdot 10^6$		
	(O_3	$1.0 \cdot 10^{-11}$	$1.0 \cdot 10^{12}$	10.0)		
Cl	CH_4	$1.0 \cdot 10^{-13}$	$4.0 \cdot 10^{13}$	4.0	0.52	0.92
	C_2H_6	$5.9 \cdot 10^{-11}$	$3.0 \cdot 10^{10}$	1.7		
	C_3H_8	$1.4 \cdot 10^{-10}$	$1.0 \cdot 10^{10}$	1.4		
	$HCHO$	$7.3 \cdot 10^{-11}$	$1.0 \cdot 10^{10}$	0.73		
	C_2H_2	$2.0 \cdot 10^{-10}$	$1.0 \cdot 10^{10}$	2.1		
	C_2H_4	$6.0 \cdot 10^{-10}$	$5.0 \cdot 10^9$	1.5		
				$\sum R_{RH} = 11$		
	(O_3	$1.2 \cdot 10^{-11}$	$1.0 \cdot 10^{12}$	12.0)		
Br	$HCHO$	$1.1 \cdot 10^{-12}$	$1.0 \cdot 10^{10}$	0.01	0.984	60
	HO_2	$1.7 \cdot 10^{-12}$	$1.0 \cdot 10^{-8}$	$2.0 \cdot 10^{-4}$		
				$\sum R_{RH} = 2.0 \cdot 10^{-2}$		
	(O_3	$1.2 \cdot 10^{-12}$	$1.0 \cdot 10^{12}$	1.2)		
I	HO_2	$3.8 \cdot 10^{-13}$	$1.0 \cdot 10^8$	$3.8 \cdot 10^{-5}$	0.99997	$3.1 \cdot 10^4$
	(O_3	$1.2 \cdot 10^{-12}$	$1.0 \cdot 10^{12}$	1.2)		

**rate constants taken from* [Sander et al. 2003]

Due to the fast photolysis of the IO radical the IO/I ratio is between 1 and 10 for typical NO_x and O_3 levels [Platt and Janssen 1995; Vogt et al. 1996], well below ratios found for BrO/Br and ClO/Cl which are in the order of 100 and 1000 respectively [Barrie et al. 1988]. Figure 2.5 shows a schematic overview of the halogen chemistry in the troposphere adapted from Platt and Janssen [1995].

2.2.3.2 Sources of Reactive Halogen Species in the Troposphere

Halogen release mechanisms have been the subject of a number of model, laboratory and field investigations. Despite some still unresolved details, two main sources have been identified: Halogen release from sea salt and the photolysis of photolabile organohalogens.

Halogen Release from (Sea) Salt The release of halogens from sea salt via heterogeneous reactions was introduced by Holland [1978] two decades ago. In the early 1990s the first release mechanisms were described by Fan and Jacob [1992], Mozurkewich [1995], Platt and Lehrer [1996], Sander and Crutzen [1996] and Vogt et al. [1996]. Evidence from laboratory measurements was reported by Oum et al. [1998], Behnke et al. [1997], Fickert et al. [1999] and Kirchner et al. [1997] in the past years.
By weight, sea salt contains 55.7% Cl^-, 0.19% Br^- and 2×10^{-5}% I^- [Holland 1978]. Through sea ice surfaces, salt deposits on snow and aerosol particles, sea salt is in contact with the atmosphere. It represents a large reservoir of halogens, which is available at almost every coastline and - in form of aerosols - present over the open sea. However, the absolute atmospheric halogen input from sea salt remains uncertain [Platt and Lehrer 1996; Wennberg

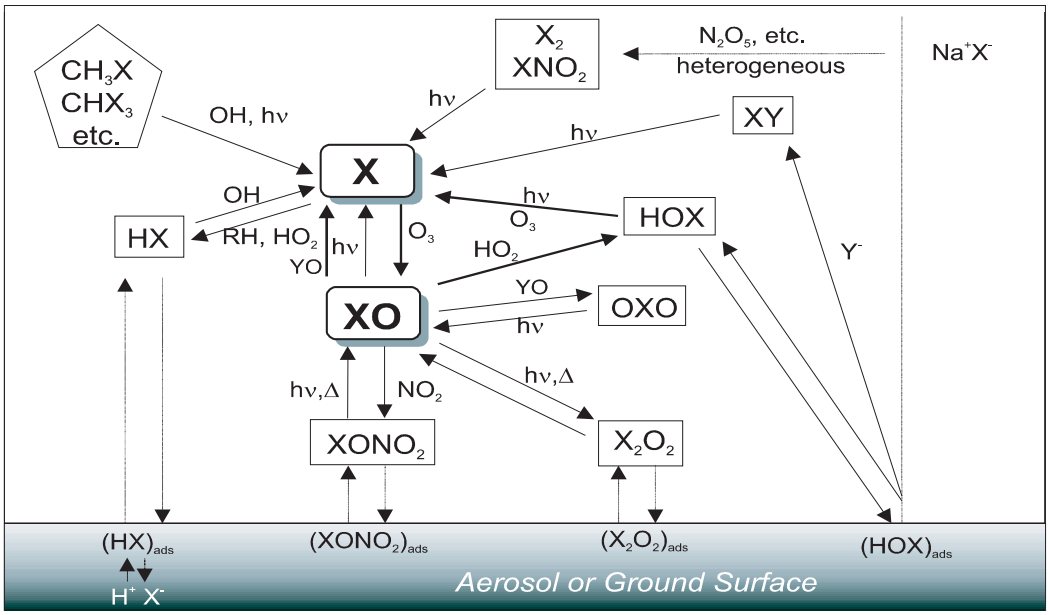

Figure 2.5: Schematic overview of tropospheric halogen chemistry (X = Cl, Br, I), adapted from Platt and Janssen [1995]. Heavy lines indicate ozone-destruction sequences. Sources of RHS are the release from sea salt and the photolysis of halocarbons.

1999; Platt and Stutz 1998]. On land, marshes and salt lakes as the Dead-Sea are mostly very efficient local sources of halogens [Hebestreit et al. 1999].
The most effective release process of reactive halogen species from (Sea) salt is the *autocatalytic or halogen-catalyzed liberation*. This process is based on the uptake of gaseous HOX (as produced by reactions 2.53a and 2.53b) on acidic salt surfaces [Fan and Jacob 1992; Tang and McConnell 1996; Vogt et al. 1996], followed by the formation of an (inter-) halogen molecule in the aqueous phase(reaction 2.53d):

$$X + O_3 \longrightarrow XO + O_2 \tag{2.53a}$$
$$XO + HO_2 \longrightarrow HOX + O_2 \tag{2.53b}$$
$$(HOX)_g \longrightarrow (HOX)_{aq} \tag{2.53c}$$
$$(HOX)_{aq} + (Y^-)_{aq} + (H^+)_{aq} \longrightarrow (XY)_{aq} + H_2O \tag{2.53d}$$
$$(XY)_{aq} \longrightarrow (XY)_g \tag{2.53e}$$
$$XY + h\nu \longrightarrow X + Y \tag{2.53f}$$

net: $$X + HO_2 + (Y^-)_{aq} + (H^+)_{aq} + O_3 \xrightarrow{h\nu} X + Y + H_2O + 2O_2$$

The (inter-)halogen molecule XY (e.g. Br_2 or BrCl) is highly volatile and quickly released to the gas phase (reaction 2.53e), being readily photolyzed during daytime (table 2.7) to further react quickly with ozone to form again XO or YO (2.41a or 2.41b).
The above described process is particulary effective regarding bromine and was denominated as *"bromine explosion events"* by Platt and Lehrer [1996] since it can lead to an exponential growth of the gas phase BrO concentration. Indeed several of this explosion events have

been observed in polar regions in springtime, both for the Arctic [Hausmann and Platt 1994; Tuckermann et al. 1997; Martínez et al. 1999; Hönninger and Platt 2002] and in the Antarctic [Kreher et al. 1997; Friess 1997; Friess 2001] boundary layer. However, the occurrence of bromine explosion events is bound to a number of prerequisites described in the separate paragraph below.
The current understanding is that bromine is mainly released by the autocatalytic process, while chlorine is a by-product since bromine release is preferred to chlorine, even though it is much less abundant in a sea salt solution [Fickert et al. 1999]. However, the simultaneous release of small amounts of BrCl leads to a 'bromine-catalyzed liberation of chlorine'. A 'chlorine explosion' is much less probable due to very inefficient gas-phase conversion of Cl to HOCl and the rapid removal of chlorine atoms through the reaction with methane (Table 2.9). An 'iodine explosion' is not expected to occur since the concentration of iodine in sea salt is too small. However, previous reactive iodine chemistry can lead to strong enrichments in particulate iodine, which are known to occur [Gäbler and Heumann 1993]. Additionally, reactive iodine can accelerate the release of Br and Cl from sea salt due to faster gas phase reactions [Vogt et al. 1999].

Autocatalytic bromine release - the bromine explosion The mechanism suggested to cause the observed sudden BrO enhancements in the boundary layer is the autocatalytic release of bromine involving heterogeneous reactions on acidic sea salt surfaces (aerosols or ice particles) [Fan and Jacob 1992; Tang and McConnell 1996; Vogt et al. 1996]. The primary bromine release mechanism as illustrated in figure 2.2.3.2 is started by the the uptake of gaseous HOBr (process 2.54a):

$$(HOBr)_g \longrightarrow (HOBr)_{aq} \tag{2.54a}$$
$$(HOBr)_{aq} + (Cl^-)_{aq} + (H^+)_{aq} \longrightarrow (BrCl)_{aq} + H_2O \tag{2.54b}$$
$$(BrCl)_{aq} + (Br^-)_{aq} \longrightarrow (Br_2Cl^-)_{aq} \tag{2.54c}$$
$$(Br_2Cl^-)_{aq} \longrightarrow (Br_2)_{aq} + (Cl^-)_{aq} \tag{2.54d}$$
$$(Br_2)_{aq} \longrightarrow (Br_2)_g \tag{2.54e}$$
$$Br_2 + h\nu \longrightarrow 2Br \tag{2.54f}$$
$$2(Br + O_3) \longrightarrow 2(BrO + O_2) \tag{2.54g}$$
$$2(BrO + HO_2) \longrightarrow 2(HOBr + O_2) \tag{2.54h}$$

net: $$HOBr + (Br^-)_{aq} + (H^+)_{aq} + 2HO_2 + 2O_3 \xrightarrow{h\nu} 2HOBr + H_2O + 4O_2$$

In the aqueous phase HOBr reacts with ions of chlorine or bromine to forming (inter-)halogen molecules which are rapidly emitted to the gas phase due to their low solubility. The photolysis of Br_2 and BrCl leads to the release of two halogen atoms for each halogen atom taken up by the sea salt surface as HOBr. This leads to an exponential growth of gaseous reactive bromine, the *bromine explosion* [Platt and Lehrer 1996]. The release of Br_2 is preferred over BrCl, even if Br is much less abundant in a sea salt solution [Fickert et al. 1999]. The principal mechanisms involved in the autocatalytic bromine release could also be reproduced by Lehrer [1999] using a 1D model including the above described gas phase and heterogeneous

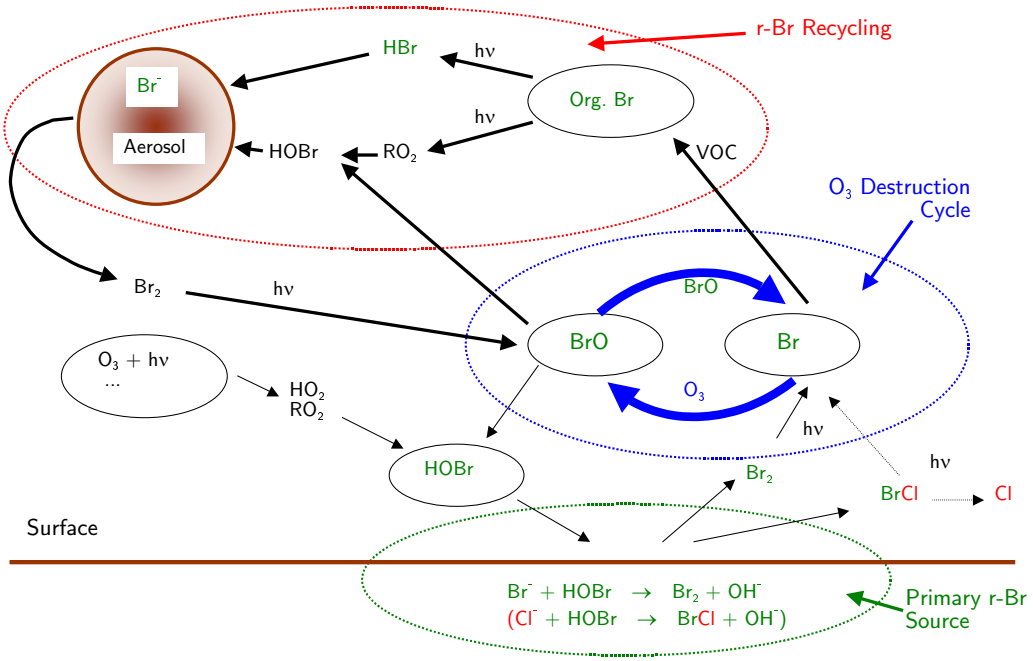

Figure 2.6: Overview of the tropospheric bromine chemistry including the bromine explosion mechanism.

reactions (on the sea ice surface as well as on the aerosol) and turbulent vertical mixing in the boundary layer.
The following prerequisites are necessary for a bromine explosion to take place:

1. The bromine release from sea salt only occurs for pH<6.5 (due to reaction 2.54b [Fickert et al. 1999]). The necessary acidity of the salt surface can be supplied by uptake of gaseous HCl or other strong acids, such as HNO_3 and H_2SO_4 [Keene et al. 1998; Lehrer 1999]. The average pH of sea water lays in the range of 7.3-8.3.

2. The heterogeneous processes only lead to an exponential increase in gaseous reactive bromine if more than one bromine atom is produced for each scavenged HOBr molecule. This is the case as long as the release of Br_2 is preferred to that of BrCl as e.g. reported by Fickert et al. [1999].

3. To sustain the high concentrations of the reactive bromine, the meteorological conditions must prevent boundary layer air from mixing with free tropospheric air. During late winter and early spring, strong inversion layers in the lowermost 1000 m of the polar atmosphere effectively prevent upward mixing of boundary layer air.

4. Since the aerosol usually cannot provide enough surface area to release the observed amounts of reactive bromine, areas with highly enriched salt concentration are required. This is obviously given for salt-pans as formed at the dead sea. In polar regions sea ice surfaces can be strongly enriched in sea salt. These are present as surface brines (a liquid layer with a high salinity on the frozen sea ice) and frost flowers on freshly frozen sea ice

5. The autocatalytic bromine release and the subsequent destruction of ozone requires light, so bromine explosions only occur after polar sunrise.

6. An initial small amount of reactive bromine is needed to start the heterogeneous bromine release on these sea salt surfaces.

7. The released bromine causes the destruction of ozone in the marine boundary layer. When all ozone is consumed, reactive Br is converted into HBr and either taken up by the aerosol or deposited at the surface as bromide(Br^-). It can re-enter the gas phase during another bromine explosion.

8. After the inversion layer breaks up ozone is mixed in from higher altitudes.

The large accumulation of sea ice and snow at polar regions in winter is a rich source of halogens in spring, when the emergence of sunlight and the presence of a strong inversion layer allows the occurrence of bromine catalyzed ozone destruction episodes. Depending on atmospheric conditions, this cycle can restart several times during polar spring or basically every day for stable conditions as found in the dead sea region.

Halogen Release from Degradation of Organohalogens More than 3800 organohalogen compounds, mainly containing chlorine or bromine (a few with iodine and fluorine), are produced by living organisms or are formed during natural abiogenic processes, such as volcanoes, forest fires, and other geothermal processes. The oceans are the single largest source of biogenic organohalogens, which are biosynthesized by myriad seaweeds, sponges, corals, tunicates, bacteria and other marine life. Terrestrial plants, fungi, lichen, bacteria, insects, some higher animals and even humans also account for a diverse collection of organohalogens. The breakdown of organohalogen compounds is approximately: organochlorine, 2200; organobromine, 1950; organoiodine, 95; organofluorine, 100. A few hundred of these compounds contain both chlorine and bromine [Gribble 2003].
In contrast to the terrestrial environment, where only very low or no concentrations of volatile brominated and iodinated compounds were found, marine organisms seem to be negligible contributors for chlorinated compounds [Laturnus et al. 2000]. Global estimates of organohalogen emission fluxes are associated with significant uncertainty, arising from data precision and coverage, choice of air-sea exchange parameterizations and model assumptions. Although an annual atmospheric input of approximately $10^8 - 10^{10}$ g bromine and $10^7 - 10^8$ g iodine, marine macroalgae are apparently not the major source of halogens on a global scale, as the release is up to four orders of magnitude lower than a presumed annual flow from the oceans. The ice algae community, phytoplankton [Tokarczyk and Moore 1994] and other minor sources contribute significantly to halogen budgets. Despite this, macroalgae may be more important on a local scale due to their occurrence at a high biomass in the coastal regions [Mäkelä et al. 2002; Laturnus 2001; Giese et al. 1999].
Methyl halides (CH_3X) are the most abundant form of gaseous halogens, reaching a global annual source strength about 3.5–5 Teragrammes methyl chlorine (CH_3Cl), 0.8 Tg CH_3Br and 3 Tg methyl iodine respectively [Ballschmiter 2003]. However, the regional distribution of the emissions fluxes is quite inhomogeneous. In the case of CH_3Cl about 85% of global

emissions occur in the equatorial region (ranging from 30°N to 30°S) [Keene et al. 1999]. Other measurable organohalogen species include polyhalogenated compounds like bromoform (tribromomethane, $CHBr_3$) or iodoform (triiodomethane, CHI_3), dibromo- and diiodomethane (CH_2Br_2, CH_2I_2). Also, short-chained organic halogens including different halogen species such as CH_2ClI or CH_2IBr [Wayne et al. 1995] have been detected in the atmosphere in significant amounts (see Table 2.10). The estimated annual oceanic input from combined algae sources to the atmosphere are $10^{10} - 10^{12}$ grammes Bromine and $10^{11} - 10^{12}$ g Iodine per year respectively [Giese et al. 1999]. Anthropogenic bromine emissions ($10^{10} - 10^{12}$ g Br yr^{-1}) are of similar magnitude as the biogenic sources. Whereas biogenic emissions seem to consist primarily of $CHBr_3$, the primary compound emitted by anthropogenic activity is CH_3Br [Goodwin et al. 1997]. Fumigation and industrial emissions and especially in the tropics biomass burning are the most important anthropogenic sources of halogenated hydrocarbons, which lead to an estimated man–made production of $(10 - 50) \cdot 10^9$ g CH_3Br/year [Manøand Andreae 1994].
In contrast to CFCs, which are photostable in the troposphere, most brominated and iodinated halocarbons can be photolyzed even at low UV intensity in the planetary boundary layer or the free troposphere. Table 2.10 shows the typical mixing ratios and photolytic lifetimes in the troposphere for several halogenated hydrocarbons of importance for the tropospheric halogen budget.

Due to the relatively long lifetime the most abundant organohalogen compound, CH_3Br, is more likely to play a significant role in the stratosphere compared to $CHBr_3$ (0.8 years and 1.2 months respectively). Particulary striking are the comparatively short lifetimes of the iodinated hydrocarbons. Especially as the iodide content of sea salt is only of the order of 10^{-5} % [Holland 1978], iodocarbon photolysis deserves more attention as RHS source than the iodine release from sea salt. As an example the photolytic lifetime of CH_3I is about hundred times shorter than its lifetime with respect to the reaction with OH [Sander et al. 2003] and photolysis of the alkyl iodides occurs on a much shorter timescale than for the equivalent bromine or chlorine compounds [Carpenter et al. 1999]. Indeed, the photochemical breakdown of organic halides such as CH_2I_2,CH_2ICl and CH_3I are probably the major source of reactive iodine in the marine boundary layer.

The atmospheric Iodine cycle The main origin of organic iodine in seawater appears to be marine algae. The mechanism for production of monohalogenated compounds as CH_3I involves a halide ion methyl transferase enzyme [Wuosmaa and Hager 1990], found in both macroalgae(seaweeds) and microalgae(phytoplankton), whereas di- and trihalogenated halocarbon production (as CH_2I_2,CH_2ICl,$CHBr_2Cl$) involves the haloperoxidase enzyme, present in a wide range of terrestrial and marine organisms [Wever et al. 1991]. Haloperoxidases catalyze the oxidation of halides by hydrogen peroxide, which is released as part of normal cell metabolism and during defense reactions. The resulting reactive electrophile halogenating species can react with available organic material within the cell via the iodoform reaction to form volatile organohalogens thtat are released to the surrounding seawater or air. Under conditions of oxidative stress, e.g. at elevated temperatures or when

Table 2.10: Lifetime and typical tropospheric mixing ratios of brominated and iodinated hydrocarbons.

Compound	Location	Concentration[ppt]		Reference	Lifetime
		Mean	Range		
CH_3Br	W.Ireland	13.9	9.3-26.1	CAR99	0.8 years[a]
$CHBr_3$	W.Ireland	6.8	1.0-22.7	CAR03	1.2 months[b]
	Tasmania	2.6	0.7-8.0	CAR03	
	Spitzbergen	0.45	0.02-0.2	SCH93	
	Asian Seas	1.2	0.3-7.1	YOK97	
	Antarctic	6.3±6	1.0-37.4	REI92	
CH_2Br_2	W.Ireland	1.44	0.28-3.39	CAR03	4 months[c]
	Tasmania	0.43	0.10-1.39	CAR03	
C_2H_5I	W.Ireland	0.2	0.1-0.5	CAR99	40 hours[d]
CH_2BrCl	Spitzbergen	<0.5		SCH93	5 months[e]
$CHBr_2Cl$	W.Ireland	0.44	0.13-1.62	CAR03	1.2 months[e]
	Tasmania	0.19	0.05-0.78	CAR03	
	Spitzbergen	0.3	<0.01-1	SCH93	
CH_3I	W.Ireland (spring)	0.43	0.12-1.47	CAR99	5 days[d]
	W.Ireland (summmer)	3.78	1.30-12.03	CAR00	
	Spitzbergen	1.04	<0.004-2.12	SCH93	
	Asian Seas	0.63	0.24-2.0	YOK97	
	Tasmania	2.6	1.0-7.3	CAR03	
C_2H_5I	W.Ireland (spring)	0.06	<0.02-0.21	CAR99	40 hours[d]
	W.Ireland (summmer)	0.16	<0.02-0.50	CAR00	
	Asian Seas	0.09	0.03-0.31	YOK97	
	Spitzbergen	0.20	<0.02-2.28	SCH93	
CH_2ICl	W.Ireland (spring)	0.11	<0.02-0.21	CAR99	5 hours[d]
	W.Ireland (summmer)	0.16	<0.02-0.50	CAR00	
	Spitzbergen	0.07	<0.004-0.18	SCH93	
	Alert	0.01	<0.01-0.05	YOK96	
	Tasmania	0.04	0.0-0.39	CAR03	
CH_2IBr	W.Ireland (spring)	0.08	<0.02-0.32	CAR99	45 minutes[d]
	W.Ireland (summmer)	0.06	<0.02-0.30	CAR00	
CH_2I_2	W.Ireland (spring)	0.05	<0.02-0.36	CAR99	5 minutes[d]
	W.Ireland (summmer)	0.10	<0.02-0.46	CAR00	
	Spitzbergen	0.46	<0.08-1.02	SCH93	

CAR99 [Carpenter et al. 1999] CAR00 [Carpenter et al. 2000] CAR03 [Carpenter et al. 2003]
REI92 [Reifenhäuser and Heumann 1992] SCH93 [Schall and Heumann 1993] YOK96 [Yokouchi et al. 1996]
YOK97 [Yokouchi et al. 1997]
[a] [Colman et al. 1998] [b] [Moortgat et al. 1993] [c] [Mellouki et al. 1992]
[d] [Vogt et al. 1999] [e] [Bilde et al. 1998]

exposed to grazing, H_2O_2 would otherwise build up to high levels with fatal consequences for the health of the organism [Carpenter 2003].

CH_3I is emitted into the atmosphere mainly as a result of biological methylation of iodine and is readily photolyzed to produce iodine atoms, which may influence the atmospheric ozone budget. The predominant source of atmospheric CH_3I has been considered to be marine organisms. Considerable evidence has supported the notion that macroalgae (seaweed such as kelp) are CH_3I sources, but many laboratory culture experiments have indicated that this production (10^7 to 10^8 $g\ year^{-1}$) is insignificant compared with the global CH_3I flux ($1 - 4 \times 10^{11}$ $g\ year^{-1}$). This appears to be due to the limited distribution of macroalgae only in coastal regions and hence the limited biomass available. Microalgae (phytoplankton) are widely distributed in the ocean and have a greater biomass than macroalgae. However, several laboratory studies have shown that microalgal production (10^9 to 10^{10} $g\ year^{-1}$) also seems to be insufficient to account for the global flux. Therefore, the involvement of other organisms such as bacteria has been inferred, but no direct evidence has yet been reported. The main reaction path for reactive iodine is cycle (2.44) involving HO_x radicals which is more efficient in destroying ozone at the observed iodine levels than the cycle involving the IO self reaction (2.41). Model calculations have shown that the IO/HO_x cycle accounts for up to 75% of the ozone destruction if 6 ppt of inorganic iodine are present in the MBL [Stutz et al. 1999] (see Figure 2.4). The importance of reactive iodine on the tropospheric ozone budget could thus be comparable to the photolytic ozone loss processes involving HO_x if only a few ppt of reactive iodine are present. In contrast to the other halogens I atoms do not react with hydrocarbons to form HI. However, HI is formed in the reaction of iodine with HO_2,

$$I + HO_2 \longrightarrow HI + O_2 \tag{2.55}$$

In case of iodine the reactivation of I from the HI reservoir via the reaction

$$HI + OH \longrightarrow I + H_2O \qquad\qquad k = 3 \cdot 10^{-11} cm^3 molec^{-1} s^{-1} \tag{2.56}$$

can take place, but is slow due to the lifetime of HI due to reaction with OH of about 7 to 9 hours (at typical OH concentrations of $1{\times}10^6$molec/cm^3). The iodine compounds $IONO_2$, I_2O_2 and INO_2 with photolytic lifetimes of less than 1 hour act only as temporary reservoir species and not as a sink for reactive iodine.

The fate of reactive iodine is presently not completely understood, however, since large aerosols are usually enriched in iodine (in the form of iodate IO_3^-), irreversible uptake of inorganic iodine on aerosols seems to be an important loss mechanism for reactive iodine. Vogt et al. [1999] have suggested the uptake of the IO dimer I_2O_2 on aqueous aerosol surfaces or the self- reaction of IO in the aqueous phase, followed by a hydrolysis reaction:

$$IO + IO \longrightarrow I_2O_2 \tag{2.57a}$$

$$I_2O_2 + (H_2O)_{aq} \longrightarrow (HOI)_{aq} + (IO_2)^-_{aq} + (H^+)_{aq} \tag{2.57b}$$

$$IO + IO + H_2O \longrightarrow (HOI)_{aq} + (IO_2)^-_{aq} + (H^+)_{aq} \tag{2.57c}$$

$$(IO_2)^-_{aq} + (H_2O_2)_{aq} \longrightarrow (IO_3)^-_{aq} + H_2O \tag{2.57d}$$

The formation of iodate (IO_3^-) is a possible loss process for reactive iodine since reactions (2.57) lead to an accumulation of this compound in the aerosol. Another possible sink are OIO radicals as products of the IO self reaction (for rate constants and branching ratios see Table 2.8):

$$IO + IO \longrightarrow OIO + I \tag{2.58}$$

Although initially it was thought that OIO is photostable, recent studies have shown that photodissociation of OIO can proceed via two channels [Atkinson et al. 2003]:

$$\begin{aligned} \mathrm{OIO} + \mathrm{h}\nu &\rightarrow \mathrm{I} + \mathrm{O_2} \qquad (\lambda \leq 3987\,\mathrm{nm}) && (2.59)\\ &\rightarrow \mathrm{IO} + \mathrm{O}(^3\mathrm{P}) \qquad (\lambda \leq 415\,\mathrm{nm}) && (2.60)\\ & && (2.61) \end{aligned}$$

Channel (2.59) would enhance O_3 depletion, since the combination of reactions (2.58) and (2.59) removes two O_3 molecules, whereas channel (2.60) would lead to a null cycle. Several groups [Cox et al. 1999; Ingham et al. 2000] have shown that OIO has a strong absorption spectrum consisting of sequences of bands grouped in triplets between 480 and 645 nm. However, the bond dissociation energy for OI–O has been calculated from quantum theory to be $288 \pm 16\ kJ\ mol^{-1}$ [Misra and Marshall 1998], corresponding to a photo-dissociation threshold for OIO via channel (2.60) of approximately 415 nm. Indeed, Ingham et al. [2000] failed to observe O atoms produced from the photolysis of OIO at 532 nm. In contrast, channel (2.59) is close to thermoneutral [Misra and Marshall 1998], so that absorption in these visible bands could lead to I atom production. According to [Ashworth et al. 2002] the photolysis lifetime of OIO is about one second and almost certainly leads to I+O_2. This is in agreement with observations as OIO has only be detected after sunset so far [Allan et al. 2001; Hebestreit 2001; Plane et al. 2001]. Other sinks for OIO are the rapid reaction with NO (k(300 K) = 6.34×10^{-12} cm^3 molec.$^{-1}$ s^{-1}) and possibly with OH leading to a reconversion of OIO into reactive iodine:

$$OIO + NO \longrightarrow IO + NO_2 \tag{2.62a}$$

$$OIO + OH \longrightarrow IO + HO_2 \tag{2.62b}$$

Measurements of Hebestreit [2001], who observed OIO for the first time in the boundary layer, suggest that the reaction with NO (2.62a) is the most important loss process for OIO. The estimated lifetime of OIO with respect to this reaction is approximately 20 minutes. The NO mixing ratios during the measurements performed at Mace Head, Ireland, were in the range of 0.25 - 1 ppb.

Hoffmann et al. [2001] pointed out that another possible fate of OIO and IO is the polymerization of IO and OIO to higher iodine oxides I_xO_y forming aerosols as reported from laboratory experiments[Cox and Coker 1983; Harwood et al. 1997; Hönninger 1999]. Hoffmann et al. [2001] argue that this process could be responsible for bursts of new particles frequently observed in the coastal environment during low tide [O'Dowd 2001]. Furthermore it could explain the enrichment of iodate in marine aerosols, although the detailed mechanisms are completely unclear to date.

As a result the formation of OIO can possibly be an important sink for reactive iodine, particularly under low NO_x conditions. Figure 2.7 summarizes the current knowledge of iodine chemistry in the troposphere.

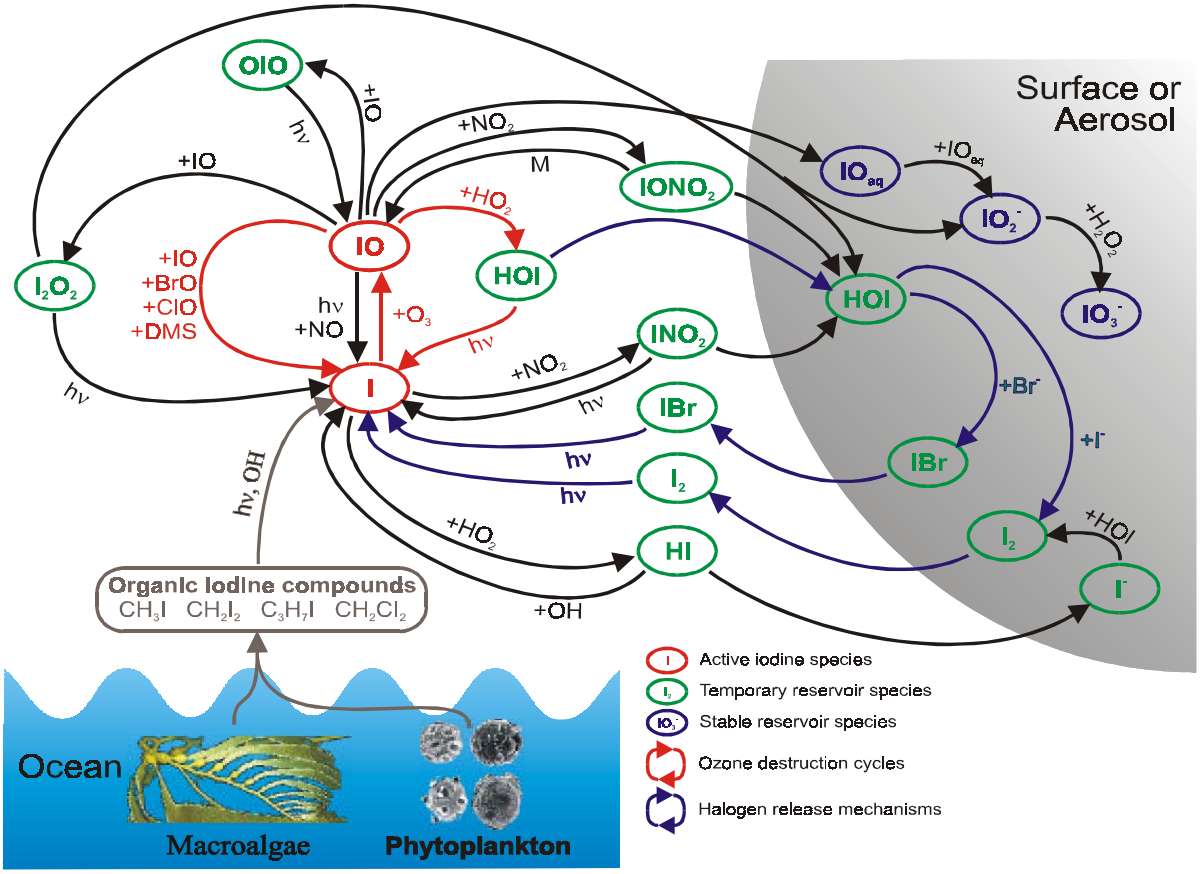

Figure 2.7: Overview of the tropospheric iodine chemistry: Source gases are shown in brown, red arrows indicate ozone depleting catalytic reaction cycles, and blue arrows indicate heterogeneous release processes. Adapted from Platt and Janssen [1995] and Vogt et al. [1999]

Halogen release via the attack of strong acids on halides The attack of strong acids such as H_2SO_4 on sea salt aerosols is known to release gaseous halogen compounds as e.g. HX:

$$H_2SO_4 + 2(NaX)_{aerosol} \longrightarrow 2HX + Na_2SO_4 \tag{2.63}$$

A recycling of gaseous HX via heterogeneous reactions is possible and is supposed to be of mayor importance in polar regions [McFiggans et al. 2000; Sander et al. 1999; Vogt et al. 1999] and in the remote marine boundary layer [Seisel and Rossi 1997]. On the surface of sea salt aerosols the reaction of HOX with HX is followed by the release of the (inter)halogen molecule XY to the gas phase [Abbatt 1994; Abbatt 1995; Abbatt and Nowak 1997] where it is rapidly photolyzed (reactions 2.53a to 2.53f and Table 2.7). Seisel and Rossi [1997] discovered a reaction that requires cold and acidified aerosol surfaces. Therefore this reaction

of nitrous acid (HONO) and Br^-

$$HONO + Br^- \longrightarrow BrNO + H_2O \tag{2.64}$$

could be of importance in polar regions but not at mid latitudes. Significant HONO production from the snowpack by photochemical reactions was found by Zhou et al. [2001] in the Canadian arctic.

Halogen release via NO_y species Anthropogenic emitted species like NO_2 and N_2O_5 have been found to release halogens from sea salt [Finlayson-Pitts and Johnson 1988; Finlayson-Pitts et al. 1989; Mozurkewich 1995]. In the presence of nitrogen oxides heterogeneous reactions on aerosol surfaces (like reaction 2.65) are known to produce halogenated nitrogen oxides which are photolabile (reaction 2.66) or which may also react directly with sea salt (2.67)[Schweitzer et al. 1999]:

$$(N_2O_5)_g + (NaX)_s \longrightarrow (XNO_2)_g + (NaNO_3)_s \tag{2.65}$$

$$XNO_2 + h\nu \longrightarrow X + NO_2 \tag{2.66}$$

$$(XNO_2)_g + (NaX)_s \longrightarrow (NaNO_2)_s + (X_2)_g \tag{2.67}$$

Under atmospheric conditions reaction 2.65 is very slow [Mozurkewich 1995]. However, in contrast to the other halogen release mechanisms described at the beginning of this section, the formation of XNO_2 and X_2 can proceed without light, leading to an accumulation of these photolabile species before sunrise ('dark source' of RHS). Nagao et al. [1999] observed O_3 depletion events in the sub-tropical marine boundary layer and proposed night-time halogen release followed by photolysis at sunrise for these events. Nevertheless, this source is the more effective the higher the NO_x values are, i.e. the more polluted the atmosphere is. Therefore it cannot be expected to be the dominant process of halogen release in the remote marine boundary layer. The uptake of NO_3 by aqueous solutions of NaX leads to another night-time mechanism [Gershenzon et al. 1999]:

$$(NO_3)_g + (NaX)_s \longleftrightarrow (NO_3 - NaX)_s;\ (NO_3 - NaX)_s \longrightarrow NaNO_3 + (X)_s \tag{2.68}$$

The uptake coefficient was found to be near 0.01 for sea water by Rudich et al. [1996], while Seisel and Rossi [1997] found 0.05 for dry NaCl.

2.2.3.3 Sinks of Reactive Halogen Species in the Troposphere

The first step in the loss process of RHS in the troposphere is their reaction with hydrocarbons (RH, e.g. CH_4, see reaction 2.49) or peroxy radicals (HO_2 and organic peroxy radicals RO_2, see reaction 2.50) to form hydrogen halides HX. The final loss of these compounds from the atmosphere is due to wet (after uptake on water-droplets of clouds or fog or on aerosol surfaces) and/or dry deposition (by sedimentation or surface reaction) on the earth's surface, including snow and ice surfaces, vegetation, buildings etc. As a result gaseous species are removed, at least temporarily, from the atmosphere. HX are readily soluble in water, which leads to efficient wet deposition on the ground or on aerosol surfaces and thus - at least

temporarily - to a removal of RHS from the atmosphere. The different halogens show different behavior concerning their reaction with hydrocarbons (cf. table 2.9. Cl reacts fast with all hydrocarbons, Br only with unsaturated hydrocarbons or oxidized species like aldehydes and carbonyls leading to the formation of HX. Iodine atoms cannot react with saturated or unsaturated hydrocarbons [Miyake and Tsnogai 1963]. Additionally, Br atoms can add to the C=C double bond of olefins leading to brominated organic compounds. The lifetime of the respective compound with respect to photolysis determines the efficiency of Br loss. For a detailed description consult the actual reviews of Sander et al. [2003] and Atkinson et al. [2003]. For chlorine the most important sink is the reaction with hydrocarbons by reaction 2.49. In principle, the reactivation of halogen atoms from the reservoir compound HX is possible by the reaction with OH

$$HX + OH \longrightarrow X + H_2O \tag{2.69}$$

However, as can be seen from table 2.11 the reaction is endothermic and therefore negligible for fluorine. For chlorine, bromine and iodine the production rates of X atoms by reaction 2.69 can be estimated using the simple relation:

$$\frac{d}{dt}[X] \;=\; [OH] \cdot k(HX + OH) \cdot [HX] \tag{2.70}$$

The resulting production rates and rate constants for reaction 2.69 are shown in table 2.11. Measurements of hydrohalous acids HX reported in literature restrict to the stratosphere [Douglass and Kawa 1999; Chartrand and McConnell 1998]. Therefore an estimation of typical values for the remote marine boundary layer was done using the model MOCCA [Vogt et al. 1999]. The HX concentrations values correspond to highest daytime mixing ratios of 1 ppt BrO, 0.2 ppt ClO and 0.8 ppt IO in the model respectively.
The calculated halogen atom production rates lead to the conclusion that reaction 2.69 is of minor importance under tropospheric conditions.

Table 2.11: Enthalpy and rate constants of reaction (2.69) at 298 K [Sander et al. 2003].

Halogen	Enthalpy ΔH $[kcal\ mol^{-1}]$	k(HX+OH) $[cm^3 molec.^{-1} s^{-1}]$	[HX] $^{(a)}$ molec. cm^{-3}	$\frac{d}{dt}[X]$ $^{(b)}$ [atoms s^{-1}]
F	15.0			
Cl	-18.2	8.0×10^{-13}	5×10^8	4.2×10^2
Br	-33.7	1.1×10^{-11}	8×10^7	9.1×10^2
I	-49.9	3.0×10^{-11}	4×10^6	1.3×10^2

$^{(a)}$ estimation for remote marine boundary layer using MOCCA[Vogt et al. 1999]
$^{(b)}$ [OH]=$10^6 molec.cm^{-3}$

2.3 Dimethylsulphide(DMS)

Since [Lovelock 1972] postulated in 1972 that DMS could account for the "missing" global flux of gaseous sulphur from the oceans to the atmosphere, some 150 oceanographic cruises have compiled data on its ubiquity and supersaturation in surface seawater [Kettle et al. 1999]. Today it is well recognized that Dimethylsulfide (DMS) and its precursor, dimethylsulfoniopropionate(DMSP), along with dimethylsulfoxide(DMSO), form the major pool of organic sulfur in the marine environment [Andreae and Crutzen 1997; Scarratt et al. 2000]. The production and transformation of these compounds comprise an important part of the sulfur cycle. DMS is readily oxidized in the atmosphere to form sulfate aerosols which are thought to be climatically important due to their ability to scatter sunlight and their role in the formation of cloud condensation nuclei. Both these processes increase the planetary albedo and exert a cooling influence on the climate. Recent estimates [Kettle and Andreae 2000] of the DMS emission flux range from 15×10^{12} to $33 \times 10^{12} gramsSulphuryear^{-}1$, enough to make a major contribution to the atmospheric sulphur burden and, therefore, to the chemistry and radiative behavior of the atmosphere.

2.3.1 Sources and production of DMS

It was originally thought that phytoplankton produce DMS directly, and many authors still imply this when describing the oceanic biogeochemical sulfur cycle. Factors controlling phytoplankton activity (e.g. light, temperature and nutrients) were therefore expected to control DMS production. This view provided the basis for the hypothesis of a feedback between oceanic phytoplankton and climate. The CLAW hypothesis proposed by Charlson, Lovelock, Andreae and Warren [Charlson et al. 1987] in the late 80's suggested that DMS is released by marine phytoplankton, enters the troposphere, and is oxidized to sulfate particles, which then act as cloud condensation nuclei (CCN) for marine clouds. Changes in CCN concentration affect the formation rate of cloud droplets, which influences cloud albedo and consequently climate. Large-scale climate change, in turn, affects the phytoplankton in the oceans and thereby closes the feedback loop (Fig. 2.8). One of the main criticisms of the CLAW hypothesis was its evolutionary feasibility, as climate regulation would imply an improbable altruistic behavior of phytoplankton for the biosphere. The authors of CLAW proposed that the energetic cost of DMS production could be justified by means that cloud feeding by DMS would favor phytoplankton by enhancing the return of nitrogen (a generally limiting resource in the surface ocean) through rainfall and by lessening harmful UV input. However, not all phytoplankton species (not even all clones within species) produce equivalent amounts of the DMS precursor. Moreover, as many organisms other than DMS producers have a high Nitrogen demand and are sensitive to UV, the benefits of DMS production would be shared with concurrent organisms.
In the years since publication of the CLAW hypothesis, over 1000 papers have been published discussing the biogeochemistry of DMS (and its precursors) and its link to climate. According to current knowledge there is no need to invoke either altruism or selfish adaptation related directly to DMS to explain the exhalation of atmospheric sulfur by plankton on an evolution-

ary basis. It was shown that phytoplankton do not have metabolic pathways for the direct synthesis of DMS, instead they produce large amounts of non-volatile dimethylsulfoniopropionate (DMSP). This compound performs several important physiological and ecological functions of benefit for the producer. It is involved in osmoprotection and cryoprotection in algae, it can act as a methyl donor and is the precursor of cues for chemosensory attraction in the marine food web [Simò 2001]. It is now agreed that DMS is produced by the enzymatic cleavage of DMSP via DMSP-lyase to DMS and acrylate. While phytoplankton are known to be the principal source of DMSP, bacteria are thought to provide the major mechanism for transforming DMSP to DMS in seawater [Gabric et al. 1993; Wolfe and Steinke 1996; Yoch et al. 1997]. There are also a few species of phytoplankton which are known to possess DMSP-lyase, and it is speculated that there may be others. However, linking phytoplankton to DMS through DMSP is not straightforward (Figure 2.9). Attempts to correlate DMS to phytoplankton biomass (chlorophyll–a concentration) or activity (primary production) on large spatial or temporal scales have failed [Kettle et al. 1999]. This might be not only because of the taxonomy (some species produce more DMSP than others do) dependence of DMSP production in algae, but also because most DMSP breakdown into DMS requires DMSP being released extracellularly. Exudation by healthy algae represents only a small fraction of DMSP release, which occurs mostly through cell lysis (autolysis and viral attack [Fuhrman 1999]) and grazing [Wolfe and Steinke 1996]. In grazing, a fraction of the algal DMSP is assimilated by the grazer. Some of the released DMSP is then converted into DMS by algal and/or bacterial DMSP lyases, either free in solution, attached to particles or in the guts and vacuoles of grazers. A second major mechanism of DMSP degradation by bacteria is demethylation, which does not produce DMS. The ratio of DMSP cleavage to demethylation is variable and often expressed as a DMS production yield. DMSP cleavage is generally thought to be the less significant of the 2 processes, and DMS production yields measured in marine waters fall typically between 5 and 30% [Kiene 1993] which may decrease as a phytoplankton bloom ages [van Duyl et al. 1998].

Once produced, DMS is consumed biologically [Kiene 1993] within one to several days. With the exception of very particular conditions, DMS concentrations are generally constrained to between 0.5 and 10 nM. Such a narrow range suggests that losses occur in tight coupling with production processes. Indeed, not only biological consumption but also significant photolysis and ventilation rates have been found coupled to DMS production in the open ocean. Most studies show that bacteria are a major sink for DMS. Therefore, because bacterioplankton are involved in both DMSP and DMS utilization (Fig. 2.9), factors controlling bacterial activity (such as UV-B radiation, temperature, nutrients and dissolved organic matter quality) ultimately also play a role in controlling DMS concentration in the water.

The atmospheric DMS concentration finally depends on the sea to air flux of DMS (f_{DMS}), a factor resulting from the DMS concentration in seawater C_w and the gas transfer velocity K_w,

$$f_{DMS} = K_w * C_w \tag{2.71}$$

K_w can be derived from wind speed (u) and sea surface temperature (T, in Celsius) using the relationship given by [Liss and Merlivat 1986]

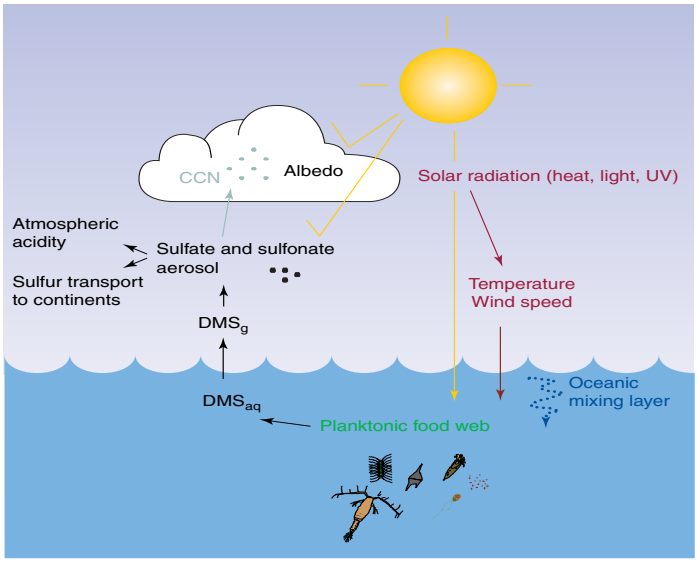

Figure 2.8: The feedback system linking oceanic plankton and climate through the production of atmospheric sulfur. The original CLAW hypothesis postulated that production of dimethylsulfide (DMSaq) by phytoplankton, and its subsequent ventilation (DMSg) and oxidation in the atmosphere, feeds cloud condensation nuclei (CCN) in marine stratus, thereby increasing cloud albedo. If the consequent reduction in solar irradiance made phytoplankton produce less DMS, then a negative feedback would operate, thus stabilizing climate. Although this hypothesis is still conjecture, recent advances suggest that it is not only phytoplankton but the whole food web that releases DMS and that the response of net DMS production to changes in solar radiation might operate through the profound effects of surface vertical mixing on oceanic biogeochemistry and food-web dynamics.

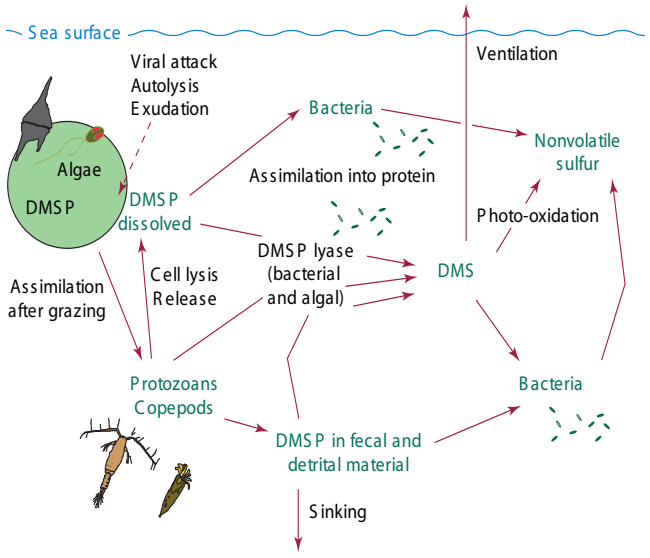

Figure 2.9: The fate of phytoplanktonic dimethylsulfoniopropionate (DMSP) in seawater. DMSP is released from the cell through exudation and, most importantly, by cell lysis and grazing. A fraction is assimilated by grazers, whereas the rest is either cleaved to dimethylsulfide (DMS) by algal and bacterial DMSP lyases, or used by heterotrophic bacteria through other pathways. DMSP acts both as a source of carbon and a source of sulfur for methionine and subsequent protein synthesis. DMS is also consumed by bacteria, and lost through photooxidation. Only a small fraction (5-30%) escapes this tight cycling and vents to the atmosphere[Kiene1993]. DMSP cycling is an integral part of the food web, and foodweb dynamics control DMS emission to the atmosphere.

$$K_w = 0.17 \cdot [A(T)]^{-2/3} \cdot u \quad (2.72)$$
$$(u \leq 3.6\ m/s) \quad (2.73)$$
$$K_w = 0.17 \cdot [A(T)]^{-2/3} \cdot u + 2.68[A(T)]^{-1/2} \cdot (u - 3.6) \quad (2.74)$$
$$(3.6 < u < 13\ m/s) \quad (2.75)$$
$$K_w = 0.17 \cdot [A(T)]^{-2/3} \cdot u + 2.68[A(T)]^{-1/2} \cdot (u - 3.6) + 3.05[A(T)]^{-1/2} \cdot (u - 13) \quad (2.76)$$
$$(u \geq 13\ m/s) \quad (2.77)$$

The factor $A(T) = S_{DMS}(T)/S_{CO2}(T)$ is the relation of the Schmidt Numbers of CO_2 and DMS at the temperature T, which can be obtained using the equation from [Saltzman et al. 1993]: $S_{DMS} = 2674 - 147.12\ T + 3.726\ T^2 - 0.038\ T^3$. At 20 °C the factor $S_{CO2}(20\,^{\circ}\mathrm{C}) = 595$. Inserting typical values in the equations given above a rough approximation leads to $K_w \sim u^2$ and $K_w \sim T$, thus wind speed is a crucial factor defining the DMS flux.

2.3.2 The atmospheric oxidation chain of DMS

Local sea–to–air flux of DMS(F_{DMS}), long range transport, marine boundary layer(MBL) height variation and oxidation by radicals are assumed to be the major factors controlling atmospheric DMS concentrations. The atmospheric biogenic sulphur cycle, shown schematically in Figure 2.10, is divided into several steps [Nilsson and Leck 2002].
The residence time of DMS in the atmosphere is in the order of one to a few days under clean marine conditions. After diffusion from the sea surface the ***gas–phase oxidation of DMS*** is readily started. Hydroxyl radicals (OH) have been identified as the major photochemical sink of DMS in the clean marine atmosphere [Ayers et al. 1995; Sciare et al. 2000]. However, model results reveal that the measured OH levels are not sufficient to explain the observed DMS daytime variation. Other oxidizing species as BrO [von Glasow et al. 2002; Toumi 1994], the heterogeneous reaction of DMS and ozone in the aqueous phase [Gershenzon et al. 2001; Barcellos da Rosa et al. 2003] and multiphase chemistry in general [Campolongo et al. 1999] have been proposed to explain model shortcomings. In polluted areas the nitrate radical (NO_3) when present at nighttime, can exceed by far the oxidation capacity of OH [Allan et al. 2000], reducing the lifetime of DMS to few hours or even minutes. The ***gas–to–particle transformation of the DMS oxidation products***, mainly Dimethylsulphone(DMSO), Methane sulfinic acid(MSA) and sulphur dioxide SO_2, leads to the formation of aerosols and cloud condensation nuclei(CCN). The cycle is closed by ***removal of these products*** from the atmosphere by dry and wet deposition(Figure 2.10).
Although significant research progress has been achieved within the last decade, the very complex chemical and physical pathways which lead from gaseous DMS to sulphur particles remain a challenge for further investigations. An illustration of the oxidation chain leading from Dimethylsulphide to the presumably final oxidation product, Methane sulphonic acid(MSA), is given in Figure 2.11. Although a relatively detailed representation of the chemical pathways was intended, not all investigated chemical reactions involved in the DMS oxidation chain are shown in Figure 2.11. It becomes evident that nearly all radical species found in the marine boundary layer contribute to the oxidation process, although their rela-

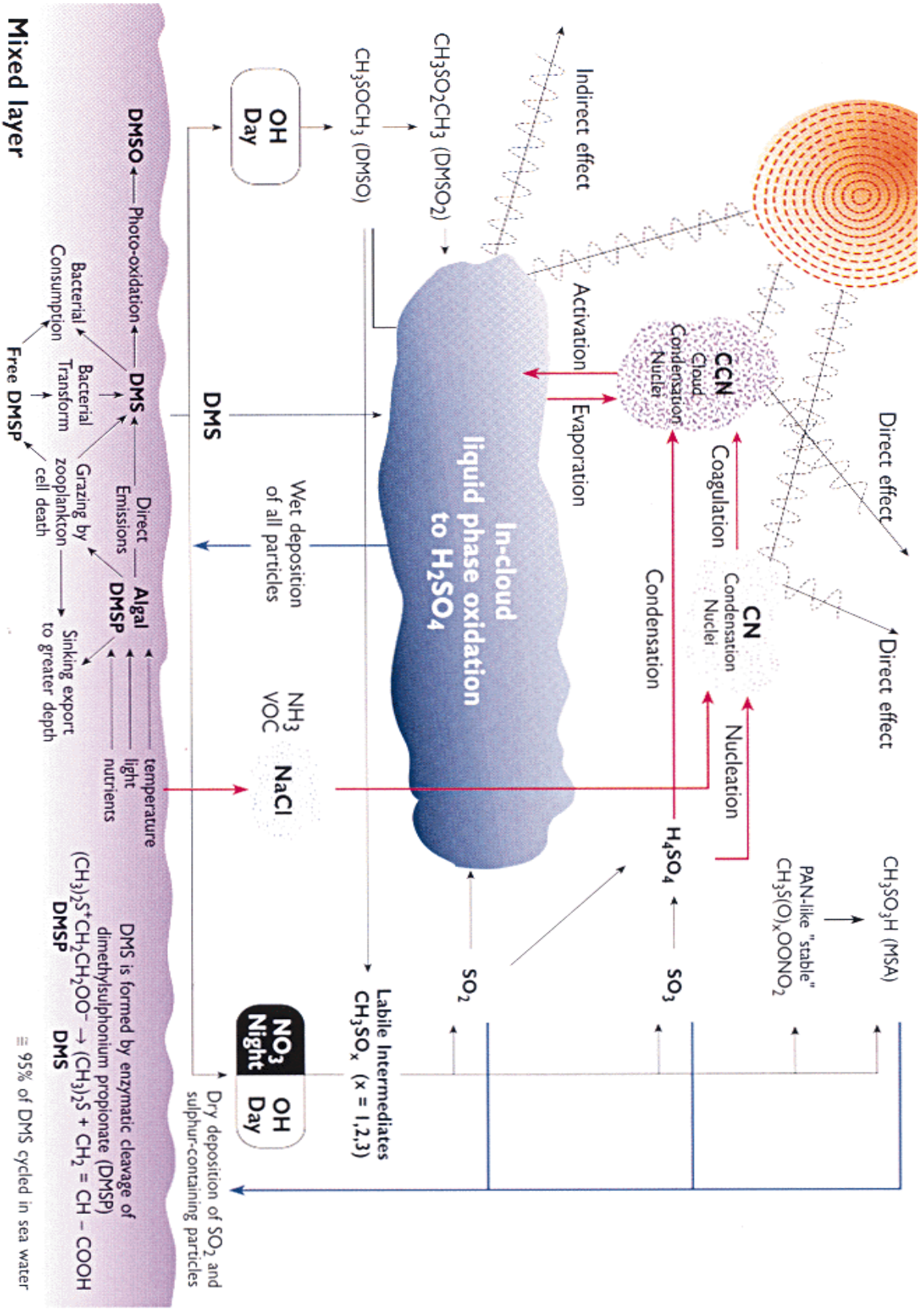

Figure 2.10: The atmospheric DMS cycle (adapted from [Andreae et al. 1999; Liss et al. 1997]).

tive contribution can change significantly from step to step of the chain. The ramifications of the oxidation pathways are numerous and their importance is largely dependent on the concentration of trace gases in the environment, as will be shown in the analysis chapter of this thesis(Chapter 5).
The corresponding rate constants to the reactions depicted in Figure 2.11 are given in table 2.12. In spite of the amazing number of publications available so far concerning the fate of Dimethylsulphide in the atmosphere, most of the kinetic rate constants of its oxidation chain are based on estimations made by [Yin et al. 1990]. Thank to the abundant laboratory studies performed within the framework of the EL CID project, significant knowledge was won regarding the implication of bromine [Aranda et al. 2002; Ballesteros et al. 2002; Riffault et al. 2003] and chlorine [Díaz-de Mera et al. 2002; Martínez et al. 2002; Riffault et al. 2003; Rodríguez et al. 2003] in the DMS oxidation process. Other achievements have been the studies on gas phase reactions of OH with DMSO and MSA [Arsene et al. 2002; Kukui et al. 2003] as well as on a number of heterogeneous reactions involved in the DMS cycle [Barcellos da Rosa et al. 2003; Bardouki et al. 2002].
In the following a short introduction to the DMS oxidation chain as depicted in Figure 2.11 is given. The discussion is started with the omnipresent OH radical (section 2.3.2.1). After this first step, further elucidations will focus on the implication of nitrogen species(section 2.3.2.2) and halogens (section 2.3.2.3) to the DMS oxidation process and in particular on the nitrate radical NO_3 and bromine oxide BrO whose depletion efficiency can regionally surpass the one reached by OH. At the end of this section a brief introduction to heterogeneous reactions and other depletion mechanisms involved in the cycle is given (section 2.3.2.4).

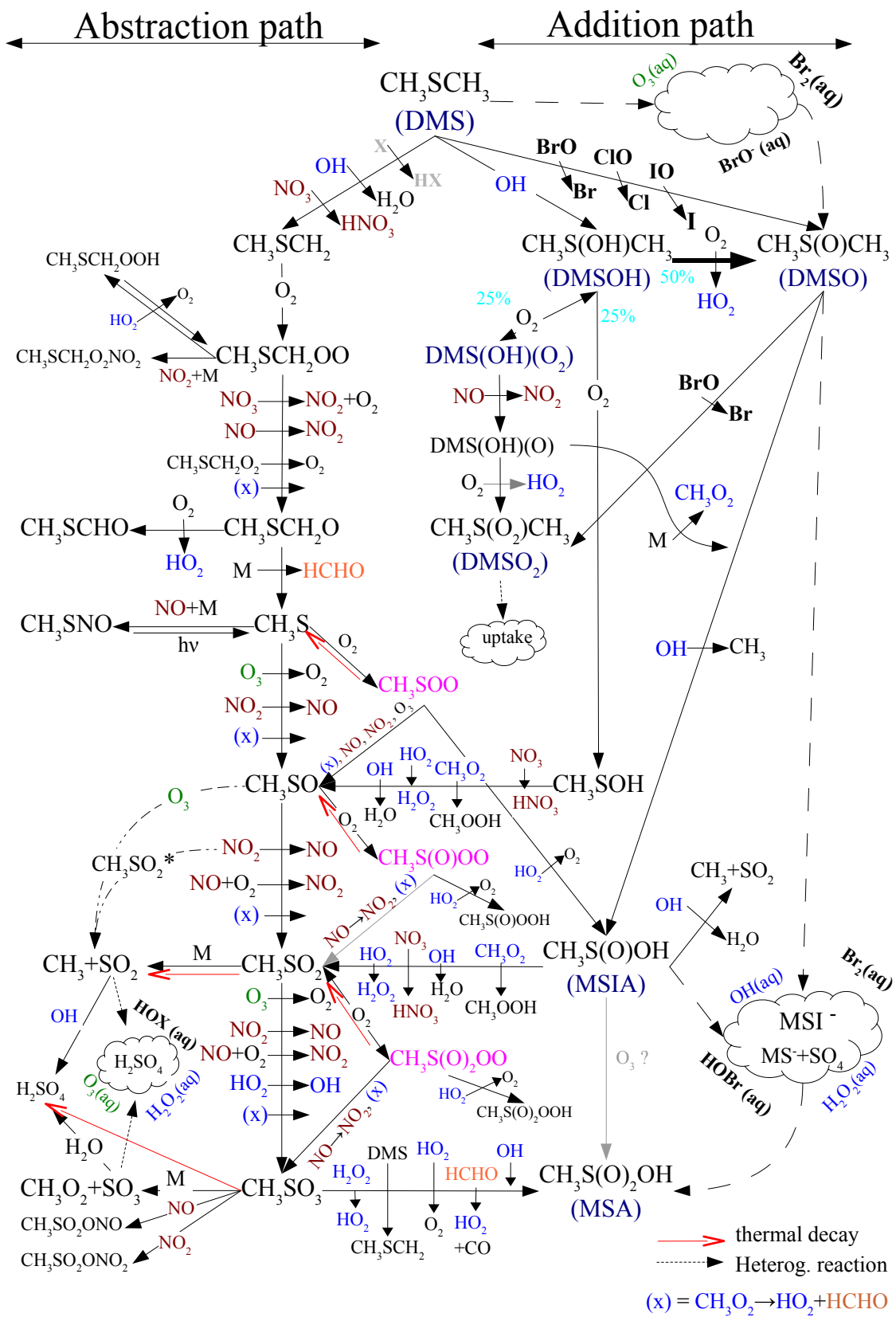

Figure 2.11: The oxidation chain of DMS in the atmosphere.

Table 2.12: Overview of reactions and corresponding rate constants involved in the DMS oxidation cycle.

	Reaction		Rate constant$[cm^3\ molec.^{-1}\ s^{-1}]$ k(T)=A*exp(B/T) A	B	(T=298 K)	Ref.
	H Abstraction					
2.78	DMS+OH	$\rightarrow CH_3SCH_2+H_2O$	1.13×10^{-11}	-253	4.8×10^{-12}	ATK03
2.79	$CH_3SCH_2+O_2$	$\rightarrow CH_3SCH_2O_2$			5.7×10^{-12}	ATK03
2.80	CH_3SCH_2OO+NO	$\rightarrow CH_3SCH_2O+NO_2$	4.9×10^{-12}	260	1.2×10^{-11}	ATK03
2.81	$CH_3SCH_2OO+NO_2+M$	$\rightarrow CH_3SCH_2O_2NO_2$			9×10^{-12}	ATK03
2.82	$CH_3SCH_2OO+HO_2$	$\rightarrow CH_3SCH_2OOH+O_2$			1.5×10^{-12}	YIN90
2.83	$CH_3SCH_2OO+CH_3O_2$	$\rightarrow CH_3SCH_2O+CH_3O+O_2$			1.8×10^{-13}	YIN90
2.84	$2*CH_3SCH_2O_2$	$\rightarrow 2\ CH_3SCH_2O+O_2$			1.0×10^{-11}	ATK03
2.85	CH_3SCH_2O+M	$\rightarrow CH_3S+HCHO$			10	YIN90
	OH Addition					
2.86	DMS+OH	$\rightarrow$DMS(OH)	1)		1.7×10^{-12}	ATK03
2.87	$DMS(OH)+O_2$	$\rightarrow DMSO+HO_2$			2.0×10^{-12}	KOG96
2.88	DMSO+OH	$\rightarrow CH_3SO_2H+CH_3O_2$			9.0×10^{-11}	KUK03
2.89	$DMS(OH)+O_2$	$\rightarrow CH_3SOH+CH_3O_2$			1.0×10^{-12}	KOG96
2.90	$DMS(OH)+O_2$	$\rightarrow DMS(OH)O_2$			1.0×10^{-12}	KOG96
2.91	DMS(OH)+M	$\rightarrow CH_3SOH+CH_3O_2$			5.0×10^{5}	YIN90
2.92	DMS(OH)(OO)+NO	$\rightarrow DMS(OH)O+NO_2$			5.0×10^{-12}	YIN90
2.93	DMS(OH)(OO)+M	$\rightarrow DMS(OH)+O_2$			10	YIN90
2.94	$DMS(OH)O+O_2$	$\rightarrow DMSO_2+HO_2$			1.2×10^{-12}	YIN90
2.95	DMS(OH)O+M	$\rightarrow$MSIA$+CH_3O_2$			1.5×10^{7}	YIN90
2.96	$DMSO_2+O_3$	$\rightarrow$products			$< 1 \times 10^{-19}$	FAL00
2.97	$DMSO_2+NO_3$	$\rightarrow CH_3S(O)_2CH_2OO$			$< 2 \times 10^{-15}$	FAL00
2.98	$DMSO_2+OH$	$\rightarrow CH_3S(O)_2CH_2OO$			1.5×10^{-13}	FAL00
2.99	$CH_3S(O)_2CH_2OO+NO$	$\rightarrow CH_3S(O)_2CH_2O$			5.0×10^{-12}	YIN90
2.100	$CH_3S(O)_2CH_2O$	$\rightarrow CH_3SO_2+HCHO$			10	YIN90
	Other radicals+DMS					
2.101	$DMS+NO_3$	$\rightarrow CH_3SCH_2+HNO_3$	1.9×10^{-13}	520	1.1×10^{-12}	ATK03
2.102	$DMS+HO_2$	$\rightarrow$products			$< 5 \times 10^{-15}$	ATK03
2.103	$DMS+O_3$	$\rightarrow$products			$< 1 \times 10^{-18}$	ATK03
2.104	$DMSO+NO_3$	$\rightarrow DMSO_2+NO_2$			5.0×10^{-13}	FAL00
	Halogens in the DMS oxidation cycle					
2.105	DMS+Br	$\rightarrow$products			4.9×10^{-14}	BAL02
2.106	DMS+BrO	$\rightarrow$DMSO+Br			4.4×10^{-13}	ATK03
2.107	DMS+Cl	$\rightarrow$products			3.3×10^{-10}	ATK03
2.108	DMS+ClO	$\rightarrow$DMSO+Cl			9.0×10^{-15}	ATK03
2.109	DMS+IO	$\rightarrow$DMSO+I			1.3×10^{-14}	ATK03
2.110	DMSO+Br	$\rightarrow$HBr+products			1.1×10^{-14}	RIF03
		$\rightarrow CH_3$+products			1.2×10^{-15}	RIF03
2.111	DMSO+BrO	$\rightarrow DMSO_2$+Br			4.0×10^{-14}	RIF03
2.112	DMSO+Cl	$\rightarrow$HCl(90%),CH3(10%)			2.1×10^{-11}	RIF03
2.113	DMSO+ClO	$\rightarrow$products			$< 1.6 \times 10^{-14}$	RIF03
2.114	$DMSO_2$+Br	$\rightarrow$products			1×10^{-15}	BAL02
2.115	$DMSO_2$+BrO	$\rightarrow$products			3×10^{-15}	BAL02

Table 2.12: Overview of reactions and corresponding rate constants involved in the DMS oxidation cycle.

	Reaction		Rate constant$[cm^3\ molec.^{-1}\ s^{-1}]$ k(T)=A*exp(B/T) A	B	(T=298 K)	Ref.
2.116	$DMSO_2$+Cl	→products			2.4×10^{-14}	FAL00
2.117	CH_3S+O_3	→CH_3SO+O_2	1.15×10^{-12}	432	4.9×10^{-12}	ATK03
2.118	CH_3S+NO+M	→CH_3SNO+M	$3.3 \times 10^{-29}(T/300)^{-4}[N_2]$		4.0×10^{-11}	ATK03
2.119	CH_3S+NO_2	→CH_3SO+NO	3.0×10^{-11}	210	6×10^{-11}	ATK03
2.120	CH_3S+O_2	→CH_3SOO			1.5×10^{-14}	BAR95
		→CH_3O_2+SO_2			$< 3 \times 10^{-18}$	JPL02
2.121	CH_3S+CH_3O_2	→CH_3SO+HCHO+HO_2			6.1×10^{-11}	YIN90
2.122	CH_3SOO	→CH_3S+O_2			5×10^5	CAM99
		→CH_3SO_2			1	SAL95
2.123	CH_3SOO+O_3	→CH_3SO+2 O_2			$< 8.0 \times 10^{-13}$	JPL02
2.124	CH_3SOO+NO	→CH_3SO+NO_2			1.1×10^{-11}	ATK03
2.125	CH_3SOO+NO_2	→CH_3S+products			2.2×10^{-11}	ATK03
2.126	CH_3SOO+HO_2	→MSIA+O_2			4×10^{-12}	YIN90
2.127	CH_3SOO+O_2	→CH_3O_2+SO_2			2×10^{-17}	TUR93
2.128	CH_3SOO+CH_3O_2	→CH_3SO+HCHO+HO_2			5.5×10^{-12}	YIN90
2.129	CH_3SO+O_3	→CH_3+SO_2+O_2			3.2×10^{-13}	BOR03
		→CH_3SO_2+O_2			≈ 0	BOR03
2.130	CH_3SO+NO_2	→CH_3SO_2+NO			1.2×10^{-11}	KUK00
		→CH_3+NO+SO_2			3.5×10^{-12}	SAL95
2.131	CH_3SO+NO+O_2	→CH_3SO_2+NO_2			8.0×10^{-11}	ATK03
2.132	CH_3SO+O_2	→CH_3SOOO			7.7×10^{-18}	YIN90
2.133	CH_3SO+CH_3O_2	→CH_3SO_2+HCHO+HO_2			3.0×10^{-12}	YIN90
2.134	$CH_3S(O)OO$	→CH_3SO+O_2			1.7×10^2	YIN90
2.135	$CH_3S(O)OO$+NO	→CH_3SO_2+NO_2			1×10^{-11}	JPL97
2.136	$CH_3S(O)OO$+HO_2	→$CH_3S(O)OOH$+O_2			3.0×10^{-12}	YIN90
2.137	$CH_3S(O)OO$+CH_3O_2	→CH_3SO_2+HCHO+HO_2			5.5×10^{-12}	YIN90
2.138	2 $CH_3S(O)OO$	→2 CH_3SO_2+O_2			6.0×10^{-12}	YIN90
2.139	$CH_3S(O)OO$+CH_3S	→CH_3SO_2+CH_3SO			7.0×10^{-11}	YIN90
2.140	$CH_3S(O)OO$+CH_3SO	→2 CH_3SO_2			8.1×10^{-12}	YIN90
2.141	CH_3SO_2+NO+O_2	→CH_3SO_3+NO2			$1.1 \times 10^{-11(1)}$	ATK03
2.142	CH_3SO_2+NO_2	→CH_3SO_3+NO			2.2×10^{-11}	JPL02
2.143	CH_3SO_2+O_3	→CH_3SO_3+O_2			6.3×10^{-13}	SAL95
2.144	CH_3SO_2+HO_2	→CH_3SO_3+OH			2.5×10^{-13}	YIN90
2.145	CH_3SO_2+CH_3O_2+M	→CH_3SO_3+HCHO+HO_2			2.5×10^{-13}	YIN90
2.146	CH_3SO_2+M	→CH_3O_2+SO_2	2.6×10^{11}	-9056	1.6×10^{-2}	AYE96
2.147	CH_3SO_2+O_2	→$CH_3S(O)_2OO$			2.6×10^{-18}	YIN90
2.148	CH_3SO_2	→CH_3O_2+SO_2			1.0×10^2	RAY95
2.149	$CH_3S(O)_2OO$+NO	→CH_3SO_3+NO_2			1.0×10^{-11}	JPL97
2.150	$CH_3S(O)_2OO$+HO_2	→CH_3SO_2OOH+O_2			2.0×10^{-12}	YIN90
2.151	$CH_3S(O)_2OO$+CH_3O_2	→CH_3SO_3+HCHO+HO_2			5.5×10^{-12}	YIN90
2.152	$CH_3S(O)_2OO$	→CH_3SO_2+O_2			1.7×10^2	YIN90
2.153	CH_3SO_3	→H_2SO_4+CH_3O_2			1.2×10^{-3}	SAL95
2.154	CH_3SO_3+M	→CH_3O_2+SO_3	1.1×10^{17}	-12057	0.3	AYE96
2.155	CH_3SO_3+OH	→MSA			5.0×10^{-11}	YIN90

Table 2.12: Overview of reactions and corresponding rate constants involved in the DMS oxidation cycle.

	Reaction		Rate constant[cm^3 $molec.^{-1}$ s^{-1}] k(T)=A*exp(B/T) A	B	(T=298 K)	Ref.
2.156	CH_3SO_3+HO_2	→MSA+O_2			5.0×10^{-11}	YIN90
2.157	CH_3SO_3+DMS	→MSA+CH_3SCH_2			6.8×10^{-14}	YIN90
2.158	CH_3SO_3+HCHO	→MSA+HO_2+CO			1.6×10^{-15}	YIN90
2.159	CH_3SO_3+NO	→$CH_3S(O)_2ONO$			3.0×10^{-15}	YIN90
2.160	CH_3SO_3+NO_2	→$CH_3S(O)_2ONO_2$			3.0×10^{-15}	YIN90
2.161	CH_3SO_3+H_2O_2	→MSA+HO_2			3.0×10^{-16}	YIN90
2.162	CH_3SO_3+HONO	→MSA+NO_2			6.6×10^{-16}	YIN90
2.163	CH_3SO_3+CH_3SH	→MSA+HCO			3.0×10^{-16}	YIN90
2.164	CH_3SO_3+CH_3SOH	→MSA+CH_3SO			3.0×10^{-16}	YIN90
2.165	CH_3SO_3+MSIA	→MSA+CH_3SO_2			3.0×10^{-16}	YIN90
2.166	CH_3SO_3+CH_3OH	→MSA+HO_2+HCHO			1.0×10^{-16}	YIN90
2.167	CH_3SO_3+CH_3OOH	→MSA+CH_3O_2			3.0×10^{-16}	YIN90
2.168	CH_3SOH+OH	→CH_3SO+H_2O			1.0×10^{-10}	HER94
2.169	CH_3SOH+NO_3	→CH_3SO+HNO_3			3.4×10^{-12}	YIN90
2.170	CH_3SOH+HO_2	→CH_3SO+H_2O_2			8.5×10^{-13}	YIN90
2.171	CH_3SOH+CH_3O_2	→CH_3SO+CH_3OOH			8.5×10^{-13}	YIN90
2.172	$CH_3S(O)OH$+OH	→CH_3+SO_2+H_2O			9.0×10^{-11}	KUK03
		→CH_3SO_2+H_2O			1.6×10^{-11}	YIN90
2.173	$CH_3S(O)OH$+NO_3	→CH_3SO_2+H_2O			1.0×10^{-12}	YIN90
2.174	$CH_3S(O)OH$+HO_2	→CH_3SO_2+H_2O_2			1.0×10^{-15}	YIN90
2.175	$CH_3S(O)OH$+CH_3O_2	→CH_3SO_2+CH_3OOH			1.0×10^{-15}	YIN90
	SO+O_2	→SO_2+O	1.6×10^{-13}	-2280	7.6×10^{-17}	ATK03
	SO+O_3	→SO_2+O_2	4.5×10^{-12}	-1170	8.9×10^{-14}	ATK03
	SO+NO_2	→SO_2+NO			1.4×10^{-11}	ATK03
	SO+OH	→SO_2+H			8.6×10^{-11}	JPL02
	SO_2+OH+M	→$HOSO_2$+M	$1.3 \times 10^{-12}(T/300)^{-0.7}$		1.3×10^{-12}	ATK03
	$HOSO_2$+O_2	→HO_2+SO_3	1.3×10^{-12}	-330	4.3×10^{-13}	ATK03
	SO_3+H_2O	→H_2SO_4			$5.7 \times 10^{4} s^{-1}$ (*)	JPL02
	SO_3+NH_3	→products			2×10^{-11}	JPL02

[Atkinson et al. 2003] (ATK03), [Ayers et al. 1996] (AYE96)
[Barcellos da Rosa et al. 2003] (BAR03), [Ballesteros et al. 2002] (BAL02)
[Barone et al. 1995] at 227K (BAR95), [Borissenko et al. 2003] (BOR03)
[Campolongo et al. 1999] (CAM99), [Falbe-Hansen et al. 2000] (FAL00)
[Hynes and Wine 1996] (HYN96), [Koga and Takana 1996] (KOG96)
[Kukui et al. 2000](KUK00), [Kukui et al. 2003] (KUK03)
[Ray et al. 1995] (RAY95), [Riffault et al. 2003] (RIF03)
[Saltelli and Hjort 1995] (SAL95), [Turnipseed et al. 1993] (TUR93)
[Yin et al. 1990] (YIN90)
1) $\frac{1.0\times10^{-39}[O2]exp(5820/T)}{1+5.0\times10^{-30}[O2]exp(6280/T)}$
(1) only measured until 242K, (*) at 50% relative humidity

2.3.2.1 In the clean marine boundary layer - the role of OH and RO_x

The reaction of DMS with the hydroxyl radical(OH) has been analyzed in several laboratory studies [Arsene et al. 1999; Barnes et al. 1988; Yin et al. 1990]. It is known that the reaction of OH radicals with DMS proceeds through two independent channels: H–atom abstraction from the methyl group and OH radical addition to the Sulphur atom. The initial steps of the reaction chain are represented below:

Abstraction path

$$^{\cdot}OH + CH_3SCH_3 \rightarrow CH_3SCH2^{\cdot} + H_2O \quad (2.176)$$

$$CH_3SCH2^{\cdot} + O_2 \rightarrow \text{products: } SO_2, \text{MSA}, \ldots \quad (2.177)$$

Addition path

$$^{\cdot}OH + CH_3SCH_3 \rightarrow CH_3S(OH)CH_3 \quad (2.178)$$

$$CH_3S(OH)CH_3 \xrightarrow{M} OH + CH_3SCH_3 \quad (2.179)$$

$$CH_3S(OH)CH_3 + O_2 \rightarrow \text{products: DMSO}, ??? \quad (2.180)$$

The rate constants of all reactions are given in Table 2.12. The yield of products of DMS oxidation via OH is strongly dependent on temperature. As shown in Figure 2.3.2.1, increasing the temperature will favor the abstraction pathway and hence SO_2 formation, whereas the addition channel and thus dimethyl sulphoxide(DMSO) formation is dominant in cold environments [Arsene et al. 1999]. As a survey, average temperatures prevailing during the three field studies to be presented in this thesis (Chapter 4) are indicated. It becomes evident that the abstraction branch should dominate in the hot in the Mediterranean (Crete), whereas for the subpolar location in the Hudson Bay the yield of DMSO should increase considerably. After this initial step, the hydroxyl radical has no major contribution to the abstraction path but plays a crucial role in the formation and depletion of methane sulphinic acid(MSIA) in the gas phase as in the aqueous phase(section 2.3.2.4).
Reactions of DMS with peroxides are not well established so far, but are expected to be much slower than reactions with OH. Laboratory results of Mellouki and Ravishankara [1994] suggest $5e^{-15}\ cm^3\ mol^{-1}\ s^{-1}$ as an upper limit for the rate constant of DMS with HO_2. However, peroxy radicals reactions have to be considered for nearly all chain links of the abstraction path and in particular for all transitions between hydroxygenated and oxygenated species, as for the conversion from CH_3SO_2 to MSA.

2.3.2.2 The polluted boundary layer – The Nitrate Radical

In polluted coastal environments the nitrate radical NO_3, when present at nighttime, can be a more efficient sink for DMS compared to the hydroxyl radical (OH) during day. The relevance of the reaction of NO_3 and DMS was first noted by Winer et al. [1984] and has a the rate constant in the same range as the OH+DMS reaction. As the mixing rates reached by the nitrate radical can surpass those of OH by one or two orders of magnitude, the effects on DMS can be dramatic. In polluted areas the nitrate radical (NO_3), when present at nighttime, can be a more efficient sink for DMS compared to the hydroxyl radical (OH) during day.
Since its discovery the mechanism of this reaction has received much attention [Andreae et al.

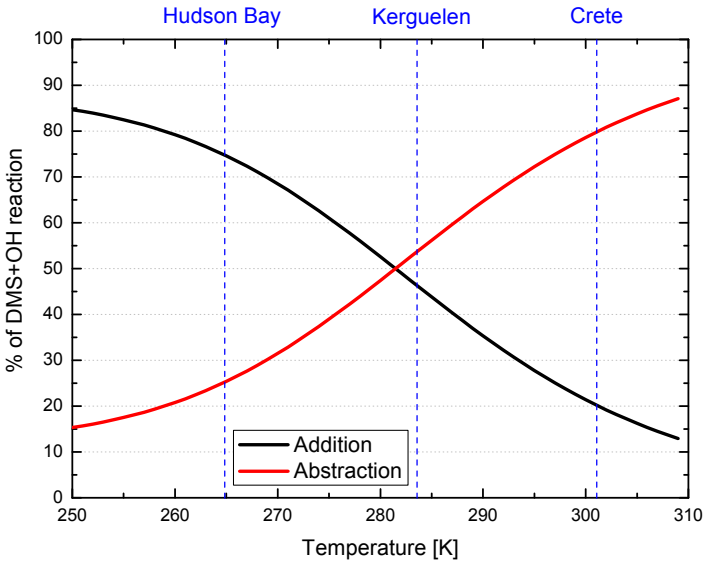

Figure 2.12: Relative contribution of the addition or abstraction path to the DMS+OH in dependence of ambient temperature.

1985; Yvon et al. 1996; Ravishankara et al. 1997; Gölz et al. 1993] and it is now agreed that the DMS + NO_3 reaction proceeds almost exclusively ($\geq 98\%$) via hydrogen abstraction followed by recombination of the CH_3SCH_2 radical with O_2 [Butkoskaya and LeBras 1994; Platt and Le Bras 1997]:

$$NO_3 + CH_3SCH_3 \rightarrow HNO_3 + CH_3SCH_2 \quad (2.181a)$$

$$CH_3SCH_2 + O_2 \xrightarrow{M} CH_3SCH_2O_2 \quad (2.181b)$$

$$CH_3SCH_2O_2 + NO_3 \rightarrow CH_3S + CH_2O + NO_2 + O_2 \quad (2.181c)$$

In the absence of NO during night, reaction (2.181c) will lead to the removal of a second NO_3 [Le Bras et al. 1993].
Having a glance on the oxidation chain as depicted in Figure 2.11 and the corresponding rate constants given in Table 2.12 shows that the cycle is also very sensitive to the abundance of NO_2 and NO. The presence of NO seems to be an unalterable condition for the formation of dimethyl sulphone $DMSO_2$ and both NO and NO_2 together with ozone rule the fate of the abstraction path. Still little is known about the adduct reactions of NO and NO_2 to the organic compounds formed along the abstraction path. Although most of the compounds formed are presumably quite sensitive to photolytic and thermal decay, their presence may inhibit MSA formation particulary during nighttime.

2.3.2.3 Interactions of DMS with reactive halogen species

Due to the numerous laboratory studies named at the begin of this section a more detailed estimation of the contribution of halogen compounds to the DMS oxidation can be held by now. The most efficient reactions of DMS, DMSO and $DMSO_2$ correspond to the reaction

with the Chlorine atom [Díaz-de Mera et al. 2002; Martínez et al. 2002]. However, due to the commonly more than 1000 times higher mixing rates found, reactions involving the Bromine radical (BrO) are probably the most relevant regarding organic sulphur depletion. The reaction of BrO with DMS can be become a dominant sink for DMS during bromine events as observed in the arctic in spring.

$$\mathrm{DMS} + \mathrm{BrO} \rightarrow \mathrm{DMSO} \tag{2.182}$$

The exclusive product of this was found to be Dimethylsulphoxide [Ingham et al. 1999]. Reactions of BrO with the oxidation products of DMS are at least one order of magnitude slower. In NO_x free environments the reaction of BrO with DMSO could be the exclusive source of $DMSO_2$[Riffault et al. 2003; Ballesteros et al. 2002].
The contribution of Iodine to the DMS oxidation chain seems to be quite slow. The only investigated reaction so far, DMS+IO, is ten times slower than the corresponding BrO reaction. Further investigations on the role of halogens in the sulphur cycle have been performed by [Aranda et al. 2002], who investigated the kinetics and products of the BrO+CH_3SH reaction and [Rodríguez et al. 2003] with a study of Cl reactions with aliphatic thiols.
In addition to the gase phase reactions, halogen compounds contribute to the production of sulfate in the aqueous phase [Vogt et al. 1996]:

$$\mathrm{HO_X(aq)} + \mathrm{S(IV)} \rightarrow \mathrm{S(VI)} \qquad (\mathrm{X{=}Cl,\ Br}) \tag{2.183}$$

and might have a relevant contribution to the depletion of DMSO and MSIA as derivable from the rate constants given in section 2.3.2.4.
Model results of von Glasow and Crutzen [2003] for the pristine marine boundary layer have shown that the inclusion of halogen emissions as expectable for the open ocean, changes the diurnal cycle of sulphur species by starting the destruction of DMS earlier in the morning whereby the mixing ratios of the oxidation products (DMSO, MSA and SO2) also peak earlier in the course of day.

2.3.2.4 Multiphase reactions

Heterogeneous and multiphase reactions on solids and in liquids have the potential to play a major role in determining the composition of the gaseous troposphere. In the context of tropospheric chemistry involving condensed species, it is important to distinguish between heterogeneous chemistry as that which is constrained to the surface of a solid, and multiphase chemistry which takes place in the bulk of the liquid medium. A detailed description of the principles and consequences of heterogeneous and multiphase chemistry can be found in [Ravishankara 1997].
One of the most notorious and investigated examples for multiphase chemistry in the troposphere is the oxidation of SO_2 to sulfuric acid. Two decades ago [Penkett et al. 1979] showed that SO_2 could be oxidized by H_2O_2 and O_3 in liquid droplets in the atmosphere, and it is now accepted that a significant fraction of SO_2 is oxidized by multiphase reactions [Calvert 1985]. Another notorious example for multiphase chemistry is wet deposition, a mechanism

Table 2.13: Overview of multiphase reactions involved in the DMS oxidation cycle.

	Reaction	k $[M^{-1}s^{-1}]$	T [K]	Solution	Reference
	$DMS+O_3 \rightarrow CH_3S(O)CH_3$	$(4.1 \pm 1.2) \times 10^8$	291	pure Water	BAR03
	$\rightarrow$	$(1.8 \pm 0.5) \times 10^8$	274.4	pure Water	BAR03
	$\rightarrow$	$(3.2 \pm 1.0) \times 10^8$	288	0.1 M^{-1} NaCl	BAR03
	$DMS+OH \rightarrow CH_3S(O)CH_3$	5.2×10^9	298	pure Water	BAR03
	$MSI^- + H_2O_2 \rightarrow MS^-$	$(1.2 \pm 0.2) \times 10^{-2}$	303	pure water	BDK02
	$MS^- + H_2O_2 \rightarrow$ products	$< 1 \times 10^{-5}$	303	pure water	BDK02
	$DMSO + H_2O_2 \rightarrow MSA$	$< 1 \times 10^{-5}$	303	pure water	BDK02
	$MSI^- + OH \rightarrow MS^-$	1.2×10^{10}	295	pure water	BDK02
	$DMSO + OH \rightarrow MS^-$	4.5×10^9	295	pure water	BDK02
	$DMS + BrO^- \rightarrow$ products	$(1.6 \pm 0.1) \times 10^5$	275	pH=9.7	BAR03b
	$DMSO + BrO^- \rightarrow$ products	(0.8 ± 0.1)	275	pH=9.7	BAR03b
	$MSI^- + HOBr \rightarrow$ products	$(0.35 \pm 0.04) \times 10^3$	275	pH=7	BAR03b
	$MS^- + HOBr \rightarrow$ products	(0.20 ± 0.04)	275	pH=7	BAR03b
	$DMS + Br_2 \rightarrow$ products	$(0.6 \pm 0.4) \times 10^7$	275.5	pH=3.3	BAR03b
	$DMSO + Br_2 \rightarrow$ products	$(2.1 \pm 1.6) \times 10^3$	275.5	pH=3.3	BAR03b
	$MSIA + Br_2 \rightarrow$ products	$(1.1 \pm 0.6) \times 10^6$	275.5	pH=3.3	BAR03b
	$MSA + Br_2 \rightarrow$ products	$(1.5 \pm 0.9) \times 10^3$	275.5	pH=3.3	BAR03b
	$SO_2 + O_3 \rightarrow H_2SO_4$	2.4×10^4		pure water	SEI86
	$SO_3^{2-} + O_3 \rightarrow H_2SO_4$	1.5×10^9		pure water	SEI86
	$SO_3^{2-} + HOCl \rightarrow H_2SO_4 + Cl$	7.6×10^8		pH=9-10	VOG96
	$SO_3^{2-} + HOBr \rightarrow H_2SO_4 + Br$	5.0×10^9		pH=9-10	VOG96
Gas phase reactions (for comparison)					
	$DMS+OH \rightarrow$ products	$\approx 2.6 \times 10^9$	298	gas phase	ATK03
	$DMS+NO_3 \rightarrow CH_3SCH_2+HNO_3$	$\approx 8.5 \times 10^8$	298	gas phase	ATK03
	$DMS+O_3 \rightarrow CH_3S(O)CH_3$	$\approx 5.0 \times 10^2$	298	gas phase	ATK03

[Atkinson et al. 2003] (ATK03), [Barcellos da Rosa et al. 2003] (BAR03)
[Bardouki et al. 2002] (BDK02), [Betterton 1992] (BET92)
[Seinfeld 1986] (SEI86), [Betterton 1992] (BET92)
[Vogt et al. 1996] (VOG96), [Barnes 2003] (BAR03b)

for the ultimate removal of chemicals from the atmosphere.
The most visible forms of condensed matter in air are clouds (including fog), which are primarily solid or liquid water. Water is also the most abundant reactant for heterogeneous and multiphase reactions. Other media for heterogeneous and multiphase reactions available in the troposphere are organic, sulfate and sea-salt aerosols as well as soot. The sea-salt aerosols present in the marine boundary layer are formed by bursting bubbles which generally have the composition of sea water, being therefore highly concentrated solutions of halides at times enriched in constituents from the sea surface.
The tropospheric multiphase reaction is initiated by diffusion of one or more molecules in the gas-phase to the surface of a droplet, at a rate determined by pressure, water content of air, and the gas-phase diffusion coefficient. Subsequently the molecule is incorporated into the liquid phase at a speed determined by the mass accommodation coefficient α, followed by diffusion in the liquid droplet, at a rate controlled by liquid phase diffusion and the radial concentration gradient. The efficiency of the reaction in the liquid phase is then dictated by the rate coefficient for the reaction and the concentration of the second reactant. Upon reaction, the products can either remain in the droplet, undergo further reactions, or diffuse out to the gas phase.
As most of the factors controlling the multiphase reaction are dependent on the considered chemical species the relative importance of the heterogeneous process will depend on the reactivity in the gas-phase. If the gas phase removal is fast, heterogeneous reactions are unlikely to compete.
The role of heterogeneous reactions in the DMS oxidation cycle was not considered in atmospheric models until lately [Campolongo et al. 1999]. The attention to multiphase chemistry was evoked by the results of [Lee and Zhou 1994], who found the aqueous phase reaction of DMS and ozone to be largely more efficient than the gas phase reaction and postulated significant implications for atmospheric chemistry. Later studies of [Gershenzon et al. 2001] and [Barcellos da Rosa et al. 2003] confirmed this results. The latter study also investigated the effect of adding salt to the solution, observing a reduction of the rate constant about 25% in 0.1 M^{-1} NaCl. The overview of rate constants for multiphase reactions involved in the DMS oxidation cycle given in Table 2.13 also includes the most recent findings from laboratory studies performed within the framework of the EL CID project.
Studies of the aqueous phase reactions of DMS, DMSO and dissociated MSA and MSIA with the hydroperoxyl and the hydroxyl radical have shown that reactions of these compounds with H_2O_2 are slow. A high efficiency was found for the reaction of OH with the readily soluble compounds DMSO and MSIA (i.e. MSI^-), both yielding MS^- as the end product [Bardouki et al. 2002]. Atmospheric implications of the aqueous phase reactions of DMSO and MSIA with OH can be quite important in clouds. Assuming OH concentrations in the range of $5 - 50 \times 10^{-14} M^{-1}$ [Herrmann et al. 2000] the lifetime of DMSO and MSI^- would range from 3–30 and 7–70 minutes for DMSO and MSA respectively. However, according to Jacob [2000] heterogeneous chemistry of OH is unimportant outside clouds because of the short chemical lifetime of OH in the gas phase(1 s) relative to the time scale for uptake by the

aerosol (minutes).
More laboratory results presented in the final EL CID report [Barnes 2003] have shown that DMS and the anion of MSIA react rapidly with Br_2 and HOBr(Table 2.13). It appears that these sulphur compounds may inhibit halogen activation in the aqueous phase in contrast to the gas phase, where DMS+BrO leading to DMSO + Br is a catalyst of halogen activation.
The knowledge about other depletion depletion mechanisms of DMS and its oxidation products is quite limited. Dry deposition, i.e. the transport of trace gases and particles to the earth's surface, is an important loss process for many reactive and soluble trace gases. A small collection of literature concerning dry deposition of SO_2 can be found in [Nilsson and Leck 2002]. In general very little is known from direct measurements about the deposition process of species other than O_3, SO_2 and NO, so that the major part of global models rely on a complex parametrization depending on the surface type [von Kuhlmann 2001]. For the atmospheric box model MOCCA first presented by [Sander and Crutzen 1996] empirically established values employed are 0.5, 2.0, 1.0 and 1.0 cm/s for SO_2, SO_3, MSA and DMSO respectively. Another process which could be taken into account is wet deposition. It should be most important for the soluble species as DMSO and MSIA and could probably play a significant role during abundant fog and cloud formation episodes.
Investigations also performed within the framework of the EL CID project have confirmed that direct photolysis of MSA, DMSO and $DMSO_2$ can be neglected under tropospheric conditions considering the overlap of the UV spectra with the solar spectrum.

Chapter 3

Instrumental Setup

3.1 The Active Long Path-DOAS System

The active long path-DOAS systems employed during all three field studies on Crete, Hudson Bay and Kerguelen (see sections 4.1, 4.2, 4.3) for this work have already been described elsewhere [Ackermann 2000; Geyer 2000; Alicke 2000; Hebestreit 2001]. Therefore only an overview of the different components will be given here. Figure 3.1 shows the different components needed for the LP-DOAS setup.

In the following sections the telescope, the light source, the spectrometer and detector system and finally the basics of the DOAS-fit are described.

3.1.1 The LP-DOAS Telescope

The telescope of the long path system consists of two coaxial Newtonian telescopes with transmitting and receiving optics combined in one device. In the optical axis of the telescope two elliptical plane mirrors are installed to reflect the light of both outgoing and incoming beams by 90 degrees. The main component is a parabolic mirror of 30 cm diameter and a focal length of 150 cm (Figure 3.2). The light source is placed in the focal point of the main mirror. Thus the outgoing light beam is parallel. A retro reflector array in a distance of several kilometers is used to reflect the parallel light beam exactly back into the telescope, where it is focussed onto a quartz fiber. The quartz fiber transmits the light into the spectrograph. The optical image, however, is not perfect. Since the light is not a point source the beam slightly diverges along its path through the atmosphere resulting in a loss of light depending on the distance to the retro reflectors. Because of the two plane mirrors in the optical axis of the telescope only a ring can be sent into the atmosphere leading to a light loss of 50 % compared to a fully illuminated mirror without the shade of the plane mirrors. Altogether five stepper motors control the telescope and its parts:

- Two motors are used to align the telescope on the retro reflector array (and possibly at others) in horizontal and vertical direction.
- One stepper motor carries a filter wheel equipped with various filters, e.g. UG5 from Schott, Germany (in order to remove light at wavelengths above 400 nm to reduce stray light in the spectrograph) and a baffle to record background spectra.

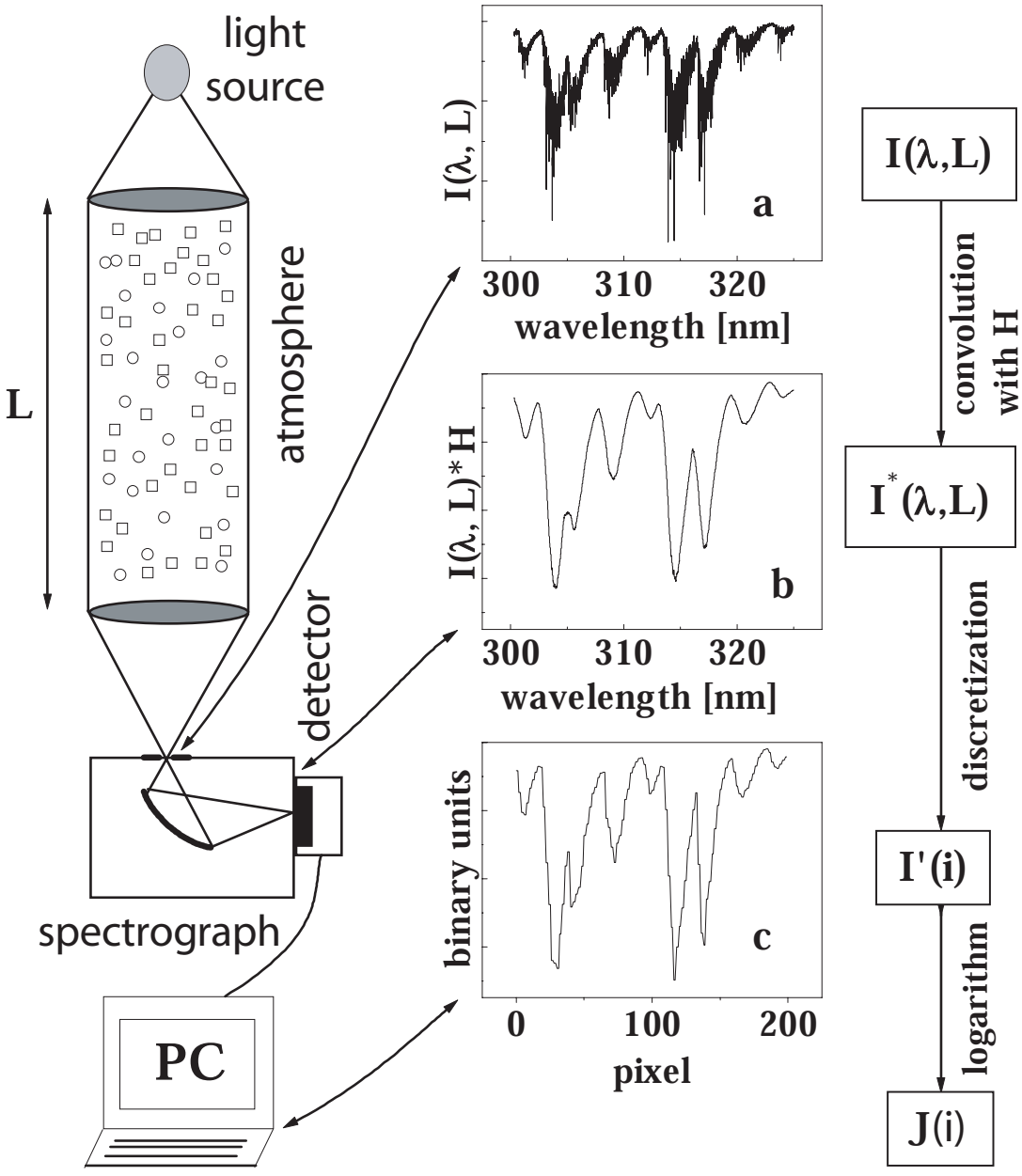

Figure 3.1: The main components of the LP-DOAS system

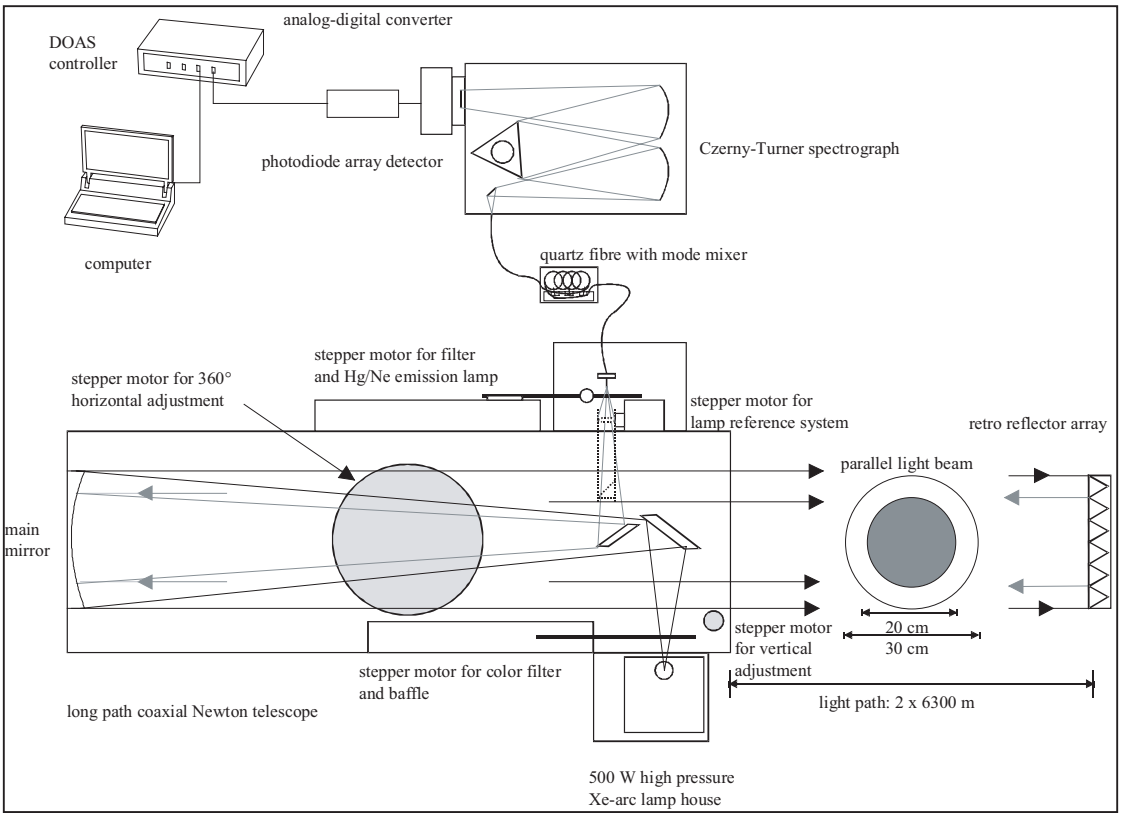

Figure 3.2: Schematic delineation of the employed Longpath-DOAS systems.

- At one motor a mercury emission lamp is mounted which can be positioned in front of the quartz fiber to determine spectral resolution and wavelength calibration at several times during the measurements.

- The fifth motor carries the lamp reference system, which can be moved into the outgoing light beam. The reference system consists of an elliptical plane mirror, which reflects a part of the light of the outgoing light beam onto a quartz lens from which it is focussed onto the quartz fiber.

3.1.2 The Light Source

The light sources of all LP-DOAS measurements in this work are Xenon high pressure short arc lamps(Figure 3.3). Gas discharge induced by high voltage producing a dense plasma in the Xenon gas bulb between anode and cathode with an extension of the brightest spot below 1 mm. The spectrum of a Xenon arc lamp is the superposition of the thermal emission according to the Planck function and individual Xenon emission lines, which are pressure broadened due to the high operating pressure of Xenon arc lamps(up to 10^7Pa under operating conditions). The distance of the electrodes is generally small resulting in a short arc length (thus reducing the divergence of the light beam emitted from the telescope) and high local light intensity. The color temperature of the used Xenon lamps of $\sim$ 6000 K is similar to

Figure 3.3: Photography of an OSRAM XBO500 Xenon-Arc-Lamp.

Table 3.1: Comparison of the employed Xenon arc lamps

lamp	PLI HSA-X5002	Narwa 250W	Osram XBO 500W
power [W]	500	250	500
voltage [V]	18	18	18
current [A]	28	14	27
lifetime [h]	200	3000	250
Ø lightspot $[mm^2]$	0.3×0.3	0.4×0.4	0.45×0.45

that of the sun with maximum spectral intensity around 500 nm. The bulb of a Xenon lamp consists of quartz glass, which is extremely resistant to the pressure and temperature. The electrode material is tungsten with endowments depending on the lamp type. The cathode has an edged peak to enhance the electron emission. In contrast the anode is made of massive material to absorb the kinetic energy of the incoming electrons. In this Ph.D. thesis mainly one type of Xenon arc lamps (HSA-X5002 supplied by PLI Inc., NJ, lamp design adapted from Hanovia lamps) was used. Only for the last campaign at Kerguelen the LP–DOAS system had to be run with the Narwa 250 W and Osram XBO 500 W Lamps. For a comparison see table 3.1. The variability of the emission features of Xenon short arc lamps caused by flaring lamp plasma was studied by Hermes [1999]. Xenon emission lines were found at several wavelengths including the red spectral region. The emission strength and pressure broadening of the Xenon lines was found to change over time and therefore the lamp structures are difficult to remove from a spectrum. It was found that lamp structures are more easily removed from a spectrum in the case of the PLI lamp as its Xenon emission bands are broader and therefore can be better reduced by high pass filter routines.

3.1.3 Spectrograph and Detector Unit

For the measurement of the atmospheric absorption spectra a Czerny–Turner spectrograph was used. This device is based on a setup originally developed by Czerny and Turner [1930]. The quartz fiber which transmits the light from the telescope to the spectrograph is mounted in the focal point (entrance slit) of the first convex mirror (collimating mirror). The parallel light from this mirror is then dispersed by a plane diffraction grating. A second convex spherical mirror unit (focussing mirror) then focusses the dispersed light onto the detector. The wavelength region observed by the detector can be changed automatically by a computer controlled stepper motor drive (tolerance 0.5 steps). In order to minimize thermal instability

the whole spectrograph unit is insulated and temperature stabilized to a few K above maximum room temperature (usually 30 ±0.2 °C). The used ACTON Spectra Pro 500 with a focal length of 500 mm was equipped with a plane diffraction grating (aperture ratio f/6.9, entrance slit (fiber exit) width of 200 μm, grating 600 grooves/nm, dispersion: 3.08 nm/mm (or 0.077 nm/pixel), spectral resolution: 0.54 nm). For recording the spectra, a 1024 pixel photodiode array detector (PDA) was mounted in the focal plane of the spectrograph. A detailed discussion of the usage of photo diode arrays as DOAS detectors is given by Stutz 1991 and Stutz and Platt 1992. The principal component of the unit is a photo diode array from Hamamatsu (Type S3904-1024) with 1024 Si photo diodes (n-channel MOSFETs) of 25 μm width and a height of 2.5 mm. The PDA is placed in a housing that can be evacuated and filled with 1.2 bar Argon 5.0. Each photo diode consists of a n-p semiconductor junction. During operation an inverse voltage of 2.06 V is applied to the diode inducing a depletion layer which is almost as large as the whole diode area. Incoming light excites a number of electrons proportional to the light intensity into the conducting layer of the semiconductor. The capacity of a diode is 10 pF, the full well depth corresponds to 1.286 $\times 10^8$ photo electrons. These photo electrons reduce the applied inverse voltage. However this is also possible by thermally excited electrons. This effect is called dark current and must be considered and corrected before the evaluation procedure at low light intensities. In order to reduce dark current the PDA was cooled down to temperatures between -15 and -30 °C by a Peltier cascade. Thereby the dark current decreases exponentially regarding Boltzmann statistics.
After the integration time the PDA is read out by re-charging the photodiodes. The charge needed is amplified electronically. To prevent negative signals (which cannot be converted by the used ADC) an offset signal is added to every PDA signal. The offset is proportional to the number of scans added and must be corrected for during the evaluation process. The signals are digitized by a 16 bit analog - digital converter (full saturation corresponds to $2^{16} = 65536$ counts) and then transferred to the computer. Due to the cooling of the detector unit water vapor could freeze on the PDA surface and possibly cause etalon structures due to interference effects. Therefore the detector is evacuated and filled with dry argon as inert gas. Another effect of PDAs is the so called memory effect. That means that structures of a former spectrum can be seen in the following spectra. This effect was discussed e.g. in [Stutz 1996; Leser 2001], however its origin is unclear up to date. Usually the memory effect can be significantly reduced by multiple scans without light or just waiting for a short time.

3.1.4 The DOAS fit

In the UV spectral range, besides BrO also OClO has strong absorption features. Therefore OClO was also included in the DOAS fit for BrO. However, including OClO in the BrO fit did not yield any significant absorptions attributed to OClO. Therefore, the evaluation of OClO was optimized by narrowing down the fit interval to the range 331.5 nm to 354 nm, which contains only the three strongest UV absorption bands of the OClO molecule for the best signal to noise ratio. The mean detection limit of OClO in this analysis was 1.7 ppt (2σ) on average.
Iodine oxide (IO) was evaluated in the blue spectral range from 423-447 nm comprising the

three strongest IO absorption bands (2-0, 3-0 and 4-0) of the $A^2\Pi_{3/2} \leftarrow X^2\Pi_{3/2}$ transition of the IO radical. Besides IO, reference spectra of water vapor, NO_2, O_4, OBrO, OClO and a Xenon lamp spectrum were included in the DOAS fit. The limiting factor for optimizing the IO analysis was the correct removal of the Xenon lamp emission lines (e.g. at 438 nm and for $\lambda \geq 446\,nm$). The lowest residual structures were obtained fitting an average spectrum of all lamp references recorded throughout the campaign, achieving a mean detection limit of 1.3 ppt for IO. The strongest absorption bands of the halogen dioxides OBrO and OIO are in the green spectral range between 500 nm (OBrO) and 550 nm (OIO). Therefore an optimized DOAS evaluation for these species was performed between 541 nm and 565 nm, where both molecules exhibit four strong absorption bands. Besides the two halogen dioxides OIO and OBrO, reference spectra of water vapor, NO_2, O_4 and a lamp reference spectrum were simultaneously fitted to the measured atmospheric spectra. Variable Xenon lamp structures were again the limiting factor when analyzing the absorption spectra in this spectral range. Frequently residual structures of up to 5×10^{-3} (peak-to-peak value) due to changes of the shape of the Xenon emission lines could not be adequately described by the reference spectra included in the analysis.

3.2 Cofer mist chamber and Gas/Ion chromatography

Gaseous *Dimethylsulphide* was collected conjointly by the groups of LSCE-CNRS and ECPL Crete (J.Sciare, N.Mihalopoulos, H.Bardouki, C.Oiknomou,...) by compressing air into electropolished stainless steel canisters for variable sampling intervals depending on ambient DMS concentrations (from 15 *min* to several hours). The canisters were previously conditioned by vacuum heating and according to [Nguyen et al. 1990] no significant variations of sampled DMS concentrations should occur within 24 hours after the sampling. Nevertheless the sample analysis was performed immediately after collection. DMS was preconcentrated on a Tenax GC trap immersed in liquid nitrogen. After trapping, DMS was introduced in a packed column(Chromosil 310) by heating the trap with boiling water(90 °C). The analysis was made by using a Shimadzu Gas-Chromatograph equipped with a Sulfur Chemiluminescence Detector (Sievers 355 SCD).

Reaction Mechanism

$$\text{Sulphur compound} + O \rightarrow SO + \text{otherproducts} \quad (3.1a)$$

$$SO + O_3 \rightarrow SO_2 + O_2 + h\nu \quad (3.1b)$$

The reaction mechanism used to detect sulphur compounds is rather simple. The first step consist in the high temperature combustion (> 1800 °C) of the sampled species within a stainless steel burner to form sulphur monoxide (SO) (reaction 3.1a). Subsequently, the burned sample is conducted to a reaction cell(Figure 3.2) where a certain amount of ozone

is added invoking the chemiluminescent reaction (3.1b) with SO. The produced light passes through an optical filter and is detected by a photomultiplier tube. The results are in a linear and equimolar response to the sulphur compounds without interference from most sample matrices.
The achieved detection limit was 0.1 nanogram of DMS and the dependence of the detectors signal to the sulphur concentration was linear. DMS quantification was performed by means of a permeation tube maintained at 30 °C, calibrated against liquid standards of DMSP as described by [Belviso et al. 1993].

Due to the high solubility in water, another technique is used for sampling and analysis of

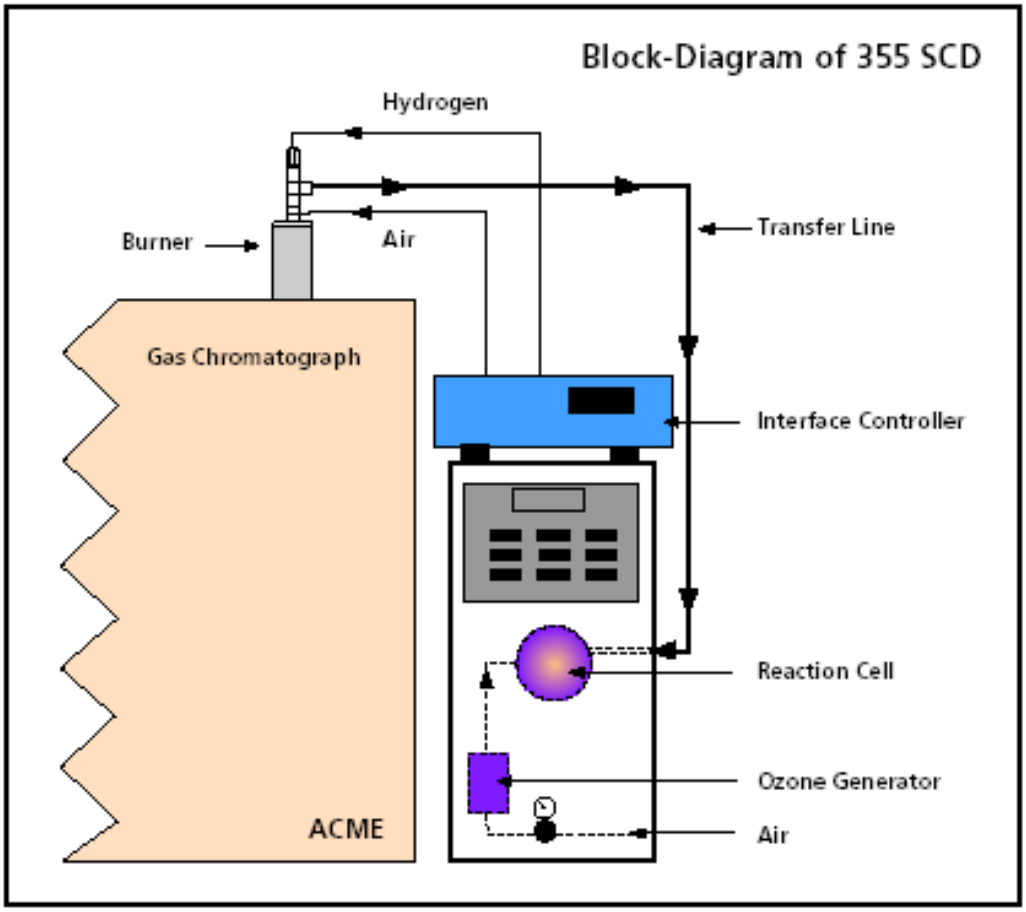

Figure 3.4: Schematic illustration of the combined Gas-Chromatograph and Sievers 335 Chemiluminescence Detector system employed for DMS measurements.

Dimethylsulfoxide(DMSO). It is based on the nebulization/reflux principle as described by [Cofer and Edahl 1986] and has been described in detail in [Sciare and Mihalopoulos 2000]. A brief synopsis follows. Using a vacuum-pump a constant air flow (15 $lmin^{-1}$) is uphold to drive ambient air through a Teflon filter (to remove aerosol particles) into one of two nebulizing nozzles of a Cofer-Chamber [Cofer and Edahl 1986]. The gas flowing past the tip of a second nozzle (see Figure 3.2) aspirates extracting solution into the flowing gas stream where it is atomized by impaction into small droplets, generating an air/droplet mist. The solution used for extraction (about 20 ml of pure water, lightly acidified to better stabilize

the trapped DMSO) is aspirated at a rate of few milliliters per minute from a reservoir. The resulting vapor/droplet mist moves upward through the reaction chamber to reach a hydrophobic membrane (PTFE Filter), which offers little resistance to the exiting gas flow but stops water droplets containing scrubbed gases. The water droplets containing DMSO collect on the surface of the membrane and coalesce into larger droplets which subsequently roll back down the collector into the reservoir to be recycled.
Once sampled, DMSO is reduced to DMS by sodium borohydride ($NaBH_4$) and DMS is subsequently analyzed by gas chromatography. By using a classic flame photometric detector (FPD) with detection limits of about 1 ng (DMS), atmospheric concentrations of DMSO down to 0.35 ppt can be achieved for sampling times of 1 h.

The collection of *Methane sulphonic acid (MSA)* was achieved by sucking air over a period

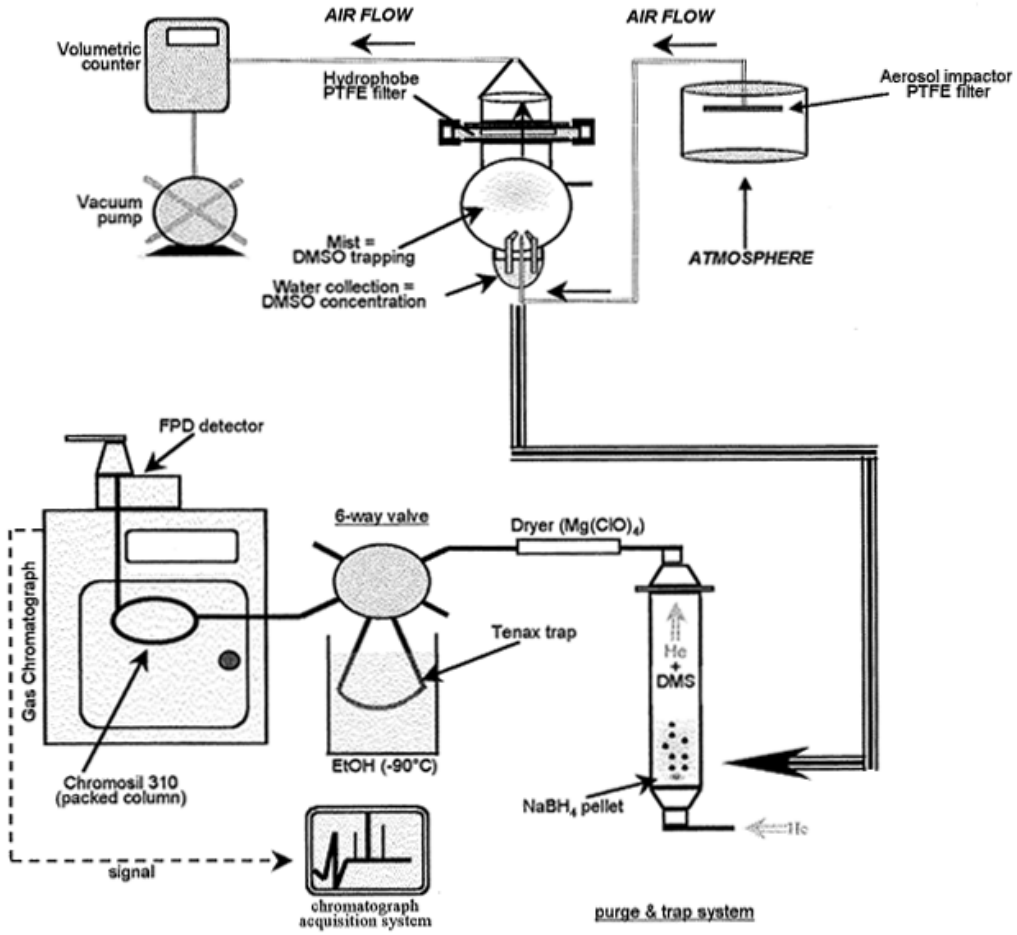

Figure 3.5: Sampling and analysis settings for atmospheric DMSO (Sciare2000d).

of several through Teflon filters using a vacuum pump with a constant flow rate of 20 l/min. The Aerosols deposited on the filter surface are extracted in the laboratory by sonication during 45 minutes in a 20 ml ultra-pure water bath. The solution is analyzed for the main anions (including MSA) and cations using Ion Chromatography. The reproducibility of these measurements was commonly better than 2% and the detection limits for all ions corresponded to 0.04 nmol/m3.

3.3 The chemical amplifier (ROX–BOX)

RO_x, mainly peroxy radicals (HO_2 and RO_2) were measured at Finokalia during the last 2 weeks of the campaign (24.07-06.08.2000) using chemical amplification. The calibrated peroxy radical amplifier (PERCA or 'ROX-BOX') was kindly provided and calibrated by T.Klüpfel (MPI-Mainz) and operated by the IUP–Heidelberg Team. The instrument utilizes modulated chemical amplification of NO_2 by HO_2 and RO_2 in the presence of NO and CO as first proposed by Cantrell and Stedman [1982].

$$\mathrm{HO_2 + NO \rightarrow OH + NO_2} \tag{3.2a}$$

$$\mathrm{OH + CO \rightarrow H + CO_2} \tag{3.2b}$$

$$\mathrm{H + O_2 \xrightarrow{M} HO_2} \tag{3.2c}$$

$$\mathrm{NO + CO + O_2 \rightarrow NO_2 + CO_2}$$

Addition of a luminol solution will produce chemiluminescence from the reaction with NO_2. The concentration of NO_2 at the outflow of the reaction chamber can then be easily determined from a commercial liquid-phase chemiluminescence detection system.
The ROX–BOX measures the sum of all oxy– and peroxy–radicals (RO_x : OH, HO_2, CH_3O, CH_3O_2 etc.). The amplification factor or chain length is proportional to $\Delta NO_2/[RO_x]$. The exact conversion factor for the single organic radicals was determined through radical calibrations performed by T.Klüpfel one day before the start of measurements at Finokalia. Besides HO_2 and RO_2 active chlorine supports chain amplification in the PERCA instrument as well (Perner et al. [1999]). In addition, the chain length is strongly influenced by ambient water vapour concentration(Mihele and Hastie [1998]). This dependence can be corrected for using ambient relative humidity data. Data points are given as running mean of 10 values, the mean standard deviation is about 3 ppt.

Chapter 4

Field Measurements

In this chapter the field work carried out within the framework of the EU–project EL–CID[1] will be described. In total three intensive field campaigns have been realized within 21 months at locations spread over the globe. The aim of the measurements was to investigate the oxidation pathways of DMS under different environmental conditions and to establish the relative contribution of radical species to the oxidation capacity in the marine boundary layer. During all three field campaigns the DOAS technique was employed by the groups of the IUP-Heidelberg to establish the concentration of measurable radical species including a set of halogen and nitrate compounds. These results are complemented by timeseries of DMS, DMSO and additional data provided by the fieldwork partners from LSCE-CNRS (France) and UCPL(Greece). The results will be complemented with a general description of all measurement locations and available meteorological parameters.
The main objectives of the field measurements was to establish the relative oxidation capacity of free radicals in the marine boundary layer and to investigate the oxidation pathways of Dimethylsulphide(DMS) under largely different environments.
The location chosen for the first campaign was on the Greek Island of Crete in the southern Mediterranean. Due to the moderately polluted environment a special emphasis was held on the investigation of nitrogen species and in essential on the nitrate radical (NO_3). The second campaign was performed in the lower arctic, at the southestern coast of the Hudson Bay (Canada). The special aim was to investigate the impact of BrO, released during bromine explosion events, on atmospheric DMS concentrations and to determine the yield of DMSO formation. The third campaign on the Islands of Kerguelen in the remote Indian Ocean offered a pristine environment. Although the hydroxyl radical is presumably the main oxidizing species in this region, the influence of other radical species has not been established yet. Due to the strong marine biological activity at the plateau of Kerguelen, DOAS measurements were performed to establish whether degradation of organohalogen species is an important source of Iodine or bromine oxide.

[1] **E**va**L**uation of the **C**limatic**I**mpact of **D**imethylsulfide

4.1 Field Campaign Crete 2000

The first field campaign of the EL CID–Project was carried out in Summer 2000 on Crete in the eastern Mediterranean. The objective of the campaign was the identification and definition of the relative importance of the main radicals (OH, NO_3, XO) involved in the DMS oxidation for mid-latitudes under moderately polluted marine conditions. The additional aim for our partners was the identification and quantification of the major DMS oxidation products, aerosol size and quantity distribution under these conditions.

4.1.1 Observation Site

Finokalia (35°20′N, 25°40′E) is a rural site located at the northern coast of Crete in the Eastern Mediterranean(local time=universal time(UT)+ 3 hours). The sampling station for in situ measurements is placed on top of a hill (130 m above sea level) facing the sea in the north within the sector 270-90°. The village Finokalia itself has 10 inhabitants and is located 3 km to the south. There are no human activities within a range of 20 km around the station. The main city of the Island, Heraklion, has 150.000 habitants and is located 70 km westward (Fig. 4.1). Although local pollution is negligible, air pollution standards are exceeded in the boundary layer throughout the region caused by West and East European pollution from the north [Mihalopoulos et al. 1997; Kouvarakis et al. 2000; Lelieveld et al. 2002]. Owing to cloud free conditions and high solar radiation intensity, the region is particulary sensitive to air pollution [Millán et al. 2000; Kouvarakis et al. 2000]. Due to the coastal environment significant concentrations of DMS are expected.
A detailed description of the station is given by Mihalopoulos et al. [1997] and Kouvarakis et al. [2000]. The station's suite of measurements includes ion speciation of aerosols, as well as dry and wet deposition measurements(e.g. sulphur, black carbon) for the past 5 years [Kouvarakis et al. 2001] as well as ozone monitoring [Kouvarakis et al. 2000].

4.1.2 Climatology

The prevailing weather pattern at Crete was clear sky and calm. No precipitation or clouds were reported during the campaign. Haze formation close to the sea surface reduced visibility during daytime at weak wind periods. As shown in the meteorological overview given in Figure 4.4, typical temperatures ranged between 20 °C at night and 30 °C around noon, with occasional maxima up to 40 °C. The air was usually dry with a relative humidity around 50% on average, descending occasionally down to 10% during relatively hot periods and reaching 90% during few nights. The Meteorological parameters state a negative exponential dependence between humidity and temperature. A linear approach for the temperature interval from $296 - 308$ K delivers a decrease of 3.8% relative humidity per degree temperature. As demonstrated by the relative frequency distribution of the wind directions shown in Figure 4.2, winds blew from northwesterly directions during the major part of the campaign period at Crete. The average wind speed was about 36 km/h (Fig. 4.4). Such a flow is a common pattern not only for Crete [Mihalopoulos et al. 1997], but for the Eastern Mediterranean in general [Alpert et al. 1990; Kallos et al. 1998]. This general

Figure 4.1: Finokalia is located at the northern coast of the Greek island Crete in the Eastern Mediterranean Sea. The main city of the island, Iraklion, is located 70km to the west.

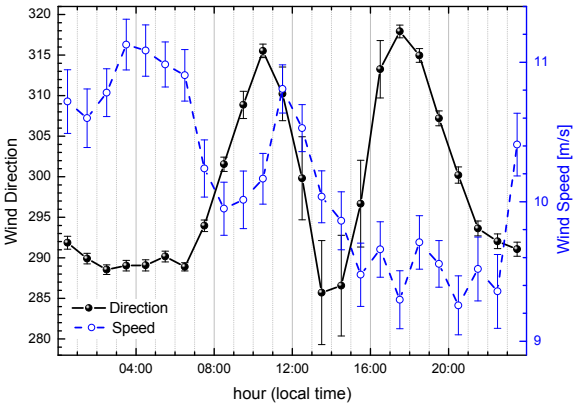

Figure 4.3: Average diurnal variation of wind direction and speed for the whole campaign period (excluding 20-24.07 and 28.07-03.08). The error bars represent the standard error of the averaged values. The diurnal pattern of Wind direction and speed may correspond to a sea-land breeze circulation.

conditions do not apply for the days ranging from 28.07 to 03.08.2000, when winds were often too weak to define a blow direction.

Excluding the period from 20-24.07 with very constant winds and the nearly windless days from 28.07-03.08.2000, a regular day–night pattern in both wind direction and speed observed was commonly observed. On average, the wind direction changed from 280° at night to 320° at noon, while the wind speed decreased continuously until sunset to reach highest speeds few hours before dawn(Fig. 4.3). This pattern could correspond to a local land-sea breeze circulation. As a consequence nocturnal entrainment of pollutants from anthropogenic sources placed along the coast towards Iraklion in the west may regularly occur.

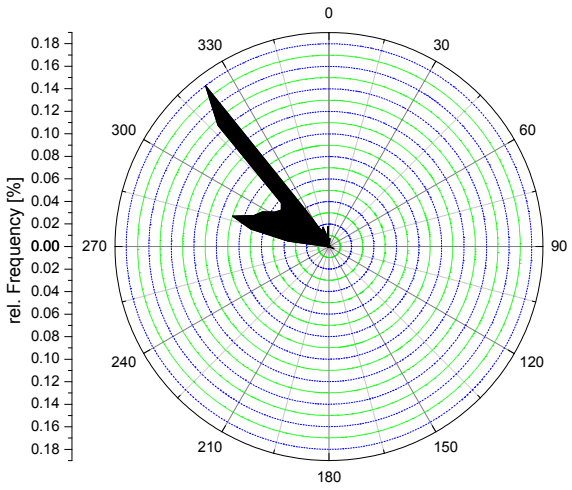

Figure 4.2: Frequency distribution of the wind direction during the measurements at Crete.

Due to the extreme dominance of the northwestern wind sector, the wind direction alone is a rather poor criterion to define the origin of trace gases arriving at Finokalia. Therefore, backward–trajectories of air masses reaching the site have been calculated employing the HYSPLIT Dispersion model (Hybrid Single–Particle Lagrangian Integrated Trajectory [Draxler and Hess 1998]) and meteorological data from the FNL and ECMWF databases. In order to determine the source regions of sampled airmasses, a complete set of 5 day backward–trajectories starting each hour throughout the whole campaign period (08.07-07.08.2000) was calculated. From this data the relative source distribution was obtained by gridding a large area around Crete with a bin resolution of $0.5 \times 0.5°$ and counting the

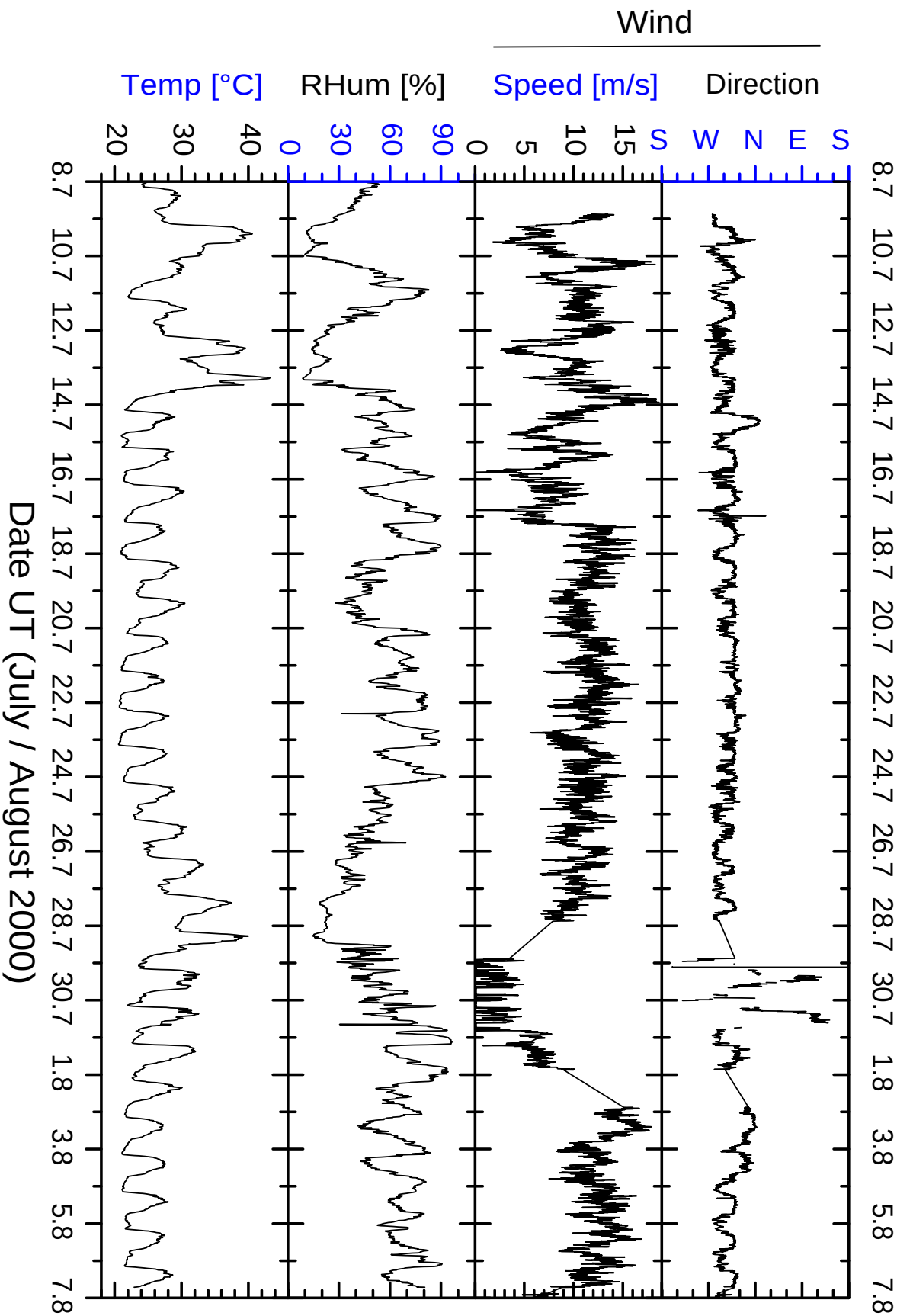

Figure 4.4: Overview of the meteorological parameters temperature, relative humidity,wind speed and direction for the whole period of measurements at Finokalia(Crete) in July/August 2000.

number of times a trajectory crossed each bin. The result of this statistical procedure is shown in Figure 4.5. As expected from the local wind parameters(Figure 4.2), long range transport from the continent in the north was a dominant pattern during the 5 weeks of measurements. The main source regions seem to be the Aegean and Balkan regions and, in extension, whole central Europe denoting the major role of eastern Europe and southern Italy.

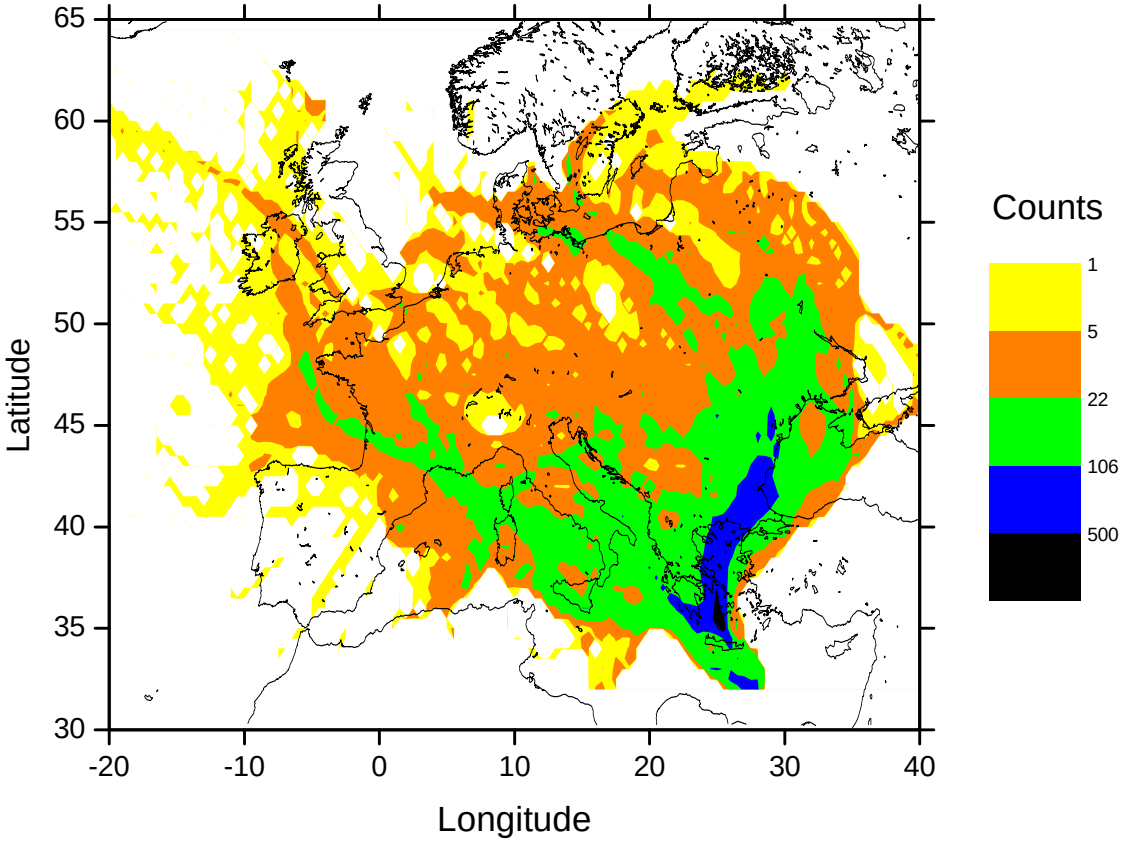

Figure 4.5: The Dispersion Model Hysplit was used to determine the origin of air masses reaching the measurement site for the whole campaign period. The coordinates obtained from hourly calculated 5–day backward trajectories over the whole campaign period have been sorted into 0.5×0.5 degree bins. Counts represent the number of times a trajectory passed the bin (logarithmic scale). The statistical result gives evidence that input from the Aegean Sea and the Balkan region has been the most important within the observed time range, followed by Eastern Europe and the south of Italy.

Pollution from Forest fires Hot, dry weather contributed to the strongest string of fires of the last decade [fir 2002] throughout southern Europe during summer 2000. The situation was particulary dramatic for Greece, where nearly 170000 hectares of wooden areas had become victim of the fires until the end of summer representing 27% of total burnt area in southern Europe in that year. Extremely intensive fire activity was reported during the first two weeks of July 2000. On July 10th about 100 fires were burning throughout the Greek main land and several islands in the Aegean Sea. The main fires were burning in

Figure 4.6: The image taken from satellite by SeaWiFS, on 14th July 2000 provides a view from the west on the Peloponnese Peninsula. The Island of Crete is visible slightly to the right of the image centre. Smoke from the fires on the Greek main land can be seen drifting across the eastern Mediterranean.

the center of Greece, mainly in the region of the city Lamia. Smaller fires also appeared in the northern province Macedonia, on the islands of the Ionian and Aegean Sea(strongest on Samos, also on Crete) and on the Peloponnese Peninsula. During this period strong winds (cooling ambient temperatures from 41 °C to 33 °C) spread the emissions of the biomass burning events throughout the whole region (Fig. 4.6). Vegetation fires are known to be a major contributor to the global budgets of several trace gases. Andreae and Merlet [2001] estimated global annual emissions from extratropical forests. Largest emissions correspond to carbonic matter (1000, 68, 3 and 4 Teragrams/year for CO_2, CO, CH_4 and non–methane hydrocarbons respectively). Although the rates for the NO_x and SO_2 are much lower (1.9 and 0.6 Tg/yr), the relative contribution to local levels can be quite important. An increase of ozone levels in the order of 10 ppb (coupled to CO rise) has been measured over biomass burning plumes [Takegawa et al. 2003].

4.1.3 Active Longpath–DOAS Measurements

Measurements of BrO, HCHO, HONO, IO, OIO, NO_2, NO_3, O_3 and SO_2 concentrations in the boundary layer have been performed using Differential Optical Absorption Spectroscopy (DOAS) as described in section 3.1. For the measurements in Crete, two retro reflector arrays were positioned at 8.16 km and at 5.18 km distance to build up the main and secondary(for hazy conditions) absorption light paths along the coastline. The reflectors were set up at 10–20 m above sea level, therefore the measurements yielded concentrations vertically averaged for the lower 150 m of the marine boundary layer at the north coast of Crete (Fig. 4.7). In a continuous measurement loop atmospheric absorption spectra were taken in the UV (295 nm - 375 nm), blue (390 nm–470 nm) and green (510 nm - 590 nm) spectral ranges. The selected

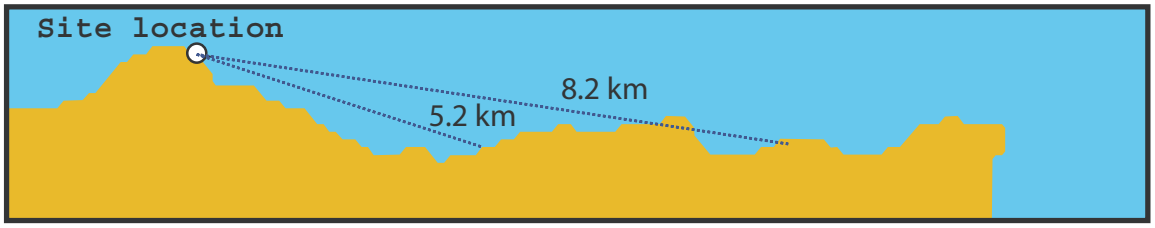

Figure 4.7: The course of the two lightpaths used for DOAS measurements at the northern coast of Crete.

Table 4.1: Concentrations and detection limits obtained from Active DOAS Longpath Measurements at Finokalia 2000.

	Concentration[ppt]		Detection limit[ppt]	
	Mean	(Max)	Average	(Lowest)
BrO	<1.5	(1.8)	1.5	(0.7)
HCHO	1207	(3177)	300	(140)
HONO	36.4	(188.5)	70	(30)
O_3	54700	(78900)	2600	(1100)
SO_2	937	(5888)	160	(60)
IO	<0.8	(8.6)	0.8	(0.2)
NO_2	459.4	(4237)	60	(12)
OIO	<4.0		4.0	(1.6)
NO_3	night: 20.8 day: <1.6	(307.7)	1.6	(0.5)

spectral bands allowed to determine the concentration of the trace gases BrO, HCHO, HONO, IO, OIO, NO_2, O_3 and SO_2. From dusk till dawn the near infrared (605 nm - 685 nm) was added to the scanning loop in order to detect NO_3.
The detection limit of the DOAS is determined by the statistical error σ multiplied with a variable factor (depending on accounted wavelength region), to take into account additional uncertainties of the fit. A general overview of all data obtained with the DOAS instrument is given in Figure 4.8. Mean and maximum concentrations are resumed in Table 4.1. A detailed discussion of all trace gases, excepting SO_2 and HCHO, is held in the following DOAS section. The results of the sulphur dioxide measurements will be discussed in a separate section 4.1.4 together with DMS,DMSO and MSA measurements. Due to the close chemical relationship of formaldehyde(HCHO) and carbon monoxide(CO), the measurements of this trace gases are both presented in section 4.1.5.

4.1.3.1 Halogen oxides

Except for isolated data points, the concentration of halogen oxides was below or equal to the detection limit (0.7 ppt for BrO, 0.2 ppt for IO) for the entire measurement period. The obtained detection limits for the halogen oxides are shown in Table 4.1. However, mean diurnal BrO and IO concentration plots show flashy features (Fig. 4.9). BrO has slightly elevated concentration levels around local noon, which could be a consequence of photolytic destruction of methyl–halides and radical chemistry (HOBr). Taking into account the few

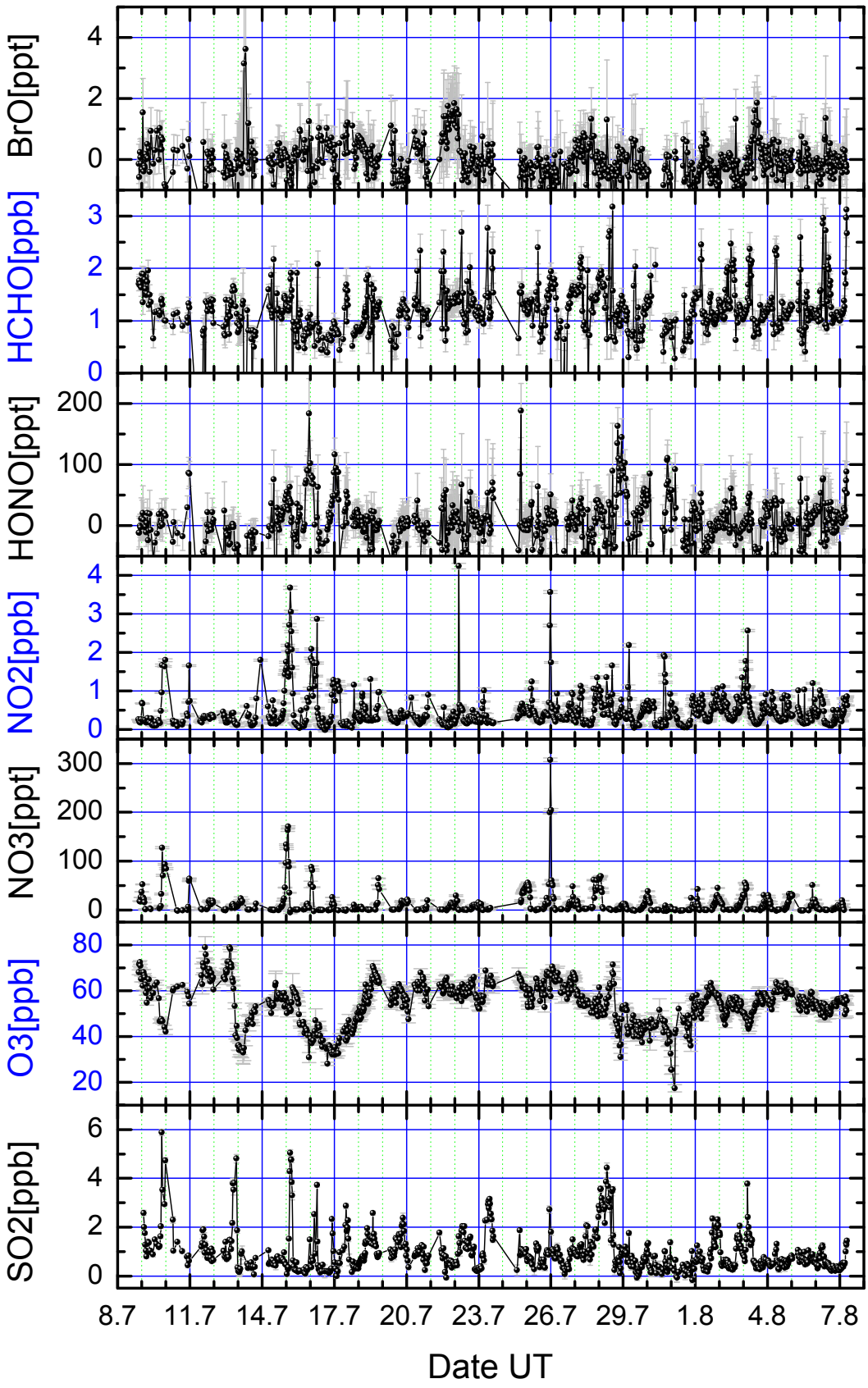

Figure 4.8: Concentrations of trace gases measured with Long-path DOAS at Finokalia(Crete) from 09.07-07.08.2000.

existing BrO values over detection limits, leads to the conclusion that average BrO levels at Crete must be very close to our limit of 0.8 ppt. As far as any argumentation on the diurnal variation is allowed due to the low concentrations, IO levels grow continuously after sunset to reach a maximum right before dawn when the average mixing ratio drops significantly due to the advent of photolytic destruction ($\lambda < 500$ nm).
Nocturnal halogen release is known to occur via heterogeneous reactions of nitrogen species as N_2O_5 and NO_3 on sea salt as described in section 2.2.3.2 on page 32. Laboratory measurements of Seisel et al. [1999] found about one order of magnitude higher NO_3 uptake coefficient for Bromine and Iodine containing salt.

4.1.3.2 Ozone and Nitrogen Species

In this section the DOAS results of nitrogen dioxide (NO_2), ozone O_3 and the nitrate radical (NO_3) will be presented. The atmospheric concentration of nitrous pentoxide (N_2O_5) will be derived from these results. Although measurements provided by our project partners from the LSCE and ECPL research groups will be presented in a separate section further below, the recordings of their NO-Monitor will be presented here due to the tight relationship between all nitrogen species.
The NO_2 series (Figure 4.8) acknowledge that Finokalia is a moderately polluted site with 460 ppt NO_2 on average in spite of the remote marine and rural location. Much higher concentration rates reaching up to 3–4 ppb have been observed during several rather isolated events with a common duration in the order of 2–3 hours. A peculiar situation is represented for the period from 13–16 July when NO_2 levels remained high from midnight until early morning hours (Fig. 4.8). This is in contrast to average diurnal variations of NO_2 observed throughout the campaign period as depicted in Figure 4.10. In general, nitrogen dioxide concentrations rise about 0.4 ppb on average within the first two hours of day after maintaining relatively stable rates during night. After reaching a maximum level of 1 ppb at about 7:30 local time(LT), the atmospheric gas phase concentration decreased continuously until sunset, growing slightly again until midnight.
Additional information on the NO_2 distribution can be obtained from satellite measurements as displayed in Figure 4.11. According to expectations, observations from the GOME instrument state consistently higher NO_2 concentrations over land. Apparently the Black Sea region is the most important source of NO_2 in the area, followed by areas with large industrial activity in Italy and the Aegean. The results show several NO_2 accumulation events above the Black Sea and the Gulf of Corinth around 13th and 23rd July, where the tropospheric vertical column density nearly doubles on a local scale within few days to drop again to background levels. These "hot spot" events are consistent with in-situ measurements at Finokalia taking into account long range transport processes derived from modelled trajectory results.
Except for one single event (on 28.07, 23:00 UT), nitric oxide (NO) concentrations remained close to detection limit (about 50 ppt) during nighttime, indicating that the impact of local pollution was rather small. During daytime significant NO concentrations were observed almost daily, exceeding 1 ppb on 15th and 29th July during particulary low wind periods

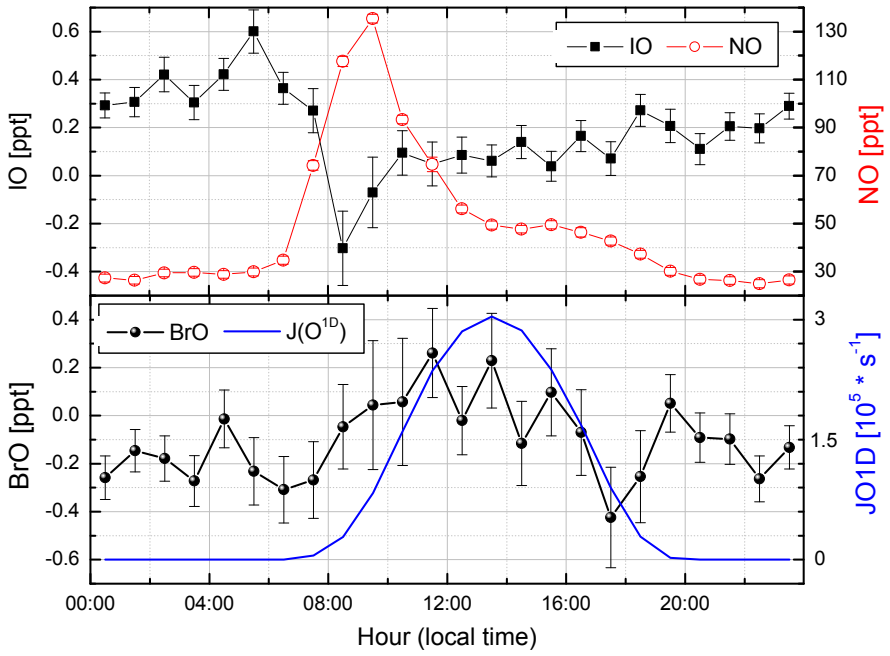

Figure 4.9: Mean diurnal variation of BrO and IO concentrations derived from DOAS measurement results. The increase of BrO levels around noon could have it's origin in photolytic destruction of methyl halides emitted by marine algae. However, as IO has the same source, a similar trend should be observed, which is not the case as the average IO ratio shows a steep decrease after sunrise. The NO-data measured with a commercial monitor (ECPL–Crete) is shown as the striking anticorrelation to IO may lead to the conclusion that NO is a direct sink for IO.

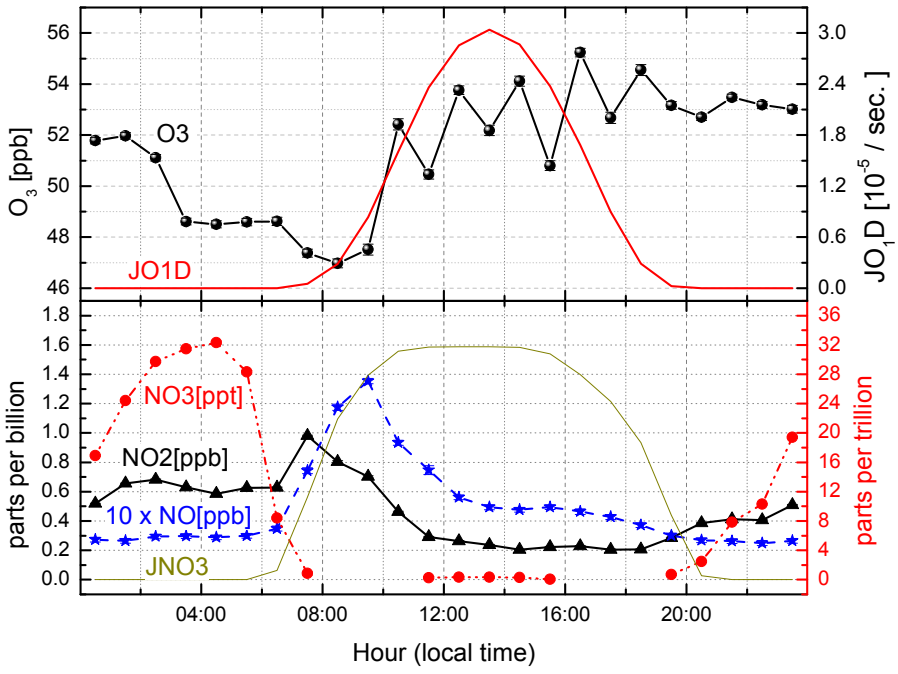

Figure 4.10: Mean diurnal variation of ozone and NO_2,NO_3 concentrations derived from DOAS measurement results. The NO-data was measured with a commercial monitor (ECPL–Crete), nighttime levels represent upper limits(detection limit of monitor was 50 ppt). The errors of the averaged values are too small to be displayed. Ozone has a minimum between 1–2 hours after sunrise and increases steadily until dusk. The opposite behavior is observed for NO and NO_2. NO_3 concentrations grow continuously during the night until the begin of photolytic destruction at dawn.

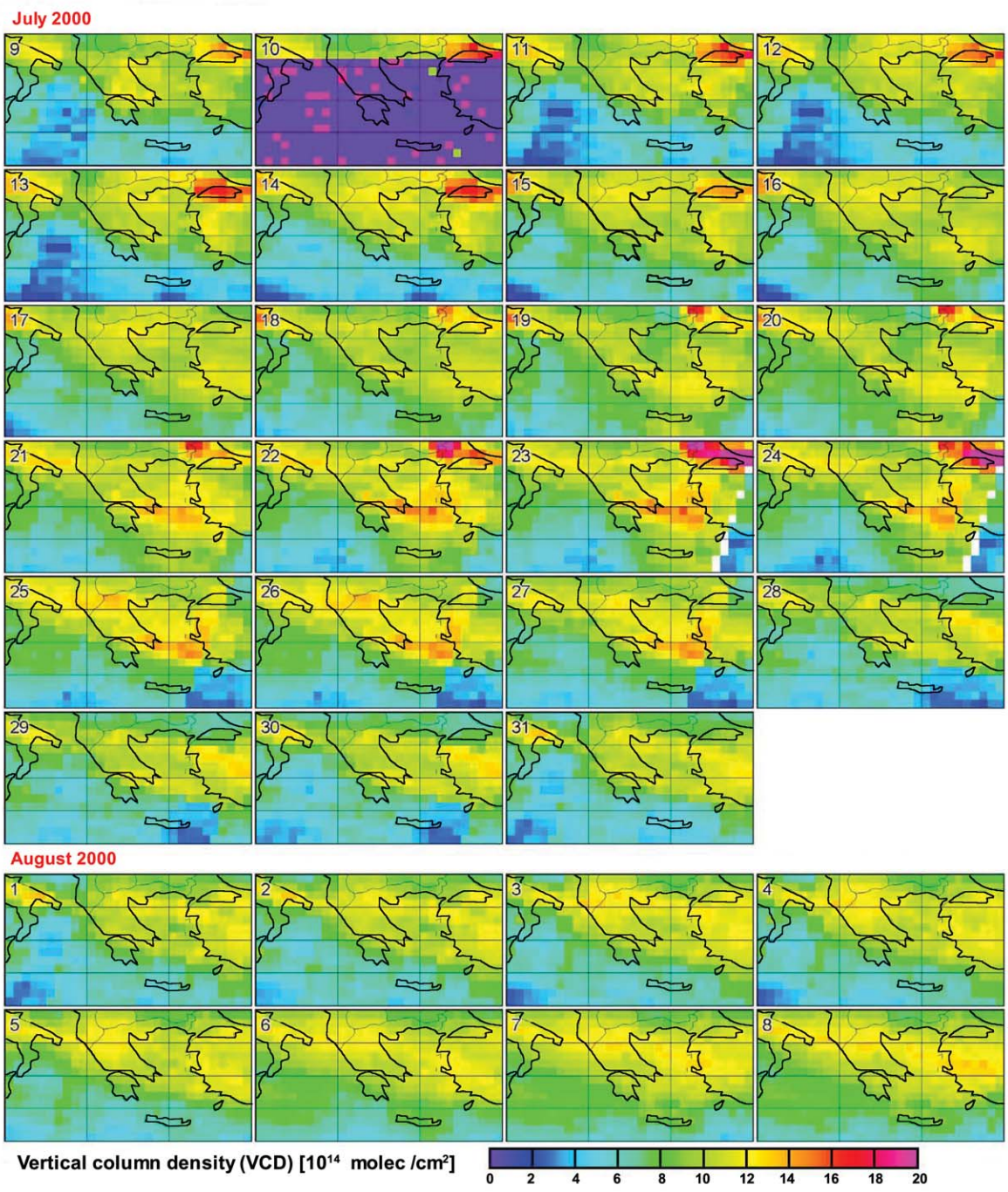

Figure 4.11: Weekly averaged tropospheric NO2 vertical column densities measured by GOME from 09th July to 08th August 2000 (e.g. "9" means average from 09-16th July). According to expectations, consistently higher NO2 concentrations are observed over land. Apparently the Black Sea region is the most important source of NO2 in the area. The results show several NO2 accumulation events, where the VCD of selected regions nearly doubles within few days to drop again to background levels. Around 13th and 23rd July "hot spots" formed above the Black Sea and the Gulf of Corinth which is consistent with observations at Finokalia taking into account long range transport modelled by the trajectory results(data kindly provided by Steffen Beirle, IUP Heidelberg).

probably evoking local pollution events. On a diurnal scale, NO rates rise from below detection limits during nighttime to about 140 ppt on average within the first 3 hours of day. As observed for NO_2, the atmospheric NO mixing ratio diminishes continuously throughout the afternoon. After sunset NO concentrations vanish quickly due to the rapid recombination with ozone and the absence (or minor influence) of local pollution sources. The relative delay in comparison to the diurnal maximum of NO_2 gives rise to the conclusion that is NO formed mostly from photolytic destruction of NO_2. At Finokalia, maximum ozone concentrations of about 79 ppb were recorded(Fig. 4.8). Even the mean concentration of 55 ppb surpasses the "ozone alarm" limit of 53 ppb established by the European community.
For ozone, the relative diurnal variation is relatively small, maintaining below 9 ppb. Nevertheless a remarkable diurnal trend does exist(Fig. 4.10). During the first hours of night the average ozone mixing ratio remains at a relatively constant level around 52 ppb. Starting at 1:30, the concentration drops roughly 3 ppb within 2 hours, to attain again a stable mixing ratio slightly below 49 ppb until dawn. At that time the average ozone level decreases further to reach the diurnal minimum of 47 ppb at 8:30 local time. After a very rapid rise within the following two hours, ozone concentrations attain more than 52 ppb and follow a positive trend until sunset.

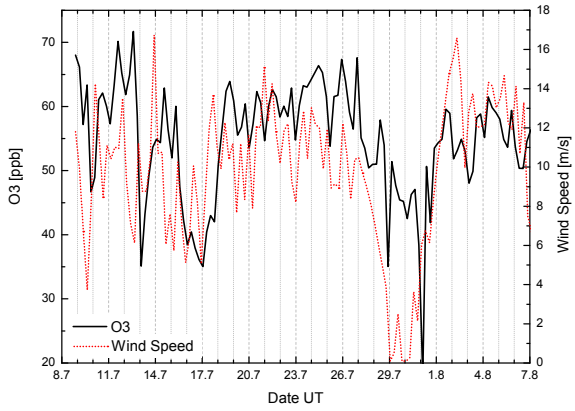

Figure 4.12: Interpolated Ozone concentration and Wind Speed. The lowest ozone levels appear during weak wind periods. However, the correlation is far from being linear and thus transport can not account for the total ozone variability.

By comparing the diurnal variations of NO,NO_2 and O_3 as measured on Crete and depicted in figure 4.10, it becomes evident that a link between these species does exist, leading to the conclusion that photochemistry plays a major role regarding atmospheric chemistry in the Mediterranean Region. Therefore, due to the high concentration of nitrogen monoxide (NO) an important quantity of ozone is probably depleted via the NO+O3 reaction within the first hours of day. Synchronous to the start of the NO decay at 9:30 LT, ozone levels rocket upward by roughly 5 ppb, to attain the diurnal maximum within one hour. As NO and NO_2 concentrations vanish over the remaining course of the day ozone levels keep rising slowly, most likely due to photolytical destruction of NO_2 and probably other photochemical processes involving carbon monoxide and hydrocarbon species. The larger variability of ozone levels throughout the early afternoon may be a consequence of the local land-sea breeze circulation (section 4.1.2) and variability of the marine boundary layer height and long range transport entrainment.

In addition to the diurnal effect, much larger variations within larger timescales of several hours, even days, have been observed for O_3 mixing ratios. On 10th, 13th, 15–19th and 28–31st July several "ozone depletion" events occurred. The stability of the Mediterranean troposphere, because of subsidence, suppresses entrainment from the free troposphere [Lelieveld et al. 2002]. Therefore the origin of air masses, as shown before by Kouvarakis et al. [2000], is expected to have the strongest impact on O_3 concentration variation. Highest ozone levels correspond to periods when strong winds blew from northerly directions, as for the stable period from 18–27.07. Obviously wind speed biases the influence of long range transport (Fig. 4.12). For the period from 28.07-01.08.2000 the absence of long range transport due to low wind speeds diminished ozone levels. The lowest O_3 values of the campaign(37 ppb), observed on July 29th, from 4:20–6:20 UT, may be a result from the combination of lacking transport and local destruction due to increased NO levels(1.57 ppb). The dominant marine input from the western (16–17.07.2000) and even southern (10th, 13th July) sector as well as the presence of extensive biomass burning events in the Aegean region(section 4.1.2) can be accounted for the depletion events in the 2nd and 3rd week of July.

Atmospheric concentration of the nitrate radical (NO_3) and nitrous pentoxide(N_2O_5) Significant nitrate radical NO_3 mixing ratios well above the detection limit of 1.6 ppt have been measured during almost every night of the 5 week campaign period. As shown in the overview of DOAS results given above (Figure 4.8) the mixing rates of NO_3 at Finokalia usually reached nighttime maxima in the order of 30–50 ppt, even above during the nights of 10,11,15,16th July and notably on July 26th when the campaign maximum of 310 ppt was observed. The average diurnal variation (figure 4.10) states that NO_3 levels commonly began to rise to detectable limits usually within half an hour after dusk and vanished quickly within few minutes after sunrise due to the advent of photolysis. The highest levels of NO_3 appeared mostly around 4 hours past midnight, following a notable decay of the precursors O_3 and NO_2 by 3 and 0.1 ppb (14% and 6% of total concentration) respectively. The mixing ratio of N_2O_5 was derived from measured NO_2 and NO_3 concentrations using relation (2.38) in section 2.2.2. The resulting nighttime mixing ratios averaged 18 ppt and ranged from the virtual detection limit 3 ppt up to 795 ppt (Figure 4.13). The ratio of N_2O_5 to NO_3 was between nearly zero and 2.6 (0.5 on average), which is significantly below relations established in Geyer et al. [2001] for measurements near Berlin (northern Germany) in summer. Significantly lower NO_2 mixing ratios and enhanced thermal decay of N_2O_5 as a result of higher temperatures prevailing for the Mediterranean site may explain this difference (Geyer et al. [2001] measured 1-15 ppb NO_2 and ambient temperatures frequently below 10 °C during nighttime). Additionally shown in figure 4.13 are the production rate P_{NO3} and the total degradation frequency $f_{NO3,total}$ derived from measured $NO_2, NO_3 \text{and} O_3$ concentrations using equations (2.28) and (5.5). The average NO_3 production rate at Finokalia was $P_{NO3} = 4 \times 10^5 \text{cm}^{-3}\ \text{s}^{-1}$, exhibiting a variation from 2×10^4 to more than $2 \times 10^6\ cm^{-3}s^{-1}$ (equivalent to $8.2e^{-4} - 0.08$ ppt s^{-1}) on the nights of 15–16 and 25–25 July when highest NO_3 levels were observed. Therefore, disregarding nocturnal sinks, detectable levels of NO_3 (i.e. above 1.6 ppt) should appear

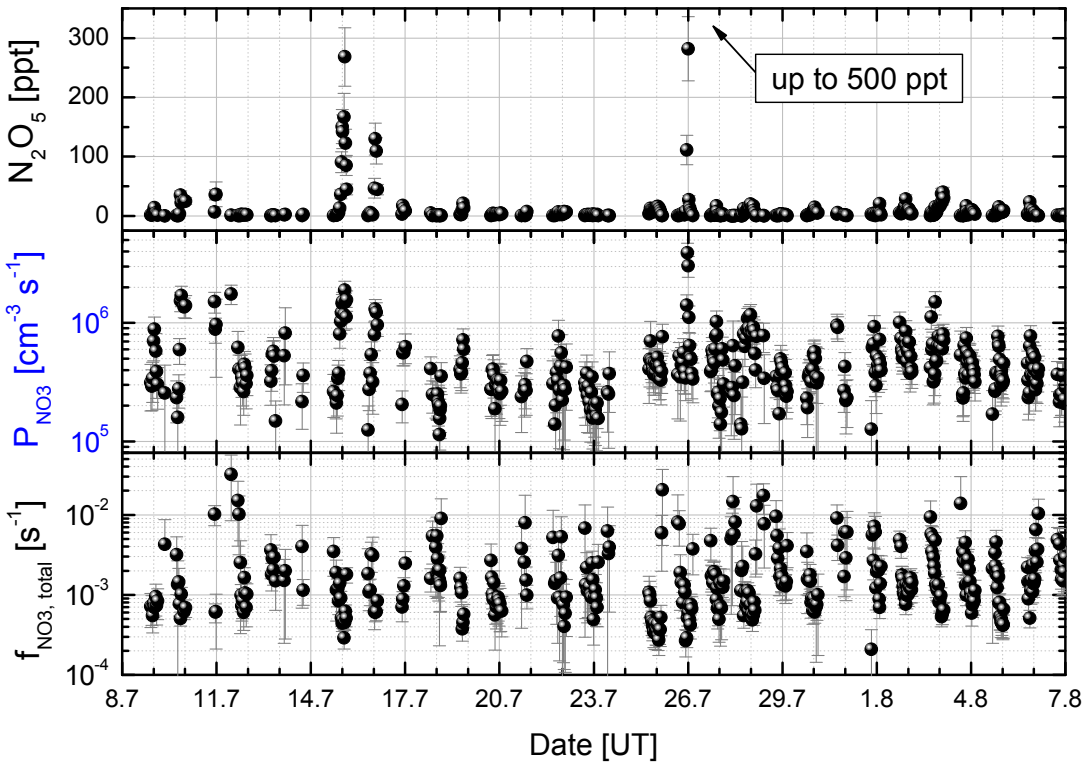

Figure 4.13: Time series of calculated N_2O_5 levels, production rate P_{NO3} and total degradation frequency $f_{NO3,total}$ from 08.07-07.08.2000 derived from measured NO_3 mixing ratios presented in Fig. 4.8 following equations (2.38), (2.28) and (5.5) assuming stationary state conditions.

within 20 seconds and 30 minutes after sunset. The total degradation frequency $f_{NO3,total}$ ranged from roughly 3 to 300 $\times$ $10^{-4}s^{-1}$ (average 2 $\times$ $10^{-3}s^{-1}$ corresponding to a mean lifetime of $\tau(NO3) = 930\ s$).

Nitrous acid (HONO) Nitrous acid (HONO), an important nighttime compound in the urban atmosphere and as a secondary source of OH [Alicke et al. 2002], remained below the detection limit (66 ppt on average) during most of the campaign. However during the nights of 15th, 16th as well as 28-31st July, HONO rose above the detection limit attaining a maximum of 180 ppt on 15th July. These events were followed by unusually high NO levels at sunrise (e.g. 1 ppb on 15th July). Local pollution is an assignable source for observed HONO, particulary for the last days of July when wind speeds were extremely low. Indeed, trajectory results state that air masses reaching Finokalia travelled along the northern coast of Crete (15,16,28,29.07) and crossed the island on 30th July(Figure 4.14). Long range transport from forest fires(section 4.1.2) could be an additional source for the high NO_x observed on 15th and 16th July.

4.1.4 Measurements of Sulphur compounds

The mean Dimethylsulphide concentration was 54 ppt, highest levels have been observed on July 13th and 17th reaching maxima of 745 and 480 ppt respectively. Increased sea–to–air

Figure 4.14: 3–hour backward trajectory results calculated for nights with HONO events using the HYSPLIT model. All trajectories ending at Finokalia at 21,23,01,03 and 05 hours local time are shown on top a route map of the northern coast of Crete. During the nights of 15,16th (purple) and 30th (orange) of July air masses travel along the northern coast of Crete, where the city of Iraklion and the arterial road of the Island, "New national road" (E75), may be important sources of pollution. During the nights of 28th,29th July (green) air masses arriving at the measurement site originate from the southwest crossing populated areas.

Table 4.2: Other measurements at Finokalia 2000

Chemical component	Timeframe(UT)	Time resolution [min] (Best)	Mean Concentration [ppt] (Max)	Detection limit [ppt] (Best)
Sievers 355 Chemiluminescence Detector (J.Sciare et al., LSCE Saclay, Gif–sur–Yvette, France)				
DMS	10.07–08.08.2000	53 (20)	54.4 (745.3)	10
Coffer mist Chamber (N.Mihalopoulos et al., ECPL, University of Crete, Iraklion, Greece)				
$DMSO$	10.07–06.08.2000	120 (100)	2.9 (15.4)	0.2
SO_2				
Filters & Ion–chromatography (ECPL–Crete)				
MSA	11.07–06.08.2000	120 (100)	8.8 (46)	0.1
Commercial Monitors(ECPL–Crete & B.Bonsang et al., LSCE)				
NO	09.07–06.08.2000	5	49 (1600)	57.5 (0.7)
NO_2			1400 (7300)	127.6
O_3			59200 (89100)	1100
$Black\ carbon$			628 (4405)*)	
CO	11.07–29.07.2000	6	118600 (205800)	

*) unit: $10^{-9} gramme/m^3$

flux could account for these observations, as for both periods trajectory results and meteorological data acknowledge a dominant input of air masses from the open Mediterranean sea in the west in combination with very strong winds (16 and 12 m/s). For the rest of the

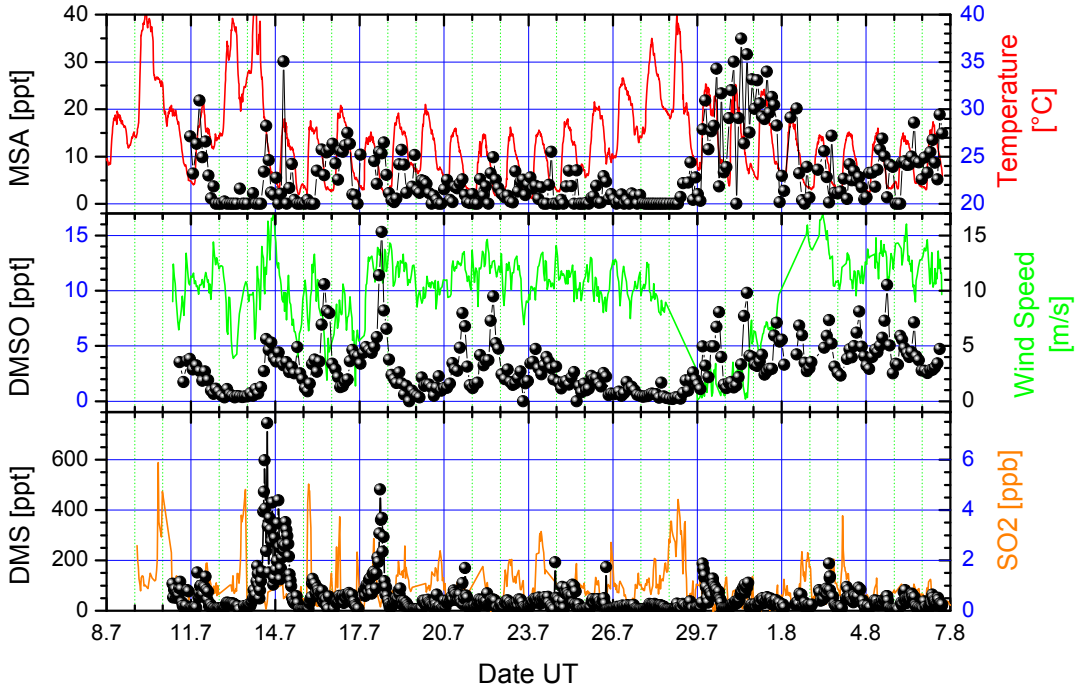

Figure 4.15: Results of Mist-Chamber and Gas Chromatograpy measurements of ECPL–Crete and LSCE–CNRS groups (Sciare et al. 2003). The highest DMS levels on July 13th and 17th coincide with periods of high input from the open sea due to strong winds blowing from westerly directions. The relation of the oxidation products DMSO and MSA to DMS, although far from being linear, is observable. Apparently there is an inverse relationship between this compounds and temperature, as lowest levels have been observed from 12–13th and 26–28th July when ambient temperature reaches 40 °C. The simultaneous dramatic increase of SO_2 levels is only reachable by anthropogenic pollution or biomass burning, which is corroborated by trajectory results reflecting highest SO_2 mixing ratios during periods with dominant input from the continental source. Another striking feature is the strong increase of MSA during the low wind period, which could be explained by accumulation of OH radicals.

campaign DMS levels reached nearly 200 ppt on several days with similar conditions.

The average concentration of the most common products of DMS oxidation, Dimethylsulphoxide(DMSO), Methane sulphonic acid(MSA) and sulphur dioxide(SO_2), amounted to 3, 5.9 and 936 ppt respectively, attaining maxima of 15.3, 34.9 and 5900 ppt. DMSO follows quite well the DMS variations although DMS and DMSO are not significantly correlated. The observed DMS to DMSO ratio increases with rising ambient temperature (Fig. 4.16), certainly a consequence of the decreasing DMSO–production yield as discussed in section 2.2.1. For DMS mixing–ratios below 100 ppt the relation of the DMS/DMSO–ratio to ambient temperature fits fairly well an exponential growth. A linear approach within the range of $20 - 35\,^{\circ}C$ leads to a gradient of 2.8 units ratio per degree Celsius. At even higher temperatures the increase of the DMS/DMSO ratio breaks off from linearity, as on July 13th when the ratio increased to 260 at 43 °C. Apparently this is also the case at DMS mixing–ratios well above 100 ppt, when the DMSO formation yield may decrease due to growing lack of oxidants to react on present DMS molecules(Fig 4.17). OH concentrations as well as relative humidity have been identified as the major factors controlling the MSA variations in the gas phase.

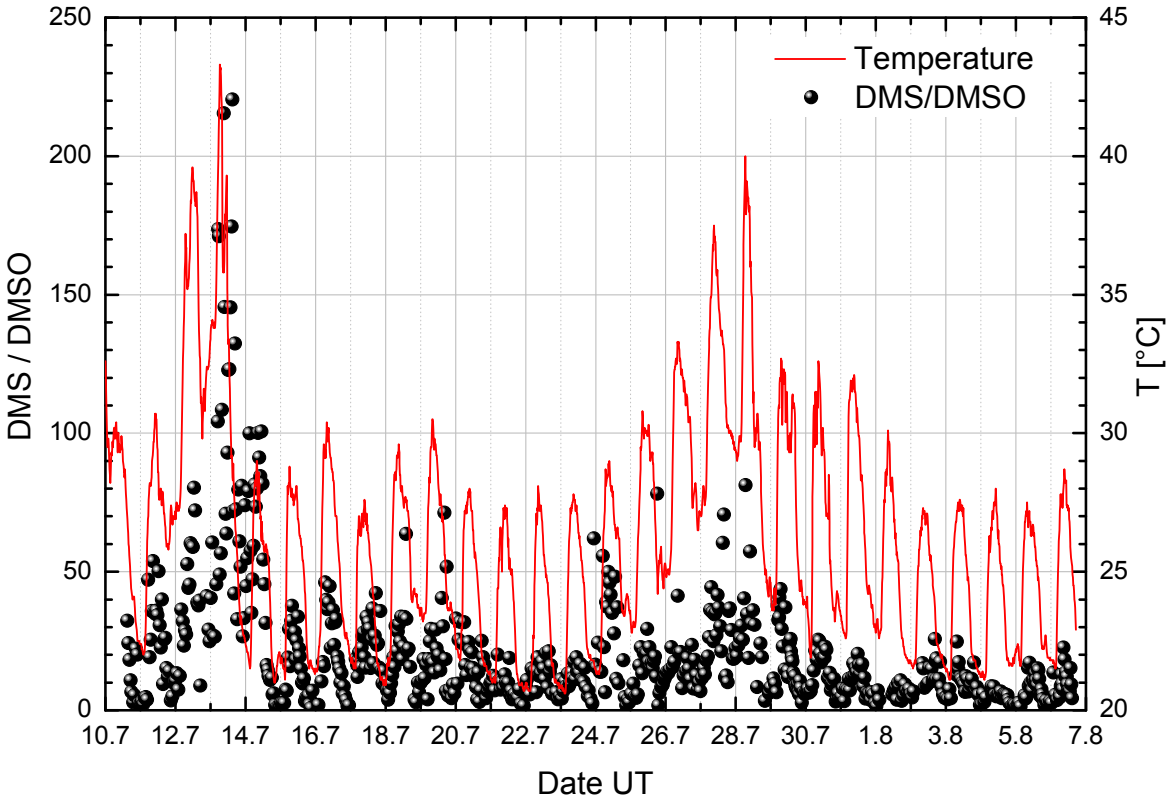

Figure 4.16: Temperature dependency of DMS/DMSO ratio.

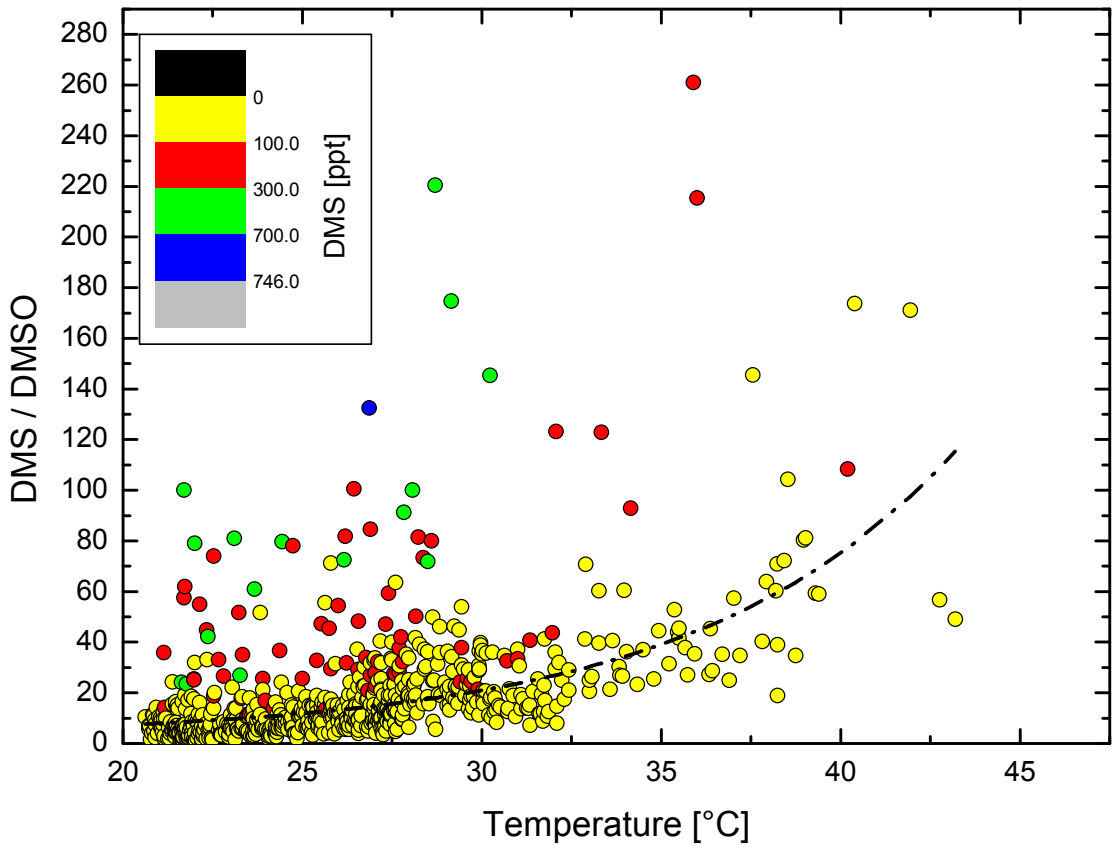

Figure 4.17: Variation of the DMS/DMSO ratio with temperature.

Based on the levels of MSA in gas and aerosol phase Bardouki et al. [2003] reached the conclusion that the DMS+OH reaction could not account for the levels of MSA observed in the aerosols. Although the formation yield of SO_2 from the DMS oxidation via OH is above 50%, ambient DMS levels are far to low to account for the observed SO_2 amount. As found earlier at Finokalia, the biogenic sulphur can account for 0.6 to 28.3% of the total non–sea sulphate concentrations([Mihalopoulos et al. 1997]). As local pollution (see section 4.1.3.2) was shown to play a minor role the high sulphur dioxide levels can only be attributed to long range transport of anthropogenic emissions from northern and eastern Europe.

An enlightening insight into DMS oxidation processes going on at Finokalia, can be obtained from the calculation of the mean diurnal variation of DMS as shown in Figure 4.18. When OH is the only significant sink of DMS, assuming a constant DMS evasion flux, the diurnal cycle of DMS should show a predawn maximum due to nighttime accumulation and a late afternoon minimum due to daytime oxidation by OH radicals [Ayers et al. 1995; Sciare et al. 2000]. A quite different diurnal variation was derived from the measurements at Finokalia. As shown in Figure 4.18 DMS mixing ratios rise continuously during the afternoon until few minutes after sunset as expected from the decrease of OH radical concentrations. However, the situation changes rapidly after sunset when DMS ratios start dropping. The decrease is particulary steep after midnight until dawn just when the presence of the nitrate radical is strongest.

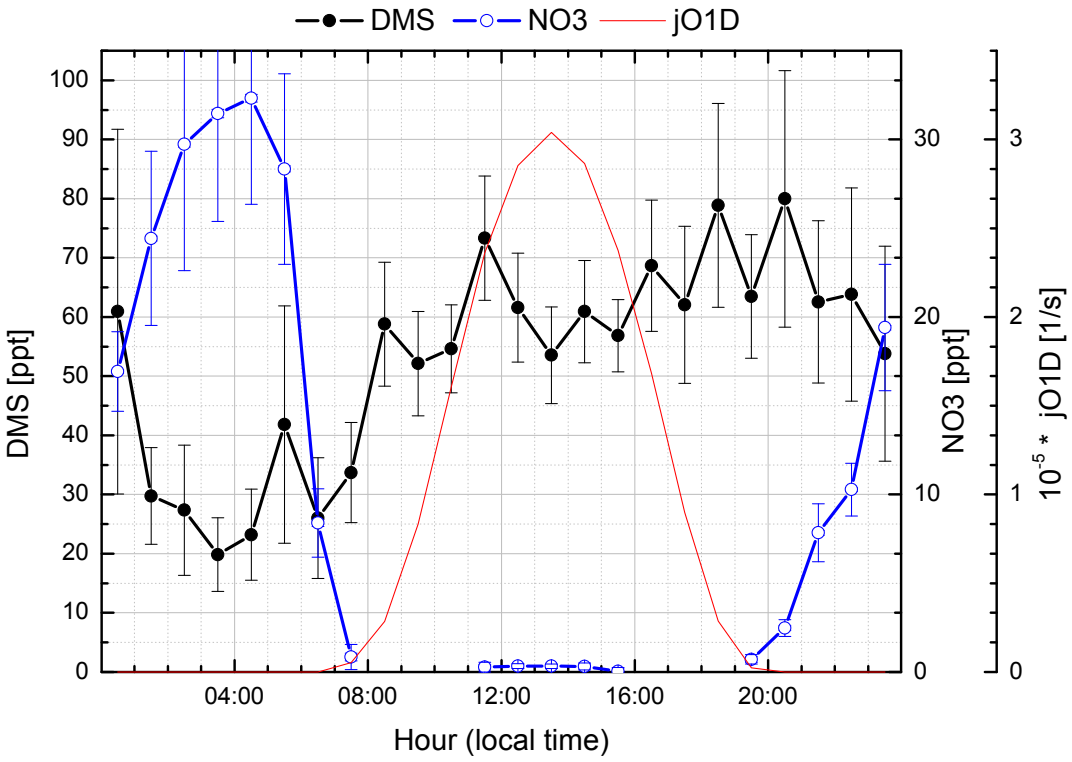

Figure 4.18: Average diurnal concentrations of DMS and NO3. The errors are the 1σ distributions of the averaged datapoints. The very prominent depletion of DMS from midnight till dawn gives evidence of a nighttime sink of DMS.

4.1.5 Formaldehyde(HCHO) and Carbon monoxide(CO)

Formaldehyde (HCHO) is the most abundant of the carbonyl compounds in the atmosphere. It is found both in the remote background atmosphere and in polluted urban atmospheres. Large amounts of formaldehyde (HCHO) are emitted directly due to industrial activity (fossil fuel combustion) and during biomass burning events [Holzinger et al. 1999]. However, depending on meteorological factors, photochemical oxidation can contribute as much as 90% to annual formaldehyde concentrations in ambient air. HCHO is a major intermediate in the degradation of methane and many other hydrocarbons. In the absence of heterogenous losses, essentially every methane molecule is converted into HCHO. In continental boundary layers, non-methane hydrocarbons (NMHCs) emitted by biogenic and anthropogenic sources dominate over methane also as a source of formaldehyde.
Through its decomposition by photolysis and reaction with the hydroxyl radical (OH), formaldehyde serves as a source of the hydroperoxyl radical (HO_2) and carbon monoxide(CO). In air masses not influenced by anthropogenic emissions, CH_2O is the most important direct precursor of CO. The average formaldehyde concentration measured in Crete was 1.2 ppb (maximum 3.2 ppb), surpassing by far typical levels for clean marine summer conditions (0.5 ppb). Diurnal maxima above 2.5 ppb HCHO were regularly observed at daytime, mostly around local noon. Yet strong fluctuations in the order of 0.5-2 ppb prevent from the definition of a regular diurnal pattern. In addition to the diurnal production, formation of 0.3-1 ppb HCHO emerged basically every night of the campaign period. However, HCHO levels and variability were consistently lower during nighttime. Despite the large solar flux, an important amount of NMHC's must be added to common CH_4 levels to vindicate the observed photochemical production. In accordance with the diurnal wind pattern (section 4.1.2) "local" pollution sources from the coast leading to Iraklion could account for the nighttime rise of HCHO mixing ratios. According to trajectory results this is particulary reasonable for the nights of 9, 15, 16 and 27-30 July. Long range transport from raging biomass burning activity on continental Crete and Samos(section 4.1.2) could eventually add to the local source on the nights of 10, 25 and 26th July. In general, although long range transport of HCHO from the main land is an unlikely source due to typical half-lifetimes in the order of 2 hours around noon in the summertime Mediterranean (taking J(HCHO)=$1.3e^{-4}s^{-1}$), entrainment of photochemical aged air-masses from continental sources is probably the reason for the observed high levels of HCHO.

Although the diurnal variation of HCHO has to be considered carefully due to the large variability of concentration levels, a diurnal trends seems to exist. HCHO exhibits an relatively small increase of 0.2 ppb within the first hours of day until noon. As NO levels are particulary high in the early morning hours (Fig. 4.10) this could be a consequence of enhanced photochemical production from the methane and NMHC sources outgoing the photochemical degradation rate. In the progress of day the importance of CH_2O sinks(photolysis rate(JO_1D) and OH radical concentration) increases rapidly and NO mixing rates start to decay after 9:30 LT. Therefore as observed in Fig. 4.19, destruction rates probably surpass production after 10:30 Local Time(LT). For the rest of the day formaldehyde concentrations follow a negative trend until sunset. An extremely steep decay is observed around 13:30

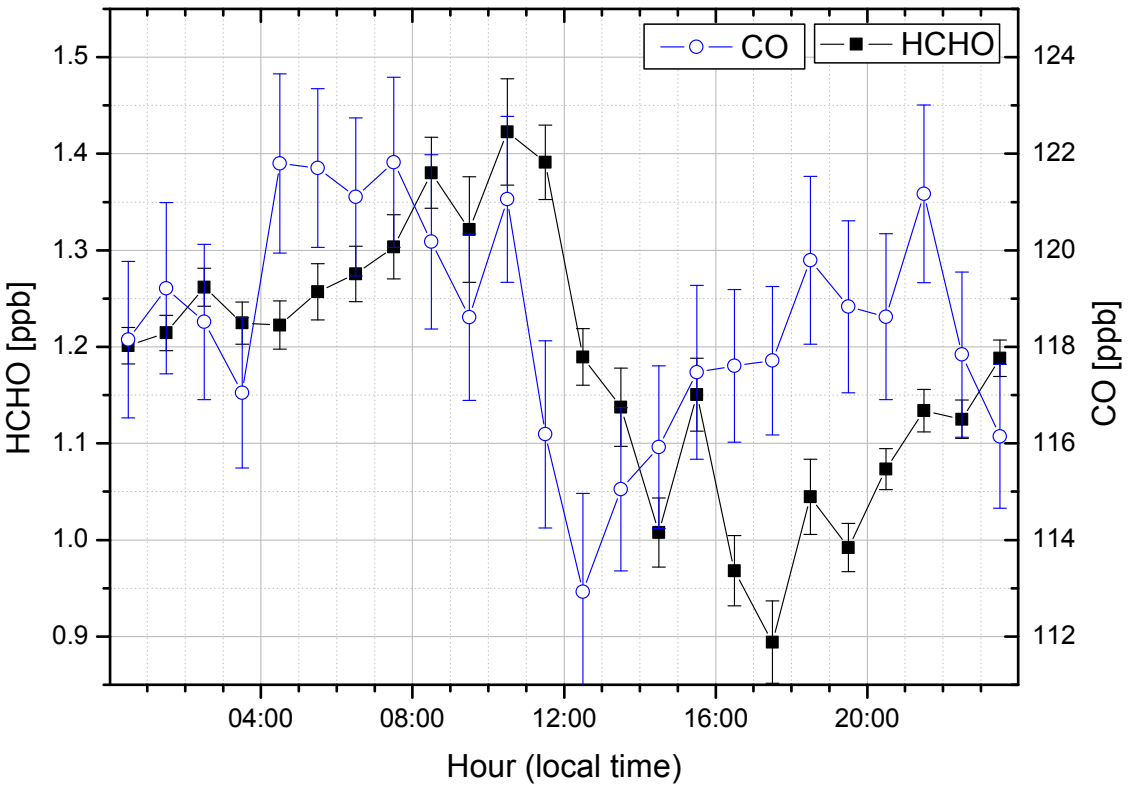

Figure 4.19: Average diurnal variation for the whole campaign period.

LT when JO_1D reaches its diurnal maximum. For the late afternoon degradation rates of formaldehyde fall again, but so does the photochemical production. In addition, NO levels reach negligible levels(50 ppt). During night HCHO levels grow again, a phenomenon only explainable by emission sources listed above.

4.1.6 ROX Measurements

RO_x, mainly peroxy radicals (HO_2 and RO_2) were measured during the last 2 weeks of the campaign (24.07-06.08.2000) at Finokalia. The instrument, a calibrated peroxy radical amplifier (PERCA or 'ROX-BOX'), was kindly provided and calibrated by T.Klüpfel (MPI-Mainz) and was operated by the IUP–Heidelberg Team. The operating method of the PERCA device is described in section 3.3. The results of the chemical amplifier measurements from 24.07–07.08 (evaluation and calibration by T.Klüpfel) are shown in Figure 4.1.6. For a better interpretation of the data, measured ozone and DMS levels as well as ambient temperature are displayed above the peroxy radical ($RO_x = HO_2 + RO_2$) concentrations. According to the well known diurnal sources, i.e. reactions of OH with CO and volatile organic compounds(VOCs) (see section 2.2.1), RO_x mixing ratios follow the daytime evolution of the actinic flux (and thus OH production) and reach maximum levels between 30 and 70 ppt one hour after local noon and decrease continously until sunset. In exception of the period from 25.-28.07.2000, RO_x levels vanish from dusk till dawn. Solar radiation is not the only factor controlling RO_x variations. Evidence exists that observed mixing ratios follow ambient ozone

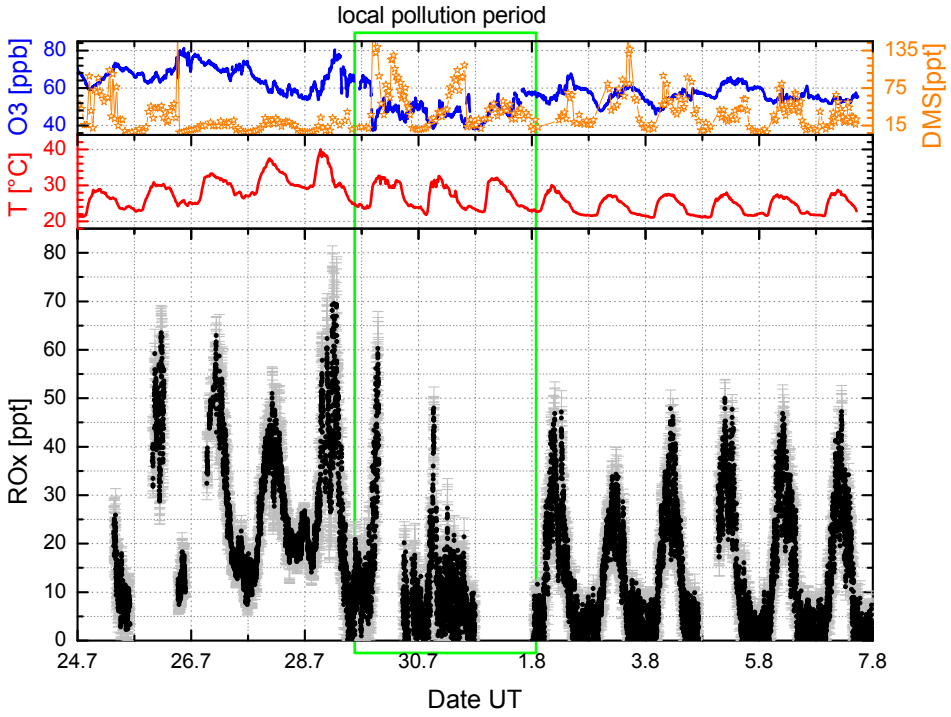

Figure 4.20: Measured ROx levels for the period from 24.07-06.08.2000 measured with the ROX–Box from MPI–Mainz operated by IUP-Heidelberg-Team. The measurements have been evaluated by T.Klüpfel, each data point represents a running mean of 10 values. Daytime levels are correlated to solar radiation input, maxima are observed one hour after local noon(GMT+3). Nighttime concentrations remain close to the detection limit with exception of the period from 25–28 July, with significant nighttime levels up to 25 *ppt*. The missing data on 25,26 and 31st July is due to instrument failure.

levels and the temperature trend and attain much higher concentrations in the first week of RO_x measurements(Fig. 4.1.6). A closer look at the data suggests a separation in three periods:

1. 25.07 00h -28.07 17h (nighttime ROX, very high O_3 levels, NO_3 up to 300 ppt, $DMS <$ 30 ppt)

2. 28.07 17h-01.08 1h (local pollution period with high NO, $O_3 < 40$ ppb, low RO_x even at daytime)

3. 01.-06.08 (low/non existent nighttime ROx, normal O_3 levels and ambient conditions).

Trajectory analysis confirm a continuous input from the balkan region and central Europe for the first period. DMS levels are the lowest of the whole measurement period. It is interesting to note that rather high ambient temperatures than the DMS-Flux(i.e.wind speed) seem to influence DMS levels. NO_3 mixing ratios are quite high in these days and surpass 50 ppt each night, reaching 300 ppt during the night of July 26th. Peroxide concentrations are very

important for this first period and attain more than 10 ppt even at nighttime.
Due to very weak winds, the origin of air masses is predominantly local or southeastern for the second period. This time interval was marked as local pollution period due to trajectory results and high NO levels observed (sections 4.1.2 and 4.1.3.2). As a consequence of nighttime NO the NO_3 levels are rather low. In spite of the low theoretical flux, DMS concentrations return to the normal range of several ten parts per trillion. Unfortunately the PERCA-Instrument failed for several hours on July 29th and whole of 31st July. Nevertheless a transition from the high RO_X period to lower daytime levels and vanishing nighttime ROX is observable. Ozone levels are quite low which was attributed to lacking transport(section 4.1.3.2).
For the first week of August, the Black Sea and further northern regions are sources of sampled air at Finokalia and ozone and DMS as well as Temperature and Humidity return to normal levels. These last days could be representative for the common meteorological situation in summer on Crete, with continuous input from northern, continental air masses.

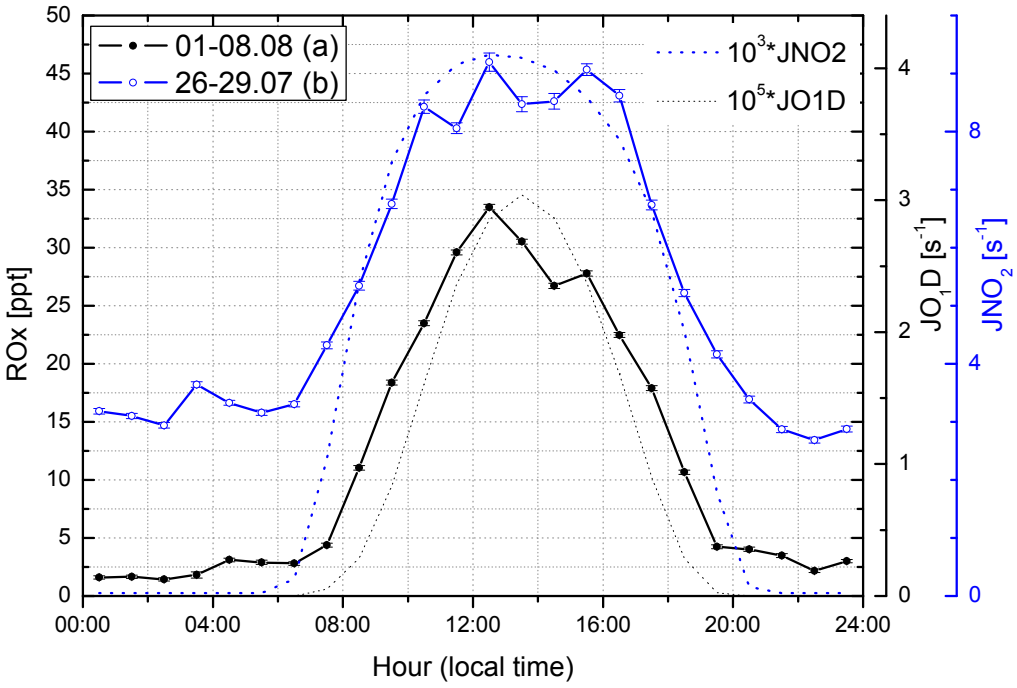

Figure 4.21: Average diurnal variation of ROx is shown for the periods from 01-08.08.2000 (a) and 27-29.07.2000 (b) in this picture. Both shapes show a large peak around local noon following solar irradiation and thus the OH production rate. However mixing ratios for period (b) are significantly higher and remain as high as 15 ppt even during nighttime. Additional OH from HONO may explain the earlier increase of ROx mixing ratios during that period as the photolysis rate of NO2 increases earlier.

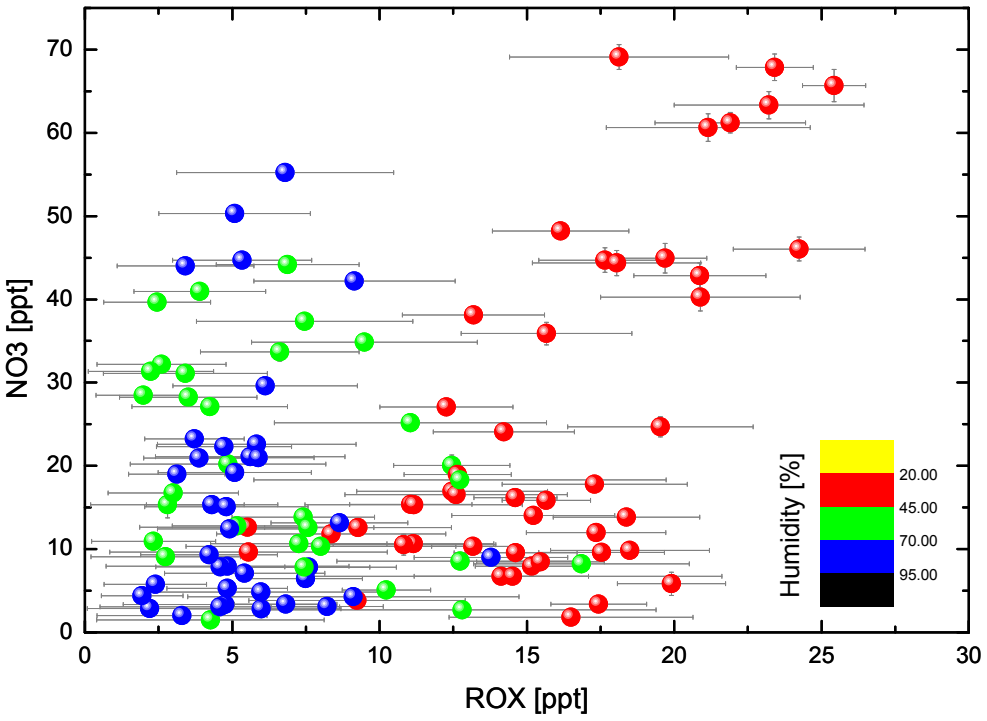

Figure 4.22: NO3 as a function of ROx for the period of 24.07-06.08.2000. Only values with NO3 and ROX over detection limit are displayed. The colour of the data points darkens with increasing relative humidity (see colour map). Highest ROx levels have been observed for the drier periods. Below 45% rel. humidity, a positive linear correlation between NO3 and ROX is observable.

4.2 Field Campaign Hudson Bay 2001

The second field campaign of the EL CID project was carried out from 15.04–09.05.2001 at Kuujjuarapik in the southeastern part of the Hudson Bay, Canada. As shown on several previous measurement campaigns [Lehrer et al. 1997; Ackermann et al. 1997] the arctic region shows exceptionally high levels of Bromine oxide radicals in spring within the first months after the dark winter period. Long term measurements performed with the DOAS instrument on the GOME satellite [Hollwedel et al. 2003] confirm this observations and state that significant BrO concentrations must spread further south. In spite of numerous measurements in polar regions, no ground based measurements have been reported for the subarctic region. The main objectives of this campaign were once again to establish the relative impact of reactive species regarding DMS oxidation, although the main effort was directed on the primary detection of BrO at lower latitudes and the possible interaction with atmospheric Dimethylsulphide. Furthermore, by comparison with data of the other 2 field campaigns, the much colder and cleaner environment was chosen to allow an investigation of the role of temperature in determining the yields of DMS oxidation products.

4.2.1 Observation Site

Kuujjuarapik (Inuit for "Little great river") is the southernmost village of the Nunavik Territorium in Quebec, Canada, and is located at the south eastern coast of the Hudson Bay at 55.31°N and 77.75°W (local time=UT-5 hours) as shown in Figure 4.23. The village is a bicultural community as the Inuit people share it with the Cree Indians, which have named the location *Whapmagootsui* ("where there are whales"). Older maps of the area occasionally employed the French and English official names which are *Poste–de–la–Baleine* and *Big Whale River*. Kuujjuarapik is nestled in sand dunes at the mouth of the Great Whale River. Beyond the village, the land is rather flat; a carpet of moss and rock unfold as far as the eye can see. During the winter months the whole area of the Hudson Bay is covered under a huge snow and ice layer. The melting starts slowly in spring but the sea remains iced until the late summer months.
The village (Population 1200) is the biggest settlement in a perimeter of at least 100 km. In general the whole Nunavik is a sparsely populated region, with close to 10.000 people living in 14 communities scattered along the coasts of Ungava Bay, Hudson Strait and Hudson Bay. As there are now firms roads, the local traffic is based mostly on 4-wheel driven motorbikes and snowmobiles. No local industry is present, whereas local pollution sources reduce to the local community power plant, the airport(frequented twice per day by small aircrafts) and other conceivable anthropogenic activities.

Due to technical and operational demands, the DOAS measurements were set up in a container about 2 kilometers north of the village right at the coast while the instruments of our colleagues were located in the laboratory of the Centre d'Etudes Nordiques (CEN) at the opposite site of the village (Figure 4.30).

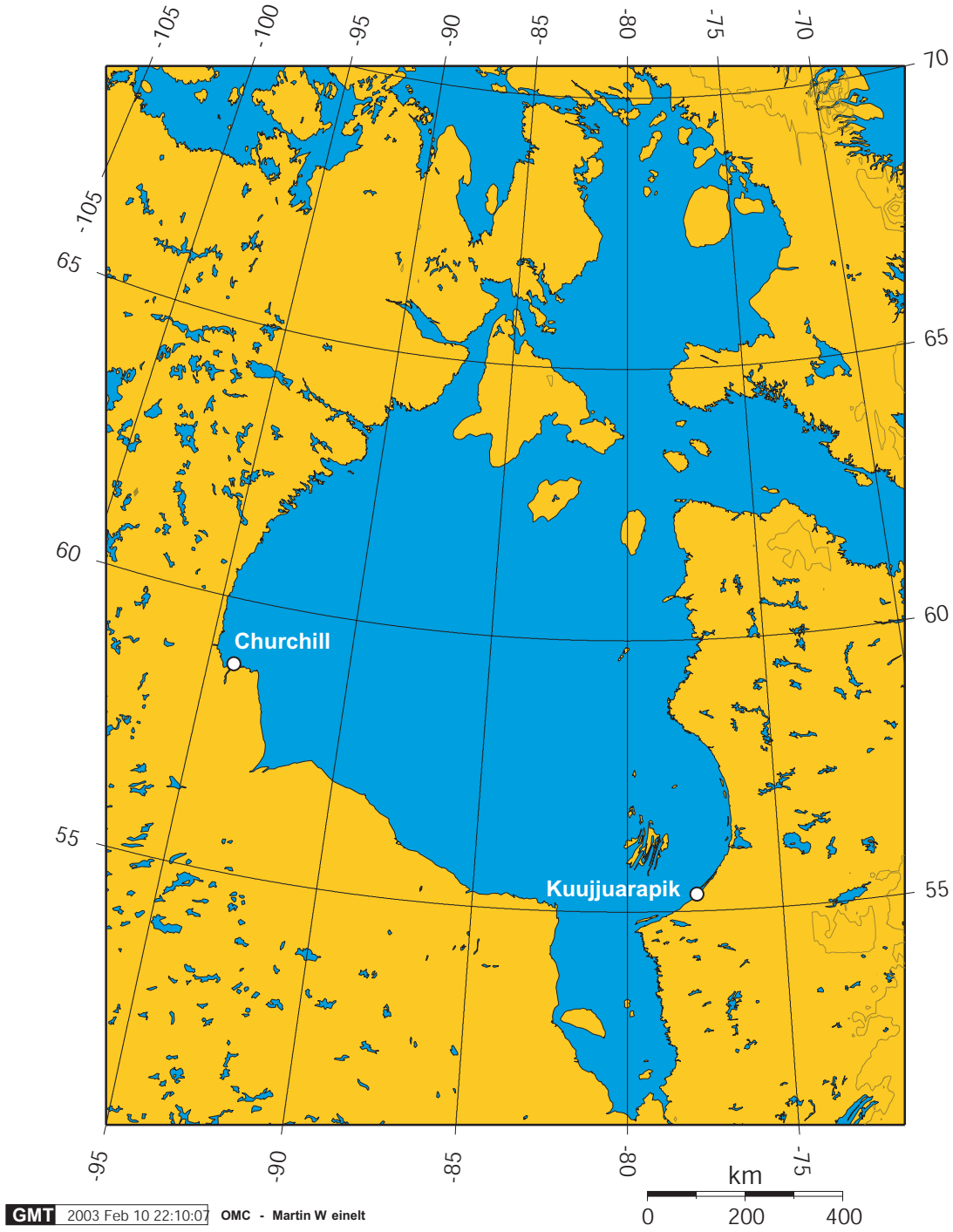

Figure 4.23: Overview map of the Hudson Bay.

4.2.2 Meteorological conditions

Meteorological conditions had a particulary important impact on measurements during the Hudson Bay Field Study as visibility changes determined the DOAS performance and northern winds were found to be rich in Bromine (section 4.2.3). An overview of meteorological parameters observed throughout the measurement period is given in Figure 4.24. Temperature, Wind and relative humidity have been recorded at the Centre d'Etudes Nordiques (CEN) weather station. The additional data regarding ambient pressure and visibility have been kindly provided by the local climate station seated at the airport of Kuujjuarapik.

At the start of measurements in mid-April, ambient temperatures were still as low as -20 °C. The whole area surrounding the site was covered with deep snow and the Hudson Bay was sealed with ice having a thickness about 2 meters. According to trajectory results, obtained once again from the HYSPLIT-Model [Draxler and Hess 1998], the input of air masses from polar regions was particulary important during the first week of measurements. This is in agreement with observed ambient conditions: high ambient pressure, icy temperatures(-20 °C to 0 °C), predominantly northern winds and frequent snowfall/storms. Within the following weeks low pressure systems usually associated with southerly and easterly winds led to gradually warmer temperatures and continental air masses reaching the site. At the end of the campaign period temperatures reached 20 °C. At that time nearly all snow in the area had melted, the main land had turned rapidly into a swamp but the sea remained covered with a blank ice layer until the end of May. Although several drain holes caused by the melted snow perforated the sea-ice, no crack initiation was observed until departure from Kuujjuarapik.

The frequency distribution of the local wind direction at Kuujjuarapik during the measurement period is shown as polar diagram in Figure 4.26. Accordingly, the Hudson Bay to the west and main land to the southeast are the dominant source regions for air masses reaching the site. In addition to wind parameters, ambient temperature and humidity seem to be valid criteria to distinguish between arctic and further meridional sources. Unsurprisingly, the chart displayed in Figure 4.27 relating temperature, humidity and wind direction, states that the air from the south is commonly dryer and warmer, most likely due to its continental origin and the improved visibility in absence of snowdrift and fog (see visibility data in Figure 4.24). Commonly, polar air has a relative humidity above 80% and is about 10 °C colder.

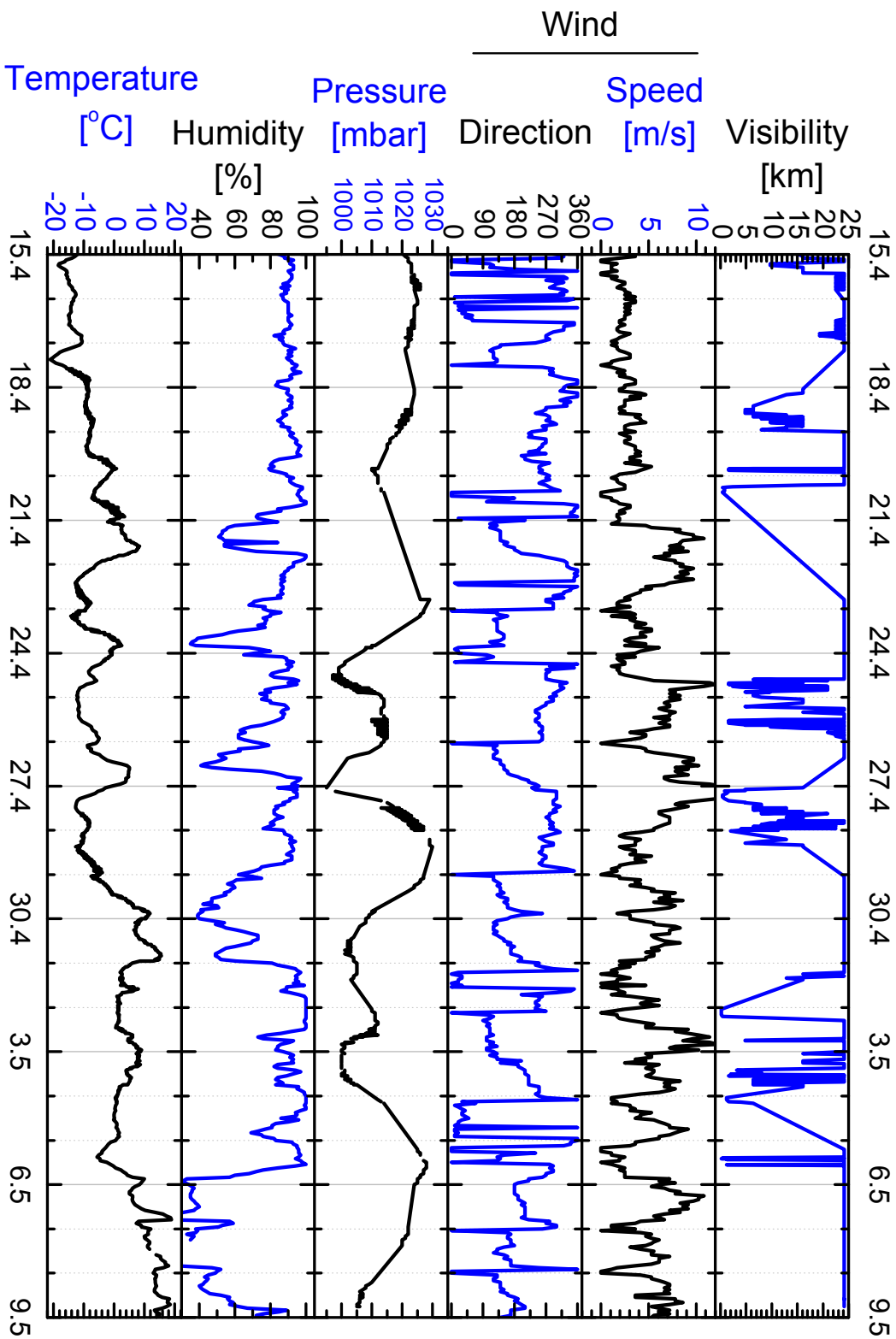

Figure 4.24: Overview of the meteorological parameters temperature, wind speed, wind direction, pressure, relative humidity and visibility for the period of the DOAS measurements at Kuujjuarapik, Hudson Bay, in April and May 2001.

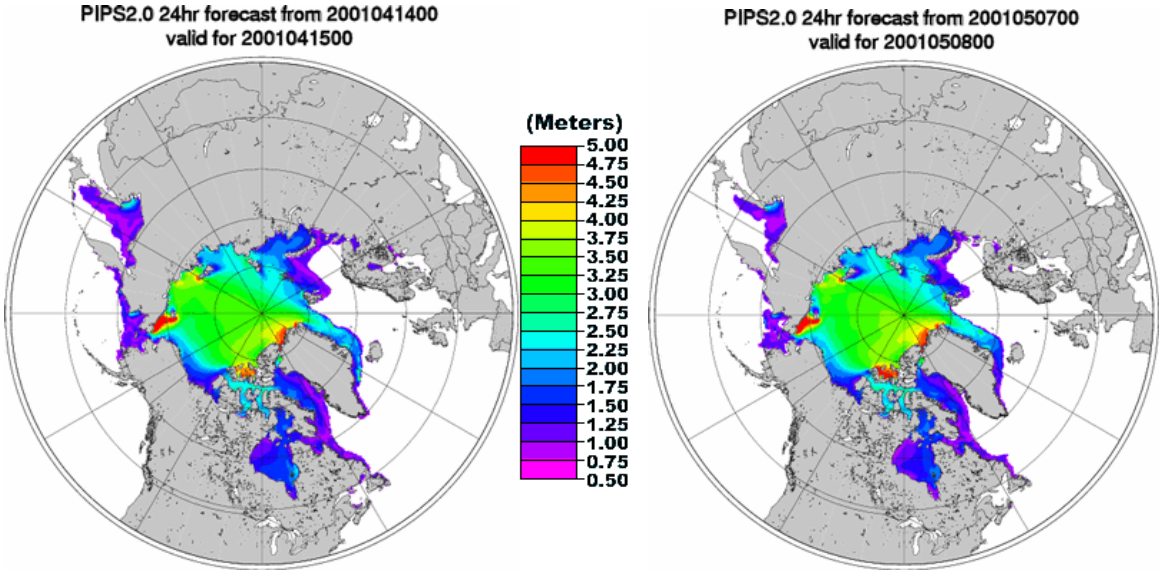

Figure 4.25: Marine Ice Thickness at the beginning and the end of the field campaign according to the Polar Ice Prediction System (PIPS 2.0), an operational model run by the Fleet Numerical Meteorology and Oceanography Center (FNMOC) for sea ice forecasting. Ice concentration data from the Special Sensor Microwave Image (SSMI) is used to initialize the system's forecast.

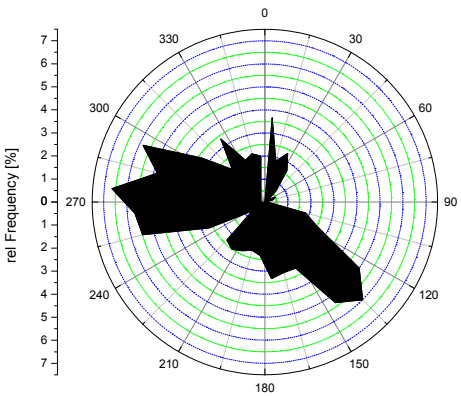

Figure 4.26: Relative frequency distribution of Wind directions at Hudson Bay from 13.04-09.05.2001.

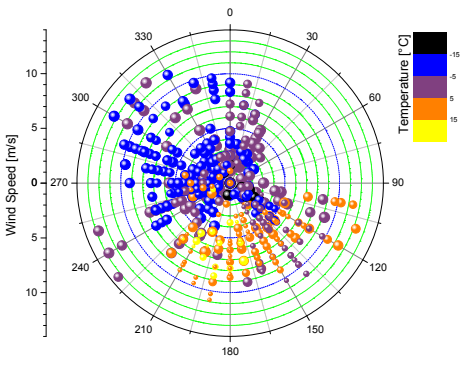

Figure 4.27: Polar Chart of Wind Speeds at Kuujjuarapik. The data points are coloured according to simultaneously measured Temperature and sized proportional two ambient humidity(small plots=dry air).

An interpretation based exclusively on the above given meteorological parameters can be quite misleading. A good example could be based on 23rd April 2001. Having a glance back on Figure 4.24 will show that winds blew from the south during almost the entire day, and the air was comparatively dry and warm. In spite of this, trajectory results (Figure 4.28) demonstrate that air masses have polar origin although they perform a quick loop southward within the last 12 hours before reaching the site.

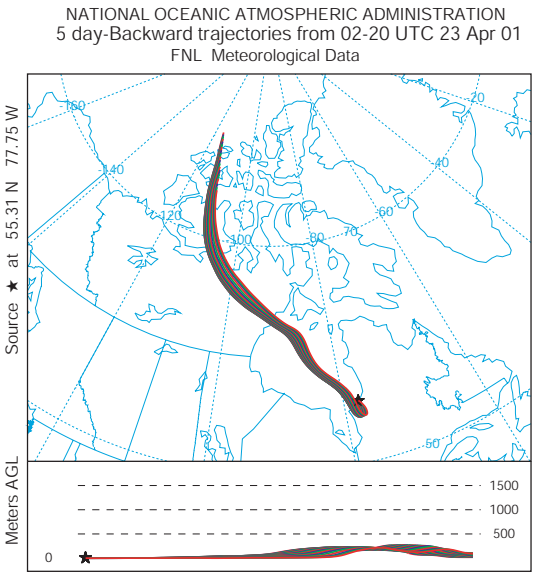

Figure 4.28: 5 day backward trajectories on 23rd April 2001. Air masses do a small loop southward before reaching the site.

As already done for the Crete campaign, the whole set of coordinates obtained from modelled 5–day backward trajectories ending at Kuujjuarapik was used to derive a waypoint frequency matrix (Figure 4.29). The results allow a more detailed statement about source regions. As already predicted from the wind distribution, the Hudson Bay to the west and south carry the major fraction of the flow reaching Kuujjuarapik. Along April however, the origin of air masses can often be found in remote regions significantly further poleward reaching up to large frozen sea ice areas of the Arctic Ocean and the Beaufort Sea (Fig. 4.25). During May a large fraction of entrained air masses have its origin notably further south reaching down to major Canadian and North American cities as Toronto and Detroit. The eastern leg of the matrix corresponds exclusively to the second week of may, when 5 day backward trajectories reached the Atlantic coast at latitudes around 60 degrees. In this area the sea was still covered with ice, although the thickness in May had decreased well below 1 meter and the sea was open 200 km off the shore(Fig. 4.25).

4.2.3 DOAS Measurements

Active long path DOAS measurements have been performed at Kuujjuarapik for the period ranging from 15th April to 8th Mai 2001. Starting few days later, and for the first time since then, a passive (M)ulti (Ax)is–DOAS telescope was operated in parallel to the longpath DOAS. The combination of both techniques led to a new insight regarding Bromine oxide distribution in the boundary layer and has been presented in [Hönninger et al. 2004].
The DOAS instruments were set up in a container about 2 km north of the village on a hillock to allow an unobstructed view to the sea few ten meters afar. The main retro reflector array was placed few ten meters above sea level close to the southernmost edge of Bill of Portland Islands, leading to a lightpath of 2*7.6 km heading almost straightly north at an average altitude of 30 m above the sea ice surface. For periods of poor visibility, a secondary reflector array was placed on shore at a distance of 1.95 km northwest from the DOAS instruments (Figure 4.30). The MAX–DOAS instrument, mounted on top of the container, received

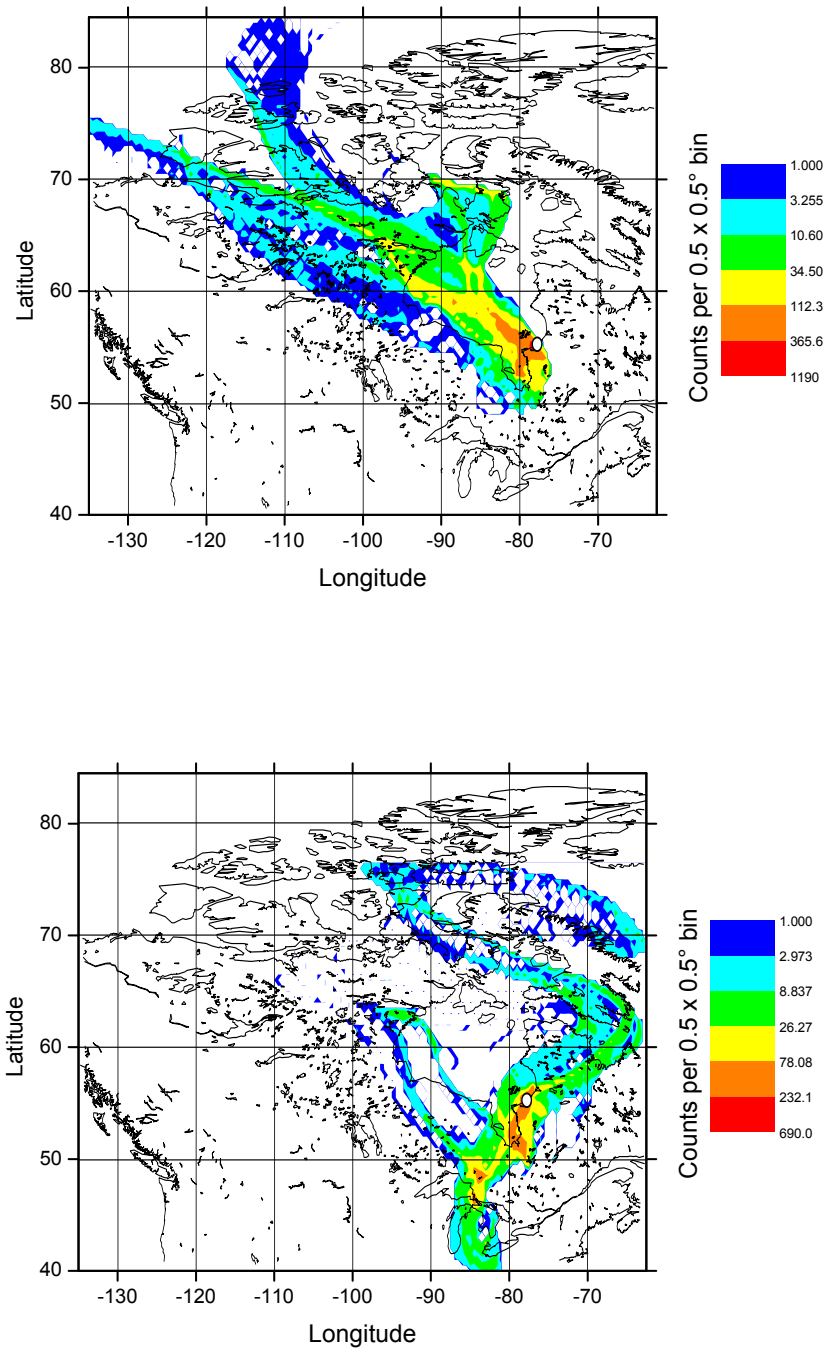

Figure 4.29: Frequency distribution of trajectories reaching Kuujjuarapik during the measurement period. Due to the largely different source regions, the results have been separated in two parts. The first two weeks of measurements (15.–29.04) are shown on **TOP**, whereas the rest of trajectories (30.04–08.05.2001) correspond to the graph on the **BOTTOM**. Apparently polar regions in the northwest and notably the iced sea surface of the Hudson Bay have been the major source regions of sampled air masses during measurements in April. The situation is largely different in May, when the input flux reaching Kuujjuarapik is prevalently southern and northeastern.

Table 4.3: DOAS–Longpath–Measurements at Kuujjuarapik(G.Hönninger, H.Leser, O.Sebastián)

Chemical component	Timeframe(UT)	Mean Concentration[ppt] (Range)	Mean Detection limit[ppt] (Minimum)
BrO	15.04–09.05.2001	2 (<0.6–28.6)	1.9 (0.6)
$HCHO$		<0	490 (160)
$HONO$		<200	200 (54)
O_3		36.9 ppb (< DL − 61.5 ppb)	3.1 (1) ppb
SO_2		<DL (<25–800)	140 (25)
IO		<1.3	1.3 (0.7)
NO_2		<80 (<80–9300)	250 (80)
NO_3		<2.0	2.0 (0.5)

light from the north with different elevation angles above the horizon as well as from zenith direction in a sequential mode. As for the measurement campaign in Crete (section 4.1.3) the continuous measurement loop for the active Long-Path-DOAS was programmed to record absorption spectra in the UV (295-375 nm), blue (390-470 nm), green (510-590 nm) and near Infrared (605-685 nm) spectral ranges. This allowed the measurement of the trace gases listed in Table 4.2.3. A special emphasis was held on all halogen oxides to define their influence on DMS oxidation. The DOAS fit to establish the concentration of trace gases was performed according to the analysis procedure described in section 3.1.4

Ozone and Bromine oxide The complete time series of BrO and ozone from active Long-path DOAS measurements at Kuujjuarapik is presented in Figure 4.31. Until the end of April, several events with BrO mixing ratios reaching up to 30 ppt have been observed. The measured levels are similar to those reported for the arctic boundary layer during spring [Hausmann and Platt 1994; Tuckermann et al. 1997; Hönninger and Platt 2002]. Simultaneously to all Bromine accumulation events, distinct ozone depletion has been observed. Commonly, ozone mixing ratios dropped 10-20 ppb below background levels (37 ppb O_3 on average) within few hours. The lowest ozone levels have been observed on 17, 24 and particularly 27 April 2001, when the atmospheric mixing ratio of ozone fell down to the detection limit of the LP-DOAS instrument (3 ppb). Unfortunately, the most intensive snowstorm of the whole measurement period did not only spoil DOAS measurements during the following night, but led to general technical breakdown, icing of the retro reflector surfaces and the consequent loss of 13 hours of data.

In general strong winds and snowdrift, a common observation during several BrO enhancement episodes, as well as fog and low cloud formation frequently reduced visibility (Figure 4.24) obliging us to fall back on the shorter lightpath to put up with a four times lower detection limit or even to stop measurements. However, most of the gaps in the LP-DOAS time series are due to arduous alignment sessions of the telescope and failures of the power generator supplying the container who gave much trouble for the first week of measurements. Unsurprisingly, 5–day backward trajectory results state that air masses reaching Kuujjuarapik during BrO accumulation periods had it's origin north of the polar circle reaching up to $85°N$. The Hysplit Model results state that during the last two weeks of April, air masses

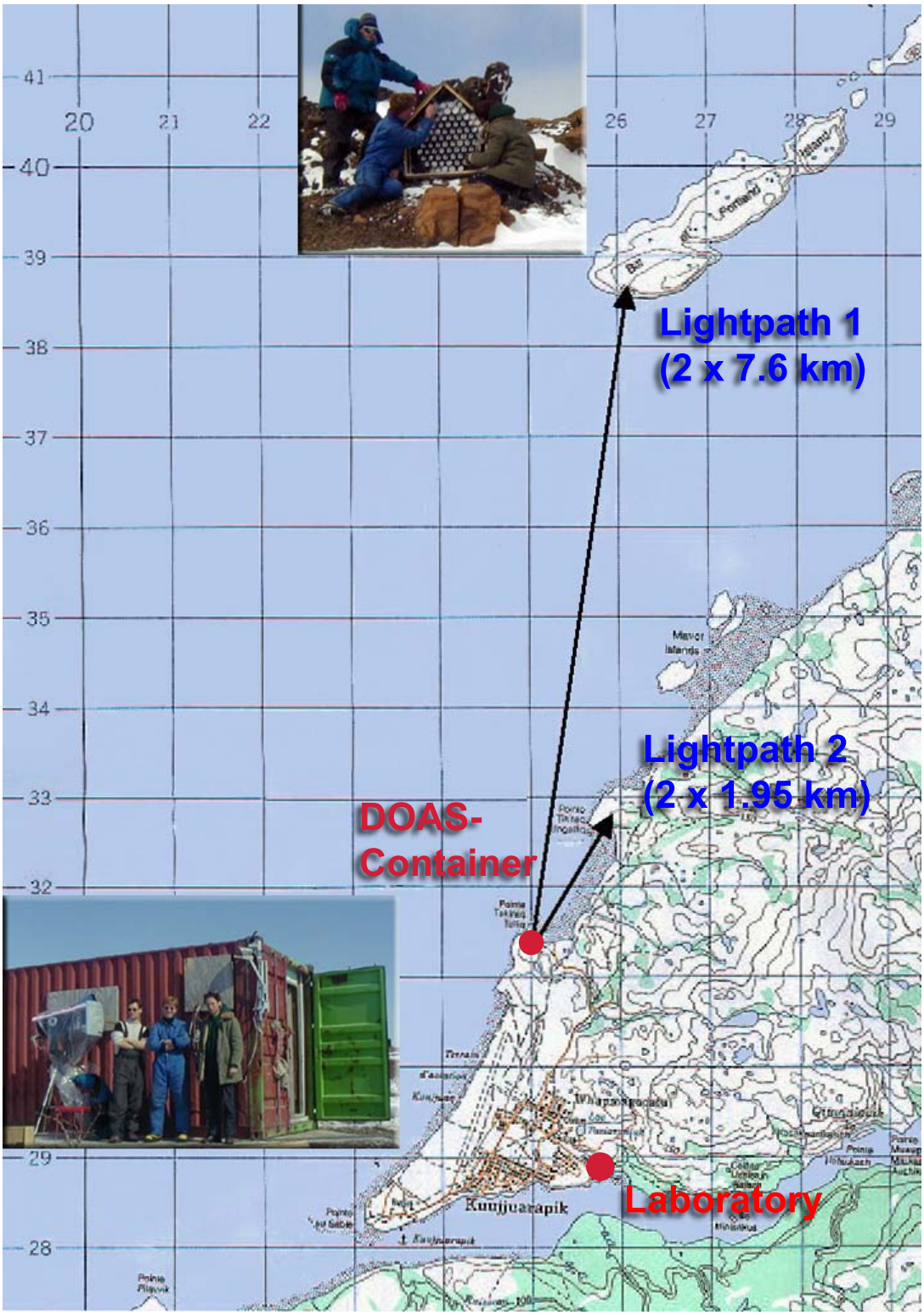

Figure 4.30: Local map of Kuujjuarapik showing the location of the CEN-Laboratory and the DOAS container as well as the two lightpaths used for the DOAS measurements.

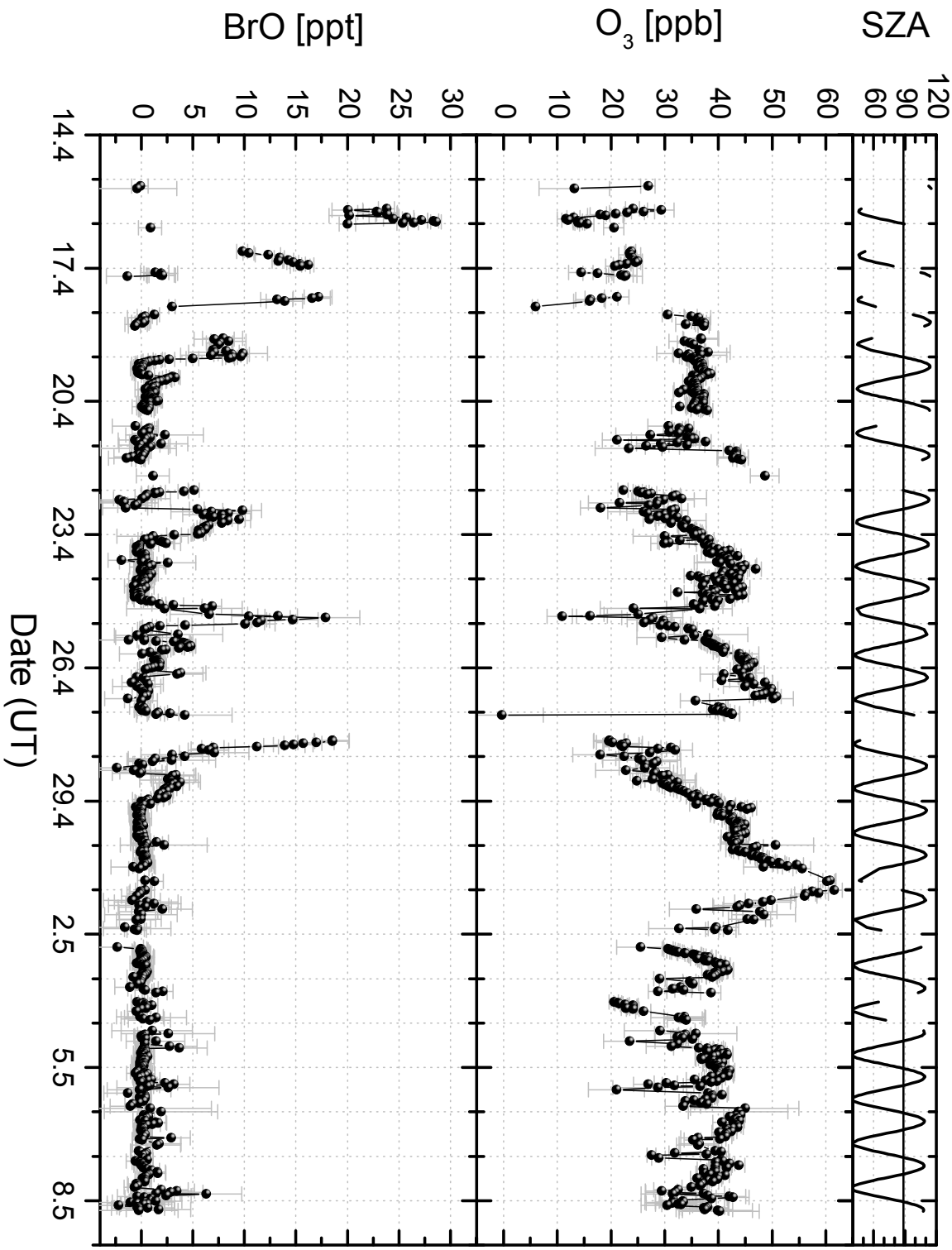

Figure 4.31: Time series of the first LP-DOAS Measurements of Bromine Oxide radicals at Kuujjuarapik, Hudson Bay. Besides BrO mixing ratios the DOAS data for ozone is shown.

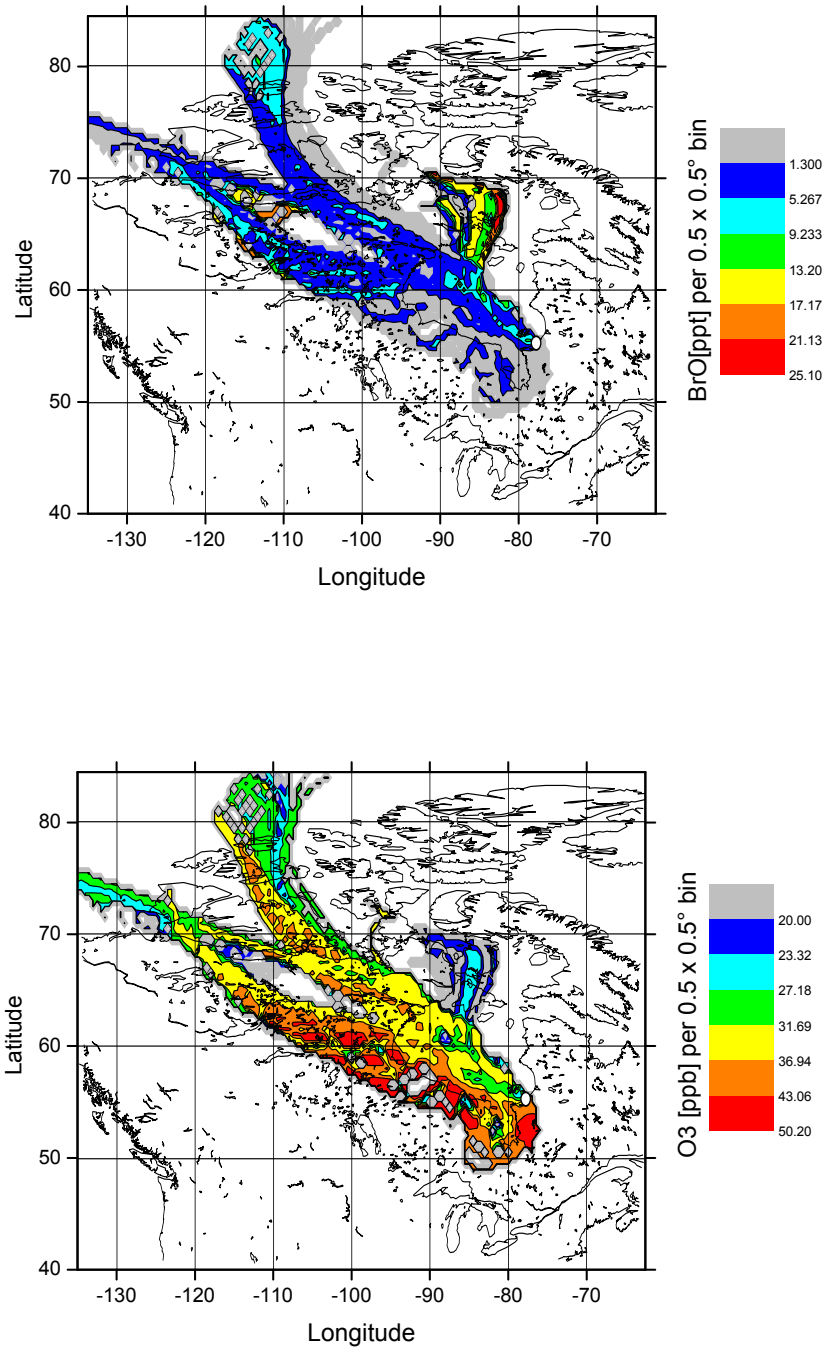

Figure 4.32: For this graph the ozone (**TOP**) and BrO (**BOTTOM**) mixing ratios measured at the ending time of calculated trajectories was assigned to all waypoints of each trajectory. Then the average concentration within a 0.5×0.5 degree bin was derived for both trace gases from concentrations assigned to all trajectory points within the bin.

reaching the site remained within the lowermost 500 m of the boundary layer and travelled several days right above the frozen Hudson Bay before reaching the site. In Figure 4.32 a BrO distribution matrix for the last two weeks of April was created by assigning the BrO mixing ratio measured at the endpoint time of each trajectory to all their waypoints (120 coordinates=5days*24hours). Then all trajectory coordinates within a 0.5×0.5 degree bin were summed up to get a mean BrO concentration matrix. The results show that the, grey shaded, areas south and east of Kuujjuarapik do not assert detectable BrO levels. Although the most adjacent thought is that this areas are negligible sources of bromine, one has to keep in mind that removal of BrO from the gaseous phase via deposition or other depletion processes may occur as well. As the gas phase reaction with ozone is presumably the most efficient sink of BrO, the distribution matrix of ozone (Fig. 4.32) can support the localization of BrO source regions. Indeed, areas with lowest average O_3 mixing ratios correspond largely to matrix bins with highest BrO levels. For the areas with no detectable BrO the region west of 100° W and north of the arctic circle (66° N) features significantly lower O_3 levels than areas east and south of the measurement site. Therefore, it is conceivable that BrO molecules formed in the arctic have been consumed by the reaction with ozone before reaching the sampling site.
Due to the entrainment of air masses from the south (Big Lake region) starting on 30th April 2001 (at 18UT), meteorological conditions at Kuujjuarapik began to change widely. Ambient temperature rose above 10 °C and abundant rainfall within the first days of May began to melt the snow cover in the area. Since the end of April, the stability of the inversion layer apparently fades as trajectory results state subsidence from higher atmospheric layers reaching up to 4000 m north of the arctic circle. Indeed, subsidence could explain ozone levels surpassing 60 ppb at the end of April. Nevertheless, throughout May BrO mixing ratios exceeded daily the detection limit of 1.3 ppt reaching levels within the range of 2-4 ppt and about 6 ppt on 8th May 2001. Although less evidently, simultaneous ozone decrease of 5 to 10 ppb was still observed (Fig. 4.31).

Other halogen oxides Besides BrO, OClO was included in the fit for the UV spectral range. The evaluation for the blue region included IO,OBrO and OClO. Within the green spectral range the evaluation was focussed on the detection of OIO and OBrO. Yet neither of these other halogen trace gases was found at concentrations above detection limits. The fitting procedure for all these trace gases has been described in section 3.1.4 and led to upper limits (i.e. detection limits) listed in table 4.4

Nitrogen species and SO_2 As expected for the remote polar region, the content of nitrate radical species in air masses sampled at Kuujjuarapik was tiny. The concentrations of the nitrate radical NO_3 and nitrous acid HONO, remained below detection limits (2 and 200 ppt respectively) over the whole measurement period. During the first two weeks of measurements, even the typically most abundant nitrogen species, NO_2, remained mostly below detection limits (250 ppt on average). For the first two weeks of measurements significant concentrations of NO_2 appeared only during the nights of 16th to 17th and 22nd to 23rd April

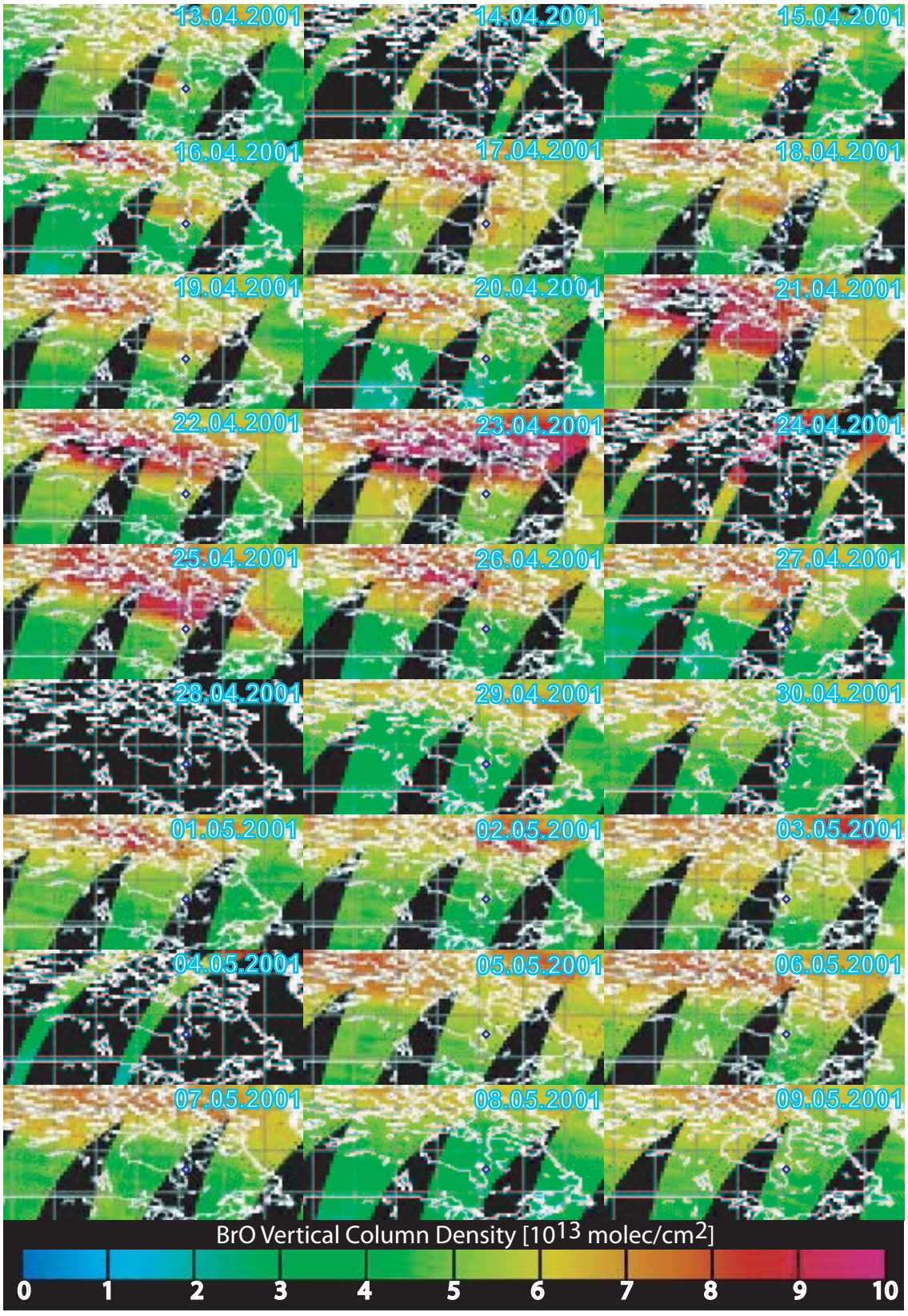

Figure 4.33: Diurnal mean vertical column density of BrO as measured with the DOAS instrument on the GOME satellite. The location of Kuujjuarapik is denoted by a small circle. GOME BrO maps kindly provided by J.Hollwedel, IUP Heidelberg.

Table 4.4: Detection limits of the investigated halogen oxides during the Hudson Bay campaign in April/May 2001. The values can be considered as upper limits of the atmospheric mixing ratios.

Species	average detection limit [ppt]	minimum detection limit [ppt]
BrO	1.5	0.6
OClO[a]	1.7	0.9
OBrO[a]	5.4	0.9
IO[a]	1.3	0.7
OIO[a,b]	6.6	1.0

[a] not detected

[b] taking the cross section by [Bloss et al. 2001]

(Figure 4.2.3). Due to the extreme strength (over 7 ppb) and short duration, both NO_2 events must be related to local pollution sources. The most conceivable local source was the gasoline engine of the power supply generator placed at the eastern side of the DOAS-container. As shown in Table 4.5 particulary weak southwestern winds obviously blew important amounts of NO_x through the lightpath of the DOAS instrument. In order to further evaluate the envi-

Table 4.5: Observations during NOx events

Period (UT)	NO_2 [ppb]	Wind Dir.	Wind Speed	ΔO_3 [ppb]	initial O_3 [ppb]	T[°C]	rHum [%]	modelled NO_3[ppt]
17.04 2:50–4:30	8	128°	1.0 m/s	-6	20	-17	90	0.15
23.04 3:14–5:00	7	129°	1.5 m/s	-8	35	-14	87	

ronmental impact of the observed NO_2 events, a simple 0D-Box-Model was created including reactions listed in table 2.6 with rate constants adapted to ambient conditions. As both NO_2 events in April occurred right before midnight, photolytical sinks can be disregarded until dawn (at 4:45 local time). The results of the model (Figure 4.34) expose that about the same amount of NO is required to reach highest observed NO_2 levels. The model states that 7 ppb NO_2 can build up within 10 minutes by simultaneous depletion of roughly 6 ppb ozone. Indeed, the measurements show an ozone decrease during both NO_2 events as shown in Table 4.5. However, one has to keep in mind that during both events about 2 ppt BrO have been measured as well and measured air may have been low in ozone before.
The use of the model also gives a suitable answer why the mixing ratio of NO_3 remained below detectable limits in spite of the abundance of its precursor species NO_2 and O_3. The important formation of N_2O_5 gives evidence that the major part of NO_3 is lost through reaction (2.37) described in section 2.2.2.2. This is not surprising as the equilibrium of both compounds is shifted three orders of magnitude towards N_2O_5 due to the much colder environment as encountered in Crete (section 4.1). In turn N_2O_5 is largely converted to HNO_3, which is one of the most important sinks for gaseous nitrates due to efficient removal from the atmosphere via deposition processes on ground.

Since the end of April, NO_2 pollution was observed almost regularly at night and the first/last hours of day. All increases of NO_2 coincide with the appearance of southerly winds as demonstrated in Figure 4.2.3 showing the relation of NO_2 and SO_2 to the wind direction. The levels of sulphur dioxide, a compound which could be formed during the oxidation pro-

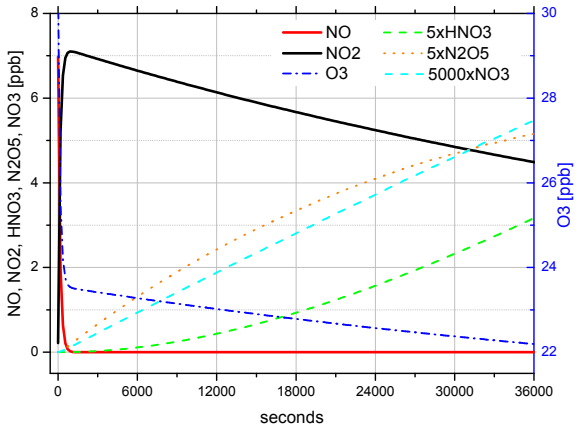

Figure 4.34: Results of a simple 0D-box model including elemental NOx reactions listed in table 2.6. Excepting the empirically established value for NO, all initial trace gas concentrations have been set to observed background levels at 03:00UT on 23.04.2001.

cess of Dimethylsulphide, remained below detection limits (140 ppt on average) throughout the campaign period excepting 7th and 8th May 2001, when mountains of waste amassed during the winter months were lit at the local incineration field located 1 km further south. The power generator, so productive in NO_x, was not a traceable source of sulphur as the levels of SO_2 do not follow those of NO_2 (Figure 4.2.3). Indeed the generator was run with unleaded gasoline which commonly has a low sulphur content. In general the NO_2 and SO_2 levels measured by DOAS are representative for clean background air, especially during BrO events which were always associated with north-westerly wind and arctic air masses reaching Kuujjuarapik. According to long term measurements from the GOME satellite [Beirle et al. 2003] the whole area of the Hudson Bay is among the poorest in NO_2 worldwide. The most contiguous major source region of NO_2 is found more than 1000 km further south, notably southeast of the Big Lakes where a belt of large Canadian and US cities (including Chicago,Detroit,New York and Toronto) provides a large NO_x emission rate. Although during the month of May air masses reaching Kuujjuarapik occasionally cross the Big Lake area (Fig. 4.29), the contribution of long range transport to background NO_x levels in the arctic is presumably small. Unless local sources exist, the levels of NO_2 and particulary SO_2 (do the very effective deposition in wet environments) are probably well below upper limits derived from the DOAS measurements.

4.2.4 DMS and the oxidation products DMSO and MSA

Simultaneously to the LP- and MAX DOAS measurements, the atmospheric concentrations DMS, DMSO and MSA have been established by our project partners from the LSCE-CNRS and ECPL-Crete. The emplacement of all required instruments was the laboratory of the *Centre d'études nordiques*(CEN), located about 2 km southeast of the DOAS measurement container, on the opposite site of the village (Figure 4.30). The time series of all three compounds are presented in Figure 4.2.4.

Atmospheric DMS was sampled into stainless steel canisters and analyzed several minutes after using the classical technique of cryotrapping and consequent gas-chromatographical

analysis as described in section 3.2. During the measurement period ranging from 15.04 to 01.05.2001, the atmospheric concentration of Dimethylsulphide did not exceed 7.72 ppt and remained as low as 1.45 ppt on average. To reach detectable levels, the sampling time for each air probe was increased to 4 hours (between 30 and 90 minutes in Crete). Atmospheric DMSO measurements using the Cofer mist chamber (section 3.2) started already on 12th April and ended at 1st May. The analysis revealed DMSO concentrations about 0.1 ppt on average, reaching a maximum of 0.8 ppt at the first day of measurements and remaining below 0.3 ppt thereafter. Methane sulphonic acid (MSA) concentrations ranged from below the detection limit to 3.75 ppt (mean of 0.62 ppt).

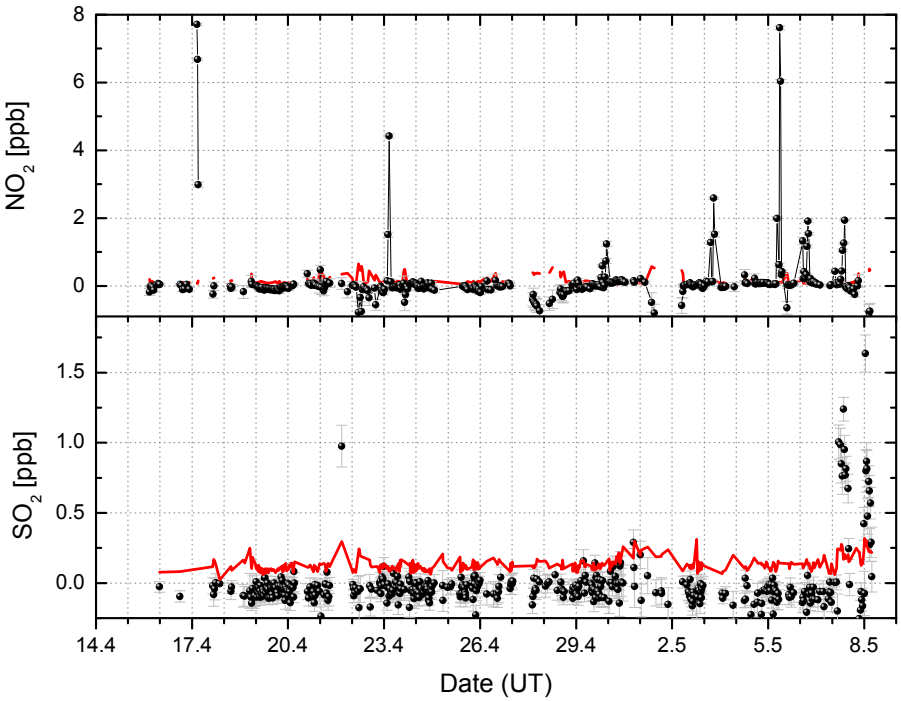

Figure 4.35: Nitrogen and sulphur dioxide levels in Kuujjuarapik measured from 15.04–09.05.2001. The red line shows the detection limit of the DOAS measurement. With exception of local pollution events, no significant concentrations of both compounds have been detected.

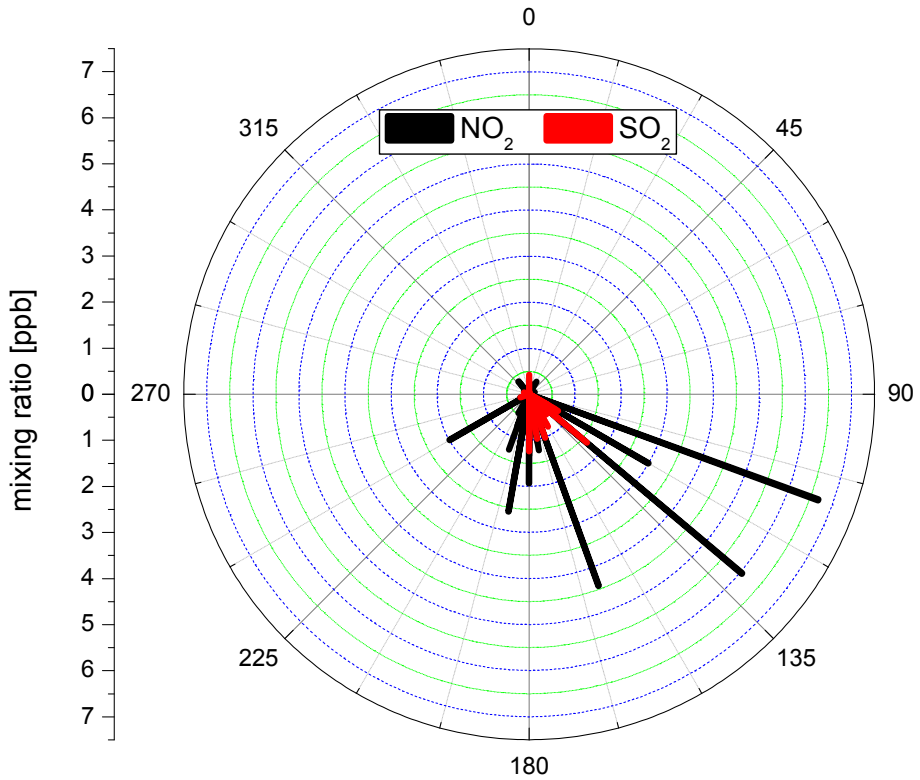

Figure 4.36: NO2 and SO2 concentration as a function of wind direction.

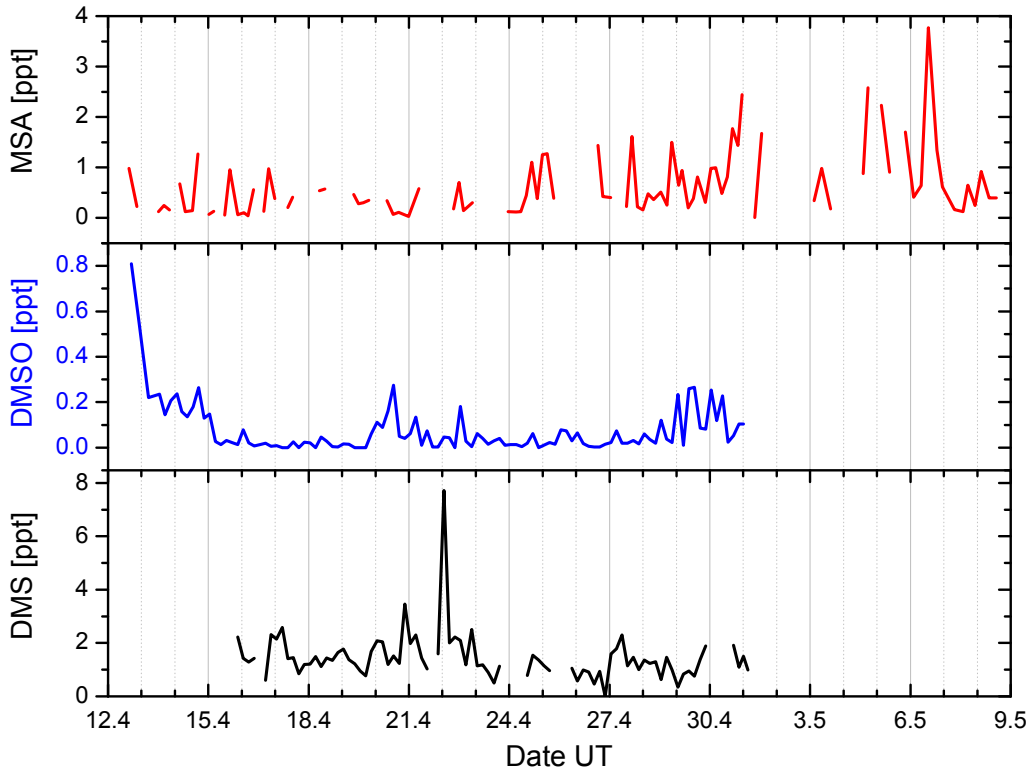

Figure 4.37: Concentrations of DMS, DMSO and MSA measured by LSCE-CNRS and ECPL groups.

4.3 Field Campaign Kerguelen 2002

For the third EL CID campaign a pristine marine site in the remote Indian Ocean was selected to offer complementary data to previous results obtained under semi-polluted (Crete) and sub-arctic (Hudson Bay) conditions. The measurements have been carried out in summertime due to the high seasonal DMS production and to allow to identify and quantify the influence of polluted/clean atmosphere on the processes controlling the DMS oxidation chain. The aim of the IUP Heidelberg Team was to establish whether halogen or other measurable radical interactions with DMS play a major role in this environment.
Besides the measurements at Kerguelen were of particular significance for model descriptions planned within the framework of the EL CID project, since any link between DMS and cloud condensation nuclei (CCN) will be best discovered in the most remote and natural environment where anthropogenic influences and other continental aerosol inputs are minimal.

4.3.1 Observation Site

The Kerguelen Islands are an archipelago located between 48–50° south and 68–70° east in the southern Indian Ocean. The archipelago, of volcanic origin, has a total surface of 7250 km^2 (120×130 km) and consists of a large Island (La Grande Terre, Ile Kerguelen or Desolation Island: 6700 km^2) and hundreds of smaller islands, islets and reefs (550 km^2). The coastline of the main island is highly irregular with a number of large peninsulas linked to the island by low narrow isthmuses. These large features are further sub-divided by fjords into smaller peninsulas.
The nearest main land to Kerguelen is the Antarctic continent about 2300 km southward. The African continent, and thus any major human settlement, is located about 3900 km further north (Fig. 4.23). Placed at the south of the subtropical convergence zone, the islands have a subantarctic climate and rain, sleet or snow falls on over 300 days a year. Due to the exposure to the winds of the "Roaring Forties" strong westerly gales are common and the average wind speed is still as high as 9 m/s in the relatively calm summer months. Due to the oceanic climate the annual range of temperatures experienced on the island is unusually low.

The inland of Kerguelen is rich in valleys and ridges with the highest point, the glaciated Mount Ross, reaching a height of 1850 m. Ice covers nearly one third of the island and the abundant rainfall combined with glacial meltwater keeps numerous streams and lakes full of water. Due to the strong winds vegetation is reduced mainly to tussock grass, mosses and the tasty Kerguelen cabbage. In spite of unfortunately effective sealing activity in the previous centuries the Kerguelen Islands are settled by a large number of sea-birds, sea-elephants, seals and other mammals.
The archipelago forms part of the autonomous French Overseas Territory of "Territoire des Terres Australes et Antarctiques Françaises (TAAF)", due to this status a permanent settlement named *Port–aux–français* (49° 21'S, 70° 13'E) is maintained at the south-eastern coast of the main Island (Fig. 4.3.1). The base has a total population of 120 including military

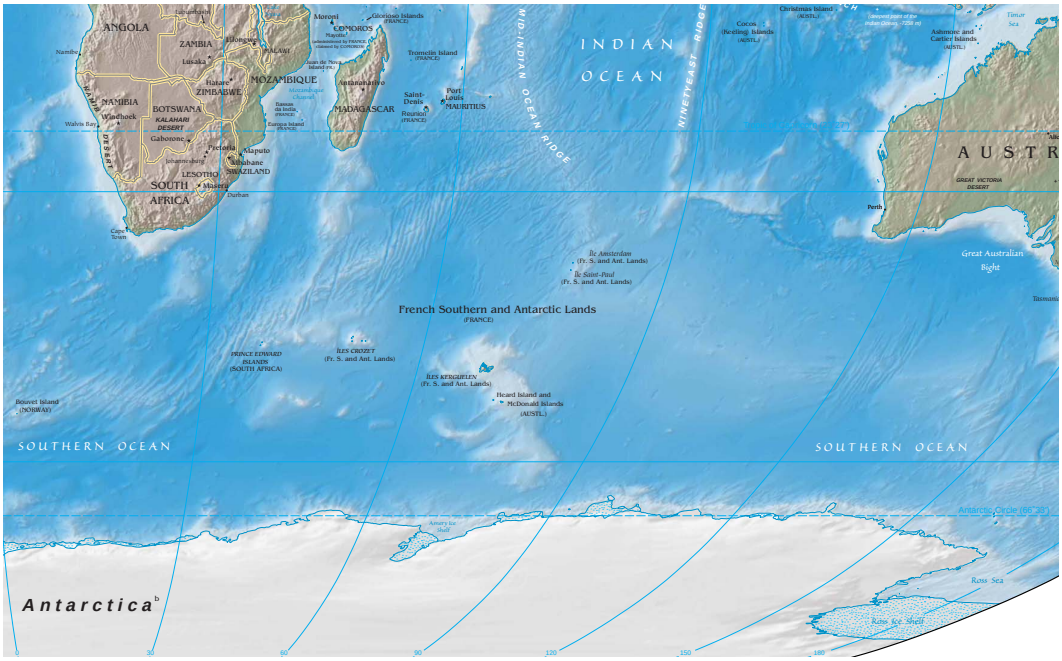

Figure 4.38: Region map around the island of Kerguelen.

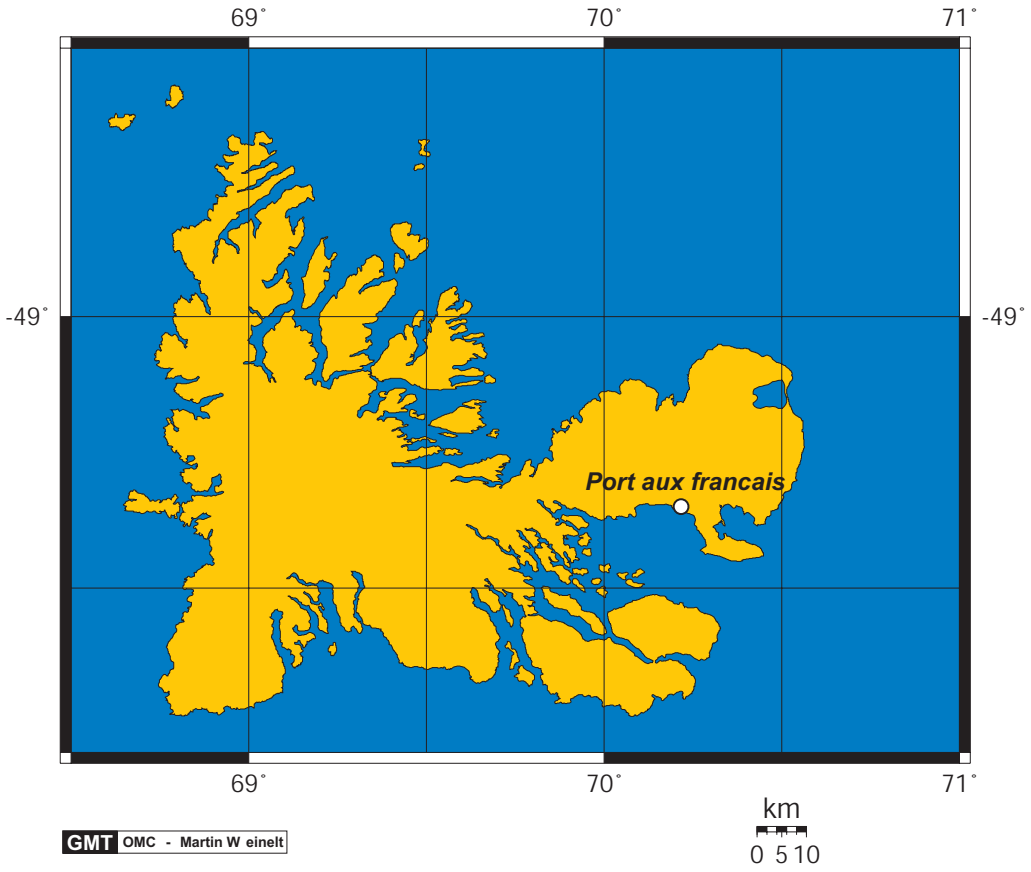

Figure 4.39: Local map of the island of Kerguelen.

and research staff in summer. All instruments were set up in an old military building at the western edge of the station, few meters off the shore at about 10 m over sea level, facing the Bay of Morbihan in the South within the sector 160–270°.

4.3.2 Meteorological conditions

Figure 4.43 gives an overview of the most relevant meteorological parameters recorded during the measurement period on Kerguelen kindly provided by the permanent Meteorological Station at Port–aux–français (Meteo France). Due to the remote marine condition and the emplacement inside the subtropical convergence zone the meteorology of Kerguelen is ruled by the non ceasing interaction of tropical high and sub-Antarctic low pressure systems (Figure 4.3.2). As a consequence the most common meteorological observation at Kerguelen were strong (north)westerly winds with an average speed of 9 m/s reaching 23 m/s as a maximum (Fig. 4.3.2). Trajectory results obtained using the Hysplit Model [Draxler and Hess 1998] state a dominant westerly flux of air masses reaching the measurement site having its origin within the belt from 40-60° South. Low wind episodes (below 6 m/s) were characterized by input from the northern and eastern sector which may be a source of local pollution.
Due to the high speed of clouds the weather situation at Kerguelen exhibited a large variability from blue sky to overcast conditions within few hours. Haze formation, probably due to turbulent mixing, condensation and aerosol formation, frequently reduced the visibility right above the marine surface. On days with blue sky, low level clouds occasionally formed above the water surface of the bay of Morbihan, crossing the absorption light path of the DOAS, deranging measurements(see Figure 4.40. The air humidity increased from 60% at noon to nearly 80% at night on average.

Mean temperatures ranged between 7 °C at night and 13 °C during noon, raising up to 21 °C on the low wind period from 11-12.02.2002 and falling down to 3 °C in the rainy and stormy week of 20-26 February.

4.3.3 Active Longpath–DOAS Measurements

The longpath DOAS was operated over a period of more than 4 weeks, ranging from 21st January to 21st February 2002. Apart from few technical emendations the LP-DOAS instrument was the same as applied in the Hudson Bay(section 4.2.3). Due to a delivery bottleneck, Xenon Arc Lamps of the types Osram XBO 500RT and Osram Narwa 250W replaced the commonly used PLI 500 lamps(section 3.1.2). Two light paths with retro reflector arrays at 4.5 km(Pointe Du Harem) and 9 km(Pointe Guite) distance from the Laboratory were set up initially. Due to the exposure to strong wind blow, the arrays were additionally sheltered inside large wooden cargo boxes anchored to the ground (Fig. 4.45). Both boxes were set up at few meters from the shore and at approximately 10 m above sea level(Fig. 4.3.3). Therefore the absorption path was nearly horizontal an measurements yielded concentrations right above the sea surface. Probably due to the abundant aerosol formation or/and the minor performance of the applied Xenon Lamps the yield of light coupled back into the DOAS telescope was rather poor on the longer light path. Due to the strength and variability of the

Figure 4.40: Cloud formation right above the sea surface disturbing DOAS measurements

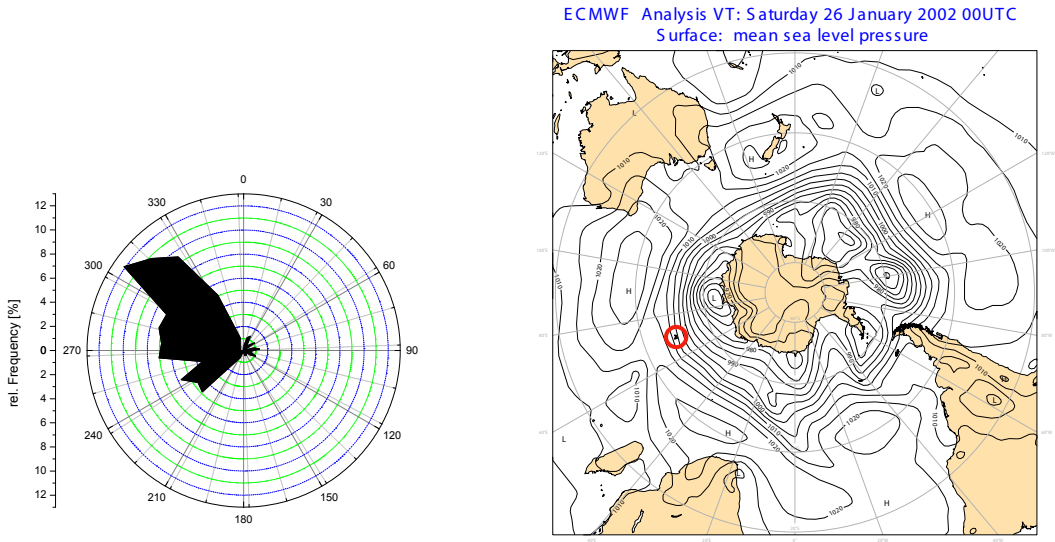

Figure 4.41: **Left:** Frequency distribution of wind direction during the Kerguelen campaign. **Right:** Sea level pressure on 20th February 2002 at 00 Universal time. The displayed chart is representative for the commonly observed Meteorological situation in the area.

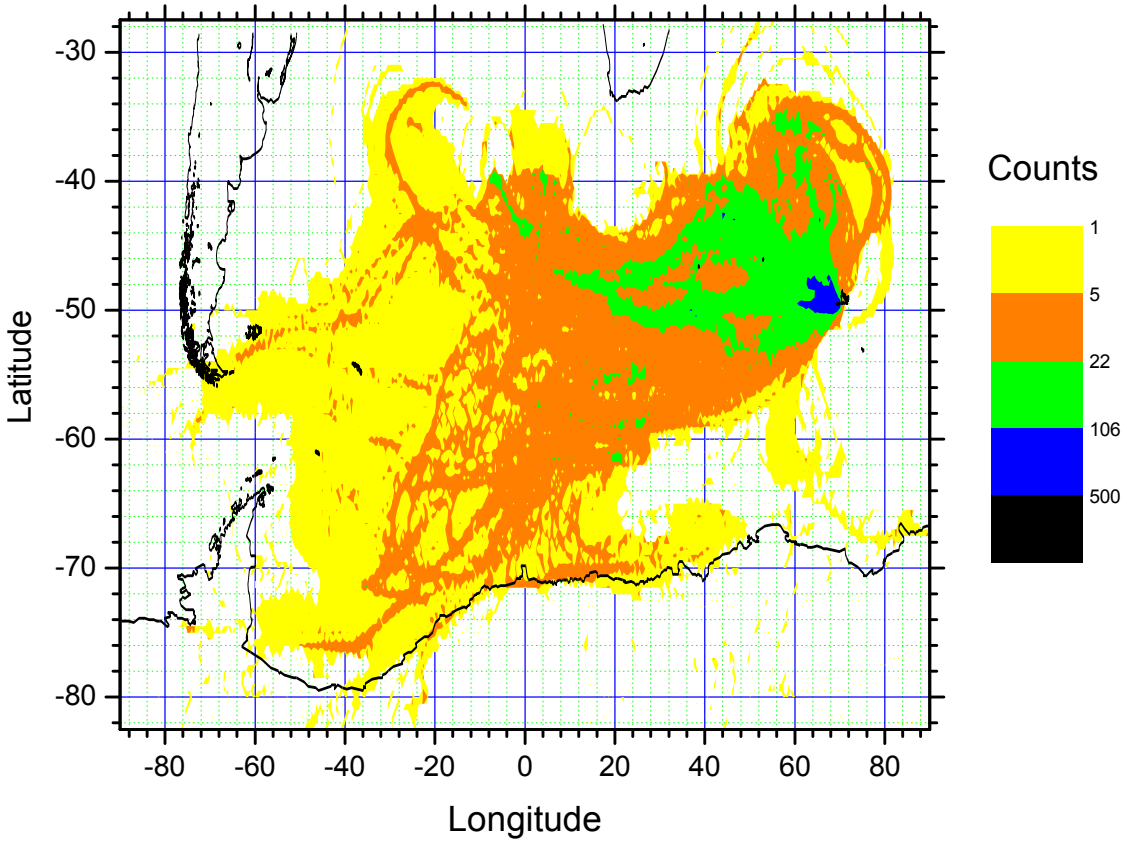

Figure 4.42: Gridded distribution of the origin of air masses during the Kerguelen campaign. The distribution is based on 5day backward trajectory results from the Hysplit model. Count denotes the number of times a trajectory crossed the 0.5x0.5 degree bin.

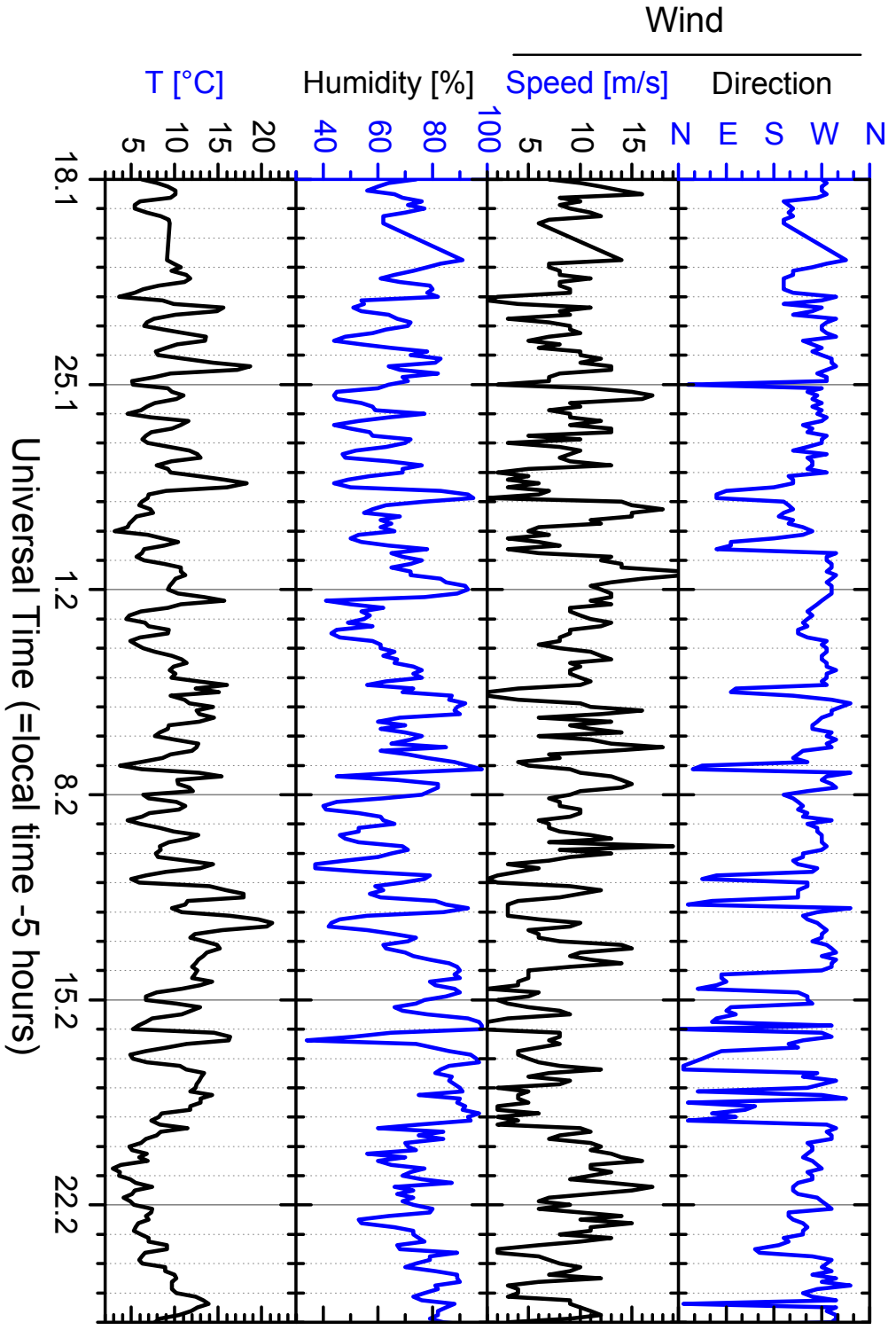

Figure 4.43: Meteorological parameters for the Kerguelen Field campaign (19.01-26.02.2002) provided by MeteoFrance.

Table 4.6: DOAS–Longpath–Measurements at Kerguelen 2002(O.Sebastián, J.Zingler)

Chemical component	Timeframe(UT)	Mean Concentration[ppt] (Range)	Mean Detection limit[ppt] (Minimum)
BrO	21.01–21.02.2002	<1.4	1.4 (0.4)
$HCHO$		<380 (<100–730)	380 (100)
O_3		11900 (1200–17600)	3100 (800)
SO_2		<50 (<14–920)	50 (14)
IO		<1.4 (< 0.3–5.5)	1.4 (0.3)
NO_2		<100 (< 23–5130)	100 (23)
NO_3		<2	2 (1.5)

Xenon-Emission lines of the initially employed *Osram XBO 500 Watt* lamps, a switch to the *Narwa 250W* type was done after the first 2 weeks of measurements. The *Narwa 250Watt* lamps have minor total power, but should allow a higher light-yield due to the minor extension of the lamp spot. In the second week of February the array on the long lightpath was shifted few meters further south to the top of a rocky ridge(total pathlength: 2*10 km) , roughly 50 m above sea level in an attempt to reduce excessive absorption in the water surface layer. In spite of this efforts the major part of the measurements had to be performed on the shorter lightpath facing Pointe du Harem forcing us to put up with a higher detection limit. Due to technical blackouts of the stepper motors of the DOAS instrument no automatic alignment was possible, leading frequently to the loss of data between the last check after midnight and the first one hour after dawn(about 6:00 local time). Due to the breakdown of the remaining stepper motors and the controller unit, the DOAS measurements ended on 21st February.
An overview of all measurements performed using the Longpath-DOAS system is given in Table 4.6. As for the previous campaigns in Crete and Kuujjuarapik (sections 4.1.3 and 4.2.3) the DOAS instrument recorded absorption spectra in the UV(295-375 nm) and visible blue (395-475 nm) as well as green (510-590 nm) spectral ranges. During night scans of the near infrared (605-685 nm) were added to the measurement loop. Due to the primary goal to detect any relation of ambient DMS levels with iodine oxide concentrations, the routine was modified to scan preferably the blue region. Therefore concentration data of trace gases fitted in that region (i.e. NO_2,IO) have a much higher time resolution (15 min) in comparison to other data (aprox. 30 min). The evaluation procedure was carried out using the same procedure applied on previous campaigns. In addition to the MFC programm, an analogous evaluation using WinDOAS was performed leading to similar results.

Halogen oxides The measured time series of iodine and bromine oxide (IO and BrO) are shown in Figure 4.3.3. Other measurable halogen compounds as OIO and ClO remained below detection limits (1.8 and 2.5 ppt respectively). Due to the confinement to the short lightpath the detection limits are notably worse than those obtained on previous campaigns(about double). Bromine oxide observations above the detection limit of 1.6 ppt are restricted to few single events reaching 2 ppt as maximum. This is in agreement with expectations as under present conditions bromine sources reduce to the release from sea salt aerosols and the degradation of organohalogens(see section 2.2.3). Although local emissions of organobromines

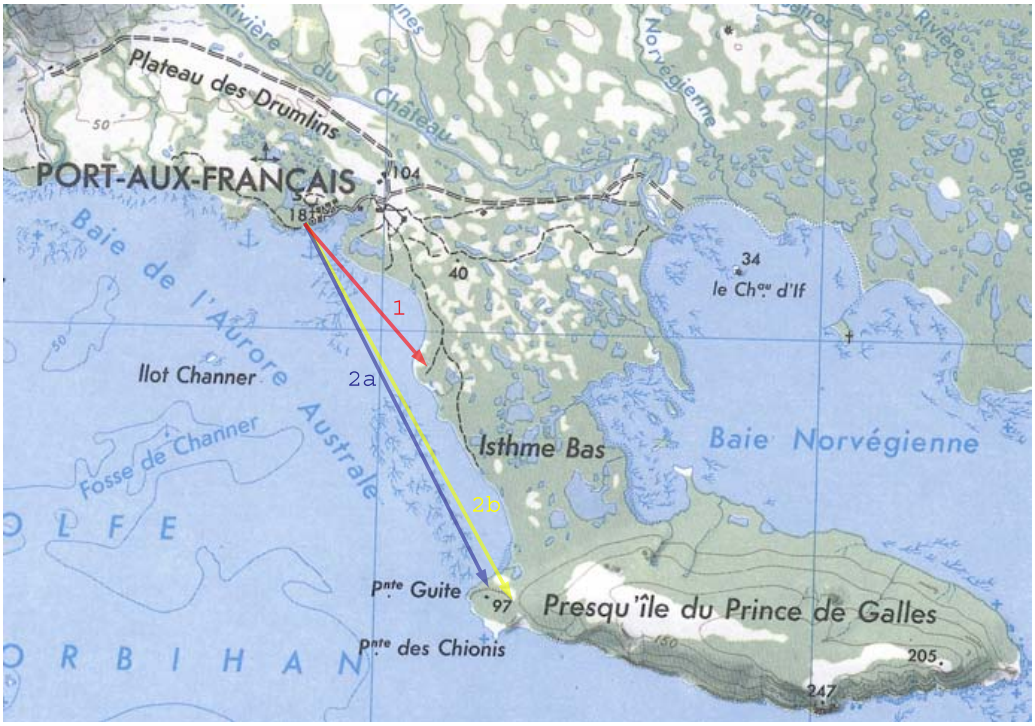

Figure 4.44: Lightpaths at Kerguelen

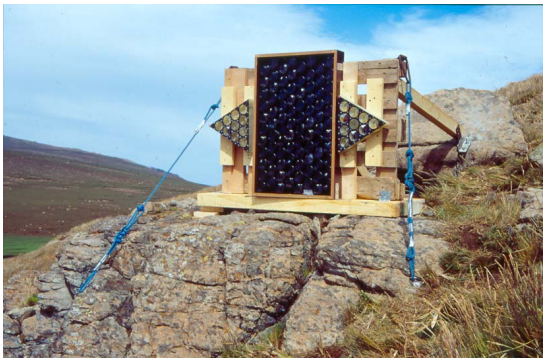

Figure 4.45: Set up of retro reflectors arrays at Pointe Guite for the long ligthpath for DOAS measurements. The left picture shows the initial setup of the retro reflector array inside a sheltering cargo box. On the right the second set up with the array attached to a shipping pallet fixed on top of the Pointe Guite (about 50 m above sea level) is shown.

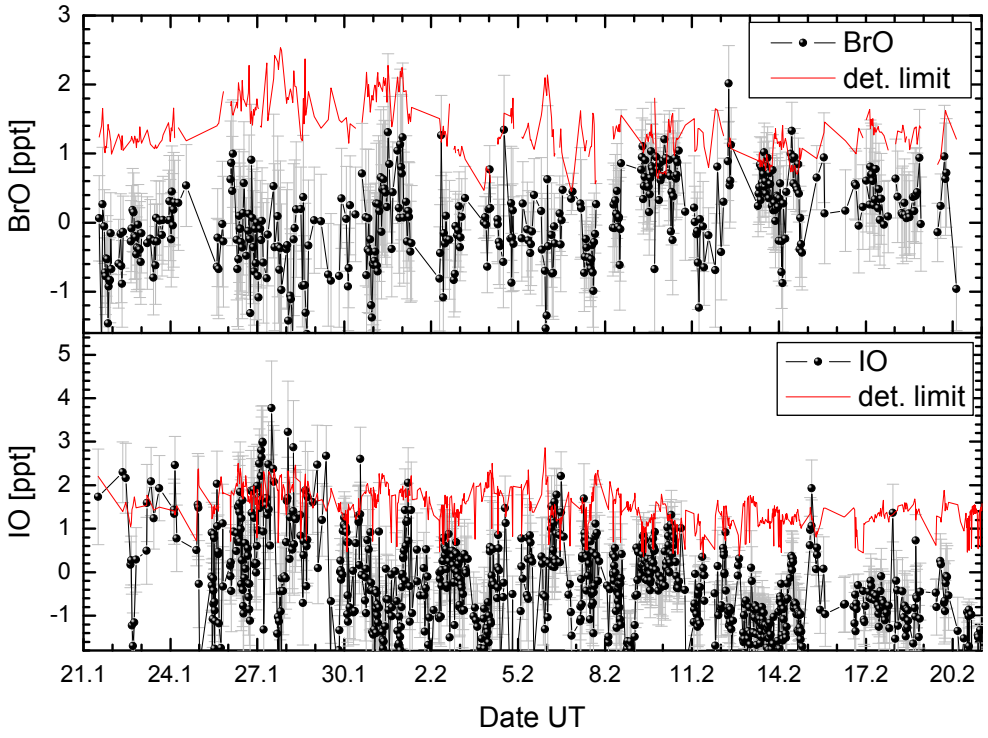

Figure 4.46: Concentrations of the halogen oxides of Iodine and Bromine measured with the longpath DOAS instrument for the period of 21.01-21.02.2002.

might be important, their photolytic lifetime is long enough to be blown away before any reactive bromine formation can be observed. Therefore measurements of bromine at Kerguelen presumably represent marine background concentrations in agreement with observations of [Leser et al. 2003] on board the research vessel Polarstern in the Atlantic Ocean.
Iodine monoxide was detected notably within the first two weeks of measurements up to levels of 5.5 ppt. After the begin of February, IO measurements above detection limits reduce to single events (Fig. 4.3.3). The measured concentrations are too low to play a major role in DMS oxidation (section 2.3.2.3) which, as shown before by [Sciare et al. 2000], is dominated by the DMS+OH reaction pathway. However the results of a photochemical box model incorporating the recycling of iodine through marine aerosol [McFiggans et al. 2000] indicates that, assuming IO levels in the order as observed in Kerguelen, the direct iodine-catalyzed destruction of ozone in the boundary layer may well be similar to the losses caused by odd-hydrogen photochemistry and dry deposition. Most of the enrichment should be due to the accumulation of iodate(e.g. NaIO3), although other iodine species may also be present, depending on the rate of aerosol recycling(section 2.2.3.2). Another possible role of iodine is the denoxification of the MBL which could be significantly enhanced as a result of aerosol uptake of $IONO_2$, formed from recombination of IO and NO_2.

Measurements of NO_x and SO_2 – Impact of local pollution sources For the most part of the measurement period the atmospheric mixing ratio of nitrogen and sulphur dioxide remained below their respective detection limits (100 ppt for NO_2 and 50 ppt for

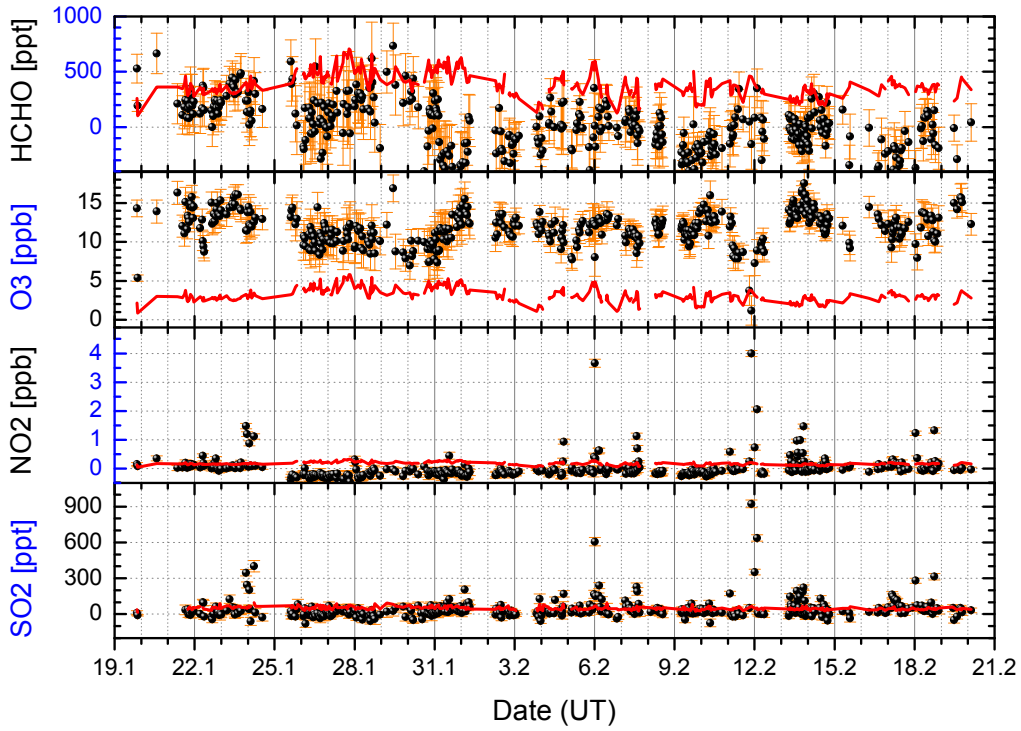

Figure 4.47: Mixing ratios of NO_2, SO_2, HCHO and ozone measured with DOAS recorded from 21.01-21.02.2002. Note that NO2 data was taken from measurements in the visible wavelength region with significantly higher scanning frequency.

SO_2). However, several spikes of both compounds are present in the measured time series (Fig. 4.3.3). As the chemical lifetime of NO_x is only a few days, long range transport from continental sources can not account for measured levels. The simultaneous appearance, short duration and, for remote conditions, unusual strength of NO_2 and SO_2 accumulation events indicate the presence of local pollution sources. The most likely source are the power generators of the base at Port-aux-Français at roughly 100 m distance northeast of the measurement building and the ships "Curieuse" and "Aventure" which occasionally anchored and operated in front of the harbor few meters southeast.
In spite of sporadic NO_2 blasts no formation of nitrate radicals NO_3 was observed. The measured mixing ratios remained below the detection limit of 2 ppt over the whole campaign period.

Ozone and CO Ozone concentrations are available from the longpath DOAS instrument and a commercial O3 Monitor (LSCE Group). Excluding single values assignable to instrument failures, both time series agree fairly well within errors. O_3 ranged within 1.2 and 17.6 ppb (average 11.9 ppb), thus notably below levels observed at Crete and the Hudson Bay (sections 4.1 and 4.2).
A large set of previous measurements, all over the southern hemisphere reaching from Antarctica [Oltmans and Levy II 1994] over mid-latitudes (Cape Grim 41°S [Ayers et al. 1995], Amsterdam Island 37°S [Gros et al. 1998]) up to tropical regions(Samoa 14°S [Oltmans and Levy II 1994]) report a seasonal cycle in ozone mixing ratios with a pronounced summer

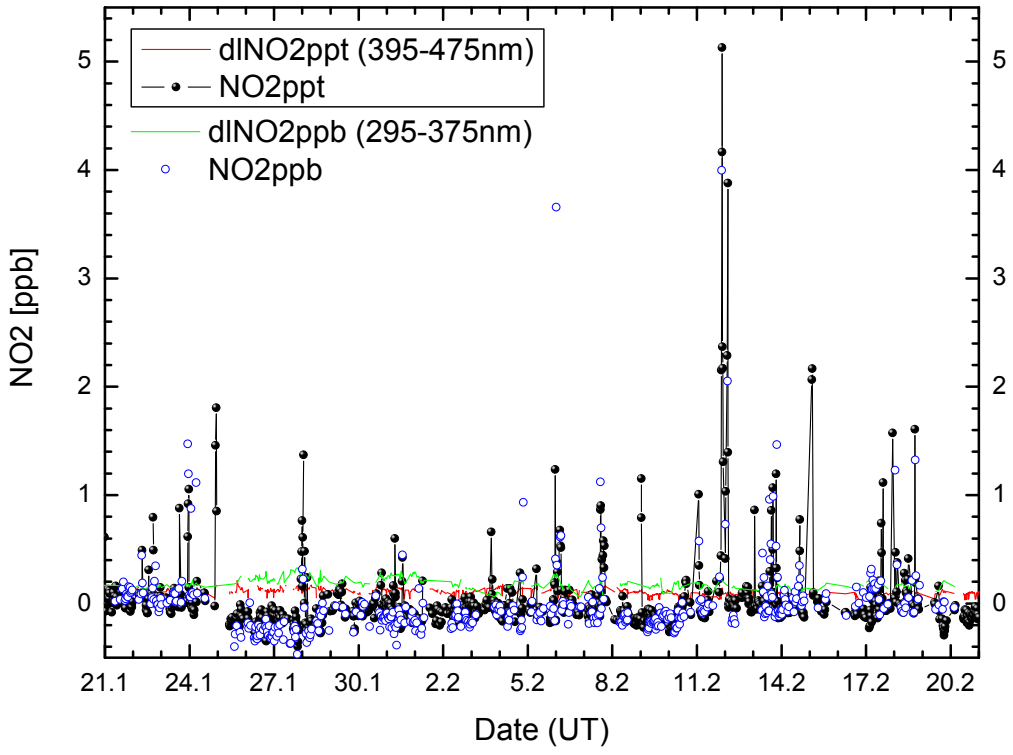

Figure 4.48: Comparison of NO2 results for the UV and VISIBLE wavelength region. Note that time resolution in the VIS is about three times narrower(average 34min for VIS, 100min for UV).

minimum (around 15 ppb in January) and a winter maximum (around 30 ppb in July). It has been suggested that this O_3 seasonal variation mainly reflects increased contribution of stratospheric O_3 during winter [Roelofs and Lelieveld 1997] and enhancement of the photochemical destruction of ozone during summer in NO_x-poor air [Ayers et al. 1992].
According to the low mixing ratios of nitrogen compounds measured with DOAS (NO_2,NO_3, HONO) and assuming that levels of NO are commonly up to one order of magnitude below those of NO_2, total NO_x (=NO+NO_2) levels should commonly remain below 50-100 ppt. In such "low NO_x" environments, carbon monoxide(CO) and hydrocarbons will contribute to the destruction of ozone:

$$\mathrm{CO + OH \rightarrow CO_2 + H} \tag{4.1a}$$

$$\mathrm{H + O_2 \xrightarrow{M} HO_2} \tag{4.1b}$$

$$\mathrm{HO_2 + O_3 \rightarrow OH + 2\ O_2} \tag{4.1c}$$

$$\mathrm{CO + O_3 \rightarrow CO_2 + O_2}$$

However, photochemical destruction processes are insufficient to explain observed variations of the ozone mixing ratios. The average diurnal (photochemically induced) variation of O_3 is less than 1 ppb (section 5.4), far below changes of more than 5 ppb measured on a 1-2 day scale. The impact of the numerous local pollution events is difficult to quantify due to fast transport processes and unstable meteorology.
A particulary strong ozone depletion event was observed on 12th February, when O_3 dropped from 15 ppb to nearly zero within 24 hours. As the lowest concentration was observed about 1 hour after local midnight, other than photochemical sinks have to be considered for this event. Simultaneously to the ozone depletion the strongest local pollution event was observed ($NO_2 > 5$ ppb and $SO_2 > 900$ ppb). Considering simultaneous NO emissions of 100-200 ppt (25-50 times lower than NO_2), the lifetime of ozone molecules would be reduced to 2.5-5 hours. Another interesting point is that, although halogen oxide levels remained fairly low throughout the campaign, the maximum level of BrO (2 ppt) was observed at the end of the ozone depletion period. The recorded data is insufficient to constrain any link between halogens and ozone. However, the frequent observation of halogen oxides throughout the campaign period requires the presence of a continuous background of halogen precursors. It is conceivable that photochemical destruction of ozone in the Indian ocean is enhanced by reaction with halogen atoms at concentrations around 1 ppt.

4.3.4 Measurements of project partners

The entire DMS-DMSO-MSA dataset obtained during the campaign at Kerguelen is presented in Figure 4.3.4. Unlike observations of [Sciare et al. 2001] at Amsterdam Island (37°S 77°E) for similar conditions (i.e. pristine summertime Indian ocean), the variations of DMS (and DMSO) at Kerguelen do not show an evident correlation to the wind speed or direction(Figure 4.3.4). Different lifetime of DMS between Amsterdam and Kerguelen Islands together with different oceanic sources can induce a more pronounced atmospheric transport of DMS at Kerguelen and explain this difference. Due to the location further

Table 4.7: Measurements of project partners at Kerguelen 2002(LSCE-CNRS, ECPL-Crete)

Chemical component	Measurement technique	Timeframe(UT)	Time resolution [minutes]	Concentration range[ppt] (Mean)	
DMS		19.01-21.02.2002	60	9.5–887.2	209.5
DMSO		21.01-21.02.2002	3	0.5–12.8	3.4
MSA				0.2–56.3	9.5
CO		17.01-21.02.2002	4	(30–85) ppb	40.3
C2H4		21.01-21.02.2002	30	33–660	131.5
isoC4H8		21.01-21.02.2002		3–270	44.3

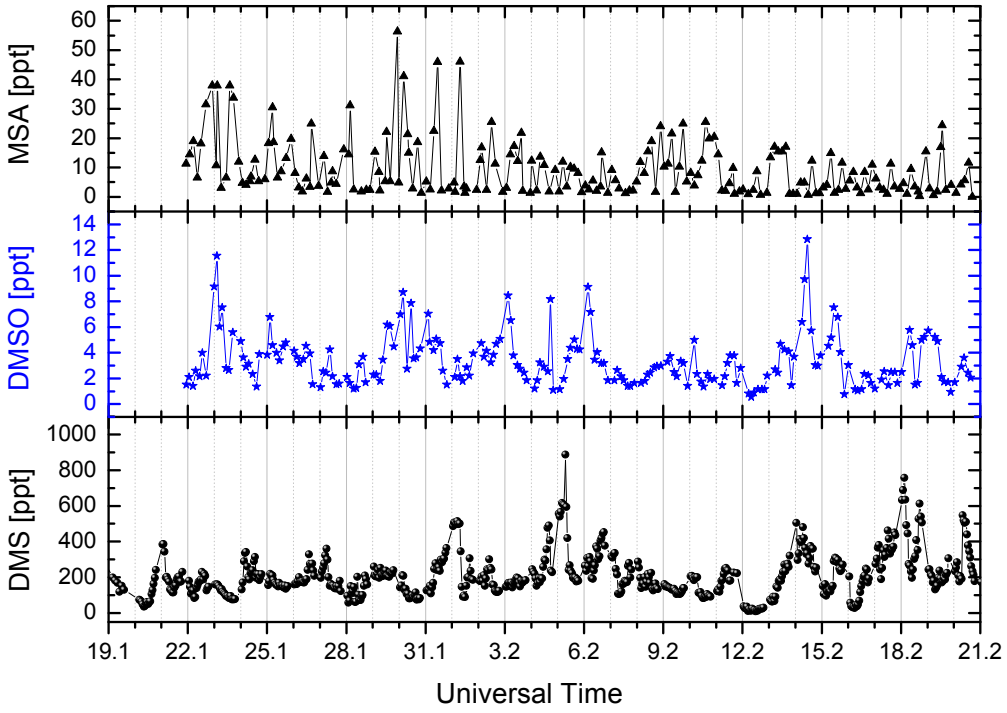

Figure 4.49: Gas phase concentrations of DMS, DMSO and MSA measured from 22.01 to 21.02.2002 at Kerguelen.

south (Kerguelen 49°S 69°E) the estimated zonal mean 24-hour average OH at Kerguelen is below half the concentration at Amsterdam ($14 \times 10^5 molec.cm^{-3}$ vs. $6 \times 10^5 moleculescm^{-3}$ [von Kuhlmann 2001]). Taking additionally into account the ambient temperature difference between both islands (about 8 °C in January) the average lifetime of DMS against oxidation via OH is about 2 days at Kerguelen and 1 day at Amsterdam.

During the cruise from La Reunion to Kerguelen Island in the first and second week of January, seawater samples were taken to determine the spatial distribution of DMSp. In 3 hour intervals the concentration of both, total and dissolved DMSp was determined allowing a statement about the dilution rate of this compound. As shown in Figure 4.52 the total concentration of DMSp in seawater was rather low at La Reunion and became quite important around Amsterdam Island increasing to maximum levels within the first half of the crossing towards Kerguelen (40–45°S) to decrease slightly again further south. Apparently there is no mayor link to Chlorophyll A emissions presented in section 4.3.2. However, the drop of

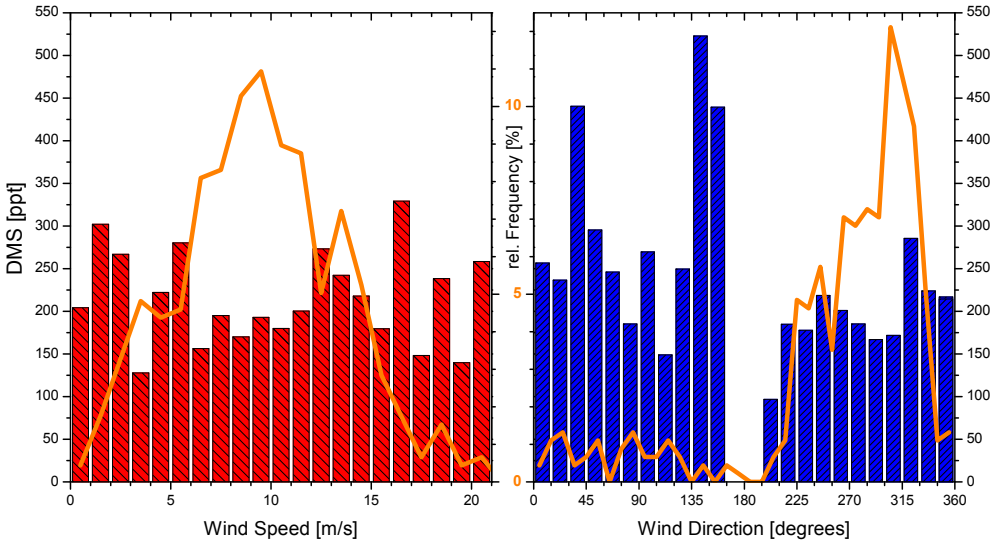

Figure 4.50: Statistical distribution of DMS concentrations measured from 22.01 to 21.02.2000 against Wind speed and direction. Apparently atmospheric DMS concentrations are nearly independent on wind speed. The high variability of DMS levels in the eastern sector is a consequence of poor statistics due to the low relative frequency of measurements(denoted by fat orange lines). A similar argumentation could apply to the wind speed dependency due to the overweight of the 9-11 m/s range.

the sea surface temperature along the cruise reduces distinctly the percentage of dissolved DMSp, which is above 60% in the proximity of La Reunion and decreases below 30% in the 20 °C colder waters at Kerguelen (Figure 4.53).
Following equations given in section 2.3.1, the variation of sea surface temperatures(SST) from 18.8 °C at Amsterdam to 4.9 °C at Kerguelen (Fig. 4.52) is expected to reduce the sea to air flux of DMS by a factor of 1.5 (assuming identical seawater DMSp concentrations). On the other hand, the sea surface temperature plays a minor role when considering that the average wind speed measured at Kerguelen (9 m/s) in January/February 2002 is about 3 m/s higher than those at Amsterdam Island for the same period. Due to the quadratic dependence on wind speed, the overall DMS flux would be 2 times larger at Kerguelen. Taking average meteorological conditions described above and dissolved DMSp concentrations of 67.3 nM and 25 nM for Amsterdam and Kerguelen Island respectively, the resulting DMS flux is 14.6 and 8.2 $\mu molm^2day$. The 1.8 times greater flux at Amsterdam is in agreement with atmospheric measurements, as average gaseous DMS mixing ratios for the period from 22.01-21.02.2002 amount to 366 ppt (AMS) and 211 ppt (KER) respectively, i.e. 1.7 more at Amsterdam (Table 4.8).

Unlike observations in Crete (section 4.1.4, the factors controlling DMS levels in the austral ocean seem to be more related to the source strength and location as the concentration of radical species was too low to account for observed DMS concentration changes.

Carbon monoxide and hydrocarbons (gas phase) The variation of carbon monoxide and several non methane hydrocarbons (NMHC's) is reported in Figure 4.3.4. The level of CO was typically in the range of 30-40 ppb and presented a very regular diurnal varia-

Table 4.8: Comparison of parameters defining the sea-to-air flux of DMSp and measured DMS concentrations at Kerguelen(KER) and Amsterdam(AMS) Islands.

	Windspeed	SST	DMSP [nM]		Sea to air flux[$\mu molm^2day$]		Mean DMS
	[m/s]	[°C]	dissolved	total	dissolved	total	[ppt]
AMS	6	18.8	67.3	120.4	14.6		366
KER	9	4.9	25	69.0	8.2		211

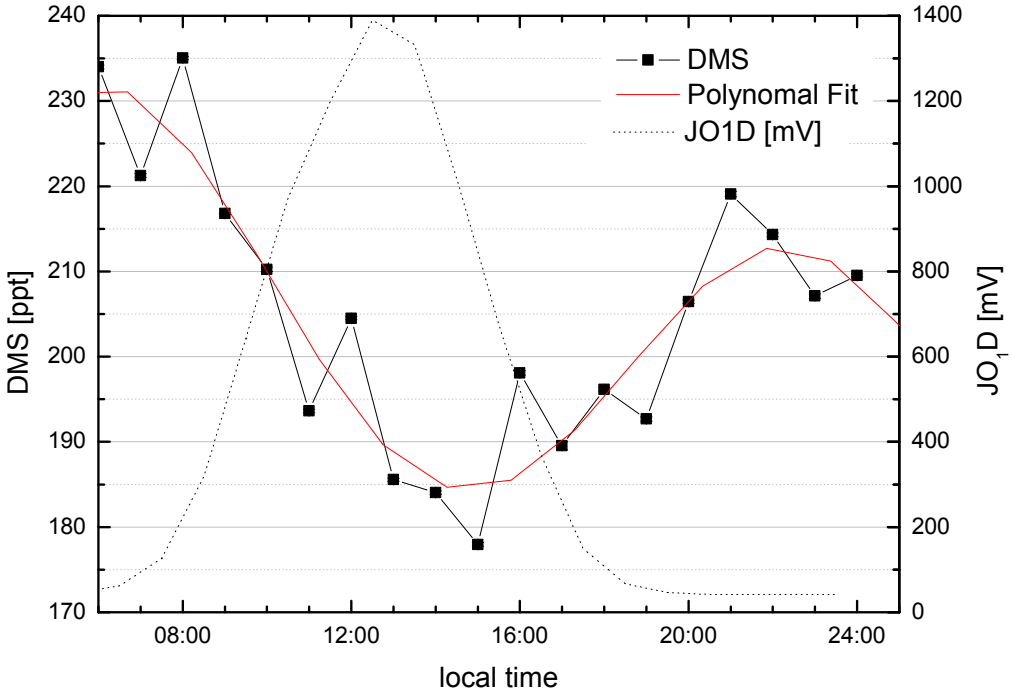

Figure 4.51: Average diurnal variation of the DMS mixing ratio using the available dataset from 17.01-21.02.2002.

tion with maxima around 16 hours local time. This is in agreement with background levels previously observed at similar latitudes. For non methane hydrocarbons and particularly for alkenes, significant mixing ratios of the order of 10 to 200 ppt were observed, all featuring a very regular diurnal variability reaching maximum mixing ratios in the early afternoon (Figure 4.3.4). A remarkable exception represents the period extending from 17-20 February 2002 where CO and NMHC levels rise notably (CO reaching up to 60-70 ppb).
Knowing the processes of alkene formation in the marine environment by photodegradation of dissolved organic matter in the sea surface, the variations of NMHC concentrations can be perfectly explained by the influence of UV radiation at the sea surface, and subsequent outgassing of alkenes into the atmosphere. The comparison of the diurnal variation of alkenes and UV radiation ($J(O^{1D})$ actinic flux) shows a very clear correlation, which suggests that the dominant source of alkenes is of photochemical origin. In spite of the high seawater supersaturation in the summer months, marine sources, i.e. sea-to-air flux of CO have a minor impact on the the marine boundary layer CO burden [Bates et al. 1995]. Instead, atmospheric CO levels at Kerguelen are most likely controlled by oxidation of naturally emitted methane

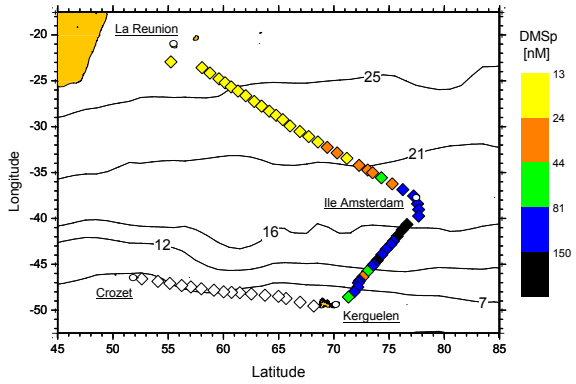

Figure 4.52: Total dimethylsulfoniopropionate(DMSp) concentration in seawater measured from 05.-13.01.2002 on the cruise from La Reunion to Kerguelen Islands on board the research vessel "Marion Dufresne" by J.Sciare and colleagues from LSCE and ECPL research groups. The labelled horizontal curves expose the sea surface temperature in degrees Celsius (Reynolds SST dataset, PODAAC Product 119).

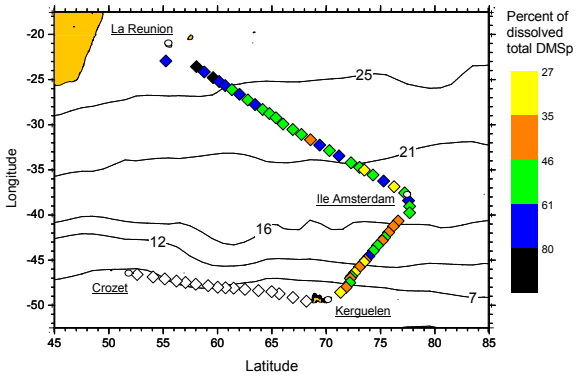

Figure 4.53: Variation of the percentage of dissolved DMSp. The dilution rate follows a distinct negative trend towards lower temperatures.

and NMHC and occasional input from continental sources. As a matter of fact, during the exceptional period from 17-20 February 2002, trajectory results state a dominant input of air masses reaching Kerguelen after travelling several days at latitudes much further north (even below 30°S). Continental sources may have added CO and NMHC to these air masses which remained few meters above sea level during the whole 10–day simulation period and reached Kerguelen in the order of 3-4 days after passing potentially polluted sectors(Figure 4.55).

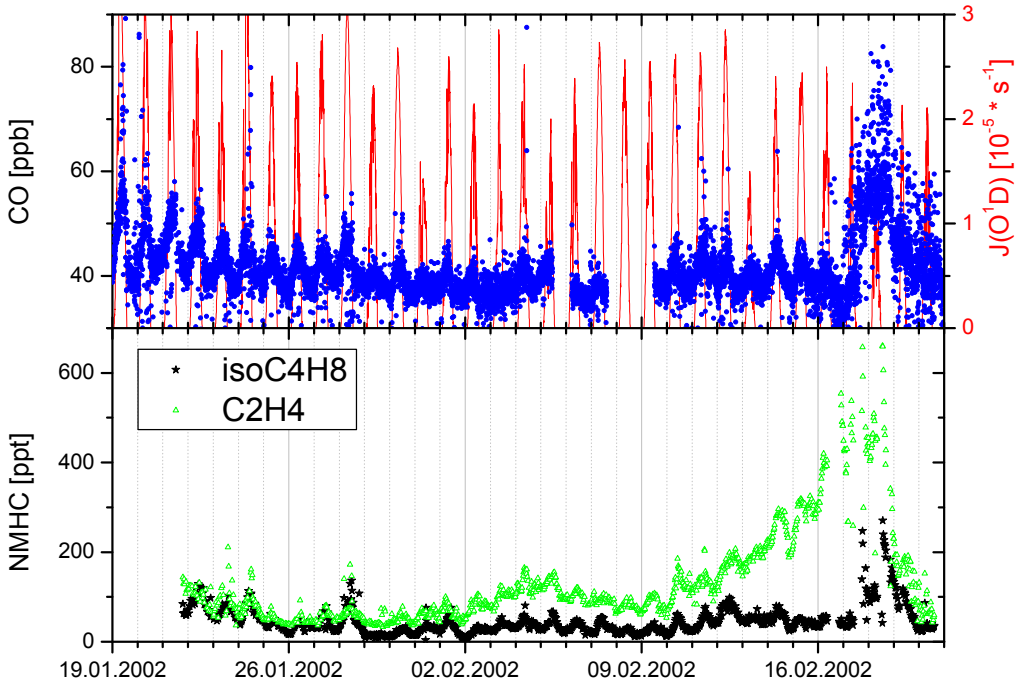

Figure 4.54: Variation of carbon monoxide and non-methane hydrocarbons along the measurement period from 19.01-21.02.2002 on Kerguelen Islands.

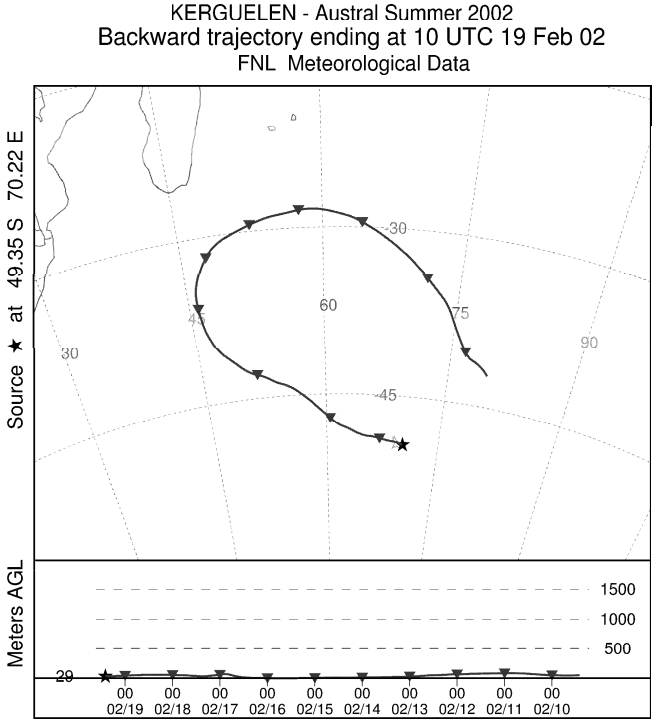

Figure 4.55: 10 day backward trajectory result (using the Hysplit model) ending at Kerugelen on 19th February at 10 hours universal time.

Chapter 5

Analysis of Results and Discussion

5.1 The oxidation pathways of DMS for average conditions in Crete

To elucidate the implication of trace gases in the oxidation chain of Dimethylsulphide a suitable method is to follow the reaction steps depicted in Figure 2.11. The rate constants given in Table 2.12 allow an estimation of the lifetime of DMS and the intermediate products until the formation of Methane sulphonic acid (MSA) in the end. For gas phase reactions this calculation is rather simple as in addition to the rate constant only the concentration of the reaction partner(trace gas) is needed:

$$\tau(species) \ = \ ([tracegas] * k)^{-1} \tag{5.1}$$

For heterogeneous reactions the estimation of lifetimes less simple, as one requires to know the concentration of the considered trace gas in the aqueous phase. As already described in section 2.3.2.4 the mass transfer in to the aqueous phase is highly dependent on the trace gas species and the composition of the aerosol. When assuming conditions of gas–liquid equilibrium, i.e. that the species is well mixed in the aqueous phase, the fractionation between the bulk gas and the aqueous phase is given by the Henry's law solubility constant H(T) [Jacob 2000]:

$$H(T) \ = \ [X(aq)]/P_x \tag{5.2}$$

where P_x is the partial pressure of X in the gas phase. The equilibrium fractionation f of a species between the gas and the aqueous phase is:

$$f = [X(aq)]/[X(g)] \ = \ H(T) * L * R * T \tag{5.3}$$

where H is the Henrys law solubility constant (in $[M\ atm^{-1}]$), L the liquid water content (cm^3/cm^3), R the gas constant ($0.082\ dm^3 atm K^{-1} mol^{-1}$) and T the temperature (in Kelvin). The gas phase concentration has to be converted from the common unit $molecules/cm^3$ to mol/l.

To concentration of species X in the aqueous phase can then be obtained by solving equation 5.3 to obtain [X(g)]. Over the range of typical values of L in cloud $10^{-6} - -10^{-8}$ a

species is dominantly in the gas phase if $H(T) < 10^4 Matm^{-1}$ and dominantly in the cloud-water $H(T) > 10^6 Matm^{-1}$. For a non-cloud aerosol (L$< 10^{-9} cm^3/cm^3$), only species with a very high Henry coefficient as HNO_3 ($H = 4.3 \times 10^{11}$) still partitions preferentially in the aqueous phase.

Although the above described equilibrium fractionation applies to most species of interest, this is not true for short-lived species as the hydroxyl radical OH with lifetimes below one second as no equilibrium can be reached before destruction. Other species as ozone and NO_3 have too low solubility to be well mixed in the aqueous phase before being expelled again out of the aerosol. For these species the mass transfer limitation produces an accumulation at the surface of the aerosol. If the Henry's Law equilibrium is not achieved, chemical rate calculations require that concentration gradients within the droplets are taken into account. Another point is that, depending on the trace gas species, the Henry constants given in Literature show a significant variability [Sander et al. 2003; Sander 1999]. As an example, the uncertainty range for the Henry constant of O_3 in pure water according to Sander et al. [2003] is in the range between 50%–100%, whereas for DMS an uncertainty factor between 10–100 is given.

As notably for OH and O_3 a determination of aqueous phase concentrations is not possible without further knowledge about aerosol characteristics, typical concentrations of H_2O_2 and OH radicals and ozone, reported for the liquid phase in clouds are taken [Herrmann et al. 2000; Lelieveld and Crutzen 1991; Jacob 1986]. Outside of clouds a 300 times smaller value is taken according to the decrease of the liquid water content from the average in clouds $3 \times 10^{-7} cm^3/cm^3$ to a non-cloud aerosol ($L < 10^{-9} cm^3/cm^3$). In Table 5.1 mean concentrations of trace gases as measured with DOAS, chemical amplifier and other instruments as indicated are given. The values for OH are taken from measurements reported by [Berresheim et al. 2003] at Finokalia in Summer 2001. Concentrations of other halogen species and H_2O_2 not retrievable from literature have been estimated using the most recent version 7.0 of the chemical box model MOCCA(Model Of Chemistry Considering Aerosols) kindly provided by Jana Moldanová and first presented in Sander and Crutzen [1996, Vogt et al. [1996]. Recent results using this version of MOCCA have been presented in Pszenny et al. [2004]. The model was constrained by averaged meteorological parameters and measured trace gas mixing ratios as well as photolysis rates of NO_2, NO_3 and ozone (JO1D) obtained during the campaign period on Crete. The applicability of the MOCCA to simulate conditions in Crete, and in particular for halogens, has been shown before [Hönninger 2002]. Figure 5.1 and Figure 5.1 represent the fate of the DMS oxidation chain in Crete during day and night respectively. Both Figures are based on the complete reaction scheme depicted in Figure 2.11, but only the most effective reactions for each chain step are shown. During daytime, the OH radical initiates DMS oxidation preferably on the abstraction path (DMS Lifetime 8 hours) as a consequence of the high ambient temperatures in prevailing in Crete(section 2.3.2.1). As no cloud formation was observed during the entire campaign period (section 4.1.2) the average OH and O3 concentrations in the aqueous phase as given in Table 5.1 have been divided by a factor 300 as indicated before. Nevertheless, the aqueous phase concentration of O_3 appears to be largely overestimated as the aqueous phase reaction of ozone with DMS would

Table 5.1: Average trace gas concentrations at night (20-06 hours Local time) and day, derived from measurements, taken from literature or estimated using the MOCCA Model.

Trace gas	Mean Concentration $[molec./cm^3]$		Source
	Night (20-06 LT)	Day	
BrO	$< 2 \times 10^7$	$< 2 \times 10^7$	DOAS
HCHO	2.9×10^{10}	2.8×10^{10}	
HONO	3.9×10^8	2.4×10^6	
IO	$< 1.3 \times 10^7$	$< 1.3 \times 10^7$	
NO2	1.3×10^{10}	9.6×10^9	
NO3	4.7×10^8	$< 4.0 \times 10^7$	
O3	1.3×10^{12}	1.3×10^{12}	
SO2	2.2×10^{10}	2.4×10^{10}	
ROx	3.2×10^6	6.0×10^8	Chem. Ampl.
HO2	2/3 ROx		
RO2	1/3 ROx		
DMS	1.1×10^9	1.5×10^9	GC
DMSO	7.1×10^7	7.6×10^7	Mist chamber
MSA	1.2×10^8	1.5×10^8	IC
CO	2.9×10^{12}	2.9×10^{12}	Monitor
NO	0	1.6×10^9	Monitor
Br	3.7	1.9×10^5	MOCCA
Cl	64	2.1×10^4	
ClO	1.3×10^6	1.2×10^7	
H2O2	3.0×10^{10}	3.0×10^{10}	
OH	7.7×10^2	9.3×10^6	BER03
	Mean diurnal Concentration [M]*)		
$H_2O_2(aq)$	$10 - -200 \times 10^{-6}$		a)
OH(aq)	$5 - -50 \times 10^{-14}$		a)
$O_3(aq)$	$5 - -50 \times 10^{-14}$		a)

[Herrmann et al. 2000; Lelieveld and Crutzen 1991; Jacob 1986]
[Berresheim et al. 2003]
*) divided by 300 if no clouds present

produce significant amounts of DMSO all over the day. This is not realistic in consideration of the quite low levels of DMSO observed (below 4 ppt on average). Particulary at night DMSO levels would be significantly enhanced due to the absence of sinks for DMSO as the OH radical. Due to extremely dry environment it is quite likely that multiphase chemistry can only occur right at the sea surface or within the first hours of night when condensation and slight fog formation was occasionaly observed.

At nighttime concentration levels observed, the nitrate radical outranges by far the efficiency achieved by the OH radical during day regarding depletion of DMS. During night the oxidation of DMS should occur exclusively along the abstraction path. As a consequence of the high levels of O_3 attained in Crete, the reaction of CH_3SO with ozone in addition to the thermal decay and 3rd body reaction of CH_3SO_2 and CH_3SO_3 clearly inhibit MSA formation both during day and night. During day MSA will be formed preferentially by the relatively fast reaction of CH_3SO_3 with the hydroperoxy radical HO_2 (Lifetime 50 s), whereas at night the formation rate is several orders of magnitude lower and may not even occur as CH_3SO_2 decomposes readily and contributes rather to sulfuric acid formation. A contrary effect is induced by NO and NO_2 which should enhance the yield of MSA formation notably during day.

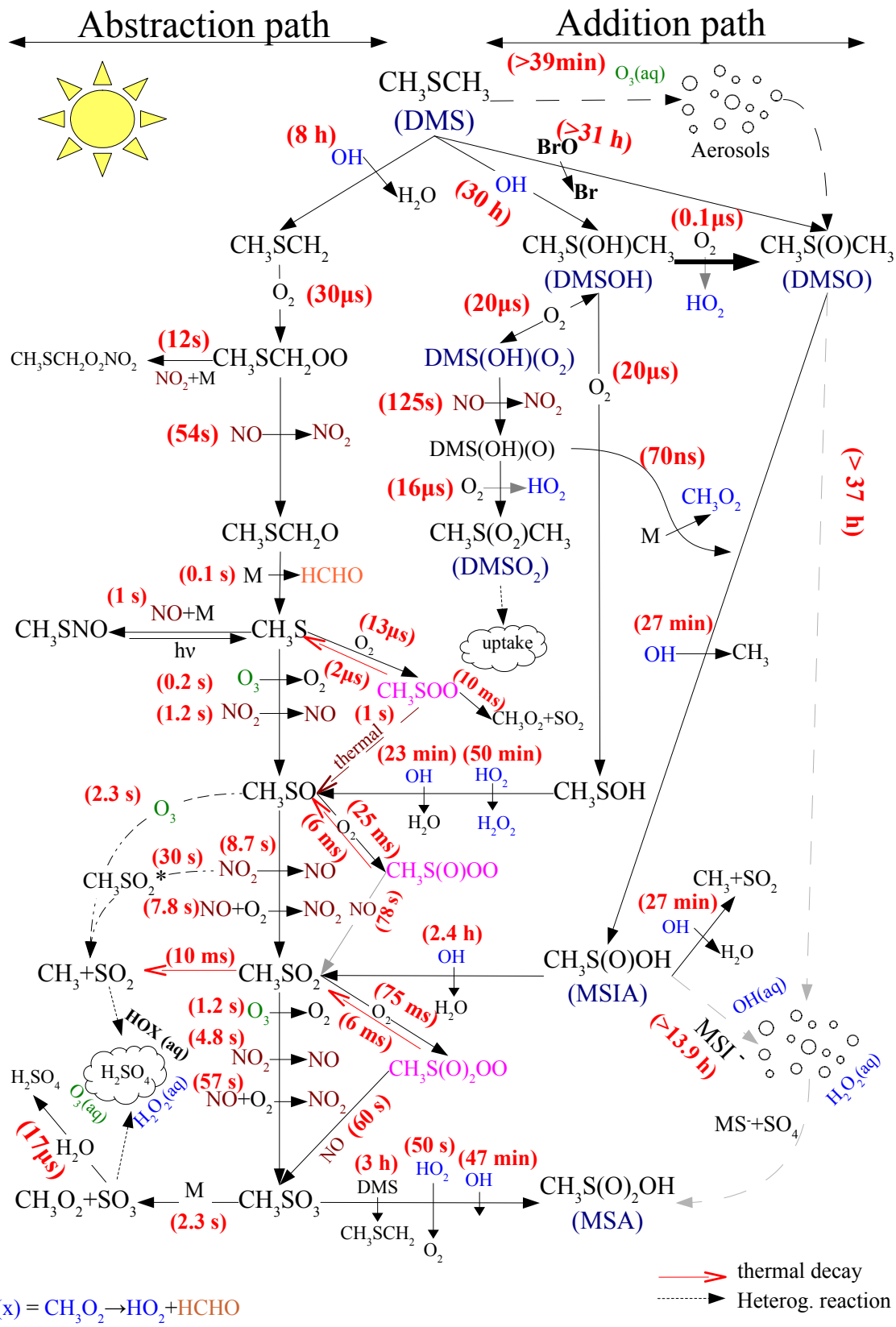

Figure 5.1: Oxidation chain of Dimethylsulphide for average daytime mixing ratios established during the measurement campaign at Crete during Juli-August 2000.

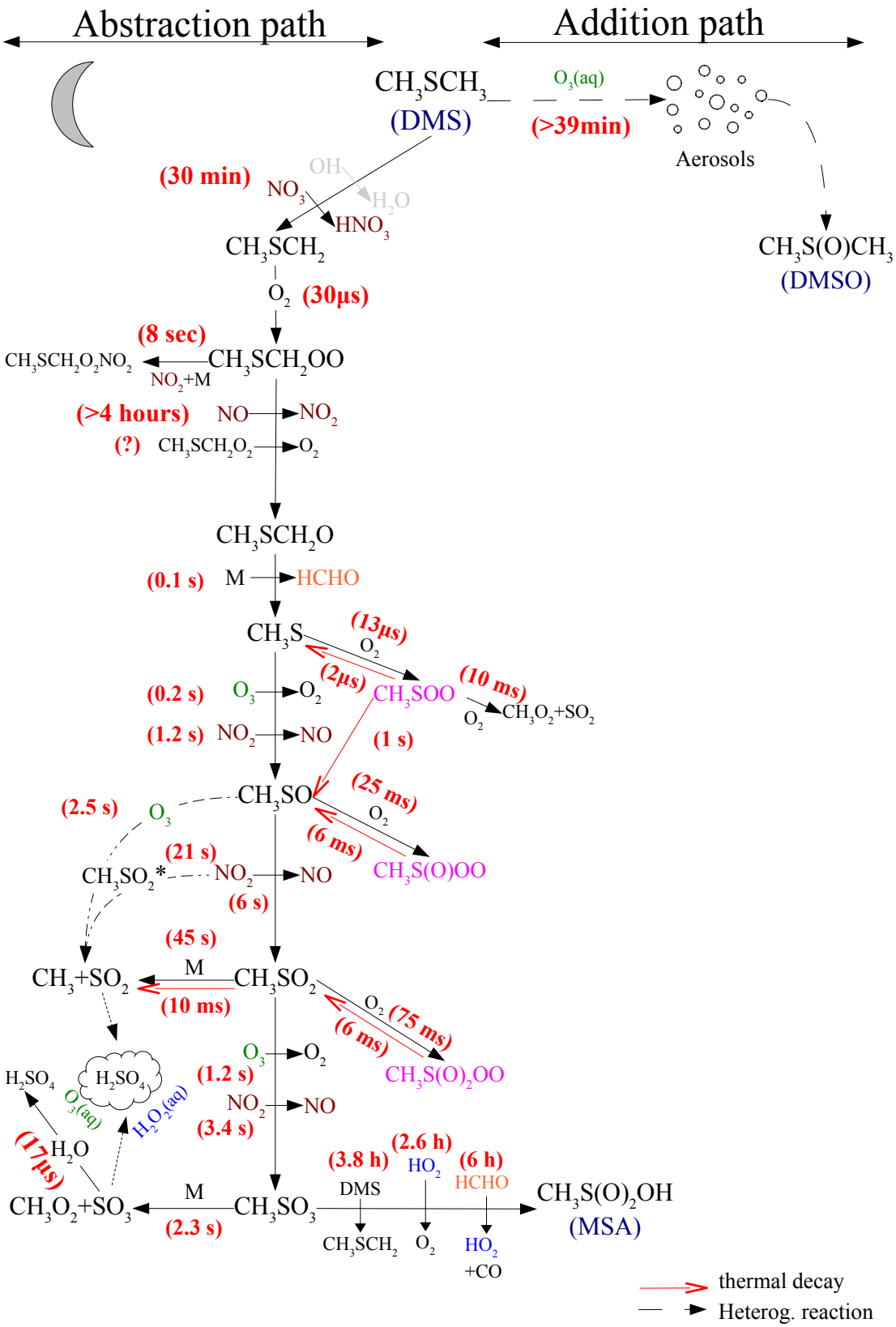

Figure 5.2: Oxidation chain of Dimethylsulphide during night for average mixing ratios established during the measurement campaign at Crete (Juli-August 2000).

5.2 Analysis with a focus on NO_3

5.2.1 NO_3 lifetime

The most common method to determine the relative importance of indirect or direct depletion of NO_3 is a correlation plot of its lifetime, $\tau(NO_3)$, against the concentration of its precursor NO_2. Since the island of Crete is at several hundred kilometers distance from the main land, transport of pollutants to the measurement site takes several hours. For average campaign conditions (301 K and 0.5 $ppbNO_2$) the lifetime of NO_3 against conversion to N_2O_5 is 71 seconds, while the lifetime of N_2O_5 before thermal decay is as short as 13 s. As under this conditions an equilibrium of NO_3 and N_2O_5 will be attained within few minutes, the chemical system is assumed to have reached steady state. Then the total degradation frequency f_{total} of NO_3 can be derived from its measured mixing ratio and correspondent production rate P_{NO3}(using equation 2.28):

$$\frac{d}{dt}[NO_3] = P_{NO3} - [NO_3]\, f_{total} = 0 \tag{5.4}$$

$$f_{total} = \frac{[NO_2][O_3]k_{2.27}(T)}{[NO_3]} = \frac{1}{\tau(NO_3)} \tag{5.5}$$

The inverse of the degradation frequency, $\tau(NO_3)$, can be associated with the $1/e$ lifetime of the nitrate radical. Because of the thermal equilibrium (2.38) between NO_3 and N_2O_5, any loss processes of dinitrous pentoxide (combined to the total degradation frequency $f_{N2O5-total}$) are indirect sinks of NO_3. The corresponding indirect degradation frequency f_{indir} is given by

$$f_{indir} = K_{eq}[NO_2]f_{N2O5-total} \tag{5.6}$$

The concentrations of NO_3 and N_2O_5 can be related using a simplified reaction scheme consisting of the NO_3 production reaction (2.27), the thermal equilibrium (2.38) between NO_3 and N_2O_5 as well as definitions of the total degradation frequencies of both compounds:

$$k_{2.27}[NO_2][O_3] + k_{2.36}[N_2O_5] = f_{dir}[NO_3] + k_{2.37}[NO_2][NO_3] \tag{5.7}$$

$$k_{2.37}[NO_2][NO_3] = f_{N2O5-total}[N_2O_5] + k_{2.36}[N_2O_5] \tag{5.8}$$

Comparison of the latter to equation (2.38), allows to infer an "effective steady state" constant K_{SS} among all three nitrate compounds,

$$K_{SS} = k_{2.37}/(k_{2.36} + f_{N2O5-total}) \tag{5.9}$$

which will decrease slightly below the thermodynamic equilibrium level in the presence of N_2O_5 sinks. Equations (5.7) and (5.8) can be combined to

$$[NO_3] = [NO_2][O_3]k_{2.27}(f_{dir} + [NO_2]k_{2.37}\frac{f_{N2O5-total}}{k_{2.36}+f_{N2O5-total}})^{-1} \tag{5.10}$$

The term simplifies significantly when indirect loss via N_2O_5 can be neglected(i.e. $f_{N2O5-total} \approx 0$). Inserting (5.5) will then lead to:

$$\frac{1}{\tau(NO_3)} = f_{dir} \tag{5.11}$$

In the case of negligible direct sinks ($f_{dir} = 0$) an reciprocal relationship of $\tau(NO3)$ and NO_2 is obtained from equations (5.10) and (5.5):

$$\frac{1}{\tau(NO_3)} = [NO_2]k_{2.37}\frac{f_{N_2O_5-total}}{k_{2.36}+f_{N2O5-total}} \tag{5.12}$$

It has to be remarked though, that the steady state assumption may not apply for local pollution events.

5.2.2 Relative contribution of NO_3 sinks

Equations (5.11) and (5.12) give us a criterium to determine the importance of indirect sinks by simply plotting the lifetime of NO_3 against the contemporaneous NO_2 mixing ratio as shown in Figure 5.3. According to equation (5.12) the presence of indirect sinks would

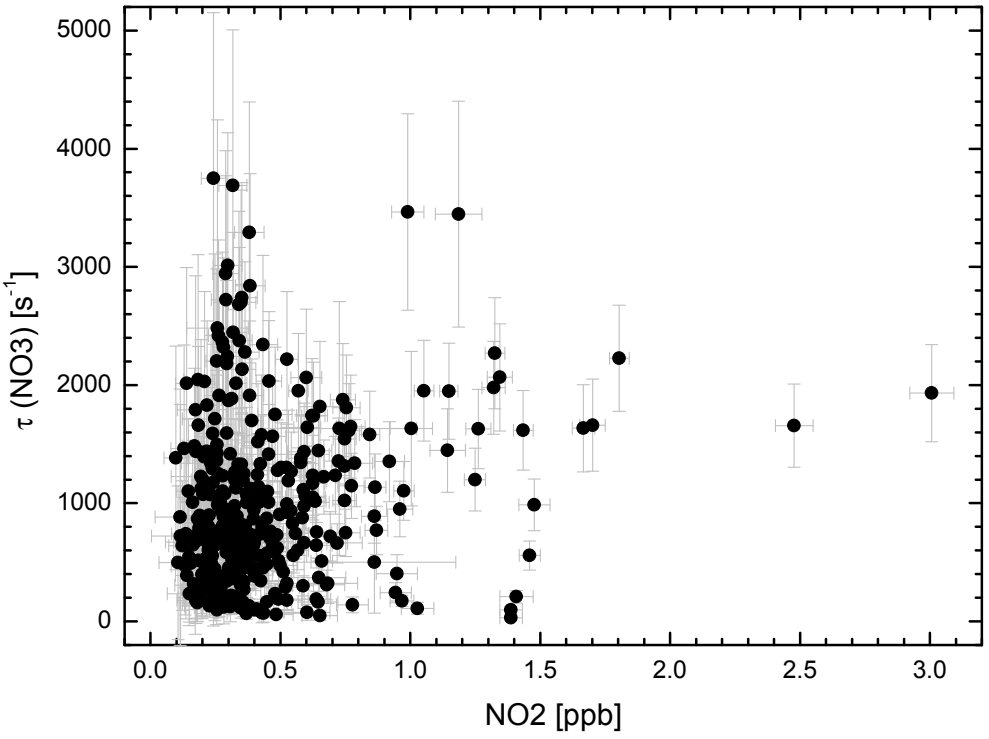

Figure 5.3: The NO3-lifetime as a function of NO2 mixing ratio. No evident correlation has been observed, which is an indicator that the importance of indirect sinks is rather small or even negligible.

lead to an inverse proportionality of $\tau(NO_3)$ and the NO_2 concentration. As no consistent correlation between both terms has been observed over the whole campaign period, indirect sinks via N_2O_5 are assumed to play a minor role in the depletion of NO_3. In the case of negligible indirect sinks the degradation frequency is given by (5.11). Combining equation (5.11) with (5.5) leads to

$$f_{dir} = \frac{1}{\tau(NO3)} = \frac{[NO_2][O_3]k_{2.27}}{[NO_3]} = \frac{PNO3}{[NO_3]} \tag{5.13}$$

As in this case the direct degradation frequency will not be zero, the production rate and concentration of NO_3 must be linearly related. This evidence is clearly acknowledged by the measured data as shown in Figure 5.4.

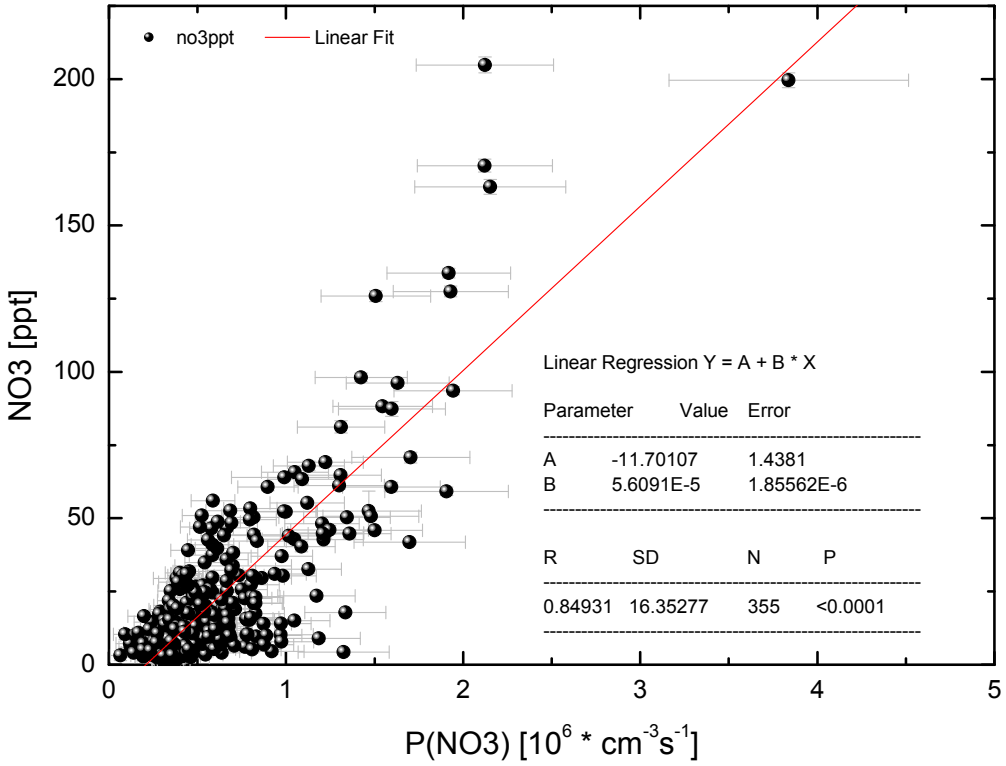

Figure 5.4: NO_3 mixing ratio as a function of its production rate. Only nighttime values over the detection limit have been considered for the fit. The linear relationship gives evidence that direct sinks must be the dominant loss mechanism for NO_3 at Finokalia.

5.2.2.1 Gas phase reactions with DMS and other VOCs

As discussed previously in section 2.2.2 among the numerous degradation mechanisms of NO_3, gas–phase reactions with NMHC's tend to be the major loss mechanism. Dimethylsulphide, at the important levels measured in the area (section 4.1.4) is surely a reaction partner to be accounted for. A comparison of measured DMS and NO_3 concentrations shows a striking anticorrelation at relatively high mixing ratios(5.5). However, this relationship is less evident for the median concentration range. Therefore rapid reactions between DMS and NO_3 are expected to influence significantly the lifetime of both compounds.

The degradation frequency of NO_3 due to the reaction with DMS is given by the concentration of DMS and the rate constant of reaction (2.181a).

$$f_{NO3-DMS} = [DMS] * k_{2.181a} \tag{5.14}$$

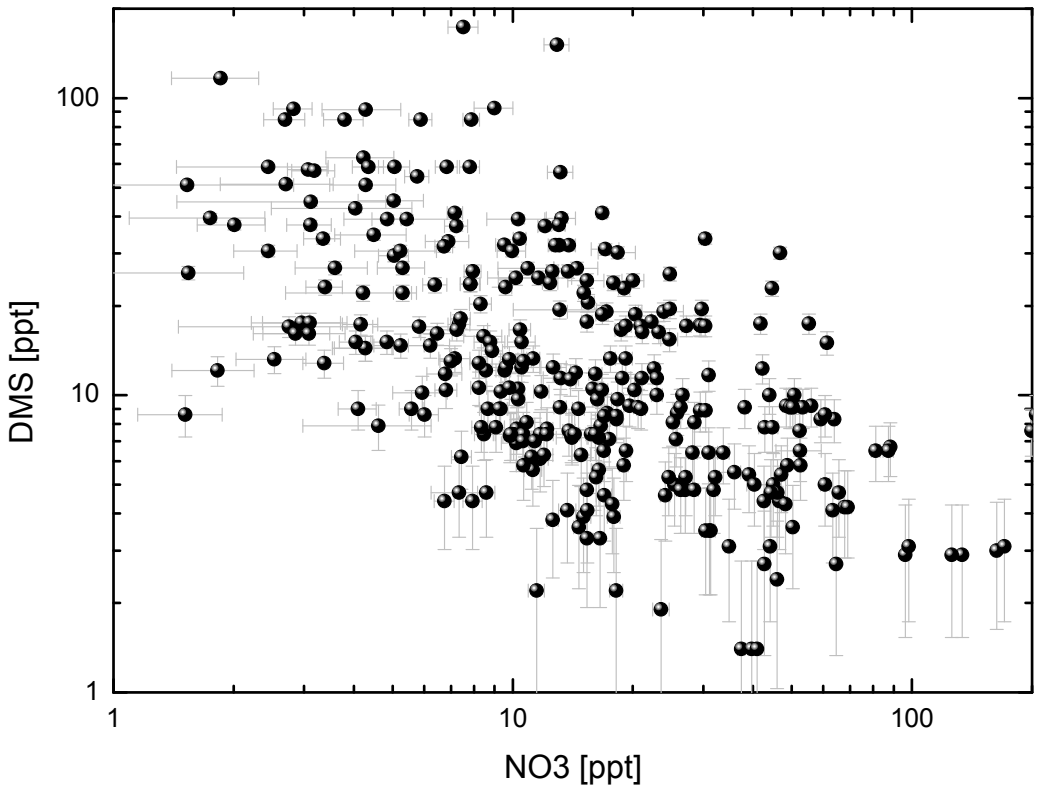

Figure 5.5: The concentration of DMS is plotted against NO_3. An inverse relationship of both compounds can be observed at higher mixing ratios, which is more diffuse in the median concentration range.

To quantify the importance of the DMS sink the resulting DMS initiated degradation frequency must be compared to the total degradation frequency of the nitrate radical as given in (5.5). This was done in Figure 5.6 by applying a linear fit on the data. The gradient of the fit result tells the relative importance of the DMS oxidation path which was found to be as high as 60.5%. Although this results, it is quite important to remark that there are obviously other factors controlling the NO_3–DMS interaction. Due to its localized sources on land, the origin of air masses should strongly define levels of NO_3. This is not true for DMS as the source regions are homogeneously distributed around the island. Higher wind speeds should increase sea-air exchange but enhance long range transport as well. Highest DMS ratios have been observed above 8 m/s, although no linear increase of DMS with wind speed was observed. Another point is that the marine boundary layer exhibits a very stable stratification in the summertime Mediterranean ([Berresheim et al. 2003] and trajectory results done for this study). The inhibition of vertical mixing limits the height of the boundary layer and thus vertical distribution. It is conceivable that the largest fraction of DMS remains near its source right above the sea surface. The distribution may be largely different

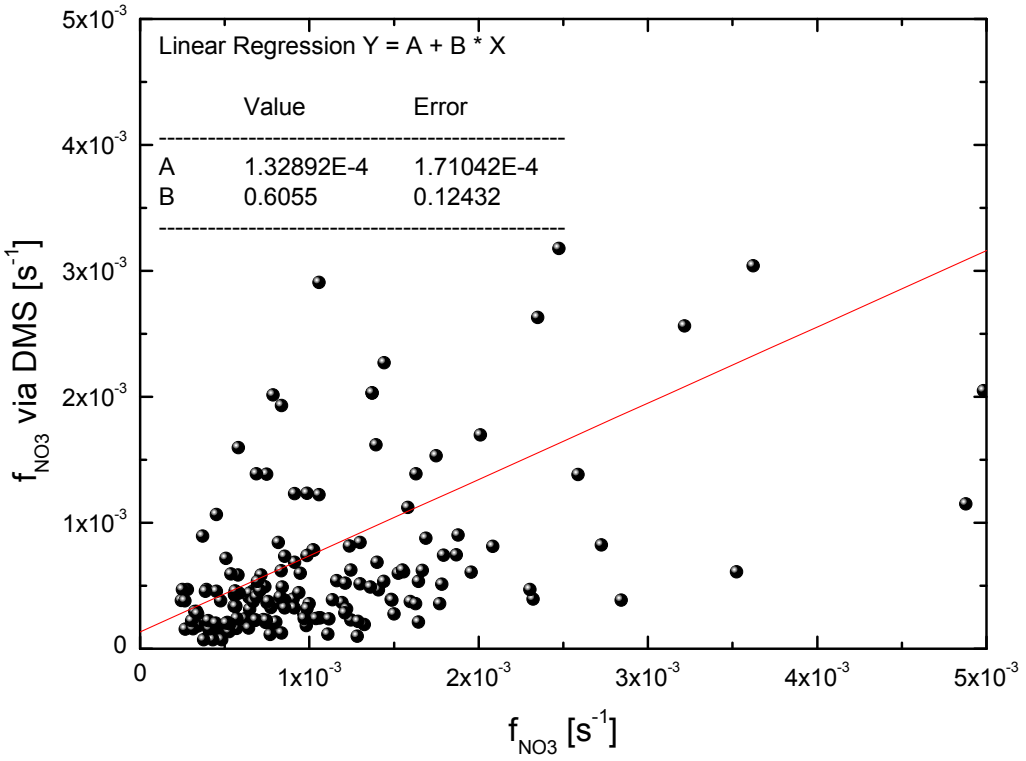

Figure 5.6: Total vs DMS initiated degradation frequency. The elevation of the linear fit states that 60.5% of the direct sink reactions if NO3 occur via reactions with DMS.

for the NO_x due to its continental origin. As a matter of fact, model results of the boundary layer height(BLH) show an important variability over continental areas. Particulary over (semi)arid regions with large surface albedo a dramatic growth of this layer is consistently observed in the late afternoon(Fig. 5.7). A quite evident explanation for this observation is Penetrative convection, a process which is less pronounced over the sea at is reduced to areas of cold advection (which are scarce in the summertime Mediterranean). Therefore anthropogenic trace gas emissions (like NO_2 or NO_3) potentially distribute throughout the boundary layer. It is therefore possible that DMS and NO_3 remain in separated layers until reaching the coast of Crete. The sampled air at the station may represent a very recent mixing of the lower boundary layer (caused by the orography). While DMS is measured in-situ at 130m ASL, the DOAS measurements (i.e. NO_3) represent an average value of the lower 130 m of the BL. Assuming the separation of DMS and NO_3 in two layers, e.g. DMS at 10 m and NO3 at 130 m, DOAS measurements may underestimate concentration levels at the site. This could explain as well lower NO3 levels observed by [Vrekoussis et al. 2003] as the shorter lightpath used for that study includes a lower fraction of the NO3 rich upper layers due to the much lower elevation angle. Another aspect is that the steady–state assumption may not be applicable for the whole dataset as in–situ mixed air masses may not have reached an

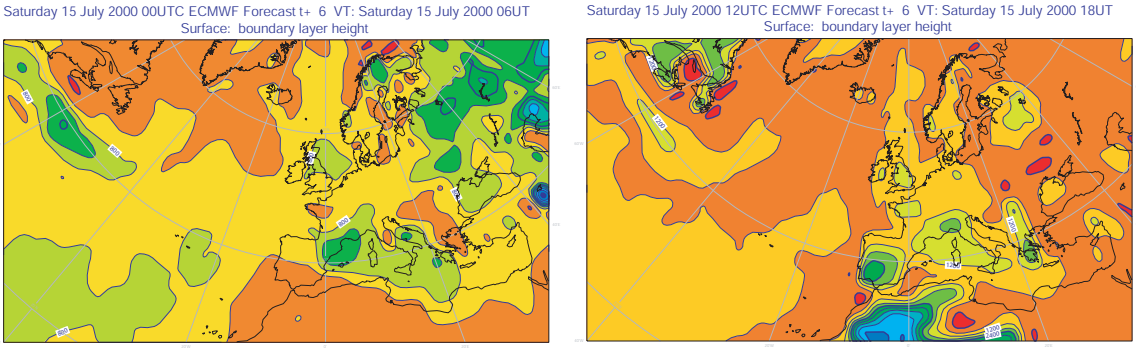

Figure 5.7: Boundary layer height forecast for 15.07.2000 at 06 and 18UT for the European Area. It is quite evident, that the mixing layer height increases significantly over the continents in the late afternoon. The effect is particulary dramatic in areas with large surface albedo and high radiation input, i.e. the saharan desert and arid regions in central Spain.

equilibrium when observed at the measurement site.

Other organic compounds, in particular isoprene and terpenes, react rapidly with NO_3. Despite none of this compounds was measured simultaneously to our measurements at Finokalia, the impact is expected to be minor. As both species are emitted largely by vegetation, their levels are expected to be low due to the marine condition of the site and since the surrounding vegetation is sparse and consists mainly of dry herbs(thyme) and bushes. Gros et al. [2003] reported Isoprene levels below 7 ppt for the same season. If supported by long range transport, emissions from forest fires could influence local VOC levels.

5.2.2.2 Heterogeneous loss of NO_3 and N_2O_5

Under conditions of high relative humidity, the effective lifetime of NO_3 was observed to be relatively short, i.e., on the order of a few minutes [Platt et al. 1981; Platt et al. 1984; Heintz et al. 1996; Geyer et al. 2001], a fact that was associated with heterogeneous losses of NO_3 and/or N_2O_5 on aerosol surfaces. The velocity of this process is ruled by three following steps:

1. Molecular diffusion in the gas–phase through the barrier to the particle surface and collision.

2. Phase–transition.

3. Diffusion in the liquid phase away from the barrier or chemical conversion.

The third step is particulary fast for N_2O_5 in aqueous aerosols and leads to the formation of nitric acid.

$$N_2O_5(aq) + H_2O(l) \rightarrow 2\,HNO_3(aq) \tag{5.15}$$

The reactive uptake of NO_3 on aqueous aerosols has been investigated by several laboratory studies([Rudich et al. 1996; Thomas et al. 1998; Poskrebyshev et al. 2001]) and is known

to proceed via the liquid phase reaction:

$$NO_3(aq) + H_2O(l) \rightleftharpoons HNO_3(aq) + OH(aq) \tag{5.16}$$

$$\tag{5.17}$$

Because of its small solubility, heterogeneous removal of NO_3 is only important under conditions were dissolved NO_3 is removed quickly from the equilibrium, for example by reactions with Cl^- or HSO_3^- ions in the liquid phase([Ravishankara et al. 1997; Poskrebyshev et al. 2001]). Otherwise, heterogeneous removal should mainly proceed via N_2O_5.
Due to the high concentration of Cl^- $(0.1-1\ M)$ in sea salt aerosols, the heterogeneous uptake of NO_3 on aerosols may be a very efficient process in the marine boundary layer. However, measurements of the tropospheric aerosol ionic composition at Finokalia ([Mihalopoulos et al. 1997; Bardouki et al. 2003] report a Cl^-/Na^+ ratio well below the the seawater rate throughout the summer. This deficit of Cl^- relative to Na^+ appears to be quite common at coastal areas and is explained by reactions of acids with sea salt. The frequency of the heterogeneous loss can be estimated using the formula of [Fuchs and Sutugin 1971]

$$\tau_{het} = n^{-1}\left(\frac{1}{4\pi r D_{mol}} + \frac{3}{4\pi v r^2} + \frac{1-\gamma}{\gamma \pi v r^2}\right) \tag{5.18}$$

n	:	Aerosol number concentration
r	:	Radius of aerosol particles
D_{mol}	:	molecular diffusion $D \simeq (1-1.5)^{-5} m^2 s^{-1}$
v	:	mean molecular velocity $v = \sqrt{\frac{3RT}{M}}$
γ	:	Uptake coefficient

The three terms of the sum correspond to the three steps of the uptake process described above. The uptake coefficient γ is a surface specific, temperature dependent factor, which describes the number of collisions needed for the phase transition and successional chemical conversion of the considered substance. At values of $\gamma < 0.1$, as measured for NO_3 and N_2O_5, the lifetime τ_{het} is determined by the slow diffusion and the other terms of equation (5.18) are negligible small. The diffusion velocity through the gas–phase (1st term) is only important for large particles, i.e. $r > 4D_{mol}v^{-1}\gamma^{-1}$. which corresponds to particles larger than $2\mu m$ for N_2O_5 and $15\mu m$ for NO_3 on sea salt aerosols($\gamma = 0.01$). The assumption of both conditions ($\gamma < 1$ and small particles) reduces (5.18) to:

$$\tau_{het} = \frac{4}{\gamma S v} = f_{het}^{-1} \tag{5.19}$$

where $S(= 4\pi r^2 n)$ is the total aerosol surface per unit volume. Due to the frequently observed haze formation during daytime, a large number of aerosols must be present in the accumulation mode ($r \simeq 0.1\ \mu m$). This is confirmed by the number size distribution profile recorded by [Schneider et al. 2003] at Crete in August 2001, which presents the classical marine distribution but shows a clear maximum in the range of $0.1 - 0.3\ \mu m$. In the same study condensation particle counter measurements revealed unusually high particle concentration levels $(2000-5000\ particles/cm^3)$ for a remote region. The total surface density S was found to decrease from about 350 $\mu m^2 cm^{-3}$ down to around 100 $\mu m^2 cm^{-3}$. Particles in the accumulation mode ($< 2\ \mu m$) consisted mostly ($> 95\%$) of ammonium sulfate ($(NH_4)_2SO_4$) and

carbonaceous aerosols produced by fossil fuel combustion(lignite) in Eastern Europe. The sea–salt content was very low. The low nitrate content was attributed to the hot environment, since ammonium nitrate, in contrast to ammonium sulfate, becomes unstable at higher temperatures. In the coarse mode ($> 2\ \mu m$) mainly mineral dust particles, but also sea salt, both of local origin were observed.

In spite of numerous studies carried out so far, the uptake coefficients of both NO_3 and N_2O_5 remain encumbered with large uncertainties. In addition, most of the reported measurements were carried out at temperatures well below average conditions at Crete (T=301 K).

Table 5.2: Uptake coefficients of NO_3 and N_2O_5 on aerosol surfaces

Surface	rH[%]	T[K]	$\gamma * 10^3$	Reference
NO_3				
H_2O		273	0.2 ± 0.1	[Rudich et al. 1996]
NaCl 0.02–0.5 M		273	$3 - 6$	
NaCl 0.1 M		293	≥ 2	[Thomas et al. 1998]
NaCl solid			46 ± 40	
NaI solid			330 ± 90	[Seisel et al. 1999]
KBr solid			200 ± 100	
soot aerosol			0.3	[Saathoff et al. 2001]
organic liquids			1.4-15	[Moise et al. 2002]
N_2O_5				
H_2O		262	30 ± 2	[George et al. 1994]
		277	13 ± 8	
		271	57 ± 3	
		282	36 ± 4	[Van Doren et al. 1990]
$(NH_4)_2SO_4$	50–93	297	$20 - 50$	[Hu and Abbatt 1997]
H_2SO_4 (50%)[1)]		301	41 ± 6	[Robinson et al. 1997]
NaCl	80–90	293	30	[Behnke et al. 1997]
soot aerosol			0.04	[Saathoff et al. 2001]

1) weight percentage of H2SO4 in Aerosol

For the uptake coefficient of NO_3 on water droplets with varying molar salt content, the studies of [Rudich et al. 1996] and [Thomas et al. 1998] discern significantly (see Table 5.2). Using the more recent value of [Thomas et al. 1998] ($\gamma \geq 2e^{-3}$ at $[Cl^-] = 0.1$ M) and $S = 350\ \mu m^2 cm^{-3}$, the degradation frequency according to (5.19) is $f = 0.61e^{-4}\ s^{-1}$. Laboratory studies of [Moise et al. 2002] report uptake coefficients in the range of $1.4 - 15 \times 10^{-3}$ for organic liquids serving as proxies for organic aerosols. These proxies are relevant since the absorption of semivolatile organics by aerosols can lead to the formation of aerosols coated by an organic liquid layer.

The rate of heterogeneous uptake is about a factor of ten higher for N_2O_5 as a consequence of the higher coefficients(Table 5.2). For the uptake on pure water we have $f = 8.3e^{-4}\ s^{-1}$ ($\gamma = 36e - 3$ at $282\ K$). Even higher rates are expected at a 50%H_2SO_4 content on the aerosol and for NH_4HSO_4 at 69% relative humidity ($f = 9.5e^{-4}\ s^{-1}$ and $f = 1.2e^{-3}\ s^{-1}$ respectively).

5.2.2.3 Other sink mechanisms

Other sink processes for nitrogen compounds is deposition to the open sea surface. Unfortunately the knowledge about this topic seems to be mostly restricted to model estimations. Within the Research Project MEAD the atmospheric flux of nitrogen to surface waters was investigated to determine the impact on marine algae growth near Denmark. It was found that approximately 70% of the deposition consists of wet deposition of highly episodic nature. Dry deposition is an order of magnitude smaller than the wet deposition on a daily scale and about a quarter smaller as accumulated values. The one-year return of extreme atmospheric wet and dry deposition was found to be around 70 and 1 $mgNitratem^{-2}day{-}1$ respectively ([Hasager et al. 2003] and reports of the MEAD project). However, wet deposition should be negligible in our case as no rainfall was observed in Crete for the whole campaign period. In July 2000 and January 2001 [Bardouki et al. 2003] measured concentrations of several ions at Finokalia, including NO_3^- whose concentration decreased from 2700 $ng\ m^{-3}$ in July to about half in winter. Therefore wet deposition can be considered much more important as dry deposition in the Mediterranean as well. Furthermore, the absence of fine mode for particle-bound nitrate was attributed to absorption of HNO_3 on sea–salt particles. This reaction moves nitrate aerosols from the fine mode ($< 1\,\mu$mdiameter) to the coarse mode ($> 1\,\mu$m) enhancing aerosol nitrate deposition. As gas phase nitric acid has a higher deposition velocity than aerosol nitrate, this reaction actually decreases the total nitrate flux to surface waters.

Homogeneous hydrolysis of N_2O_5 on water vapour could be important near the water surface due to the high evaporation rate. Mentel et al. [1996] and Wahner et al. [1998] observed homogeneous reactions of second and third order,

$$N_2O_5 + H_2O \rightarrow 2HNO_3 \tag{5.20}$$

$$N_2O_5 + 2H_2O \rightarrow 2HNO_3 + H_2O \tag{5.21}$$

The reaction constants are $k_{5.20} = 2.5 \times 10^{-22}$ and $k_{5.21} = 1.8 \times 10^{-39}[H_2O]$ respectively.

$$f_{N2O5,homo} = k_{5.20}[H_2O] + k_{5.21}[H_2O]^2 \tag{5.22}$$

The concentration of water can be derived from measured relative humidity, temperature and atmospheric pressure (taken from Wunderground) or by DOAS (e.g. in the $605 - 685\ nm$ wavelength region). Degradation frequencies of N_2O_5 due to this process were in the range of $2.9e^{-8} - 5.1e^{-5}\ s^{-1}$.

5.2.2.4 Total lifetime and degradation frequency of NO_3

An overview of all relevant NO_3 degradation rates, i.e. direct loss via reactions with DMS (fDMS), heterogeneous loss on salt particles f(het,NaCl) and the indirect processes (homogeneous and heterogeneous reaction of N_2O_5), is shown in Figure 5.8. This results demonstrate once again that DMS plays an important role in NO_3 depletion. However, the sum of all degradation rates can hardly explain the total NO_3 variation. A large number of factors remain still quite uncertain. The largest uncertainty may issue from the role of NO in the nighttime troposphere. As the lifetime of the nitrate radical can be drastically reduced by

the presence of even few ppt of NO, a lower detection limit for this molecule (50 ppt for this study) would be desirable to allow further investigation. The other aspect is the presence of NO_3 and DMS in two separated layers as discussed in section 5.2.2.1. An underestimation of NO_3 levels would lead to overestimated degradation rates. Occasionally the DMS–initiated (f_{DMS}) is larger than the total degradation frequency. A reasonable explanation for this observation is that the equilibrium was not reached at the time of the measurement. This would imply that a fraction of both, DMS and NO_3, will be consumed until reaching steady–state conditions. Further on, lower concentrations of both compounds lead to a decrease of f_{DMS} and increase of f_{total} respectively and thus to a convergence of both degradation frequencies.

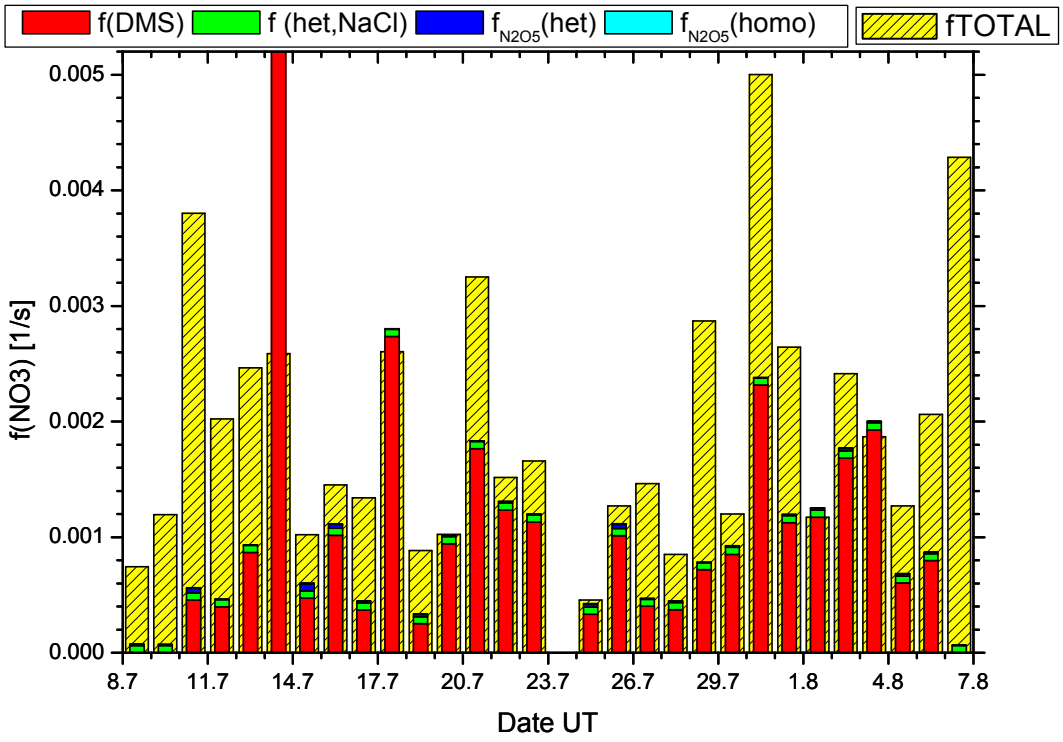

Figure 5.8: Degradation rates of relevant loss mechanisms of NO3. The bars represent average nighttime values for the dates given below(from dusk till dawn, as far data was available). For the first two and the last night of measurements the DMS concentration was not measured. Due to an instrument failure no data exists for July 24th.

Table 5.3: Relative contribution of all relevant NO3 sink mechanisms during nighttime.

Sink process	Degradation frequency $[s^{-1}]$ Average (Max)	relative contribution [%]
DMS	$1.1e^{-3}$ ($1.8e^{-2}$)	55
HCHO	$1.7e^{-5}$ ($3.4e^{-5}$)	0.8
NO	($5.9e^{-2}$)	
RO_x	$1.9e^{-3}$ ($1.2e^{-2}$)	
heterogeneous on NaCl	$6.1e^{-5}$	3
N_2O_5 (heterogeneous)	$1.6e^{-5}$ ($6.2e^{-5}$)	0.8
N_2O_5 (homogeneous)	$5.9e^{-6}$ ($5.1e^{-5}$)	0.1

5.2.3 Influence of radicals on DMS oxidation. The oxidation capacity of NO_3,OH,RO_x,O_3 and XO

The large set of measured radical concentration data gives us a chance to quantify the importance of known radicals in the DMS oxidation chain. An estimation of ambient OH radical concentrations can be derived from the measured ozone photolysis rate JO_1D by the formulas given in Berresheim et al. [2003]. An average diurnal radical profile derived from the DOAS measurements is shown in Figure 5.10.
The diurnal variation of the DMS degradation frequency is clearly dominated by the OH radical during daytime. At night the nitrate radical is the most important oxidant of DMS.

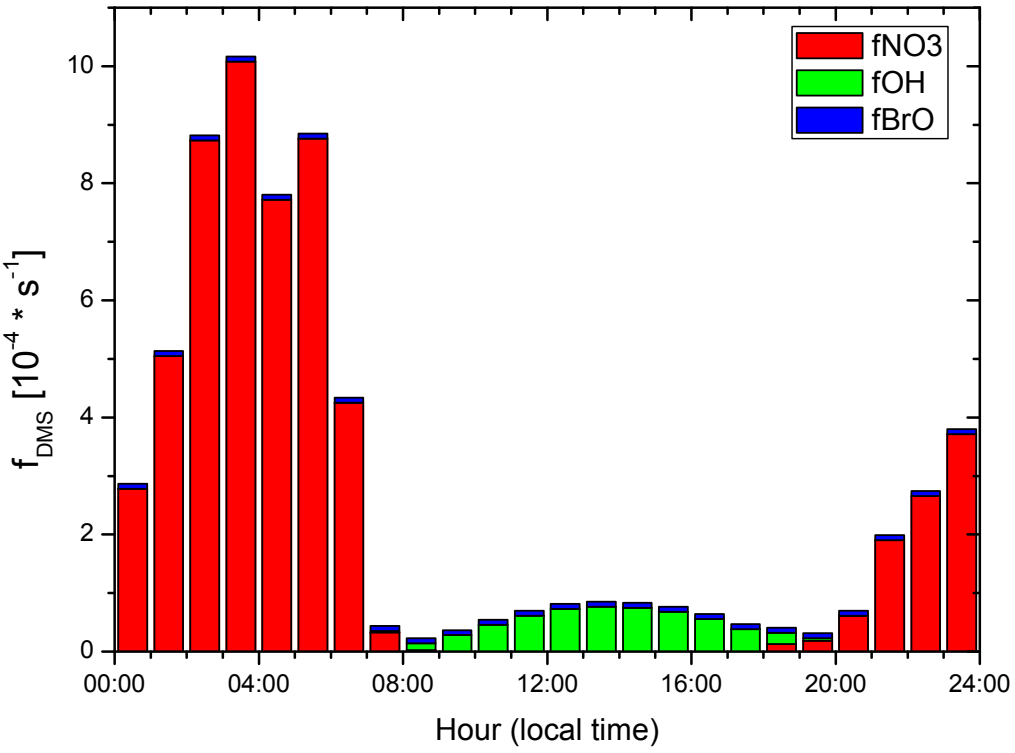

Figure 5.9: Diurnal variation of the DMS degradation frequency.

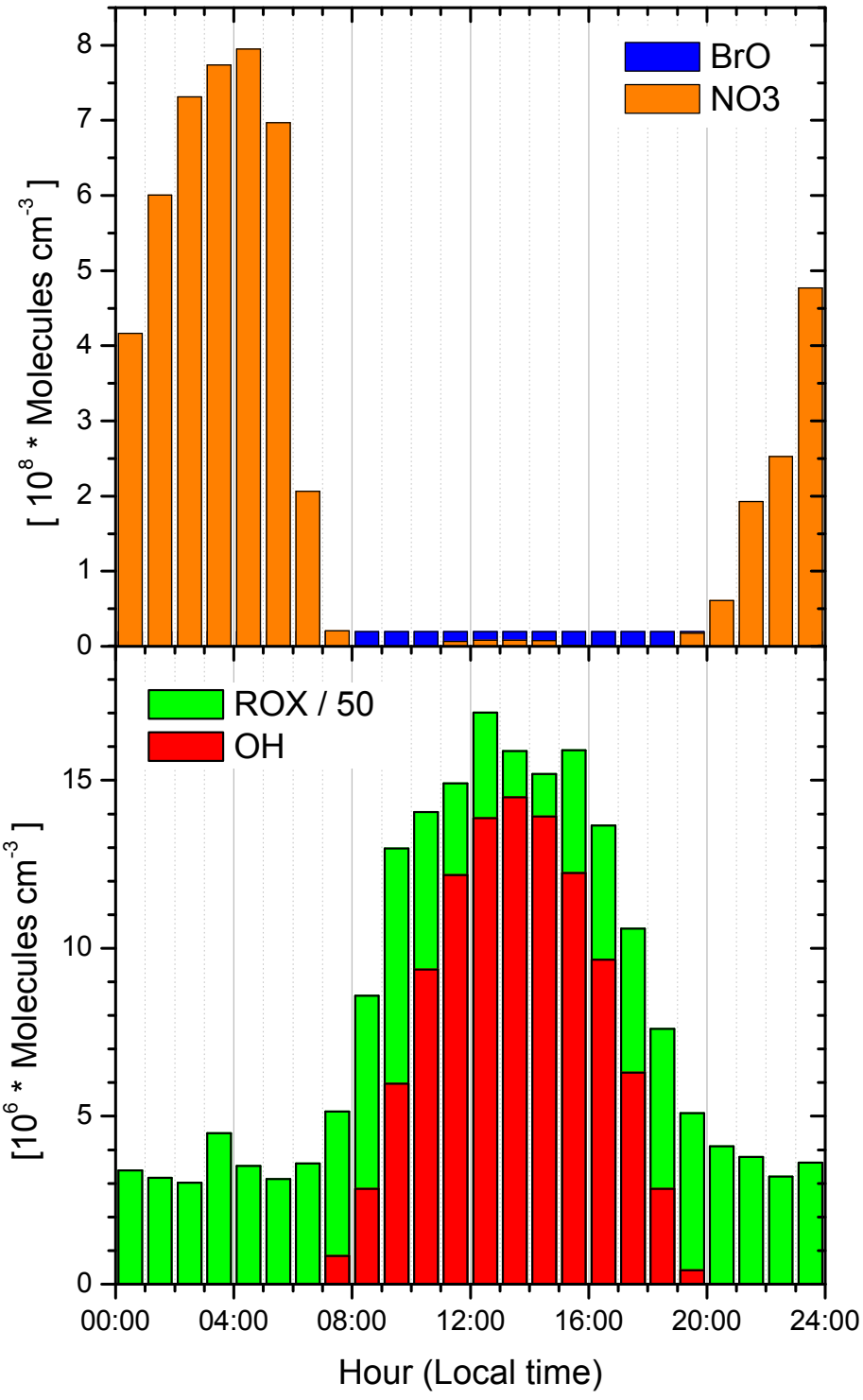

Figure 5.10: Mean diurnal radical profiles derived from the measurement data. As BrO was under detection limit, values are set to the upper limits(0.8 ppt). The OH data was calculated from the measured JO1D photolysis rate using recommendations given in (Berresheim2003).

5.3 Dimethylsulphide oxidation in the Hudson Bay

As for the Crete campaign a DMS reaction scheme corresponding to mean diurnal and nighttime trace gas concentrations was created for the field campaign at Kuujjuarapik. The measured values correspond to the period from 15.-30.04.2001 when DMS measurements have been performed simultaneously with DOAS measurements. As the mixing rates of NO_2 and SO_2 remained below detection limits (excepting local pollution events, section 4.2.3) throughout the campaign period, these values as well a number of other compounds not measured have been taken from literature [Wang et al. 2003; Ferek et al. 1995] reporting measurements in arctic and subarctic regions. The values taken from Wang et al. [2003] and are an extrapolation of monthly mean vertical profiles for April from 500 m to ground height. Therefore this additional values have to be regarded with care, as the presence of a stable boundary layer may lead to a significant underestimation of surface trace gas mixing ratios if strong local sources exist. However, the extrapolation should be sustainable for trace gases bound to anthropogenic activity as NO_x and Carbon Monoxide(CO) considering that the population density is sparse in the whole region of the Hudson Bay. Some difficulties may arise for the estimation of H_2O_2 and HCHO as snow surfaces can be respectively a considerable sink or source of these trace gases as described in [Jacob 2000]. Due to the almost exclusive arctic origin of sampled air masses throughout April (see section 4.2.2), the vertical profiles from [Wang et al. 2003] corresponding to the area within 60-80°N have been taken in spite of the further southern location of Kuujjuarapik at 55°N.
The levels of peroxides HO_2 and RO_2 have been estimated according to the relation of Photolysis Rates measured at Crete and the Hudson Bay (5 times smaller). As the concentration of the main compounds leading to nighttime production of peroxy radicals, NO_3 and volatile organic compounds (VOC) [Geyer et al. 2003], in nighttime air at Kuujjuarapik is presumably negligible compared to Crete the mixing rates of RO_x and in extension those of the OH radicals have been set to zero. Once again the levels of the halogen radicals, Br, Cl and ClO were estimated using MOCCA and the aqueous phase concentrations are taken from literature [Herrmann et al. 2000; Lelieveld and Crutzen 1991; Jacob 1986]. An overview of all values employed to establish the typical DMS oxidation scheme at Kuujjuarapik is given in Table 5.4.
All measured parameters have been employed once more to run the MOCCA Model, this time for conditions in the subarctic boundary layer. The model results allowed a raw estimation of the mixing rates of a number of halogen compounds listed in Table 5.4.

The nighttime scheme presented in Figure 5.3 shows that the oxidation of DMS is rather slow after sunset. Only the nitrate radical at the estimated upper limit concentration is conceivable as a sink for DMS in the gas phase. The aqueous phase reaction of DMS with ozone is probably more significant in the Hudson Bay than in Crete during the frequent fog formation events occuring before dawn. However, snowfall and rain which was also observed on several days of the measurement period, probably removed a large fraction of radicals in the aqueous phase by deposition to ground. The knowledge about halogens in the aqueous phase is too limited to allow precise indications. Due to its higher solubility, HOBr ($H = 6.1 \times 10^3\ M\ atm^{-1}$) could be more abundant in the aqueous phase than OH ($H = 7.8 \times 10^3\ M\ atm^{-1}$) which

Table 5.4: Average trace gas concentrations at Kuujjuarapik during the measurement period ranging from 15.-30.04.2001 derived from measurements, taken from literature or estimated using the MOCCA Model.

Trace gas	Mean Concentration $[molec./cm^3]$		Source
	Night (19-05 LT)	Day (05-19 LT)	
BrO	$< 1.3 \times 10^7$	1.2×10^8	DOAS
HCHO	$< 2.8 \times 10^9$	$< 2.8 \times 10^9$	
HONO	$< 1.4 \times 10^9$	$< 1.4 \times 10^9$	
IO	$< 1.3 \times 10^7$	$< 1.3 \times 10^7$	
NO3	$< 1.4 \times 10^7$	0	
O3	9.9×10^{11}	9.8×10^{11}	
DMS	4.0×10^7	4.0×10^7	GC
DMSO	1.9×10^6	2.5×10^6	Mist chamber
MSA	1.4×10^7	1.9×10^7	IC
NO2	5.5×10^8	2.8×10^8	WAN03
CO	4.0×10^{12}	4.0×10^{12}	WAN03
NO	0	1.4×10^8	WAN03
SO2	4.1×10^8	6.9×10^8	FER96
OH	0	9.5×10^5	WAN03,KUH01
H2O2	6.9×10^9	6.9×10^9	WAN03
HO2	0	8.0×10^7	b)
RO2	0	4.0×10^7	
Br	3.9×10^2	3.3×10^6	MOCCA
Cl	3.6	2.5×10^3	
ClO	1.9×10^6	5.0×10^6	
HOBr	5.4×10^6	3.0×10^7	
Br2	2.2×10^7	3.4×10^6	
	Mean diurnal Concentration [M]*)		
$H_2O_2(aq)$	$10 - -200 \times 10^{-6}$		a)
OH(aq)	$5 - -50 \times 10^{-14}$		a)
$O_3(aq)$	$5 - -50 \times 10^{-14}$		a)

[Herrmann et al. 2000; Lelieveld and Crutzen 1991; Jacob 1986]
(WAN03) [Wang et al. 2003], (FER95) [Ferek et al. 1995], (KUH01) [von Kuhlmann 2001]
*) divided by 300 if no clouds present
b) estimated from Photolysis Rate Relation Crete/Hudson Bay

could partly compensate the lower rate contants (Table 2.13) towards DMS and its oxidation products DMSO and MSA.
Due to the very low levels of NO and the absence of peroxy radicals, the reaction chain of DMS along the abstraction path probably stops after the second reaction step as the most rapid reaction pathway would correspond to the self reaction of CH3SCH2OO assuming concentrations levels ten times below those of DMS ($4 \times 10^6 molec./cm^3$).
In contrast to the daytime DMS reaction scheme established for Crete(section 5.1), the addition path is clearly dominant for conditions encountered in Kuujjuarapik(Figure 5.3). This is firstly caused by the 35 degrees colder average ambient temperature shifting the yield of products of the DMS+OH reaction clearly to the addition path (Figure 2.3.2.1 on page 46). However, at the mixing rates measured in the Hudson Bay, the reaction of BrO with DMS should be largely more effective than the OH reaction. The mean lifetime of DMS against reaction with BrO is about 5 hours, falling notably below during the several BrO events observed throughout the campaign period. For comparison note that the average lifetime of DMS against reaction with OH was about 8 hours in the Mediterranean (Figure 5.1), a region attaining worldwide highest OH levels in summer [von Kuhlmann 2001]. Considering that the OH production in the area of the Hudson Bay and the arctic in general is rather low throughout the year (excepting summer months), it becomes obvious that the Bromine Radical probably has a key role regarding DMS oxidation in the Arctic Boundary layer.
The exclusive product of the DMS+BrO reaction is DMSO. On the OH initiated reaction channel, the initial DMS-OH adduct reacts quickly with oxygen to form preferably DMSO as well. Formation of $DMSO_2$ is probably negligible as due to the low levels of NO, the compound initiating the $DMSO_2$ formation branch, $DMS(OH)(O_2)$, will decompose before reaction with NO is possible.
The comparison of the mean MSA to DMS ratio obtained from Crete and Kuujjuarapik results (0.12 and 0.44 respectively), states that the MSA formation yield is somewhat higher in the Hudson Bay. As the gas-phase oxidation of DMSO by means of OH is slow and MSIA preferably decomposes to form SO_2, heterogeneous reactions may have a significant contribution regarding MSA formation. As the high levels of bromine in the gas phase can probably be extended to the aqueous phase, it is likely that compounds as HOBr or BrO^- enhance the efficiency of multiphase chemistry. The other channel initiating MSA formation goes along the intermediate product CH_3SOH. Due to fast reaction of CH_3SO with ozone SO_2 will be an important product here, but MSA formation can occur as a concurrent process within few minutes.

5.3.1 Localizing the sources of DMS in the arctic spring

Given the low amount of ice free surface during winter and early spring, the expectable local flux of DMS to the air in the arctic is small. According to [Leck and Persson 1996] the fraction of open water is about 4% in the Canadian Arctic Archipelago in winter(October to April) leading to an estimated DMS flux of 0.045 $\mu\ molm^{-2}day^{-1}$. This is more than 2 orders of magnitude below the one in summer (May to September), estimated to be about 6.7 $\mu\ molm^{-2}day^{-1}$. As shown previously in Figure 4.25 on page 91, the whole area of

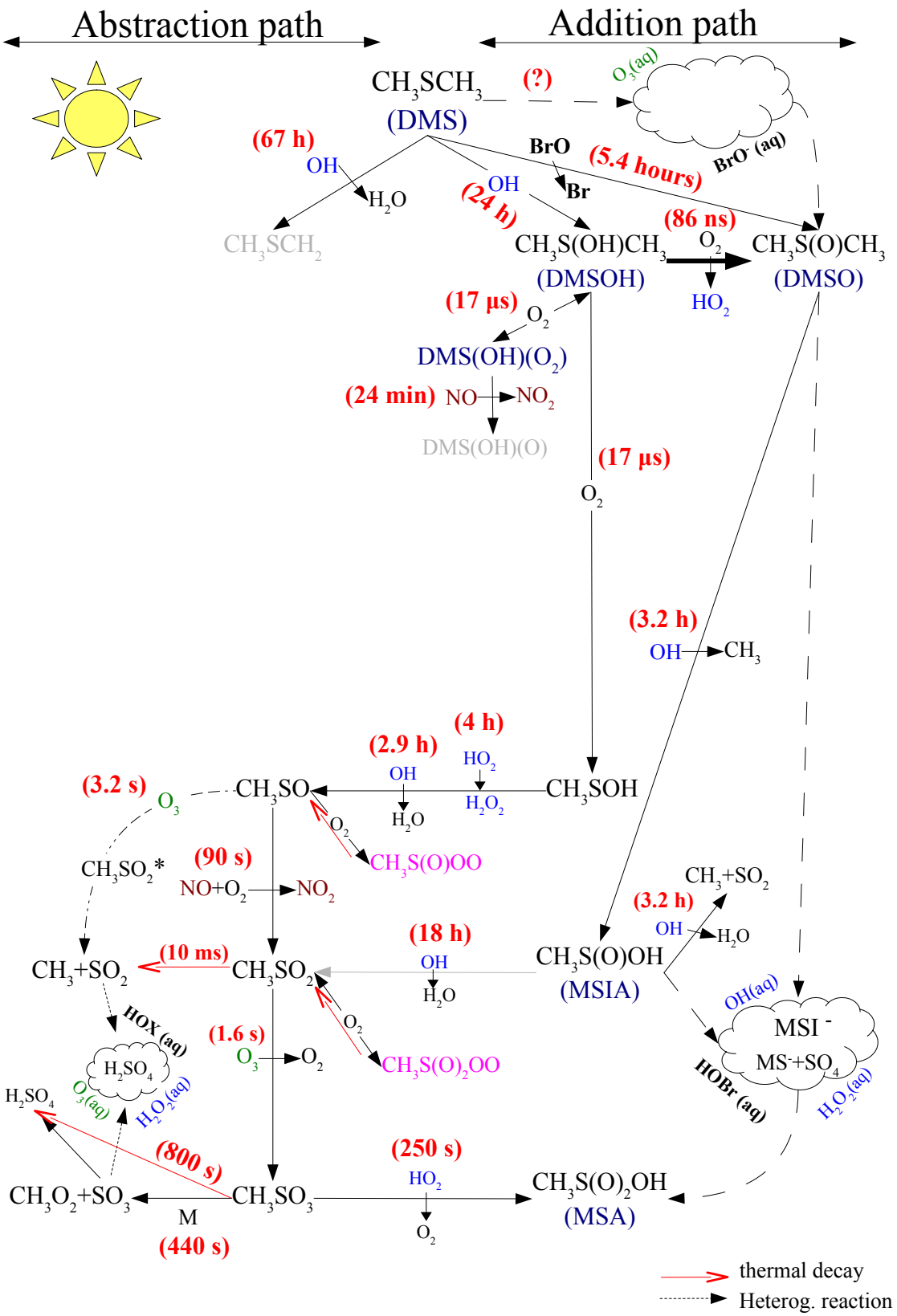

Figure 5.11: Oxidation chain of Dimethylsulphide for average daytime mixing ratios established during the measurement campaign at Kuujjuarapik in April 2001.

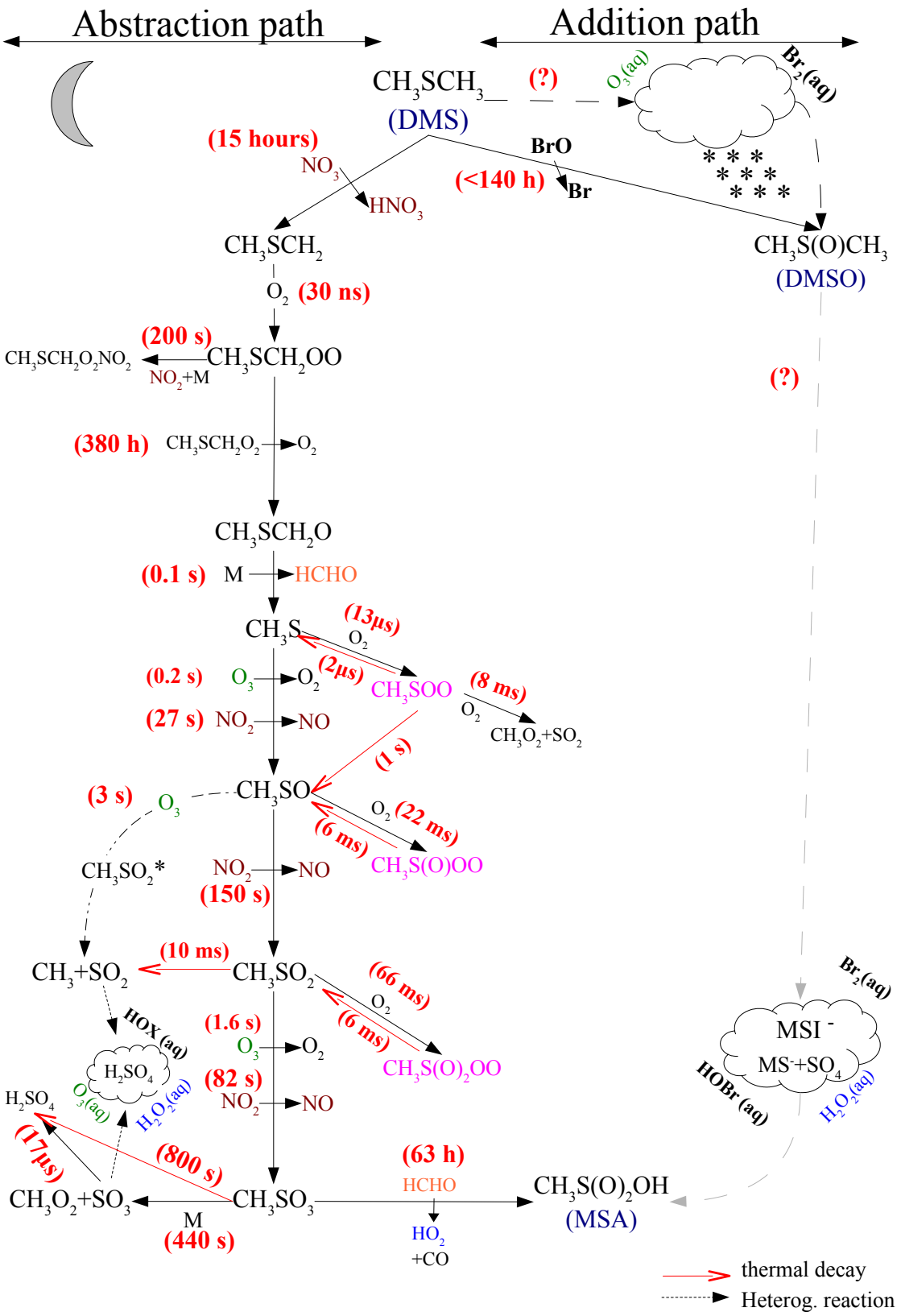

Figure 5.12: Oxidation chain of Dimethylsulphide during night for average mixing ratios established during the measurement campaign at Kuujjuarapik (Hudson Bay) in April 2001.

the Hudson Bay was covered with ice along the measurement period at Kuujjuarapik. The nearest open sea areas were located over 1000 km to the northwest, 200 km off the coast of New Foundland in the Labrador Sea (Northern Atlantic Ocean). In spite of this scenario, although tiny, still detectable amounts of DMS and its oxidation products have been measured at Kuujjuarapik(section 4.2.4). The measured mixing ratios of DMS were in the same range as those reported by Ferek et al. [1995] for April 1992 at the northern coast of Alaska. Due to the evident inhibition of local sources, it is conceivable that long range transport from open sea areas may contribute to background levels of Dimethylsulphide. However, as already shown in Figure 4.29 in section 4.2.2, trajectory results state that throughout the period of DMS measurements (i.e. last to weeks of April) air masses did not even approach the open sea sector in the northwest within 5 days before reaching Kuujjuarapik. Considering that Nilsson and Leck [2002] and Chen et al. [1999] derived DMS turnover times below 2.5 days in the Arctic Ocean through all seasons, the contribution from open sea areas to local DMS levels is probably negligible.

An interesting detail is given in the publication of Ferek et al. [1995], who collected a seawater sample from a 50 cm ice core hole about 270 km off shore. The sample was found to contain a dissolved DMS concentration of 23 $ngSulphurl^{-1}$ which is nearly equal to amounts found in the Indian Ocean near Kerguelen in the austral summer 2002 (section 4.3.4) simultaneously to atmospheric DMS mixing ratios above 200 ppt. Therefore, significant amounts of DMS are probably present in seawater under the ice even as early as in April probably due to the contribution from ice algae [Laturnus 2001; Ferek et al. 1995]. As the biological growth is linked to the amount of available light, solar radiation must have reached the sea until a given depth. This gives evidence that the ice layer is transparent to a certain extent. In addition to the seasonal reduction of thickness, the formation of melt pools and notably the removal of snow are factors favoring the transparency of the ice layer.

Although there is no definite link to DMS production, the emission of chlorophyll from surface waters is an undeniable hint of biogenic activity. Chlorophyll A concentrations measured from satellite instruments allow a localization and quantification of marine biogenic activity throughout the globe. Figure 5.3.1 shows the Chlorophyll A emission in milligrams per cubic meter for the area of the Hudson Bay as obtained from satellite provided by the SeaWiFs Project. The measurements state that the Hudson Bay and regions further poleward are not productive at all in winter, starting tiny biogenic activity at coastal areas of the Bay and the Hudson Strait in April increasing gradually in amount and extension as the ice recedes towards summer. The most important chlorophyll flux in the area around Kuujjuarapik corresponds to the eastern coast of the Hudson Bay and notably James Bay, the southern appendix of the Hudson Bay.

In order to identify possible source regions for gaseous DMS sampled during our measurements, the local chlorophyll flux and the trajectory distribution matrix as presented in section 4.2.2 (Figure 4.29), both for the last to weeks of April, have been overlaid in Figure 5.14. Although the major sources of DMS to the atmosphere are the open waters of the seas surrounding the mostly ice covered central Arctic Ocean, the comparison of trajectories and chlorophyll flux gives evidence that these areas do not contribute to local DMS levels.

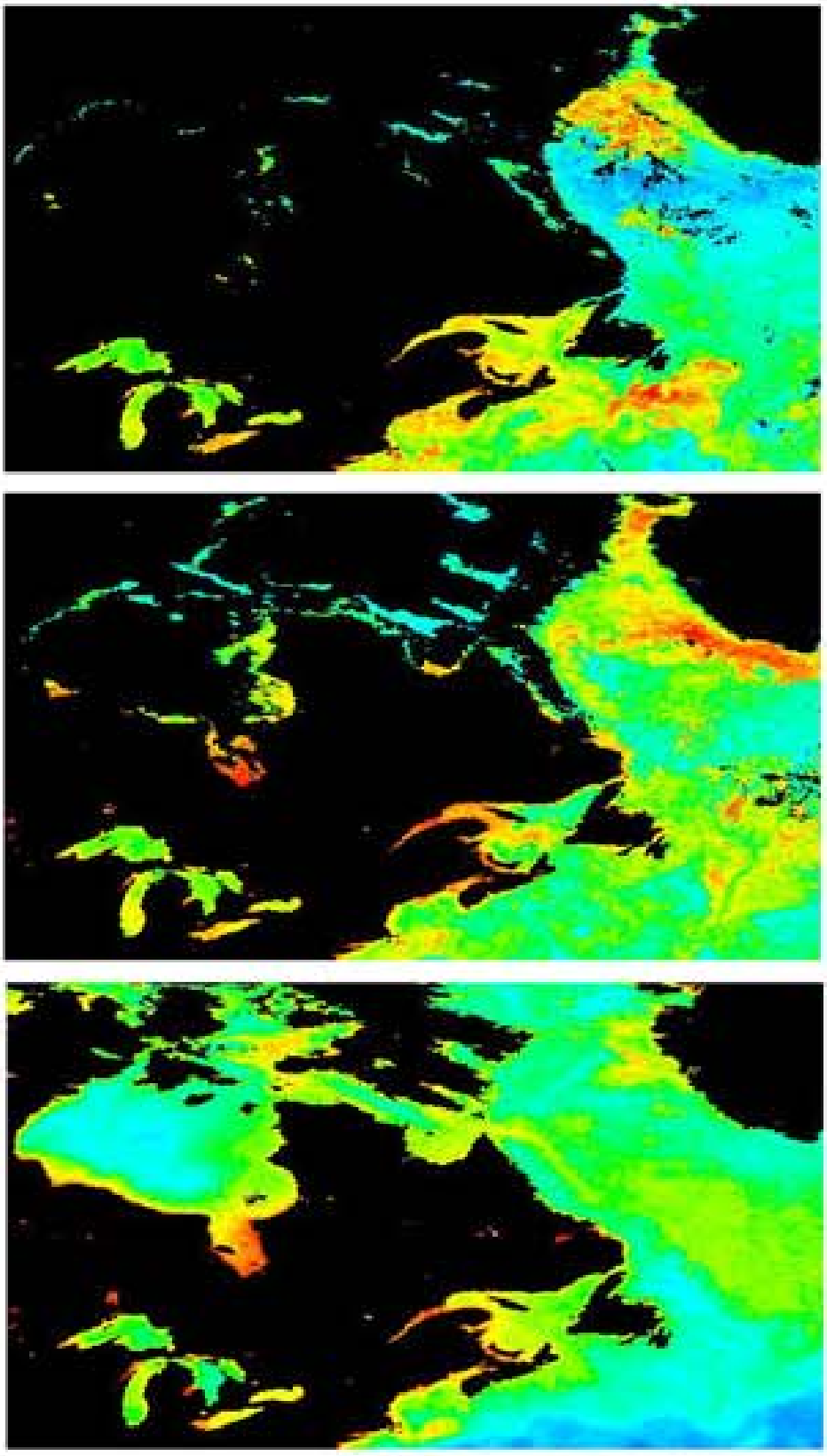

Figure 5.13: Biogenic activity (chlorophyll emission) for the area of Hudson Bay provided by the SeaWiFS Project, NASA/Goddard Space Flight Center and ORBIMAGE. The average emissions for April, May and Summer 2001 are shown from above to below.

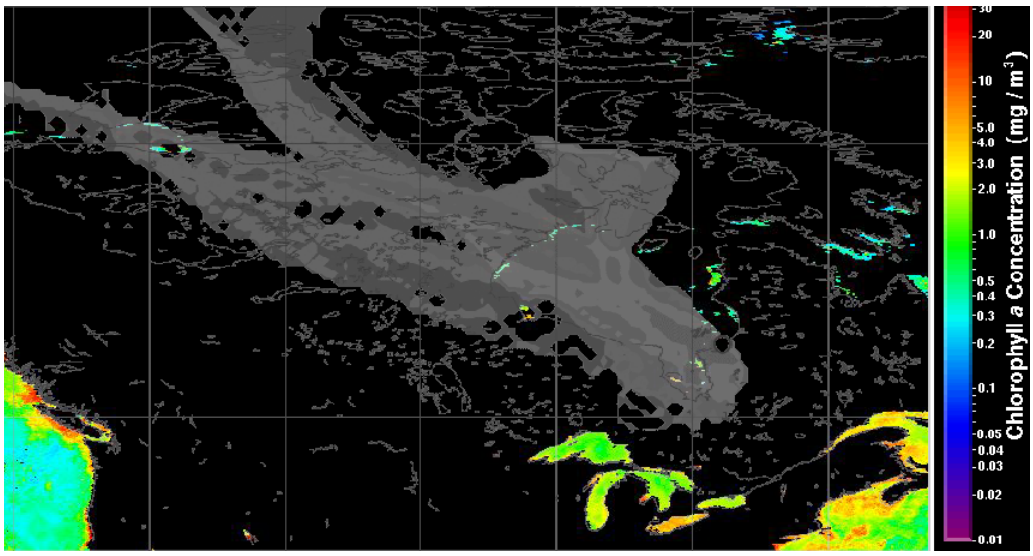

Figure 5.14: Overlaid in this figure are the Chlorophyll production measured by the SeaWifs satellite instrument and the frequency distribution matrix of air masses reaching Kuujjuarapik (Fig. 4.29) for the last two weeks of April 2001.

This is consistent with DMS measurements, as residence times of DMS in the Arctic MBL reach at least 2-3 days [Leck and Persson 1996] and advection over the pack ice area would lead to significantly higher DMS levels. Another conclusion derivable from Figure 5.14 is that neither biogenically productive areas south of the Hudson Bay, as the Big Lake region and the St. Lorenz Gulf, influenced local DMS. Therefore, the sources of DMS reaching the measurement site seem to be restricted to the coastal production of the Hudson Bay.

Another possibility to gain knowledge about DMS source regions is the DMS distribution matrix derived from trajectory results and atmospheric measurements. The procedure to create this matrix is analogous to all previous ones and has been described elsewhere (section 4.2.3). As expectable in consideration of the chlorophyll emissivity, the highest average DMS mixing ratio, surpassing 5 ppt, corresponds to air masses having travelled along the southern edge of the James Bay. Other areas with slightly superior DMS levels are found north of the Hudson Bay and on the way to the Beaufort sea.

5.3.2 What controls DMS in the arctic BL ?

In spite of the evidence that the extensive ice cover is the main reason for low DMS levels measured at Kuujjuarapik, depletion processes are surely an additional factor reducing atmospheric mixing rates of this compound. The contribution of dry and wet deposition is presumably minor regarding DMS depletion, but has to be considered for its oxidation products as DMSO and notably SO_3.Radical species such as OH, NO_3 and BrO are assumed to determine widely the atmospheric lifetime of DMS, motivating the now following discussion. When talking about the relationship of Dimethylsulphide and radical species, one of the fundamental parameters to derive is the specific atmospheric lifetime, i.e. what would be the

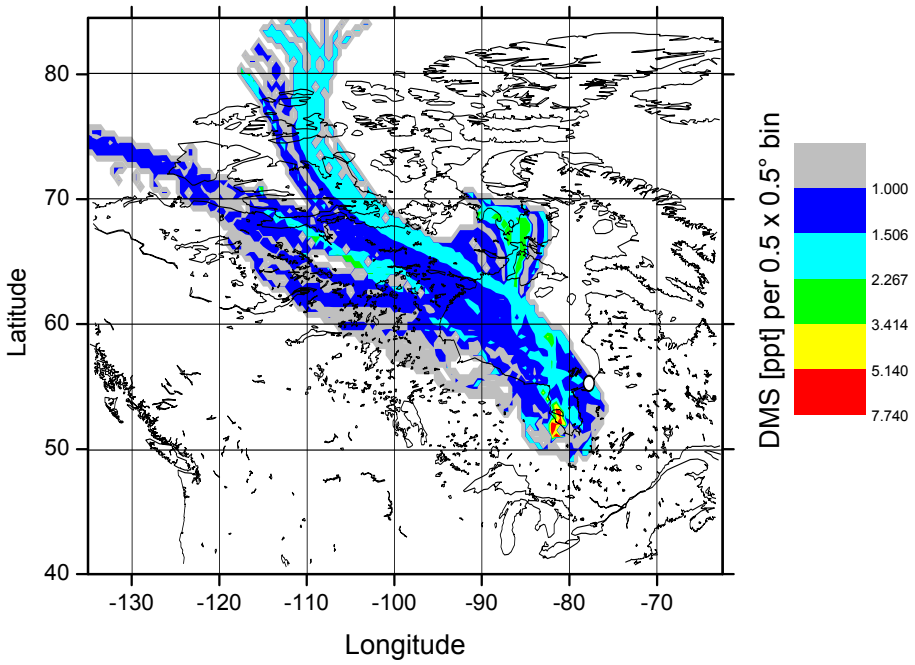

Figure 5.15: Distribution matrix of average DMS concentrations related to trajectory results.

lifetime of a DMS molecule assuming the exclusive reaction with a certain radical species at given mixing ratio ? The lifetime can be derived using the simple relationship

$$\tau_{DMS}(species) \;=\; 1/[species] \times k_{DMS+species} \tag{5.23}$$

In Table 5.5 the lifetime of DMS for the exclusive reaction with a series of radical species has been derived. The denoted concentration ranges correspond to the DMS sampling period from 15.04. until 30.04.2001. The concentrations of atomic Chlorine (Cl) [Platt and Hönninger 2003] and chlorine oxide (ClO) [Tuckermann et al. 1997] should be considered as upper limits as they correspond to typical levels found in the arctic. The OH concentration is a diurnal mean value for the month of April derived from aircraft measurements of the TOPSE Project [Wang et al. 2003] which is in the same range as the value of 0.5 molecules/cm^3 derived from model results of von Kuhlmann [2001]. Also taken from [Wang et al. 2003] is the diurnal mean value given for HO_2, which in fact was given for RO_2 radicals, therefore representing an upper limit for this radical species.

According to the results of Table 5.5, the nitrate radical at concentrations levels of the lowest DOAS detection limit (2 ppt) would be the most efficient sink of DMS. However, one has to take into consideration that background levels of NO_2, the main precursor species of the nitrate radical, remained below 80 ppt unless local pollution events occurred(section 4.2.3). According to the large set of measurements presented by [Wang et al. 2003], the levels of NO_2 in the Arctic range between 10 and 20 ppt on average in April. A more realistic

Table 5.5: Calculated DMS lifetimes for observed or derived mixing ratios during the Hudson Bay field campaign from 15.04-01.05.2001. All reaction rates derived from Atkinson2003 at T=268K if not indicated otherwise.

Reactive species	Rate constant k_{268} $[cm^3 molecule^{-1} s^{-1}]$	Concentration Range(Mean) [ppt]	DMS lifetime (Mean)
BrO	$6.1e^{-13}$ (a)	<0.6 - 28.6 (2.8)	0.6 - 30 hours (6.5 hours)
ClO	$4.5e^{-15}$ (b)	<1.3 - 3.3 (1)	28-72 days
IO	$1.3e^{-14}$	<0.8	25 days
Cl	$5.8e^{-11}$ (b)	0.4-4 $\times 10^{-3}$ (2)	2 days
OH	$1.5e^{-11}$	16×10^{-3} (3) (noon: 50×10^{-3})	26 hours (noon: 14 hours)
HO_2	$5.0e^{-15}$	14 (3)	7 days
$O_3(g)$	$1.0e^{-18}$	36200 - 61400	8 - 15 days
$O_3(aq)$	$6.34e^{-12}$ (c)	30000	5 days
NO_3	$1.1e^{-12}$	<2	>4 hours$^{(\star)}$

(1) DOAS measurements of Tuckermann et al. [1997] in the Arctic
(2) Platt and Hönninger [2003], (3) diurnal mean values Wang et al. [2003]
(a) Ingham et al. [1999], (b) Díaz-de Mera et al. [2002],
$^{(\star)}$ see comments in text below

estimation of applicable NO_3 levels can be obtained from the chemical box model MOCCA to be presented in the following section. According to the model the ratio of NO_3 is expected to be around 0.6 ppt, which would lead to a DMS-lifetime about 3days. Therefore, Bromine oxide has to be considered the most efficient species regarding DMS oxidation during the measurement period at Kuujjuarapik. This statement is substantiated by the fact that the origin of air masses reaching the site was mostly polar, whereby average OH mixing ratios may be even below estimated values.

Nevertheless, a direct comparison of the concentrations of DMS and BrO does not show any tight relationship (Figure 5.16). This was not expected anyway as the sampling time of 4 hours required for each DMS and DMSO measurement does not allow the observation of short term variations expectable for highest BrO levels observed. Another point is that the strength of the reaction between DMS and BrO is significantly below the one found for DMS and the nitrate radical in Crete(section 5.2). A meaningful step to investigate the relation of DMS and BrO is the calculation of the DMSO to DMS ratio. As the the major product of the reaction of DMS with halogens is supposed to be DMSO, the DMSO to DMS ratio should grow accordingly. In Figure 5.16 the mixing rates of BrO and ozone have been related to the DMSO/DMS ratio. The NO_2 photolysis (JNO2) rate has been included in the figure to allow an estimation of OH radical formation as no measurements of this radical species neither of the ozone photolysis rate have been performed. The time series presented for ozone correspond to in situ measurements provided by Laurier Poissant, Meteorological Service of Canada. Although recorded at the Centre d'Etudes Nordiques at few kilometers distance from the DOAS container(section 4.2.1) the data is in good agreement with DOAS measurements [Hönninger 2002]. The continuity of the ozone monitor recordings allows an estimation of BrO levels during DOAS blackout periods due to low visibility or technical reasons (anticorrelation of BrO and O_3). The comparison of the DMSO to DMS ratio to

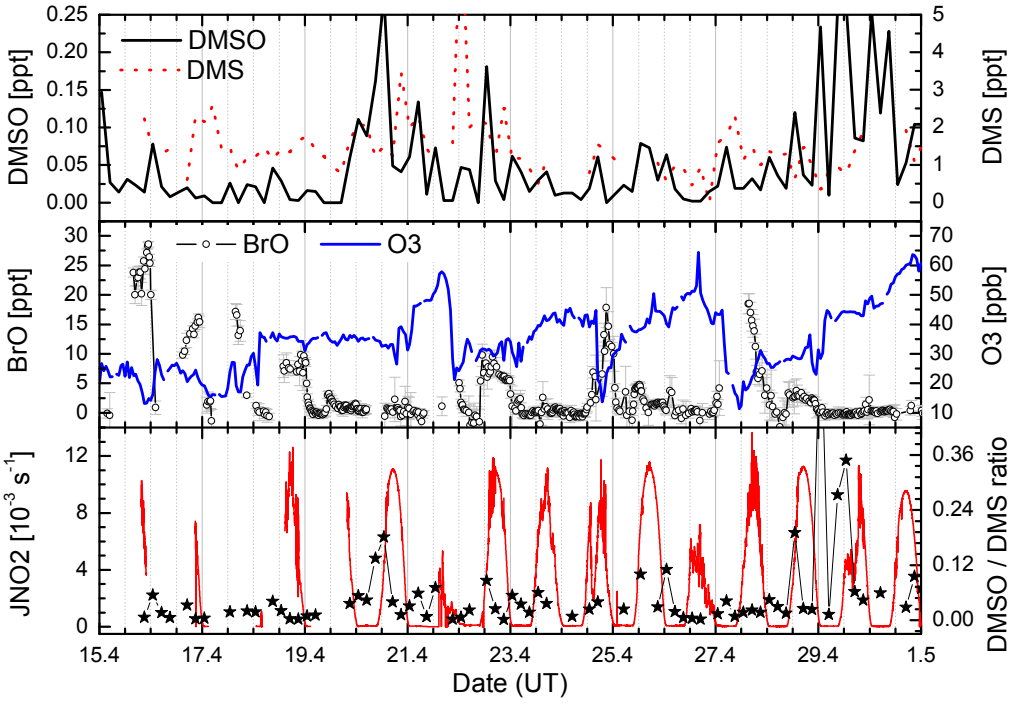

Figure 5.16: Comparison of the mixing ratio of BrO and the DMSO/DMS rate. For completion the ozone, DMS and DMSO levels are shown(see text).

Bromine oxide does not allow definitive conclusions, but as on 20,22,25,28 and 29 April the highest DMSO to DMS ratios seem to correspond to the early morning measurement at 08:00 local time. The exceptionally high DMSO levels observed on 29th April can hardly be assigned to DMS oxidation via BrO as at that time the mixing ratios of the halogen radical had decreased to background levels.

The diurnal mean variations of DMS, DMSO, BrO and ozone are shown in Figure 5.3.2. A striking observation is the strong decrease of DMS within the first hours of day, unlike the common observation in pristine marine environments depicting a minimum around noon corresponding to highest OH formation rates. Along the DMS depletion period appreciable amounts of DMSO are formed. As the highest mixing ratio of OH radicals is not achieved until noon, BrO radicals are the most suggestive species to account for the early morning depletion. As described in section 2.2.3, bromine oxide is formed rapidly after sunrise due to photolytical destruction of the nighttime reservoir species (Br_2, BrCl) and the reaction of bromine atoms with ozone whose decay is still enhanced due to photolysis until noon. The experimental observation is in agreement with model results of von Glasow and Crutzen [2003] for the pristine marine boundary layer, stating that the inclusion of halogens changes the diurnal cycle of sulphur species by starting the destruction of DMS earlier in the morning whereby the mixing ratios of the oxidation products (DMSO, MSA and SO2) also peak earlier in the course of day.

After the early morning minimum the concentrations of gaseous DMS and DMSO increase continuously until sunset. The pitch for DMS is significantly weaker until noon, when strongest depletion rates via the OH radical are achieved and mixing rates of BrO decrease

slightly due to photolytical destruction. The increase of DMS grows in strength as the photolytic flux and consequently the concentration of OH radicals recedes throughout the afternoon. The significantly slower regrowth of ozone after the rapid destruction until midday can be related to the simultaneous increase of BrO which achieves highest mixing rates right before sunset.

A reasonable argumentation explaining the simultaneous increase of BrO and DMS throughout the afternoon could be based on the existence of a DMS source that grows in strength throughout the day and vanishes after sunset. As we know from the previous section, the sources of DMS are probably melt ponds and drain holes on the ice around Kuujjuarapik which should even increase in strength further southward (James Bay). The ponds will certainly grow in extension as long as exposed to solar radiation and the consequent warming of the surface layer. According to the average diurnal soil temperature profile shown in Figure 5.18, thaw is possible throughout sunlit hours of day and seems to be strongest in the afternoon in conformity to the observed DMS formation. After sunset the decrease of temperatures should lead to a refreeze of the puddles and perforations on the sea ice cover sealing the DMS emission source. The freezing source would explain the second increase of the diurnal DMSO to DMS ratio depicted in Figure 5.3.2 as DMS is depleted forming DMSO as long as BrO radicals are available in the night. During the rest of the night no oxidizing radicals are present and both DMS and DMSO concentrations decrease conjointly throughout the night probably as a result of deposition processes.

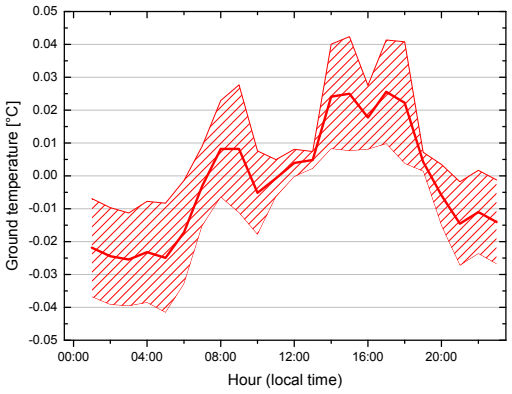

Figure 5.18: Average diurnal progression of the soil temperature from 15.-30.04.2001 at Kuujjuarapik (error margins displayed as pattern around curve).

The comparison of the base run and the model run including halogen emissions shows a decrease of NO_x in general when including halogens. The highest NO_3 concentration reached right before dawn would be 0.8 ppt in a halogen free atmosphere and reduce to 0.5 ppt for background halogen concentrations (max. 1 ppt BrO during day). At this levels, the calculated DMS lifetime would be around 10 and 17 hours respectively.

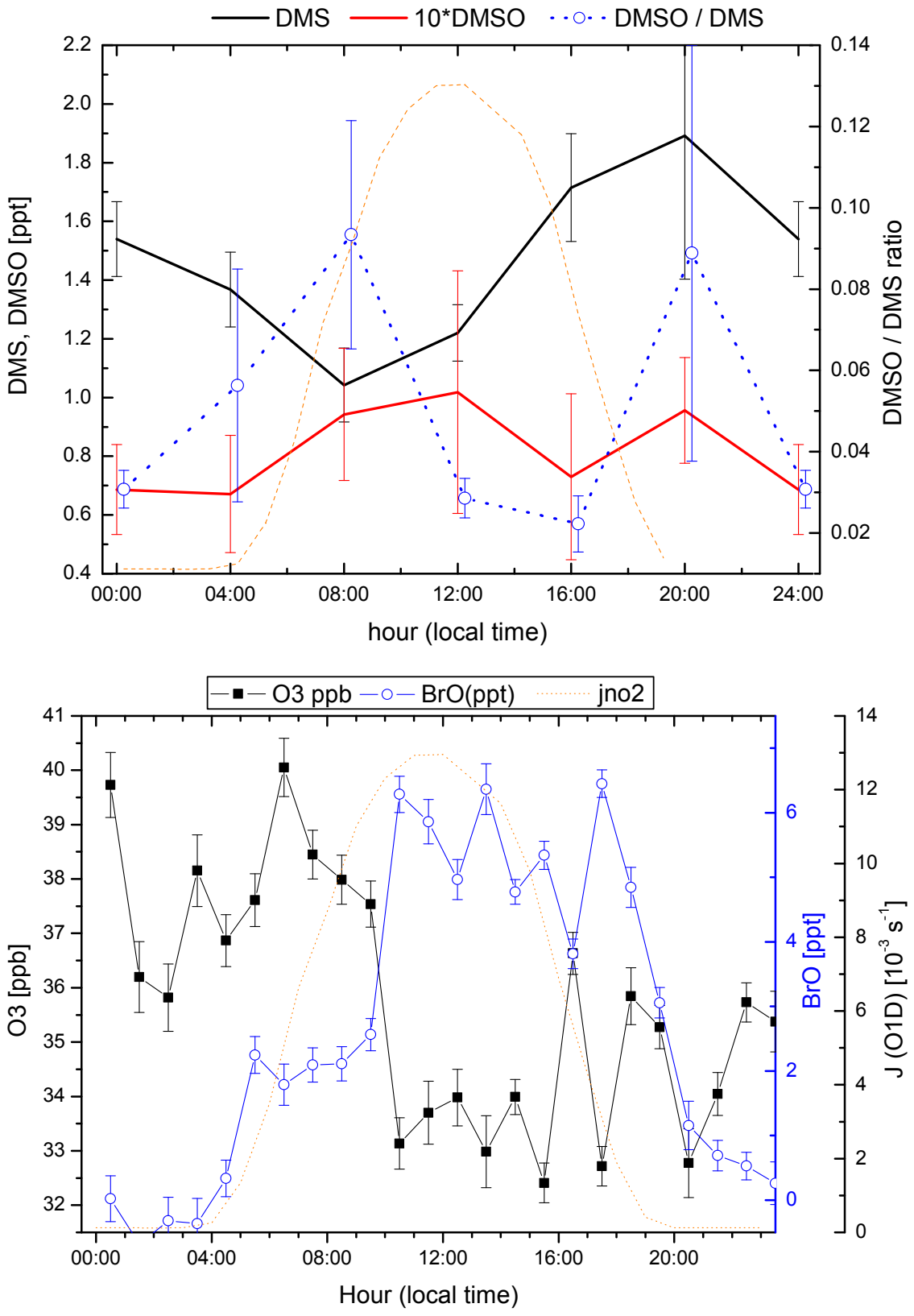

Figure 5.17: Average diurnal variation of the atmospheric mixing ratios of BrO, ozone, DMS and DMSO for the period from 15.-30.04.2001. For completion, the averaged NO_2 photolysis rate is shown in both graphs. The error bars for the DOAS results are mean errors. For DMS and DMSO the standard deviation is given.

5.4 The DMS oxidation chain at Kerguelen

As the mixing rates of most trace gases measured with DOAS on Kerguelen remained below detection limits, the established DMS oxidation schemes for the final campaign are based to an important extent on concentration levels estimated with the MOCCA model or have been extracted from the model study of [von Kuhlmann 2001]. Contrary to Amsterdam Island, atmospheric trace gas measurements reported for Kerguelen restrict to the one day study presented in [Hönninger 2002]. The results of field measurements at Cape Grim and Antarctica may be representative for the southern ocean and apply in general terms for the study in Kerguelen as well. Therefore a maximum level of NO typical for the remote Indian ocean was fed into MOCCA to obtain the correspondent diurnal variation. The concentration of OH radicals was estimated by comparison of the photolysis rates of ozone (JO1D) measured at Crete and Kerguelen using the same sensor. An overview of employed parameters is given in Table 5.6. Due to the pristine environment poor in NO_x, the concentrations of the nitrate radical NO_3 are presumably too low to have any significant effect regarding nightime oxidation of Dimethylsulphide. The mean lifetime of DMS against the reaction with NO_3 is about 35 days and unless heterogeneous reactions contribute to DMS depletion, we can assume that no nighttime sinks exist. Estimations about heterogeneous chemistry are extremely difficult for Kerguelen, due to the high variability of weather conditions, frequent rain and strong winds blowing clouds quickly past over the Islands. According to the diurnal variation of DMS derived from measurements attaing highest mixing rates right before dawn (section 4.3.4) the role of heterogeneous chemistry at night is probably negligible.

During daytime the weight of the abstraction and addition path for the DMS+OH reaction is about equal. BrO radical concentrations at the upper limit established by the DOAS measurements would significantly accelerate DMSO formation. Further on the addition path, the yield of $DMSO_2$ is once again probably negligible due to low NO levels. The reaction of DMSO+OH and the formation of CH_3SO seem to be concurrent processes ocurring on a similar time scale(3 hours). Whereas MSIA has probalby no contribution to CH_3SO_2 formation and will decay to SO_2, reaction of the DMS-OH adduct with oxygen could contribute upon a certain extent to the addition path and thus to MSA formation.
After the bottleneck of the initial DMS+OH reaction the progress on the abstraction path is much faster than on the addition path and can lead to MSA formation within 15 Minutes on average. However, due to the low levels of NO_x, as already stated for the arctic(section 5.3) the 10 times higher efficiency of the CH_3SO reaction with ozone and the thermal decay of CH_3SO_2 will inhibit strongly MSA formation.
An overall conclusion of the DMS oxidation schemes at Kerguelen is that this location probably attains the lowest DMS oxidation rates among all three field campaigns discussed in this thesis. This is certainly a consequence of absent pollution (nitrate compounds) and the low levels of oxidsing species, as OH and ozone, in general. A comparison of the DMSO to DMS and MSA to DMS rates of all three field campaigns confirms this results(Table 5.7.

Table 5.6: Average trace gas concentrations at Kerguelen over the period from 21.01.-21.02.2002, derived from measurements, taken from literature or estimated using the MOCCA Model.

Trace gas	Mean Concentration $[molec./cm^3]$		Source
	Night (19-05 LT)	Day (05-19 LT)	
BrO	$< 3.5 \times 10^7$	$< 3.5 \times 10^7$	DOAS
IO	1.1×10^6	1.8×10^7	
O3	3.2×10^{11}	3.0×10^{11}	
SO2	9.7×10^8	1.1×10^9	
DMS	5.5×10^9	5.3×10^9	GC
DMSO	7.5×10^7	9.4×10^7	Mist chamber
MSA	2.2×10^8	2.6×10^8	IC
CO	1.0×10^{12}	1.1×10^{12}	Monitor
NO2	3.6×10^8	2.1×10^8	DOAS/MOCCA a)
NO	7.8×10^5	1.1×10^8	estimated
OH	2.5×10^3	8.3×10^5	b)
H2O2	3.9×10^9	3.9×10^9	KUH01
HCHO	2.6×10^9	2.6×10^9	KUH01
HO2	3.4×10^6	1.2×10^8	MOCCA
RO2	3.9×10^7	1.3×10^8	
NO3	2.7×10^5	2.6×10^1	MOCCA
Br	2.5×10^3	2.5×10^6	MOCCA
Cl	1.2×10^1	4.8×10^3	
ClO	6.5×10^5	4.1×10^6	
	Mean diurnal Concentration [M]*)		
$H_2O_2(aq)$	$10 - -200 \times 10^{-6}$		c)
OH(aq)	$5 - -50 \times 10^{-14}$		
$O_3(aq)$	$5 - -50 \times 10^{-14}$		

a) nighttime values from DOAS, daytime values from MOCCA
b) derived from JO1D rate comparison Crete/Kerguelen
c) [Herrmann et al. 2000; Lelieveld and Crutzen 1991; Jacob 1986]
*) divided by 300 if no clouds present

Table 5.7: Comparison of the ratios of MSA and DMSO relative to DMS for the field campaigns at Crete, Kuujjuarapik and Kerguelen.

	Crete (Mediterranean Summer)	Kuujjuarapik (Subarctic Spring)	Kerguelen (Austral Summer)
MSA / DMS	0.12	0.44	0.05
DMSO / DMS	0.06	0.06	0.02

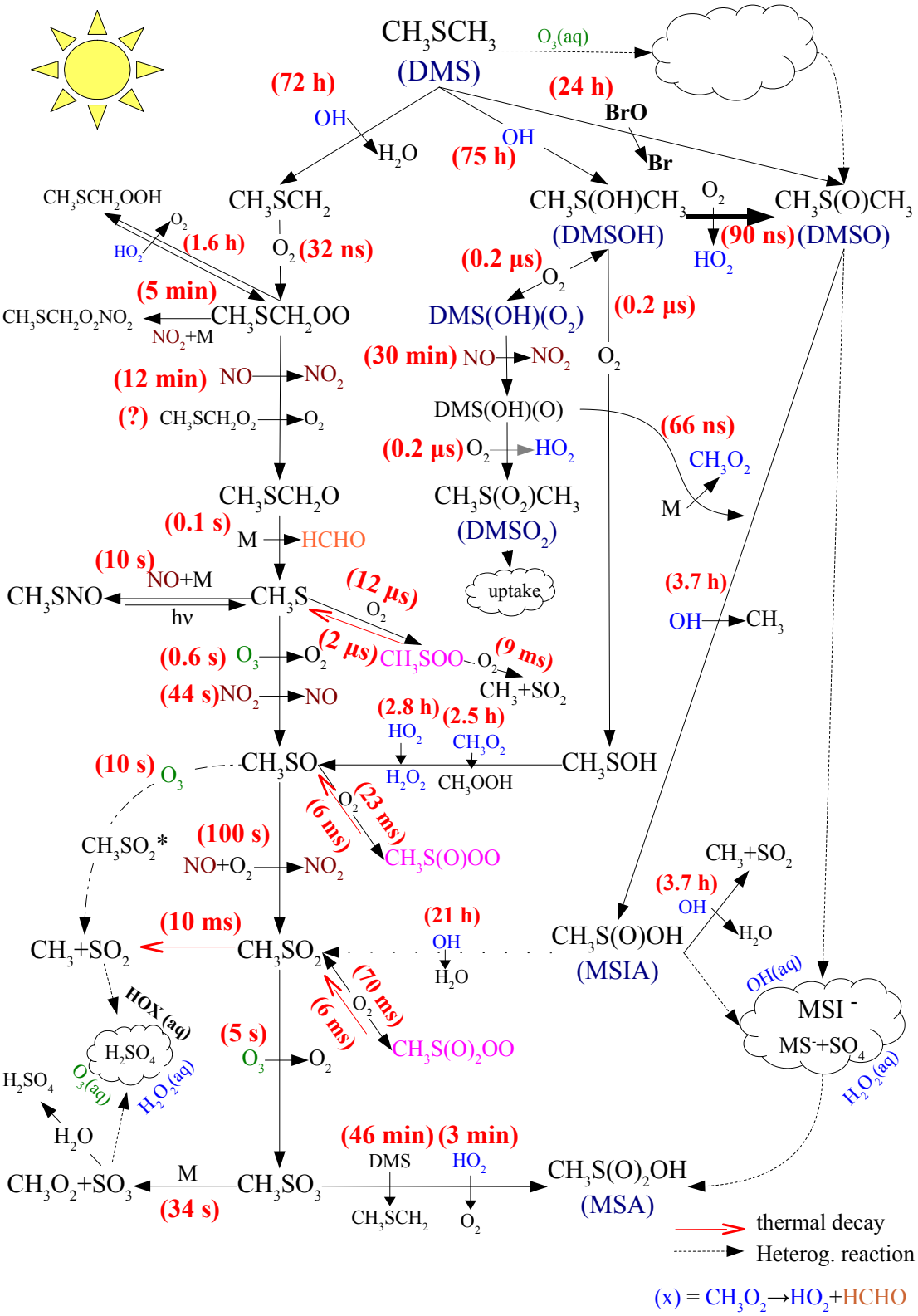

Figure 5.19: Oxidation chain of Dimethylsulphide for average daytime trace gas mixing ratios established during the measurement campaign at Kerguelen (Indian Ocean) from 21.01-21.02.2002.

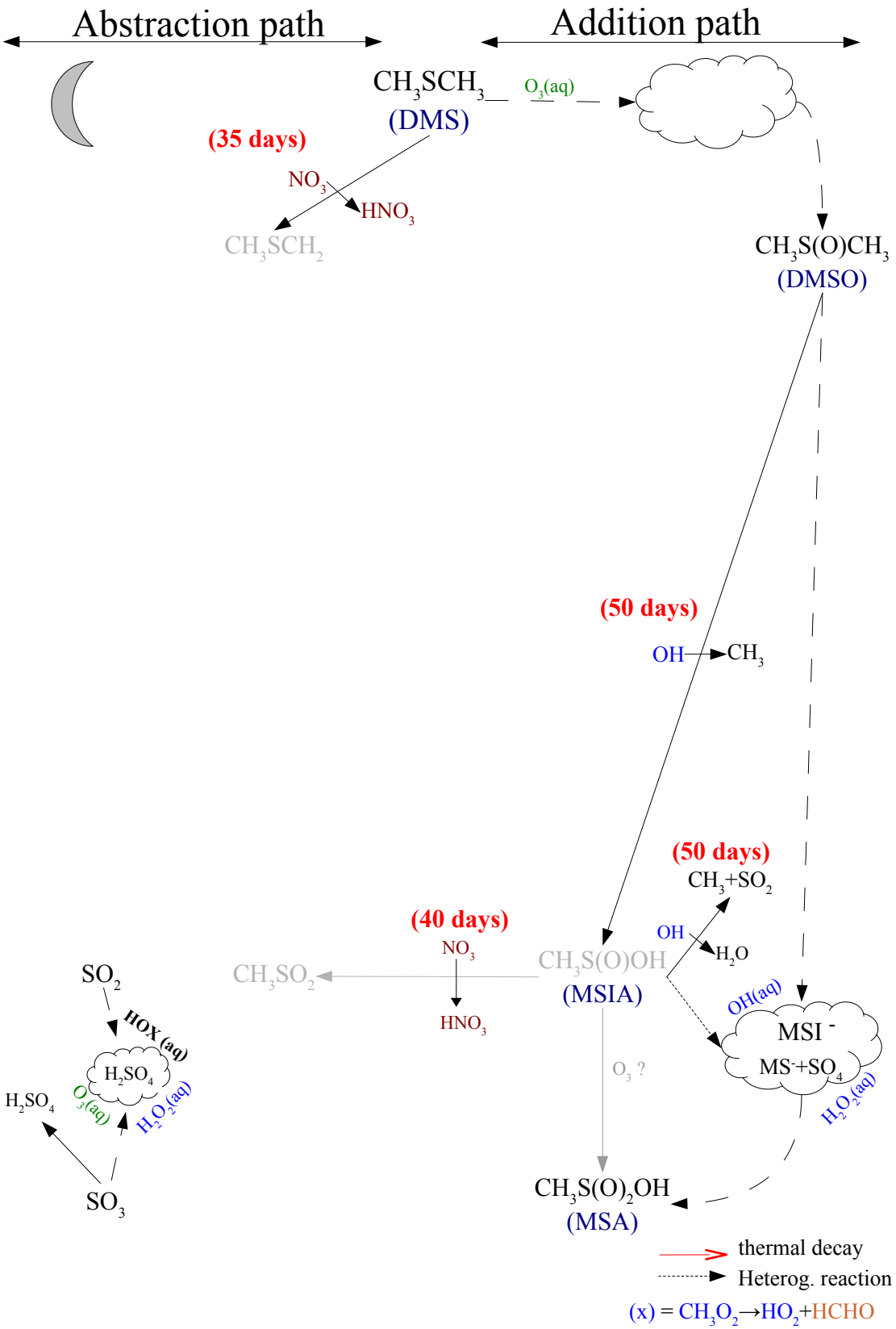

Figure 5.20: Oxidation chain of Dimethylsulphide at nighttime for mean trace gas concentrations established during the measurement campaign on Kerguelen (21.01-21.02.2002).

5.4.1 Source distribution and possible influences of halogen oxides at Kerguelen

The results of sections 4.3 and 5.4 have shown that the atmospheric concentration of halogen oxides at Port aux français is too low to have a notable impact on gaseous DMS on short time scales. Due to the increased detection limit (compared to previous measurements at Crete and Kuujjuarapik), the existence of halogen radicals in the marine boundary layer at Kerguelen can be acknowledged only for singular values. Most important concentrations of all radical species have been found for IO which is not an efficient direct sink for DMS but can have severe implications in the oxidation process as halogens in general influence the HO_x cycle and ozone destruction rates in the MBL [Vogt et al. 1999]. As OH radicals presumably are the main oxidizing species in the whole area of the remote Indian Ocean, any parameter influencing the atmospheric concentration of this radical will have an effect on the atmospheric lifetime of DMS. Due to the poorness in NO_x and in extension NO_3 around Kerguelen the role of halogen radicals gains additional importance.
The mixing rates of halogens measured at Kerguelen seem to be slightly above of those published by Allan et al. [2000] for Cape Grim($40°41'S144°41'E$) who measured maximum IO levels of 0.9 ppt in the same season. This is in agreement with significantly higher mixing rates of Alkenes measured at Kerguelen(section 4.3.4) compared to Cape Grim [Lewis et al. 2001]. According to model results presented by B.Bonsang in the final report of the EL CID project(Website: http://www.physchem.uni-wuppertal.de), the marine production of alkenes deduced from the comparison of measured and simulated variations is about one order of magnitude greater than the usual figures reported at these latitudes. This is not a surprising result when looking at Chlorophyll A measurements provided by the SEAWIFS Satellite project(Figure 5.4.1) which states high biogenic activity around all islands located on the Kerguelen-Gaussberg ridge, including the Kerguelen Islands in the north and the Heard and McDonald Islands further southeast. Within an area ranging from roughly $45 - 70°S$ and $60 - 85°E$, called the Kerguelen plateau, the ocean depth decreases below 700 meters which should allow abundant algae growth. The Chlorophyll measurements state that the highest productivity is achieved in December, at the begin of the austral summer probably as a consequence of algal bloom and decreases continuously in the following months.

One of questions one might have when looking on Figure 5.4.1 is whether the abundant chlorophyll production observed in December takes place in open sea waters or is just the outflow of coastal production at Kerguelen transported further eastward due to the wind induced sea surface current. Studies of the local distribution of marine carbon emission have shown that the convergence zone, i.e. the coast of Kerguelen, has the maximum productivity in this geographical region (up to 30 $mgCarbonm^{-2}day^{-1}$), in particular at surface waters. The land effect induces a phytoplankton enrichment, associated to a change in composition. Studies of water masses around and south of Kerguelen [Duchêne 1989] show an amazing decrease of carbon emissions (around 2.7 $mgCarbonm^{-2}day^{-1}$) once leaving the coast. The relative poorness of planktonic organisms is corroborated by measurements of water transparency: the euphotic layer (wherein surface light decreases to 1%) oscillates between $70 - 80\ m$ depth in open waters and decreases to $20\ m$ in the coastal range.

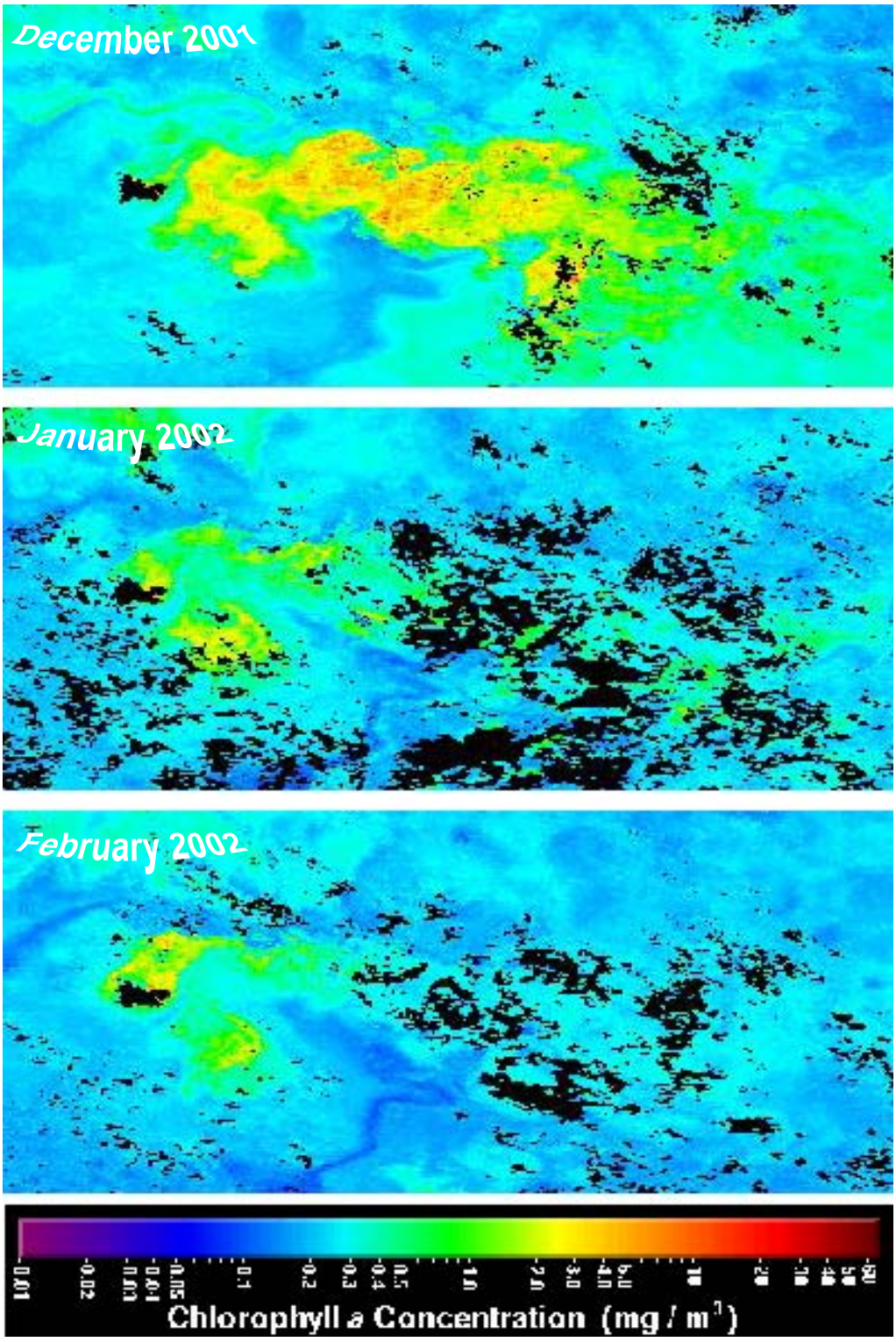

Figure 5.21: Chlorophyll A distribution in surface waters around Kerguelen Islands (48–57° S, 65–95° E) provided by the SeaWiFS Project, NASA/Goddard Space Flight Center and ORBIMAGE. The highest biogenic activity was observed at the start of the austral summer in December and decreased steadily during the following months. The large productive areas correspond with the marine plateaus surrounding Kerguelen and the Heard and McDonald Islands further southeast. All black areas on the graph correspond to regions where no Chlorophyll A was detected, including the Kerguelen Islands highlighted by a red circle.

The highest productivity of algae carbon emissions was found at the northeast of the main island and is probably a consequence of the larger extension of the Kerguelen plateau to the north and a complex mixing process of ocean currents explained in detail in [Duchêne 1989]. The measurements state that the integrated production of this area is two times higher than the average productivity found for the Antarctic ocean. This is in perfect agreement with Chlorophyll–A emissions detected by the SEAWIFS instrument(Figure 5.4.1) which also state that the strongest sources correspond to the northeastern part of the island. The large amounts of Chlorophyll detected east of the Kerguelen can not originate from local algal emissions as the sea depth increases to more than 1000 meters within few hundred kilometers further east(Figure 5.22), leading to the conclusion that algae emissions from Kerguelen and probably phytoplankton formed in the coastal layer are transported quickly off the island by the surface water flux.

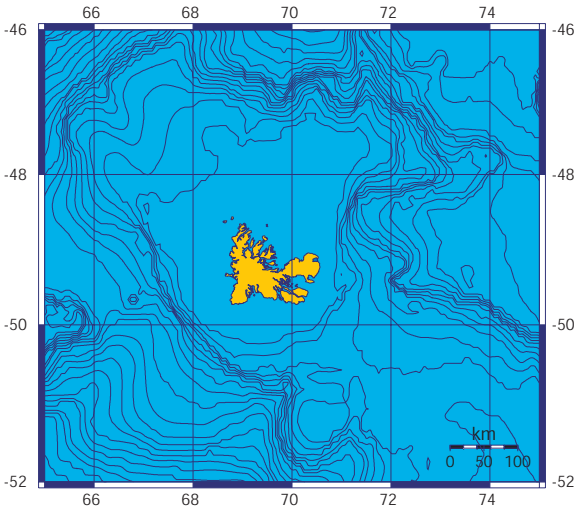

Figure 5.22: Bathymetric map of the sea around Kerguelen(GMC Map).

Another aspect which has to be taken into consideration is that Chlorophyll–A emissions and thus algal growth must not be directly related to high halocarbon emissions. First of all, Chlorophyll–A has a different formation mechanism than most of the investigated halogenated compounds. It is commonly chosen as an indicator for the biomass of phytoplankton because chlorophyll can be determined more easily than can other relevant biological parameters. Simultaneous measurements of organohalogens and chlorophyll in sea water [Schall et al. 1997] have shown that the latter could be used as an indicator for the biogenic formation of brominated compounds, whereas the correlation between chlorophyll-A and the iodinated substances was not of the same quality.
Another point is that from all organohalogen species, only bromoform(CH_3Br) and dibromomethane(CH_2Br_2) seem to have a positive correlation, indicating that both compounds share a common origin (enzymatic bromination). The studies of Schall et al. [1997] on a crossect of the Atlantic ocean found no correlation either between the iodinated and the brominated substances or between the different iodinated compounds. This is consistent with findings of [Laturnus et al. 1998] and many other studies, suggesting that a large number of different biological formation mechanisms for all these substances exists. Although the halogenation of organic matter in marine macroalgae are basically understood, the formation mechanisms for the variety of halogenated C1 to C4 compounds remain poorly known. Extensive laboratory studies of phytoplankton [Tokarczyk and Moore 1994] and macroalgae [Laturnus et al. 1998; Laturnus et al. 2000; Laturnus 2001] have shown that

emission rates of the different halogenated compounds depend largely on the contemplated algal species. For tribromomethane($CHBr_3$), the most abundant organobromine compound, highest emission rates have been found at day, nighttime or for dead, decaying algae dependent on algae species [Mäkelä et al. 2002]. Whereas measurements of iodinated hydrocarbon emissions from macroalgae species mostly show the direct and significant input of these compounds into the atmosphere during periods of low tide [Mäkelä et al. 2002; Giese et al. 1999]. The most abundantly emitted iodine species released from macroalgae seems to be diiodomethane(CH_2I_2), followed by other iodine hydrocarbon compounds as 1 or 2-iodpropane and chloroiodomethane(CH_2ClI) in varying sequential order, depending on algal species.
Due to the largely different photolytic lifetimes, ranging from 5 (CH_2I_2) and 45 minutes (CH_2BrI) to several hours (CH_2ClI) or days (CH_3I), atmospheric mixing rates of iodocarbon species often do not correspond to marine emissions. Indeed, Carpenter et al. [2003] detected exclusively CH_3I and CH_2ClI at Cape Grim during the same season as DOAS measurements in Kerguelen. The measurability of the short living iodine compounds as CH_2I_2 and CH_2BrI is bound to strong emission sources as found in intertidal regions.
Due to the extremely strong winds, the fast weather variability and the open ocean environment the measurements at Kerguelen probably can't be compared to measurements in coastal continental areas as Mace Head or Brittany. The location at Cape Grim could be a reference, although it's emplacement 10 degrees further north, the possible influence of the Australian continent and different meteorology do not allow a straightforward correlation. Most likely the measurements at Kerguelen represent marine background conditions occasionally influenced by coastal emissions enhancing the levels of IO if halocarbons are photolyzed quickly enough to allow IO formation before being blown off to the open ocean.

The role of iodine As the obtained datapoints of IO above detection limits at Kerguelen are too few to allow any statistical evaluation based on measurement results, only general considerations can be made.
It is known from Literature that unlike chlorine and bromine atoms, which react with a range of organic molecules, the major fate of iodine atoms is the reaction with O_3, forming the iodine monoxide (IO) radical. However, due to the rapid photolysis of IO a daytime steady state exists between I and IO(collectively termed IO_x) whereas this cycle has no net effect on IO_x or O_3 chemistry. Several years ago Vogt et al. [1999] presented a theoretical study using MOCCA considering iodine chemistry and its role in halogen activation and ozone loss in the marine boundary layer. The addition of iodine chemistry to the reaction scheme of the model had the effect of accelerating photochemical Br and Cl release from sea salt, causing an enhancement in ozone destruction rates in the marine boundary layer. In low NO_x environments, an important sink for ozone may arise from the reaction of IO with

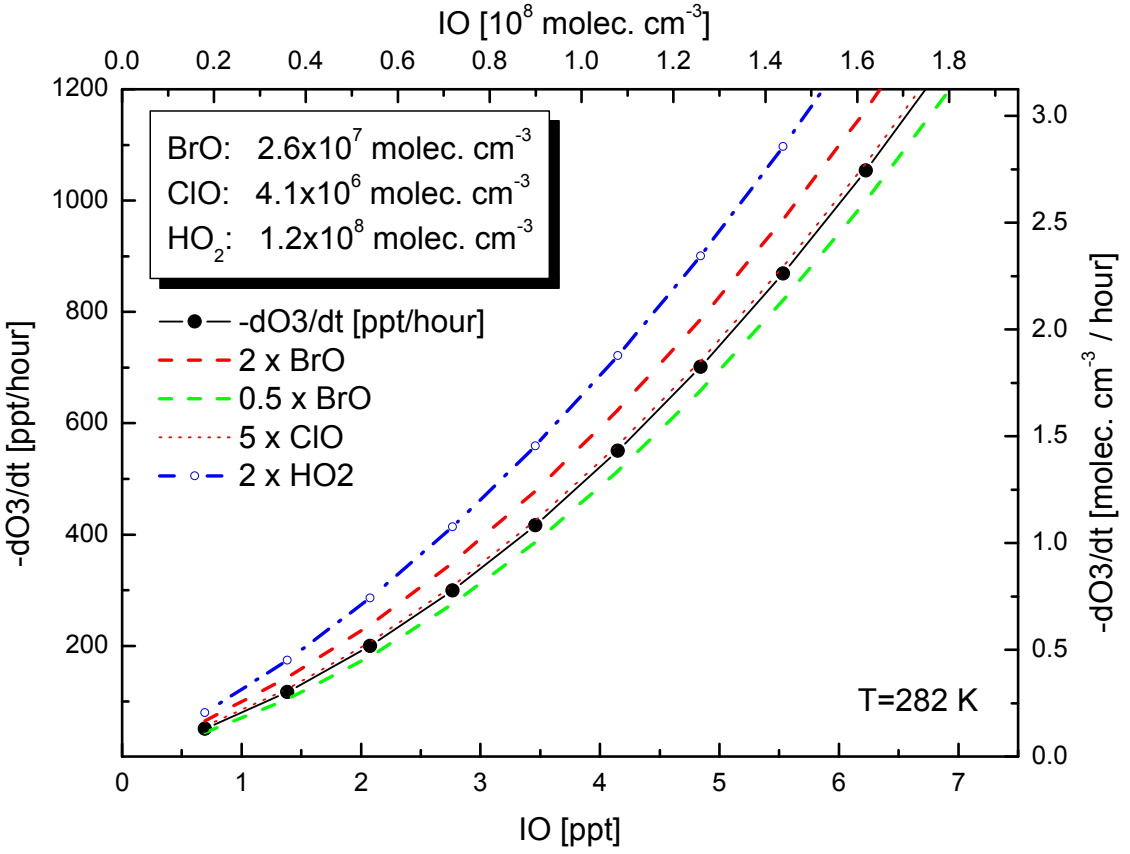

Figure 5.23: Estimation of ozone depletion rates using formula (2.47) presented in section 2.2.3. All rate constants at 282 Kelvin. The rapid increase of hourly ozone depletion rates shows that the lifetime of ozone is quite sensitive on IO mixing ratios. The assumed concentrations of all halogens are indicated. Variation of BrO within expectation limits will vary the O_3 depletion rate within 10-20%, whereas ClO has no effect on this rate.

HO_2 forming hypoiodous acid (HOI):

$$I + O_3 \longrightarrow IO + O_2 \tag{5.24a}$$

$$IO + HO_2 \longrightarrow HOI + O_2 \tag{5.24b}$$

$$HOI + h\nu \longrightarrow OH + I \tag{5.24c}$$

$$\text{net:} \quad O_3 + HO_2 \longrightarrow OH + 2\,O_2$$

Indeed, HOI is believed to be the major compound of gas phase inorganic iodine [Davis et al. 1996] and an important route to the aerosol phase. Under high NO_x conditions ozone is regenerated through the reaction of IO with NO and NO_2, whereas at NO_x levels below 500 ppt the above described cycle has been suggested as the dominant O_3 loss cycle. As discussed already in section 2.2.3 the ozone destruction destruction potential of this cycle in dependence NO_x has been investigated by Stutz et al. [1999]. As NO_x levels in Kerguelen (about 10–15 ppt) correspond to the lowermost edge of the scale of Figure 2.4, the calculated

ozone loss would be about 0.3 ppb per hour from the HOI cycle.
Stutz et al. [1999] calculated the ozone depletion rate for 6 ppt IO. As this rate is too high for Kerguelen, a more suitable estimation was done using equation (2.47) presented in section 2.2.3. All concentrations of halogen species correspond to those given in Table 5.6. The rapid increase of hourly ozone depletion rates as shown in Figure 5.23 states that the lifetime of ozone is quite sensitive on IO mixing ratios. The assumed concentrations of all halogens are indicated. Variation of BrO within the expectable limits (double or half) will vary the O_3 depletion rate within 10-20%, whereas ClO has no effect on this rate. Surely the cycle is very sensitive on HO_2 variations. Doubling the mixing rate changes the amount of ozone depletion in the range of 20-50%.
For comparison, the diurnal variation of ozone established from measurements at Kerguelen is shown in Figure 5.24. Ozone shows a decrease of roughly 0.8 ppb within 4 hours starting about 10:30 in the morning and reaching the diurnal minimum in the early afternoon around 14:30 local time. The recuperation is similarly fast afterwards and ozone regrows to original levels right before dawn. After sunset ozone concentrations drop quickly within the first 2 hours of darkness to continue decreasing slowly until the early morning. The diurnal variation of NO_2 established from DOAS measurements (Figure 5.25) delivers an easy explanation for the nighttime ozone depletion. It has been noted before (section 4.3.3) that local pollution from the power generators of the base and ships at the peer was common. Due to the regularity of ozone depletion and the minimum shortly after noon, photochemistry obviously plays an important role in the oxidation process of ozone in Kerguelen. Yet ozone photolysis alone and OH cannot account for the observed depletion amount. Considering IO mixing rates in the order of 1–2 *ppt* as average for this area of measurements, from Figure 5.23 we obtain an ozone depletion rate of 200 ppt per hour. This rate will be even higher at noon, as both IO and HO_2 will attain highest concentrations around noun and thus significantly pronouncing the drop of ozone levels. Another method to establish the influence of IO on ozone offers the model MOCCA, which was run with starting parameters given in Table 5.6 under 4 different starting conditions. First, a base run, without with no sea salt emissions and no halocarbons (i.e. no halogens at all). Second, including sea salt aerosol and thus bromine and chlorine emissions typical for the remote boundary layer. Third, including sea salt aerosols and iodocarbon emissions leading to maximal rates of approximately 1 ppt. And Fourth, multiplying iodine emissions by a factor of 10. The comparison of the model runs states that the presence of Iodine consistently reduces ozone levels leading to a decrease of roughly 500 ppt ozone per day at IO mixing rates expectable at Kerguelen (about 1 *ppt* on average). According to IO+HO2 cycle presented above, the model results state that mixing rates of HO_2 are reduced in the presence of Iodine and HOI formation exceeds slightly those of IO. As already found by [Vogt et al. 1999] the production of BrO can be enhanced in the presence of iodine. However this seems to be dependent on the levels of IO as for the high iodine environment simulated in the fourth model run, BrO concentrations drop continuously after the initial "bromine explosion". For both emission levels of iodine, DMS concentrations fall significantly and strong peaks of DMSO are observed in the morning, indicating that the additional DMS depletion is probably a consequence of enhanced BrO levels. The influence

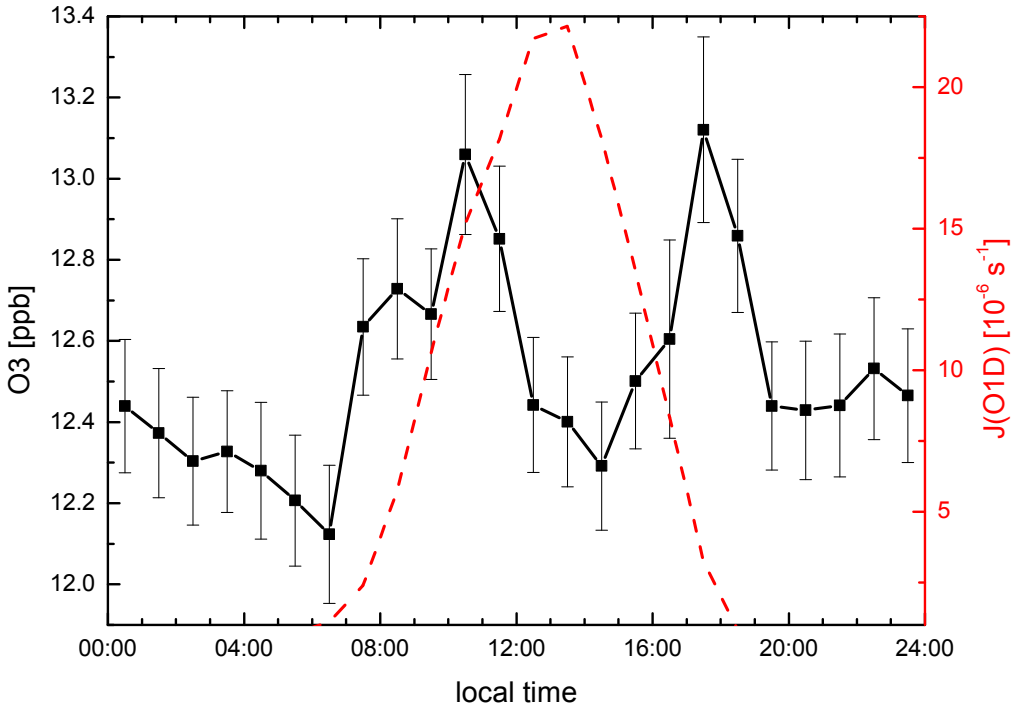

Figure 5.24: Mean diurnal variation of ozone mixing ratios established from measurements performed on Kerguelen from 21.01 to 21.02.2002.

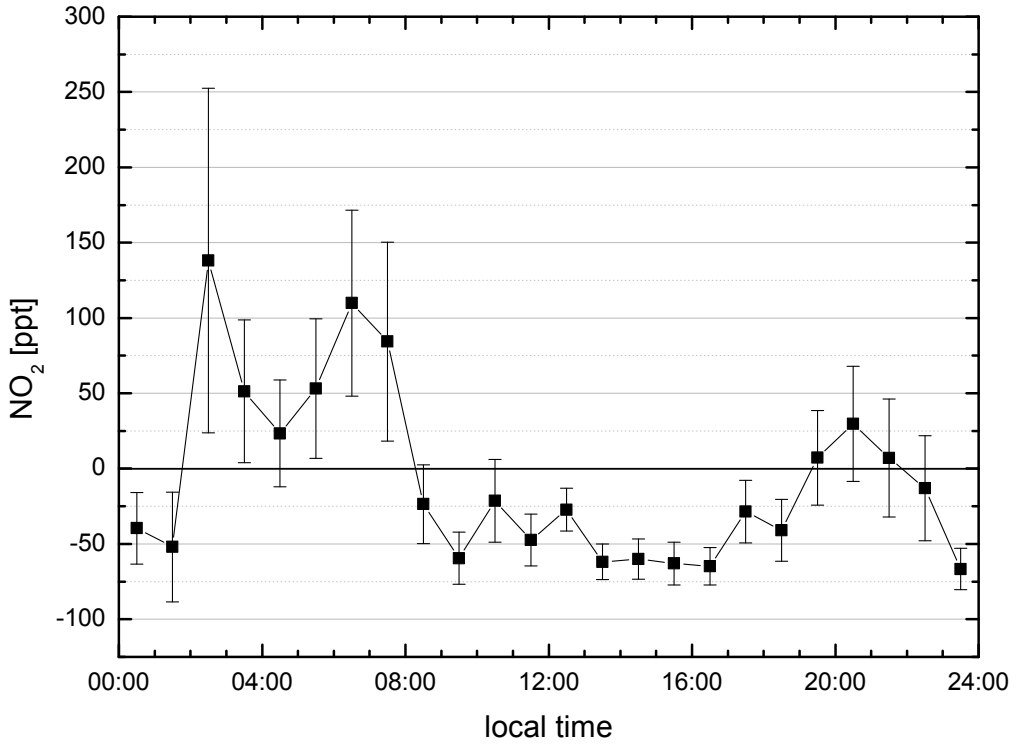

Figure 5.25: Mean diurnal variation of NO_2 as obtained from DOAS measurements performed on Kerguelen from 21.01 to 21.02.2002.

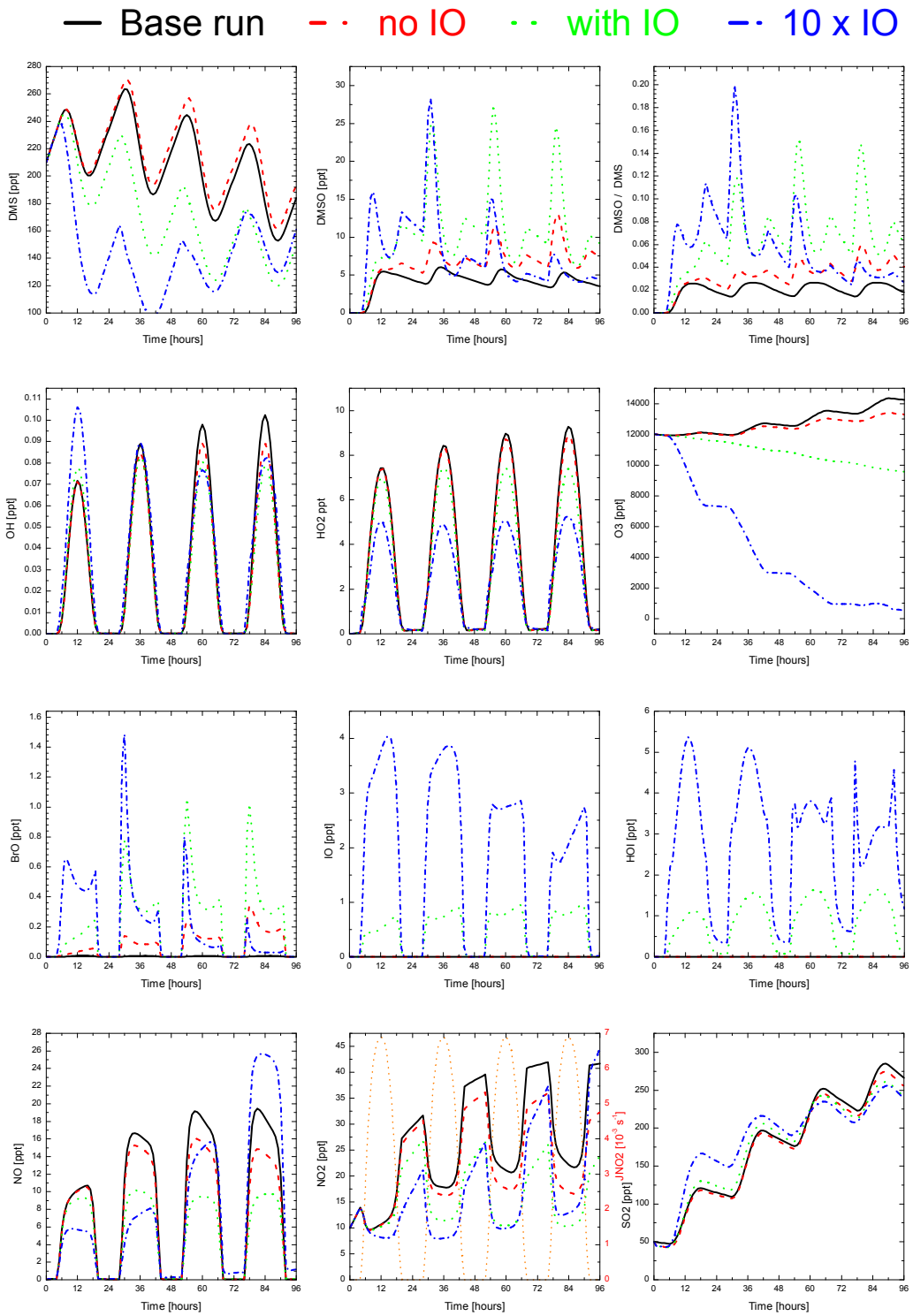

Figure 5.26: Comparison of 4 model runs of the model MOCCA [Sander and Crutzen 1996] including a base run with no halogens, a second including sea salt aerosol production of Bromine and Chlorine, a third run including iodine emissions and finally a last with tenfold iodine.

of iodine on NO and NO_2 is less clear. Obviously the presence of iodine changes the shape of the diurnal variation profile of both species but the mixing rates of NO_x do not change proportional to Iodine levels. Finally, sulphur dioxide remains nearly unchanged when iodine is added to the model, which is in agreement with expectations as the additional depletion of DMS started by halogens will occur on the addition path where no SO_2 is formed.

Bibliography

(2002). Forest Fires in Europe (2001 fire campaign). Technical Report S.P.I.02.72 EN, European Commission Joint Research Centre. European Communities 2002.

Abbatt, J. and J. Nowak (1997). Heterogeneous interactions of HBr and HOCl with cold sulfuric acid solutions: Implications for Arctic boundary layer bromine chemistry. *J. Phys. Chem. A. 101*(11), 2131–2137.

Abbatt, J. P. D. (1994). Heterogeneous reactions of HOBr wth HBr and HCl on ice surfaces at 228 K. *Geophys. Res. Lett. 21*(8), 665–668.

Abbatt, J. P. D. (1995). Interactions of HBr, HCl, and HOBr with supercooled sulfuric acid solutions of stratospheric composition. *J. Geophys. Res. 100*(D7), 14,009–14,018.

Ackermann, R. (2000). *Auswirkungen von Kraftfahrzeugemissionen in der urbanen Atmosphäre*. Ph. D. thesis, Ruprecht-Karls-Universität. ISBN 3-89825-123-3.

Ackermann, R., M. Tuckermann, and U. Platt (1997). DOAS-Measurements during the ARCTOC-Campaigns 1995 and 1996 in Ny-Alesund, Spitsbergen. In: *3rd NySMAC Meeting: Atmospheric Research in Ny-Alesund.*, NILU, Kjeller, Norway, S. 131–136.

Albritton, D. and L. Meira Filho (2001). Climate Change 2001: The Scientific Basis. Contribution of Working Group I to the Third Assessment Report of the Intergovernmental Panel on Climate Change. Technical report, Intergovernmental Panel on Climate Change. ISBN: 0521014956.

Alicke, B. (2000). *The role of nitrous acid in the boundary layer*. Ph. D. thesis, Ruprecht-Karls-Universität.

Alicke, B., A. Geyer, A. Hofzumahaus, F. Holland, S. Konrad, H. W. Pätz, J. Schäfer, J. Stutz, A. Volz-Thomas, and U. Platt (2003). OH formation by HONO photolysis during the BERLIOZ experiment. *J. Geophys. Res. 108*(D4), PHO 3–1 to PHO 3–17. 2001JD000579.

Alicke, B., K. Hebestreit, J. Stutz, and U. Platt (1999). Iodine oxide in the marine boundary layer. *Nature 397*(6720), 572–573.

Alicke, B., U. Platt, and J. Stutz (2002). Impact of nitrous acid photolysis on the total hydroxyl radical budget during the Limitation of Oxidant Production/Pianura Padana Produzione di Ozono study in Milan. *J. Geophys. Res. 107*(D22), LOP 9–1 to LOP 9–17. 2002-11-15.

Allan, B. J., G. McFiggans, J. M. C. Plane, and H. Coe (2000). Observations of iodine monoxide in the remote marine boundary layer. *J. Geophys. Res. 105*(D11), 14,363–14,370.

Allan, B. J., G. McFiggans, J. M. C. Plane, H. Coe, and G. G. McFadyen (2000). The nitrate radical in the remote marine boundary layer. *J. Geophys. Res. 105*(D19), 24,191–24,204.

Allan, B. J., J. M. C. Plane, and G. McFiggans (2001). Observations of OIO in the remote marine boundary layer. *Geophys. Res. Lett. 28*(10), 1945–1948.

Alpert, P., B. Neeman, and Y. Shay-el (1990). Climatological Analysis of Mediterranean cyclones using ECMWF data. *Tellus 42A*, 65–77.

Andreae, M., R. Ferek, F. Bermond, K. Byrd, R. Chatfield, R. Engstrom, S. Hardin, P. Houmere, F. Lemarrec, and H. Raemdonck (1985). Dimethyl sulfide in the marine atmosphere. *J. Geophys. Res. 90*, 12.891–12.900.

Andreae, M. O. and P. J. Crutzen (1997). Atmospheric Aerosols: Biogeochemical Sources and Role in Atmospheric Chemistry. *Science 276*(5315), 1052–1058.

Andreae, M. O., W. Elbert, Y. Cai, T. W. Andreae, and J. Gras (1999). Non-sea-salt sulfate, methanesulfonate, and nitrate aerosol concentrations and size distributions at Cape Grim, Tasmania. *J. Geophys. Res. 104*(D17), 21,695–21,706. 1999, Sep. 20.

Andreae, M. O. and P. Merlet (2001). Emission of trace gases and aerosols from biomass burning. *Global Biogeochem. Cycles 15*(4), 955–966.

Aranda, A., Y. Díaz-de Mera, D. Rodríguez, S. Salgado, and M. E. (2002). Kinetic and products of the BrO+ CH3SH reaction. Temperature and presure dependence. *Chem. Phys. Lett. 357*, 471–476.

Aranda, A., G. Le Bras, G. La Verdet, and G. Poulet (1997). The BrO + CH_30_2 reaction: Kinetics and role in the atmospheric ozone budget. *Geophys. Res. Lett. 24*(22), 2745–2748.

Ariya, P., J. Hopper, and G. Harris (1999). $C_2 - C_7$ hydrocarbon concentrations in the Artic snowpack interstitial air: Potential Presence of active Br within the snowpack. *J. Atmos. Chem. 34*, 55–64.

Arsene, C., I. Barnes, K. H. Becker, W. Schneider, T. Wallington, N. Mihalopoulos, and I. Patroescu-Klotz (2002). Formation of Methane Sulfinic Acid in the Gas-Phase OH-Radical Initiated Oxidation of Dimethyl Sulfoxide. *Environ. Sci. Technol. 36*(23), 5155–5163.

Arsene, C., I. Barnes, and B. K.H. (1999). FT-IR product study of the photo-oxidation of dimethyl sulfide: Temperature and O2 partial pressure dependence. *Phys. Chem. Chem. Phys. 1*, 5463–5470.

Ashworth, S., B. Allan, and J. Plane (2002). High resolution spectroscopy of the OIO radical: Implications for the ozone-depleting potential of iodine. *Geophys. Res. Lett. 29*(10), 1456.

Atkinson, R., D. Baulch, R. Cox, J. Crowley, R. Hampson, J. Kerr, M. Rossi, and J. Troe (2002). Summary of Evaluated Kinetic and Photochemical Data for Atmospheric Chemistry.

Atkinson, R., D. L. Baulch, R. A. Cox, J. N. Crowley, R. F. J. Hampson, J. A. Kerr, M. J. Rossi, and J. Troe (2003). Summary of Evaluated Kinetic and Photochemical Data for Atmospheric Chemistry.

Ayers, G., J. Cainey, H. Granek, and C. Leck (1996). Dimethylsulfide oxidation and the ratio of methanesulfonate to non sea-salt sulfate in the marine aerosol. *J. Atmos Chem. 25*(3), 307–325.

Ayers, G., S. Penkett, R. Gillett, A. Bandy, I. Galbally, C. Meyer, C. Ellsworth, S. Bentley, and B. Forgan (1992). Evidence for photochemical control of ozone mixing ratios in unpolluted marine air. *Nature 360*(6403), 446–449.

Ayers, G. P., S. T. Bentley, J. P. Ivey, and B. W. Forgan (1995). Dimethylsulfide in marine air at Cape Grim, 41 S. *J. Geophys. Res. 100*(D10), 21.013–21.022.

Ayers, G. P., R. W. Gillett, J. P. Ivey, B. Schafer, and A. Gabric (1995). Short-term variability in marine atmospheric dimethylsulfide concentration. *Geophys. Res. Lett. 22*(18), 2513–2516.

Baker, M. B. (1997). Cloud Microphysics and Climate. *Science 276*(5315), 1072–1078.

Ballesteros, B., N. Jensen, and J. Hjorth (2002). FT-IR Study of the Kinetics and Products of the Reactions of DMS, DMSO and DMSO2 with Br and BrO. *J. Atmos. Chem. 43*(2), 135–150.

Ballschmiter, K. (2003). Pattern and sources of naturally produced organohalogens in the marine environment: biogenic formation of organohalogens. *Chemosphere 52*, 313–324.

Barcellos da Rosa, M., W. Behnke, and C. Zetzsch (2003). Study of the heterogeneous reaction of O3 with CH3SCH3 using the wetted-wall flowtube technique. *Atmos. Chem. Phys. Discuss. 3*, 1949–1971.

Bardouki, H., M. Barcellos da Rosa, N. Mihalopoulos, W.-U. Palm, and C. Zetzsch (2002). Kinetics and mechanism of the oxidation of dimethylsulfoxide (DMSO) and methanesulfinate (MSI-) by OH radicals in aqueous medium. *Atmos. Environ. 36*(29), 4627–4634.

Bardouki, H., H. Liakakou, C. Economou, J. Sciare, J. Smolík, V. Ždímal, K. Eleftheriadis, M. Lazaridis, and N. Mihalopoulos (2003). Chemical composition of size resolved atmospheric aerosols in the eastern Mediterranean during summer and winter. *Atmos. Environ. 37*, 195–208.

Barnes, I. (2003). Evaluation of the Climatic Impact of Dimethyl Sulphide, End of year 3 report: 1st March 2002 28th February 2003 and FINAL Report. Technical Report EVK2-CT-1999-00033, Uni Wuppertal. February 2003.

Barnes, I., V. Bastian, and K. H. Becker (1988). Kinetics and mechanisms of the reaction of OH radicals with dimethyl sulfide. *Int. J. Chem. Kinet. 20*, 415–431.

Barone, S., A. Turnipseed, and A. Ravishankara (1995). Role of adducts in the atmospheric oxidation of dimethylsulphide. *Faraday Discussion 100*, 39–54.

Barrie, L., R. Bottenheim, R. Schnell, P. Crutzen, and R. Rasmussen (1988). Ozone destruction and photochemical reactions at polar sunrise in the lower Arctic atmosphere. *Nature 334*, 138–141.

Bates, T., K. Kelly, J. Johnson, and R. Gammon (1995). Regional and seasonal variations in the flux of oceanic carbon monoxide to the atmosphere. *J. Geophys. Res. 100*(D11), 23,093–23,101.

Bauer, D., T. Ingham, S. Carl, G. Moorgat, and J. Crowley (1998). Ultraviolet-visible absorption cross section of gaseous HOI and its photolysis at 335 nm. *J. Phys. Chem. 102*(17), 2857–2864.

Behnke, W., C. George, V. Scheer, and C. Zetzsch (1997). Production and decay of $ClNO_2$ from the reaction of gaseous N_2O_5 with NaCl solution: Bulk and aerosol experiments. *J. Geophys. Res. 102*(D3), 3795–3804.

Beirle, S., U. Platt, M. Wenig, and T. Wagner (2003). Weekly cycle of NO2 by GOME measurements: A signature of anthropogenic sources. *Atmos. Chem. Phys. Discuss. 3*, 3451–3467.

Belviso, S., P. Buat-Menard, J. P. Putaud, B. C. Nguyen, H. Claustre, and J. Neveux (1993). Size distribution of dimethylsulfoniopropionate (DMSP) in areas of the tropical northeastern Atlantic Ocean and Mediterranean Sea. *Mar. Chem. 44*, 55–71.

Berresheim, H., C. Plass-Dülmer, T. Elste, N. Mihalopoulos, and F. Rohrer (2003). OH in the coastal boundary layer of Crete during MINOS: Measurements and relationship with ozone photolysis. *Atmos. Chem. Phys. Discuss. 3*, 1183–1212.

Betterton, E. (1992). Oxidation of alkyl sulfides by aqueous peroxymonosulfate. *Env. Sci. Tech. 26*, 527–532.

Bilde, M., T. Wallington, C. Ferronato, J. Orlando, G. Tyndall, E. Estupinan, and S. Haberkorn (1998). Atmospheric chemistry of CH_2BrCl, $CHBrCl_2$, $CHBr_2Cl$, $CF_3CHClBr$ and CBr_2Cl_2. *J. Phys. Chem. 102*(11), 1976–1986.

Bloss, W., D. Rowley, R. Cox, and R. L. Jones (2001). Kinetics and Products of the IO Self-Reaction. *J. Phys. Chem. A 105*(33), 7840–7854. DOI: 10.1021/jp0044936.

Bobrowski, N., G. Hönninger, B. Galle, and U. Platt (2003). Detection of bromine monoxide in a volcanic plume. *Nature 423*(6937), 273–276.

Bobrowski, N. and G. Lowe (2003). Detection of BrO at several volcanic plumes in Italy.

Bopp, L., O. Aumont, S. Belviso, and P. Monfray (2003). Potential impact of climate change on marine dimethyl sulfide emissions. *Tellus 55B*, 11–22.

Borissenko, D., A. Kukui, G. Laverdet, and G. Le Bras (2003). Experimental Study of SO2 Formation in the Reactions of CH3SO Radical with NO2 and O3 in Relation with the Atmospheric Oxidation Mechanism of Dimethyl Sulfide. *J. Phys. Chem. A 107*(8), 1155–1161.

Boucher, O. and U. Lohmann (1995). The sulfate-CCN-cloud albedo effect. *Tellus B 47*(3), 281–300.

Boucher, O., C. Moulin, S. Belviso, O. Aumont, L. Bopp, E. Cosme, R. von Kuhlmann, M. Lawrence, M. Pham, M. Reddy, J. Sciare, and C. Venkataraman (2003). DMS atmospheric concentrations and sulphate aerosol indirect radiative forcing: a sensitivity study to the DMS source representation and oxidation. *Atmos. Chem. Phys. 3*, 4965. www.atmos-chem-phys.org/acp/3/49/.

Brown, S. S., H. Stark, T. B. Ryerson, E. J. Williams, D. K. Nicks, M. Trainer, F. C. Fehsenfeld, and A. R. Ravishankara (2003). Nitrogen oxides in the nocturnal boundary layer: Simultaneous in situ measurements of NO3, N2O5, NO2, NO, and O3. *J. Geophys. Res. 108*(D9), ACH 18 1–11. doi:10.1029/2002JD002917.

Butkoskaya, N. I. and G. LeBras (1994). Mechanism of the NO3+DMS reaction by discharge flow mass spectrometry. *Geophys. Res. Lett. 98*, 2582–2591.

Calvert, J. G. (1985). *Nature 317*, 27.

Campolongo, F., A. Saltelli, N. Jensen, J. Wilson, and J. Hjort (1999). The Role of Multiphase Chemistry in the Oxidation of Dimethylsulphide (DMS). A Latitude Dependent Analysis. *J. Atmos. Chem. 32*(3), 327–356.

Cantrell, C. and D. Stedman (1982). A possible technique for the measurement of atmospheric peroxy radicals. *Geophys. Res. Lett. 9*, 846–849.

Carpenter, L. (2003). Iodine in the Marine Boundary Layer. *Chem. Rev. 103*, 4953–4962.

Carpenter, L. J., P. S. Liss, and S. A. Penkett (2003). Marine organohalogens in the atmosphere over the Atlantic and Southern Oceans. *J. Geophys. Res. 108*(D9), ACH 1–1 to ACH 1–13.

Carpenter, L. J., G. Malin, P. S. Liss, and F. C. Kuepper (2000). Novel biogenic iodine-containing trihalomethanes and other short-lived halocarbons in the coastal East Atlantic. *Global Biogeochem. Cycles 14*(4), 1191–1204.

Carpenter, L. J., P. S. Monks, B. J. Bandy, S. A. Penkett, I. E. Galbally, and C. P. M. Meyer (1997). A study of peroxy radicals and ozone photochemistry at coastal sites in the northern and southern hemispheres. *J. Geophys. Res. 102*(D21), 25,417–25,428.

Carpenter, L. J., W. T. Sturges, S. A. Penkett, P. S. Liss, B. Alicke, K. Hebestreit, and U. Platt (1999). Short-lived alkyl iodides and bromides at Mace Head, Ireland: Links to biogenic sources and halogen oxide production. *J. Geophys. Res. 104*(D1), 1679–1690.

Carslaw, N., J. M. C. Plane, H. Coe, and E. Cuevas (1997). Observations of the nitrate radical in the free troposphere at Izana de Tenerife. *J. Geophys. Res. 102*(D9), 10,613–10,622.

Chameides, W. and J. Walker (1973). A photochemical theory of tropospheric ozone. *J. Geophys. Res. 78*(36), 8751–60.

Charlson, R., J. Lovelock, M. Andreae, and S. Warren (1987). Oceanic phytoplankton, atmospheric sulphur, cloud albedo and climate. *Nature 326*, 655–661.

Charlson, R. J., T. L. Anderson, and R. E. McDuff (1992). The sulfur cycle. In: G. H. O. . G. V. W. S.S. Butcher, R. J. Charlson (Hrsg.), *Global biogeochemical cycles*, S. 285–300. London: Academic Press.

Chartrand, D. and J. McConnell (1998). Evidence for HBr production due to minor channel branching at mid-latitudes. *Geophys. Res. Lett. 25*(1), 55–58.

Chen, G., D. Davis, P. Kasibhatla, A. Bandy, D. Thornton, and D. Blake (1999). A mass-balance/photochemical assessment of DMS sea-to-air flux as inferred from NASA GTE PEM-West A and B observations. *J. Geophys. Res. 104*(D5), 5471–5482.

Chin, M., R. Rood, S.-J. Lin, J.-F. Müller, and A. Thompson (2000). Atmospheric sulfur cycle simulated in the global model GOCART: Model description and global properties. *J. Geophys. Res. 105*(D20), 24,671–24,687.

Cofer, W. and R. Edahl (1986). A new technique for collection, concentration and determination of gaseous tropospheric formaldehyde. *Atmos. Environ. 20*(5), 979–984.

Colman, J., D. R. Blake, and F. Sherwood Rowland (1998). Atmospheric Residence Time of CH_3Br estimated from the Junge Spatial Variability Relation. *Science 281*, 392–396.

Cox, R. A. (1999). Ozone and peroxy radical budgets in the marine boundary layer: Modeling the effect of NOx. *J. Geophys. Res. 104*(D7), 8047–8056.

Cox, R. A., W. J. Bloss, R. L. Jones, and D. M. Rowley (1999). OIO and the atmospheric cycle of iodine. *Geophys. Res. Lett. 26*(13), 1857–1860.

Cox, R. A. and G. B. Coker (1983). Absorption cross section and kinetics of IO in the photolysis of CH3I in the presence of ozone. *J. Phys. Chem. 87*, 4478–4484.

Crowley, J. (2004). new IUPAC recommendation expected.

Crutzen, P. (1976). The possible importance of CSO for the sulfur layer of the stratosphere. *Geophys. Res. Lett. 3*, 73–76.

Crutzen, P. (1979). The role of NO and NO2 in the chemistry of the troposphere and stratosphere. *Annu. Rev. Earth. Planet. Sci. 7*, 443–472.

Crutzen, P. J., W. M. Whelpdale, D. Kley, and L. A. Barrie (1985). The cycling of sulfur and nitrogen in the remote atmosphere. In: M. O. A. J. N. Galloway, R. J. Charlson

(Hrsg.), *The biogeochemical cycling of sulfur and nitrogen in the remote atmosphere.*, S. 203–212. Dordrecht: D. Reidel Publishing Co.

Czerny, M. and A. Turner (1930). *Z. Phys. 61*, 792.

Davis, D., J. Crawford, S. Liu, S. McKeen, A. Bandy, D. Thornton, F. Rowland, and D. Blake (1996). Potential impact of iodine on tropospheric levels of ozone and other critical oxidants. *J. Geophys. Res. 101*(D1), 2135–2147.

Díaz-de Mera, Y., A. Aranda, D. Rodríguez, R. López, B. Cabañas, and E. Martínez (2002). Gas-Phase Reactions of Chlorine Atoms and ClO Radicals with Dimethyl Sulfide. Rate Coefficients and Temperature Dependences. *J. Phys. Chem. A. 106*(37), 8627–8633.

Dimitropoulou, C. and A. Marsh (1997). Modelling studies of NO3 Nighttime Chemistry and its Effects on Subsequent Ozone Formation. *Atmospheric Environment 31*(18), 3041 – 3057.

Douglass, A. and S. Kawa (1999). Contrast between 1992 and 1997 high-latitude spring Halogen Occultation Experiment observations of lower stratospheric HCl. *J. Geophys. Res. 104*(D15), 18739–54.

Draxler, R. and G. Hess (1998). An overview of the HYSPLIT4 modelling system for trajectories, dispersion and deposition. *Aust. Met. Mag. 47*, 295–308.

Duchêne, J. (1989). *KERGUELEN - Recherches au bout du monde.* Banyuls sûr mer: INSTAPRINT S.A.

Ehhalt (1999). Photooxidation of trace gases in the troposphere. *Phys. Chem. Chem. Phys. 1*(24), 5401 – 5408.

Ehhalt, D. H. and F. Rohrer (2000). Dependence of the OH concentration on solar UV. *J. Geophys. Res. 105*(D3), 3565–3572.

Erickson, David J., I. (1989). Ocean to atmosphere carbon monoxide flux: Global inventory and climatic implications. *Global Biogeochem. Cycles 3*(4), 305–314.

Falbe-Hansen, H., S. Sorensen, N. Jensen, T. Pedersen, and J. Hjorth (2000). Atmospheric gas-phase reactions of dimethylsulphoxide and dimethylsulphone with NO and NO3 radicals, Cl atoms and ozone. *Atmos. Environ. 34*(10), 1543 – 1551.

Fan, S. and D. Jacob (1992). Surface ozone depletion in Arctic spring sustained by bromine reactions on aerosols. *Nature 359*(6395), 522 – 524.

Ferek, R., P. Hobbs, L. Radke, and J. Herring (1995). Dimethyl sulfide in the arctic atmosphere. *J. Geophys. Res. 100*(D12), 26,093–26,104.

Fickert, S., J. W. Adams, and J. N. Crowley (1999). Activation of Br_2 and BrCl via uptake of HOBr onto aqueous salt solutions. *J. Geophys. Res. 104*(D19), 23,719–23,728.

Finlayson-Pitts, B. and S. Johnson (1988). The reaction of NO2 with NaBr: Possible source of BrNO in polluted marine atmospheres. *Atmos. Environ. 22*, 1107–1112.

Finlayson-Pitts, B. J., M. J. Ezell, and J. N. Pitts (1989). Formation of chemically active chlorine compounds by reactions of atmospheric NaCl particles with gaseous N2O5 and ClONO2. *Nature 337*(6204), 241–244.

Fishman, J. and P. Crutzen (1978). The origin of ozone in the troposphere. *Nature 274*(5674), 855–858.

Friess, U. (1997). *Spektroskopische Messungen stratosphärischer Spurenstoffe auf der Neumayer- Station (Antarktis) in den Jahren 1994/95.* Diploma thesis, Ruprecht-Karls-Universität.

Friess, U. (2001). *Spectroscopic Measurements of Atmospheric Trace Gases at Neumayer-Station, Antarctica*. Phd thesis, Ruprecht-Karls-Universität Heidelberg.

Friess, U., T. Wagner, I. Pundt, K. Pfeilsticker, and U. Platt (2001). Spectroscopic Measurements of Tropospheric Iodine Oxide at Neumayer Station, Antarctica. *Geophys. Res. Lett. 28*(10), 1941–1944.

Fuchs, N. and A. Sutugin (1971). *High-dispersed aerosols*, Band 2 of *International Reviews of Aerosol Physics and Chemistry*. New York: Pergamon.

Fuhrman, J. (1999). Marine viruses and their biogeochemical and ecological effects. *Nature 399*(6736), 541–548.

Gäbler, H. and K. Heumann (1993). Determination of particulate iodine in aerosols from different regions by size fractionating impactor sampling and IDMS. *Intern. J. Environ. Anal. Chem. 50*, 129–146.

Gabric, A., N. Murray, L. Stone, and M. Kohl (1993). Modelling the production of dimethyl sulfide during a phytoplankton bloom. *J. Geophys. Res. 98*, 22805–22816.

George, C., J. L. Ponche, P. Mirabel, W. Behnke, V. Scheer, and C. Zetsch (1994). Study of the uptake of N_2O_5 by water and NaCl solutions. *J. Phys. Chem. 98*, 8780.

Gershenzon, M., P. Davidovits, J. Jayne, C. Kolb, and D. Worsnop (2001). Simultaneous uptake of DMS and ozone on water. *Journal of physical chemistry A 105*, 7031 – 7036.

Gershenzon, M., S. Ilin, N. Fedotov, Y. Gershenzon, E. Aparina, and V. Zelenov (1999). The mechanism of reactive NO3 uptake on dry NaX (X=Cl, Br). *J. Atmos. Chem. 34*(1), 119 – 135.

Geyer, A. (2000). *The role of the nitrate radical in the boundary layer - observations and modeling studies*. Ph. D. thesis, Ruperto-Carola University Heidelberg.

Geyer, A., R. Ackermann, R. Dubois, B. Lohrmann, T. Müller, and U. Platt (2001). Long–Term observation of nitrate radicals in the continental boundary layer near Berlin. *Atmos. Environ. 35*(21), 3619–3631.

Geyer, A., B. Alicke, S. Konrad, T. Schmitz, J. Stutz, and U. Platt (2001). Chemistry and oxidation capacity of the nitrate radical in the continental boundary layer near Berlin. *J. Geophys. Res. 106*(D8), 8013–8026.

Geyer, A., K. Bächmann, A. Hofzumahaus, F. Holland, S. Konrad, T. Klpfel, H.-W. Pätz, D. Perner, D. Mihelcic, H.-J. Schäfer, A. Volz-Thomas, and U. Platt (2003). Nighttime formation of peroxy and hydroxyl radicals during the BERLIOZ campaign: Observations and modeling studies. *J. Geophys. Res. 108*(D4), PHO 5–1 to PHO 5–15.

Geyer, A. and U. Platt (2002). Temperature dependence of the NO3 loss frequency: A new indicator for the contribution of NO3 to the oxidation of monoterpenes and NOx removal in the atmosphere. *J. Geophys. Res. 107*(D20), ACL 8–1 to ACL 8–12. 2002-10-23.

Giese, B., F. Laturnus, F. Adams, and C. Wiencke (1999). Release of Volatile Iodinated C1-C4 Hydrocarbons by Marine Macroalgae from Various Climate Zones. *Environ. Sci. Technol. 33*(14), 2432–2439.

Goldan, P. D., R. Fall, W. C. Kuster, and F. C. Fehsenfeld (1988). Uptake of COS by growing vegetation: a major tropospheric sink. *J. Geophys. Res. 93*, 14,186–14,192.

Gölz, C. (1996). *Messungen von NO3-Radikalen in Regionen mit hoher natürlicher Produktion von Kohlenwasserstoffen*. Ph. D. thesis, Ruprecht-Karls-Universität Heidelberg.

Gölz, C., C. Janssen, and U. Platt (1993). Long path differential absorption spectroscopy: Measurements during the 1993 FIELDVOC campaign. In: G. Angeletti and G. Restelli (Hrsg.), *6th European Symposium*, Band Physico-Chemical Behaviour of Atmospheric Pollutants, Varese, S. 252–258. Commission of the European Community, Brussels.

Gölz, C., J. Senzig, and U. Platt (2001). NO3-initiated oxidation of biogenic hydrocarbons. *Chemosphere - Global Change Science 3*(3), 339–352.

Goodwin, K., W. North, and M. Lidstrom (1997). Production of bromoform and dibromomethane by Giant Kelp: Factors affecting release and comparison to anthropogenic bromine sources. *Limnol. Oceanogr. 42*(8), 1725–1734.

Gribble, G. (2003). The diversity of naturally produced organohalogens. *Chemosphere 52*(2), 289–297.

Gros, V., N. Poisson, D. Martin, M. Kanakidou, and B. Bonsang (1998). Observations and modeling of the seasonal variation of surface ozone at Amsterdam Island: 1994 - 1996. *J. Geophys. Res. 103*(D21), 28,103–28,109.

Gros, V., J. Williams, J. A. van Aardenne, G. Salisbury, R. Hofmann, M. G. Lawrence, R. von Kuhlmann, J. Lelieveld, M. Krol, H. Berresheim, J. M. Lobert, and E. Atlas (2003). Origin of anthropogenic hydrocarbons and halocarbons measured in the summertime European outflow (on Crete in 2001). *Atmos. Chem. Phys. Discuss. 3*, 1893–1923.

Harwood, M., J. Burkholder, M. Hunter, R. Fox, and A. Ravishankara (1997). Absorption Cross Sections and Self-Reaction Kinetics of the IO Radical. *J. Phys. Chem. A 101*(5), 853–863.

Hasager, C. B., J. Carstensen, B. Gustafsson, O. Hertel, M. Johnsson, S. Markager, and C. Ambelas Skjødth (2003). Atmospheric and marine extreme nitrogen flux events and chlorophyll-A in the Kattegat strait. In: *EGS-AGU-EUG Joint Assembly*, Band 5 of *Geophysical Research Abstracts*, Nice, S. 03366. European Geophysical Society.

Hausmann, M. and U. Platt (1994). Spectroscopic measurement of bromine oxide and ozone in the high Arctic during Polar Sunrise Experiment 1992. *J. Geophys. Res. 99*(D12), 25,399–25,414.

Hebestreit, K. (2001). *Halogenoxide in der planetaren Grenzschicht mittlerer Breiten*. Phd thesis, Ruprecht-Karls-Universität.

Hebestreit, K., J. Stutz, D. Rosen, V. Matveiv, M. Peleg, M. Luria, and U. Platt (1999). DOAS Measurements of Tropospheric Bromine Oxide in Mid-Latitudes. *Science 283*(5398), 55–57.

Hegels, E., P. J. Crutzen, T. Klüpfel, D. Perner, and J. P. Burrows (1998). Global distribution of atmospheric bromine monoxide from GOME on Earth-observing satellite ERS 2. *Geophys. Res. Lett. 25*(16), 3127–3130.

Heintz, F., U. Platt, H. Flentje, and R. Dubois (1996). Long-term observation of nitrate radicals at the Tor Station, Kap Arkona (Ruegen). *J. Geophys. Res. 101*(D17), 22,891–22,910.

Hermes, T. (1999). *Lichtquellen und Optik für die Differentielle Optische Absorptionsspektroskopie*. Diploma thesis, University of Heidelberg.

Herrmann, H., B. Ervens, H. Jacobi, R. Wolke, P. Nowacki, and R. Zellner (2000). CAPRAM 2.3: A Chemical Aqueous Phase Radical Mechanism for Tropospheric Chemistry. *J. of . Atmos. Chem. 36*(3), 231–284.

Hoffmann, T., C. D. O'Dowd, and J. H. Seinfeld (2001). Iodine oxide homogeneous nucleation: An explanation for coastal new particle production. *Geophys. Res. Lett. 28*(10), 1949–1952.

Holland, H. D. (1978). *The chemistry of the atmosphere and oceans*. New York: John Wiley and Sons.

Hollwedel, J., M. Wenig, S. Beirle, S. Kraus, S. Kühl, W. Wilms-Grabe, U. Platt, and T. Wagner (2003). Year-to-Year Variations of Polar Tropospheric BrO as seen by GOME. *Adv. Space Res. accepted, 2003.*

Holzinger, R., C. Warneke, A. Hansel, A. Jordan, W. Lindinger, D. H. Scharffe, G. Schade, and P. J. Crutzen (1999). Biomass burning as a source of formaldehyde, acetaldehyde, methanol, acetone, acetonitrile, and hydrogen cyanide. *Geophys. Res. Lett. 26*(8), 1161–1164.

Hönninger, G. (1999). *Referenzspektren reaktiver Halogenverbindungen für DOAS-Messungen*. Diploma thesis, University of Heidelberg.

Hönninger, G. (2002). *Halogen Oxide Studies in the Boundary Layer by Multi Axis Differential Optical Absorption Spectroscopy and Active Longpath-DOAS*. Ph. D. thesis, Ruperto-Carola University Heidelberg.

Hönninger, G., N. Bobrowski, and U. Platt (2002). Elevated BrO of the Salar de Unuji (Bolivia).

Hönninger, G., H. Leser, O. Sebastián, and U. Platt (2004). Ground-based Measurements of Halogen Oxides at the Hudson Bay by Active Longpath DOAS and Passive MAX-DOAS. *Geophys. Res. Lett. submitted.*

Hönninger, G. and U. Platt (2002). Observations of BrO and its vertical distribution during surface ozone depletion at Alert. *Atmos. Environ. 36*, 2481–2489.

Hu, J. and J. Abbatt (1997). Reaction Probabilities for N2O5 Hydrolysis on Sulfuric Acid and Ammonium Sulfate Aerosols at Room Temperature. *J. Phys. Chem. A 101*, 871 – 878.

Hynes, A. and P. Wine (1996). The atmospheric chemistry of dimethylsulfoxide (DMSO) kinetics and mechanism of the OH + DMSO reaction. *J. Atmos. Chem. 24*, 23–27.

Impey, G., C. Mihele, K. Anlauf, L. Barrie, D. Hastie, and P. Shepson (1999). Measurements of Photolyzable Halogen Compounds and Bromine Radicals during Polar Sunrise Experiment 1997. *J. Atmos. Chem. 34*, 21–37.

Ingham, T., D. Bauer, R. Sander, P. J. Crutzen, and J. N. Crowley (1999). Kinetics and Products of the Reactions BrO + DMS and Br + DMS at 298 K. *J. Phys. Chem. A 103*(36), 7199–7209.

Ingham, T., M. Cameron, and J. Crowley (2000). Photodissociation of IO (355 nm) and OIO (532 nm): Quantum yields for O(^3P) and I(^2P) production. *J. Phys. Chem. A 104*, 8001–8010.

Jacob, D. (1986). Chemistry of OH in remote clouds and its role in the production of formic acid and peroxymonosulfate. *J. Geophys. Res. 91*, 9807–9826.

Jacob, D. J. (2000). Heterogeneous chemistry and tropospheric ozone. *Atmos. Environ. 34*, 2131 2159.

James, J. D., R. M. Harrison, N. H. Savage, A. G. Allen, J. L. Grenfell, B. J. Allan, J. M. C. Plane, C. N. Hewitt, B. Davison, and L. Robertson (2000). Quasi-Lagrangian investigation into dimethyl sulfide oxidation in maritime air using a combination of measurements and model. *J. Geophys. Res. 105*(D21), 26,379–26,392.

Jobson, B. T., H. Niki, Y. Yokouchi, J. Bottenheim, F. Hopper, and R. Leaitch (1994). Measurements of C2-C6 hydrocarbons during the Polar Sunrise 1992 Experiment: Evidence for Cl atom and Br atom chemistry. *J. Geophys. Res. 99*(D12), 25,355–25,368.

Jöckel, P., C. Brenninkmeijer, and P. Crutzen (2003). A discussion on the determination of atmospheric OH and its trends. *Atmos. Chem. Phys. 3*, 107118.

Kallos, G., V. Kotroni, K. Lagouvardos, and A. Papadopoulos (1998). On the long-range transport of air pollutants from Europe to Africa. *Geophys. Res. Lett. 25*(5), 619–622.

Keene, W. C., M. Aslam, K. Khalil, I. Erickson, D. J., A. McCulloch, T. E. Graedel, J. M. Lobert, M. L. Aucott, S. L. Gong, D. B. Harper, G. Kleiman, P. Midgley, R. M. Moore, C. Seuzaret, W. T. Sturges, C. M. Benkovitz, V. Koropalov, L. A. Barrie, and Y. F. Li (1999). Composite global emissions of reactive chlorine from anthropogenic and natural sources: Reactive Chlorine Emissions Inventory. *J. Geophys. Res. 104*(D7), 8429–8440.

Keene, W. C., R. Sander, A. P. Pszenny, R. Vogt, P. J. Crutzen, and J. N. Galloway (1998). Aerosol pH in the marine boundary layer: A review and model evaluation. *J. Aerosol Sci. 3*, 339–356.

Kettle, A., M. Andreae, D. Amouroux, T. Andreae, T. Bates, H. Berresheim, H. Bingemer, R. Boniforti, M. Curran, G. DiTullio, G. Helas, G. Jones, M. Keller, R. Kiene, C. Leck, M. Levasseur, G. Malin, M. Maspero, P. Matrai, A. McTaggart, N. Mihalopoulos, B. Nguyen, A. Novo, J. Putaud, S. Rapsomanikis, G. Roberts, G. Schebeske, S. Sharma, R. Simó, R. Staubes, S. Turner, and G. Uher (1999). A global database of sea surface dimethylsulfide (DMS) measurements and a procedure to predict sea surface DMS as a function of latitude, longitude, and month. *Glob. Biogeochem. Cycl. 13*(2), 399–444.

Kettle, A. J. and M. O. Andreae (2000). Flux of dimethylsulfide from the oceans: A comparison of updated data sets and flux models. *J. Geophys. Res. 105*(D22), 26,793–26,808.

Kiene, R. (1993). Microbial sources and sinks for methylated sulfur compounds in the marine environment. In: J. Murrell and D. Kelly (Hrsg.), *Microbial Growth on C1 Compounds*, S. 1533.

Kirchner, U., T. Benter, and R. N. Schindler (1997). Experimental verifcation of gas phase bromine enrichment in reactions of HOBr with sea salt doped ice surfaces. *Ber. Bunsenges. Phys. Chem. 101*, 975–977.

Koga, S. and H. Takana (1996). Simulations of seasonal variations of sulfur compounds in the remote marine atmosphere. *J. Atmos. Chem. 23*, 163–192.

Kouvarakis, G., N. Mihalopoulos, A. Tselepides, and S. Stavrakakis (2001). On the importance of atmospheric inputs of inorganic nitrogen species on the productivity of the eastern Mediterranean Sea. *Global Biogeochem. Cycles 15*(4), 805–818.

Kouvarakis, G., K. Tsigaridis, M. Kanakidou, and N. Mihalopoulos (2000). Temporal variations of surface regional background ozone over Crete Island in the southeast Mediterranean. *J. Geophys. Res. 105*(D4), 4399–4408. 1999JD900984.

Kraus, A. and A. Hofzumahaus (1998). Field measurements of atmospheric photolysis frequencies for O_3, NO_2, HCHO, CH_3CHO, H_2O_2, and HONO by UV spectroradiometry. *J. Atmos. Chem. 5*(31), 161–180.

Kreher, K., P. V. Johnston, S. W. Wood, B. Nardi, and U. Platt (1997). Ground-based measurements of tropospheric and stratospheric BrO at Arrival Heights, Antarctica. *Geophys. Res. Lett. 24*(23), 3021–3024.

Kukui, A., D. Borissenko, G. Laverdet, and G. Le Bras (2003). Gas-Phase Reactions of OH Radicals with Dimethyl Sulfoxide and Methane Sulfinic Acid Using Turbulent Flow Reactor and Chemical Ionization Mass Spectrometry. *J. Phys. Chem. A 107*(30), 5732–5742.

Kukui, A., V. Bossoutrot, G. Laverdet, and G. Bras (2000). Mechanism of the Reaction of CH3SO with NO2 in Relation to Atmospheric Oxidation of Dimethyl Sulfide: Experimental and Theoretical Study. *J. Phys. Chem. A 104*(5), 935–946.

Langmann, B., M. Herzog, and H.-F. Graf (1998). Radiative forcing of climate by sulphate aerosols as determined by a regional circulation chemistry transport model. *Atmos. Environ. 32*, 2757–2768.

Laturnus, F. (2001). Marine Macroalgae in Polar Regions as Natural Sources for Volatile Organohalogens. *Environ. Sci. & Pollut. Res. 8*(2), 103–108.

Laturnus, F., F. C. Adams, and C. Wiencke (1998). Methyl halides from Antarctic macroalgae. *Geophys. Res. Lett. 25*(6), 773–776.

Laturnus, F., B. Giese, C. Wiencke, and F. Adams (2000). Low-molecular-weight organoiodine and organobromine compounds released by polar macroalgae - The influence of abiotic factors. *Fresenius J Anal Chem 368*, 297–302.

Lazlo, B., M. Kurylo, and R. Huie (1995). Absorption cross sections, kinetics of formation and self-reaction of the IO radical produced via Laser photolysis of $N_2O/I_2/N_2$ mixtures. *J. Phys. Chem. 99*, 11701–11707.

Le Bras, G., C. Goelz, and U. Platt (1993). Production of peroxy radicals in the DMS oxidation during nighttime. In: G. A. G. Restelli (Hrsg.), *Dimethylsulphide: Oceans, Atmosphere and Climate*, S. 251–260. Norwell, Mass.: Kluwer Acad.

Le Bras, G. and U. Platt (1995). A possible mechanism for combined chlorine and bromine catalyzed destruction of tropospheric ozone in the Arctic. *Geophys. Res. Lett. 22*(5), 599–602.

Leck, C. and C. Persson (1996). The central Arctic Ocean as a source of dimethyl sulfide - Seasonal variability in relation to biological activity. *Tellus 48B*(2), 156–177.

Lee, Y. N. and X. Zhou (1994). Aqueous reaction kinetics of ozone and dimethylsulfide and its atmospheric implications. *J. Geophys. Res. 99*(D2), 3597–3606.

Lehrer, E. (1999). *Polar tropospheric ozone loss*. Ph. d. thesis, University of Heidelberg.

Lehrer, E., U. Langendrfer, D. Wagenbach, and U. Platt (1997). Tropospheric Ozone Depletion Related to Air Mass characteristics. In: *3rd NySMAC Meeting: Atmospheric Research in Ny-Alesund*, NILU, Kjeller, Norway, S. 127–130.

Lelieveld, J., H. Berresheim, S. Borrmann, P. J. Crutzen, F. J. Dentener, H. Fischer, J. Feichter, P. J. Flatau, J. Heland, R. Holzinger, R. Korrmann, M. G. Lawrence, Z. Levin, K. M. Markowicz, N. Mihalopoulos, A. Minikin, V. Ramanathan, M. de Reus, G. J. Roelofs, H. A. Scheeren, J. Sciare, H. Schlager, M. Schultz, P. Siegmund, B. Steil, E. G. Stephanou, P. Stier, M. Traub, C. Warneke, J. Williams, and H. Ziereis (2002). Global Air Pollution Crossroads over the Mediterranean. *Science 298*(5594), 794–799.

Lelieveld, J. and P. Crutzen (1991). The role of clouds in tropospheric chemistry. *J. Atmos. Chem. 36*, 231–284.

Lelieveld, J., W. Peters, F. J. Dentener, and M. C. Krol (2002). Stability of tropospheric hydroxyl chemistry. *J. Geophys. Res. 107*(D23), ACH 17–1 to ACH 17–11. 2002-12-12.

Lelieveld, J., G.-J. Roelofs, L. Ganzeveld, J. Feichter, and H. Rodhe (1997). Terrestrial sources and distribution of atmospheric sulphur. *Phil. Trans. R. Soc. Lond. B 352*(1350), 149–158.

Leser, H. (2001). *Untersuchung troposphärischer Spurenstoffe mit Multiaxialer Differentieller Optischer Absorptionsspektroskopie von gestreutem Sonnenlicht (MAX-DOAS).* Diploma thesis, Universität Heidelberg.

Leser, H., G. Hönninger, and U. Platt (2003). MAX-DOAS measurements of BrO and NO2 in the marine boundary layer. *Geophys. Res. Lett. 30*(10), 44–1 to 44–4.

Levy, H. (1971). Normal atmosphere: Large radical and formaldehyde concentrations predicted. *Science 173*, 141–143.

Lewis, A., L. Carpenter, and M. Pilling (2001). Nonmethane hydrocarbons in the Southern Ocean boundary layer. *J. Geophys. Res. 106*(D5), 4987–4994.

Liss, P., A. Hatton, G. Malin, P. Nightingale, and S. Turner (1997). Marine sulphur emissions. *Phil. Trans. R. Soc. Lond. B 352*(1350), 159–169.

Liss, P. and L. Merlivat (1986). The role of air-sea exchange in geochemical cycling. S. 113–127. Dordrecht: D.Reidel Pub. Co.

Logan, J., M. Prather, S. Wofsy, and M. McElroy (1981). Tropospheric chemistry: a global perspective. *J. Geophys. res. 86*(C8), 7210–54. 20 Aug. 1981.

Lovelock, J. (1972). Atmospheric sulphur and the natural sulphur cycle. *Nature 237*, 452–453.

Mäkelä, J. M., T. Hoffmann, C. Holzke, M. Väkevä, T. Suni, T. Mattila, P. P. Aalto, U. Tapper, E. I. Kauppinen, and C. D. O'Dowd (2002). Biogenic iodine emissions and identification of end-products in coastal ultrafine particles during nucleation bursts. *J. Geophys. Res. 107*(D19), PAR 14–1 to PAR 14–14.

Manø, S. and M. Andreae (1994). Emissions of methyl bromide from biomass burning. *Science 263*, 1255–1257.

Martínez, E., A. Aranda, Y. Díaz-de Mera, D. Rodríguez, R. López, and J. Albaladejo (2002). Atmospheric DMSO degradation in the gas phase: Cl-DMSO reaction. Temperature dependence and products. *Environ. Sci. Technol. 36*, 1226–1230.

Martínez, M., T. Arnold, and D. Perner (1999). The role of bromine and chlorine chemistry for the arctic ozone depletion events in Ny Ålesund and comparison with model calculations. *Ann. Geophys. 17*, 941–956.

Mc Elroy, C., C. Mc Linden, and J. Mc Connell (1999). Evidence for bromine monoxide in the free troposphere during the Arctic polar sunrise. *Nature 397*, 338–341.

McFiggans, G., J. M. C. Plane, B. J. Allan, L. J. Carpenter, H. Coe, and C. O'Dowd (2000). A modeling study of iodine chemistry in the marine boundary layer. *J. Geophys. Res. 105*(D11), 14,371–14,386. Incl. data supplement; Postscript table; ftp://kosmos.agu.org/apend/1999JD901187/.

Mellouki, A. and A. R. Ravishankara (1994). *Int. J. Chem. Kinet. 26*, 355.

Mellouki, A., R. K. Talukdar, A. Schmoltner, T. Gierczak, M. Mills, S. Solomon, and A. R. Ravishankara (1992). Atmospheric lifetimes and ozone depletion potentials of methyl bromide (CH_3Br) and dibromomethane (CH_2Br_2). *Geophys. Res. Lett. 19*(20), 2059–2062.

Mentel, T., D. Bleilebens, and A. Wahner (1996). A Study of Nighttime Nitrogen Oxide Oxidation in a Large Reaction Chamber - the Fate of NO_2, N_2O_5, HNO_3 and O3 at Different humidities. *Atmospheric Environment 30*(23), 4007–4020.

Mihalopoulos, N., E. Stephanou, M. Kanakidou, S. Pilitsidis, and P. Bousquet (1997). Tropospheric aerosol ionic composition in the Eastern Mediterranean region. *Tellus B 49*(3), 314–326.

Mihelcic, D., F. Holland, A. Hofzumahaus, L. Hoppe, S. Konrad, P. Msgen, H.-W. Pätz, H.-J. Schäfer, T. Schmitz, A. Volz-Thomas, K. Bächmann, S. Schlomski, U. Platt, A. Geyer, B. Alicke, and G. Moortgat (2003). Peroxy radicals during BERLIOZ at Pabstthum: Measurements, radical budgets and ozone production. *J. Geophys. Res. 108*(D4), PHO 9–1 to PHO 9–15.

Mihele, C. and D. Hastie (1998). The sensitivity of the radical amplifier to ambient water vapour. *Geophys. Res. Lett. 25*, 1911–1913.

Millán, M., R. Salvador, E. Mantilla, and G. Kallos (2000). *J. Appl. Meteorol. 4*, 487.

Misra, A. and P. Marshall (1998). Computational investigations of iodine oxides. *J. Phys. Chem. A 102*(45), 9056–9060.

Miyake, Y. and S. Tsnogai (1963). Evaporation of Iodine from the ocean. *J. Geophys. Res. 68*, 3989–3993.

Moise, T., R. K. Talukdar, G. J. Frost, R. W. Fox, and Y. Rudich (2002). Reactive uptake of NO_3 by liquid and frozen organics. *J. Geophys. Res. 107*(D2), AAC 6–1 to AAC 6–9.

Moortgat, G. (2001). Important photochemical processes in the atmosphere. *Pure Appl. Chem. 73*(3), 487490.

Moortgat, G. K., R. Meller, and W. Schneider (1993). Temperature dependence (256-296K) of the absorption cross-sections of bromoform in the wavelength range 285-360nm. In: H. N. Becker and R. (Hrsg.), *The Tropospheric Chemistry of Ozone in the Polar Regions*, S. 359–370. ew York: Springer-Verlag.

Mozurkewich, M. (1995). Mechanisms for the release of halogens from sea-salt particles by free radical reactions. *J. Geophys. Res. 100*(D7), 14,199–14,208.

Nagao, I., K. Matsumoto, and H. Tanaka (1999). Sunrise ozone destruction found in the sub-tropical marine boundary layer. *Geophys. Res. Lett. 26*(22), 3377–3380.

Nguyen, B., N. Mihalopoulos, and S. Belviso (1990). Seasonal Variation of Atmospheric Dimethylsulfide at Amsterdam Island in the Southern Indian Ocean. *J. Atmos. Chem. 11*, 123–141.

Nilsson, E. and C. Leck (2002). A pseudo-Lagrangian study of the sulfur budget in the remote Arctic marine boundary layer. *Tellus B 54*(3), 213–230.

Noxon, J. F., R. B. Norton, and E. Marovich (1980). NO_3 in the troposphere. *Geophys. Res. Lett. 7*, 125–128.

O'Dowd, C. (2001). Biogenic coastal aerosol production and its influence on aerosol radiative properties. *J. Geophys. Res. 106*(D2), 1545–1550.

Oltmans, S. J. and H. Levy II (1994). Surface ozone measurements from a global network. *Atmos. Environ. 28*(1), 924.

Orlando, J., G. Tyndall, G. Moortgat, and J. Calvert (1993). Quantum yields for NO_3 photolysis between 570 and 635 nm. *J. Phys. Chem. 97*, 10.996–11.000.

Oum, K. W., M. J. Lakin, and B. J. Finlayson-Pitts (1998). Bromine activation in the troposphere by the dark reaction of O3 with seawater ice. *Geophys. Res. Lett. 25*(21), 3923–3926.

Paulson, S., M. Chung, and A. Hasson (1999). OH radical formation from the gas-phase reaction of ozone with terminal alkenes and the relationship between structure and mechanism. *J. Phys. Chem. A 103*(41), 8125–8138.

Penkett, S. A., B. M. R. Jones, K. A. Brice, and A. E. J. Eggleton (1979). *Atmos. Environ. 13*, 123.

Perner, D., T. Arnold, J. Crowley, T. Klüpfel, M. Martínez, and R. Seuwen (1999). The measurements of active chlorine in the atmosphere by chemical amplification. *J. Atmos. Chem. 34*, 9–20.

Peters, T. and A. Lotter (2003). Mesurements of halogen oxides with DOAS in Britanny, France.

Plane, J., B. Allan, and S. Ashworth (2001). On the chemistry of iodine oxides in the marine boundary layer. *Geophys. Res. Abs. 3*, 6498.

Platt, U. (1994). Differential Optical Absorption Spectroscopy (DOAS). In: M. W. Sigrist (Hrsg.), *Monitoring by Spectroscopic Techniques*. New York: John Wiley.

Platt, U., B. Alicke, R. Dubois, A. Geyer, A. Hofzumahaus, F. Holland, M. Martinez, D. Mihelcic, T. Klüpfel, B. Lohrmann, W. Pätz, D. Perner, F. Rohrer, J. Schäfer, and J. Stutz (2002). Free radicals and fast photochemistry during BERLIOZ. *J. Atmos. Chem 42*, 359–394.

Platt, U. and G. Hönninger (2003). The role of halogen species in the troposphere. *Chemosphere 52*(2), 325–338.

Platt, U. and C. Janssen (1995). Observation and role of the free radicals NO3, ClO, BrO and IO in the troposphere. *Faraday Discuss. 100*, 175–198.

Platt, U. and G. Le Bras (1997). Influence of DMS on the Ox - NOy partitioning and the NOx distribution in the marine background troposphere. *Geophys. Res. Lett. 24*(15), 1935–1938.

Platt, U., G. Le Bras, G. Poulet, J. P. Burrows, and G. K. Moortgat (1990). Peroxy radicals from night-time reaction of NO_3 with organic compounds. *Nature 348*(6297), 147–149.

Platt, U. and E. Lehrer (1996). Arctic Tropospheric Ozone Chemistry (ARCTOC), Final Report of the EU-Project No. EV5V-CT93-0318. Technical Report EV5V-CT93-0318, Institut fuer Umweltphysik.

Platt, U., D. Perner, G. W. Harris, A. M. Winer, and J. N. Pitts (1980). Detection of NO3 in the polluted troposphere by differential optical absorption. *Geophys. Res. Lett. 7*, 89–92.

Platt, U., D. Perner, H. Schroeder, G. Kessler, and A. Toenissen (1981). The diurnal variation of NO3. *J. Geophys. Res. 86*(C12), 11,965–11,970.

Platt, U. and J. Stutz (1998). HALOTROP, Results from field, laboratory and modelling studies, Final Report of the EU-Project ENV4-CT95-0019-PL950049. Technical report, University of Heidelberg.

Platt, U., A. Winer, H. Biermann, R. Atkinson, and J. Pitts, Jr. (1984). Measurement of nitrate radical concentration in continental air. *Environmental science and technology 18*, 365 – 369.

Poskrebyshev, G. A., P. Neta, and R. E. Huie (2001). Equilibrium constant of the reaction $^{*}OH + HNO_3 \longleftrightarrow H_2O + NO_3^{*}$ in aqueous solution. *J. Geophys. Res. 106*(D5), 4995–5004.

Pszenny, A., J. Moldanová, W. Keene, S. R., J. Maben, M. Martinez-Harder, P. Crutzen, D. Perner, and R. Prinn (2004). Aerosol pH and Inorganic Halogen Species in the Hawaiian Marine Boundary Layer. *Atmos. Chem. Phys. 4*(1), 147–168. SRef-ID: 1680-7324/acp/2004-4-147.

Ramacher, B., J. Rudolph, and R. Koppmann (1999). Hydrocarbon measurements during tropospheric ozone depletion events: Evidence for halogen atom chemistry. *J. Geophys. Res. 104*(D3), 3633–3654.

Rasch, P. J., M. C. Barth, J. T. Kiehl, S. E. Schwartz, and C. M. Benkovitz (2000). A description of the global sulfur cycle and its controlling processes in the National Center for Atmospheric Research Community Climate Model, Version 3. *J. Geophys. Res. 105*(D1), 1367–1386.

Ravishankara, A. R. (1997). Heterogeneous and Multiphase Chemistry in the Troposphere. *Science 276*(5315), 1058–1065.

Ravishankara, A. R., Y. Rudich, R. Talukdar, and S. B. Barone (1997). Oxidation of atmospheric reduced sulphur compounds: perspective from laboratory studies. *Phil. Trans. R. Soc. Lond. B 352*(1350), 171–182.

Ray, A., I. Vassali, G. Laverdet, and G. LeBras (1995). Kinetics of the thermal decomposition of the CH3SO2 radical and its reaction with NO2 at 1 Torr and 298 K. *J. Phys. Chem. 100*, 8895–8900.

Reifenhäuser, W. and K. G. Heumann (1992). Determinations of methyl iodide in the Antarctic atmosphere and the south polar sea. *Atmos. Environ. 26a*, 2905–2912.

Richter, A., F. Wittrock, M. Eisinger, and J. P. Burrows (1998). GOME observations of tropospheric BrO in northern hemispheric spring and summer 1997. *Geophys. Res. Lett. 25*(14), 2683–2686.

Riffault, V., Y. Bedjanian, and G. Le Bras (2003). Kinetic and mechanistic study of the X and XO (X=Cl, Br) reactions with dimethyl sulfoxide. *Phys. Chem. Chem. Phys. 5*(13), 2828–2835.

Robinson, G. N., D. R. Worsnop, J. T. Jayne, C. E. Kolb, and P. Davidovits (1997). Heterogeneous uptake of $ClONO_2$ and N_2O_5 by sulfuric acid solutions. *J. Geophys. Res. 102*(D3), 3583–3602.

Rodríguez, D., A. Aranda, Y. Díaz de Mera, B. Ballesteros, and E. Martínez (2003). Kinetic and mechanistic study of Cl reactions with aliphatic thiols. Temperatue dependence. *Phys. Chem. Chem. Phys. 5*, 514–519.

Roelofs, G. and J. Lelieveld (1997). Model study of the influence of cross-tropopause O_3 transports on tropospheric O_3 levels. *Tellus 49B*(1), 3855.

Roscoe, H. K., K. Kreher, and U. Friess (2001). Ozone loss episodes in the free Antarctic troposphere, suggesting a possible climate feedback. *Geophys. Res. Lett. 28*(15), 2911–2914. 2000GL012583.

Röth, E., S. Johänning, H. London, and S. Huber-Thives (1996). Description of a photon flux model to determine photodissociation coefficients. Berichte des forschungszentrums, Forschungszentrum Jülich.

Rudich, Y., R. K. Talukdar, A. R. Ravishankara, and R. W. Fox (1996). Reactive uptake of NO3 on pure water and ionic solutions. *J. Geophys. Res. 101*(D15), 21,023–21,032. 96JD01844.

Rudolph, J., B. Ramacher, C. PlassDulmer, K. P. Muller, and R. Koppmann (1997). The indirect determination of chlorine atom concentration in the troposphere from changes in the patterns of non-methane hydrocarbons. *Tellus 49B*, 592–601.

Saathoff, H., K.-H. Naumann, N. Riemer, S. Kamm, O. Möhler, U. Schurath, H. Vogel, and B. Vogel (2001). The loss of NO_2, HNO_3, NO_3/N_2O_5, and $HO_2/HOONO_2$ on soot aerosol: A chamber and modeling study. *Geophys. Res. Lett. 28*(10), 1957–1960.

Saltelli, A. and J. Hjort (1995). Uncertainty and sensitivity analysis of OH-initiated dimethylsulphide (DMS) oxidation kinetics. *J. Atmos. Chem. 21*, 187–221.

Saltzman, E., D. King, K. Holmen, and C. Leck (1993). Experimental determination of the diffusion coefficient of dimethylsulfide in water. *J. Geophys. Res. 98*(C9), 16481–6. 15 Sept. 1993.

Sander, R. (1999). Compilation of Henrys Law Constants for Inorganic and Organic Species of Potential Importance in Environmental Chemistry - Version 3 (April 8, 1999). http://www.mpch-mainz.mpg.de/ sander/res/henry.html.

Sander, R. and P. J. Crutzen (1996). Model study indicating halogen activation and ozone destruction in polluted air masses transported to the sea. *J. Geophys. Res. 101*(D4), 9121–9138.

Sander, R., Y. Rudich, R. von Glasow, and P. J. Crutzen (1999). The role of $BrNO_3$ in marine tropospheric chemistry: A model study. *Geophys. Res. Lett. 26*(18), 2857–2860.

Sander, S. P., B. J. Finlayson-Pitts, R. R. Friedl, D. M. Golden, R. E. Huie, C. E. Kolb, M. J. Kurylo, M. J. Molina, G. K. Moortgat, V. L. Orkin, and A. R. Ravishankara (2003). Chemical Kinetics and Photochemical Data for Use in Atmospheric Studies, Evaluation Number 14. Technical report, Jet Propulsion Laboratory.

Scarratt, M. G., M. Levasseur, S. Schultes, S. Michaud, G. Cantin, A. Vézina, M. Gosselin, and S. de Mora (2000). Production and consumption of dimethylsulfide (DMS) in North Atlantic waters. *Mar Ecol Prog Ser 204*, 13–26.

Schall, C. and K. Heumann (1993). GC determination of volatile organoiodine and organobromine compounds in seawater and air samples. *Fresenius Z. Anal. Chem. 346*, 717–722.

Schall, C., K. Heumann, and G. Kirst (1997). Biogenic volatile organoiodine and organobromine hydrocarbons in the Atlantic Ocean from 42°N to 72°S. *Fresenius J Anal Chem. 359*(3), 298–305.

Schneider, J., S. Borrmann, A. G. Wollny, M. Bläsner, N. Mihalopoulos, H. Bardouki, C. Economou, J. Sciare, and D. Worsnop (2003). Ground based particle measurement during the MINOS campaign (Crete, August 2001): Size distribution and chemical composition.

Schweitzer, F., P. Mirabel, and C. George (1999). Heterogenious Chemistry of Nytryl Halides in Relation to Tropospheric Halogen Activation. *Atmos. Environ. 34*(1), 101–117.

Sciare, J., E. Baboukas, and N. Mihalopoulos (2001). Short-Term Variability of Atmospheric DMS and Its Oxidation Products at Amsterdam Island during Summer Time. *J. Atmos. Chem. 39*(3), 281–302.

Sciare, J. and N. Mihalopoulos (2000). A new technique for sampling and analysis of atmospheric dimethylsulphoxide(DMSO). *Atmos. Environ. 34*, 151–156.

Sciare, J., N. Mihalopoulos, and F. J. Dentener (2000). Interannual variability of atmospheric dimethylsulfide in the southern Indian Ocean. *J. Geophys. Res. 105*(D21), 26,369–26,378.

Seinfeld, J. (1986). Air pollution. S. 218–229. New York: Wiley and Sons.

Seisel, S., B. Flückiger, F. Caloz, and M. Rossi (1999). Heterogeneous reactivity of the nitrate radical: reactions on halogen salt at ambient temperature and on ice in the presence of HX (X = Cl, Br, I) at 190 K. *Physical chemistry chemical physics 1*(19), 2257 – 2266. 1999, May 1.

Seisel, S. and M. Rossi (1997). The heterogeneous Reaction of HONO and HBr on Ice and on Sulfuric Acid. *Ber. Bunsenges. Phys. Chem. 101*, 943.

Simò, R. (2001). Production of atmospheric sulfur by oceanic plankton: biogeochemical, ecological and evolutionary links. *TRENDS in Ecology & Evolution 16*(6), 287–294.

Solberg, S., N. Schmidbauer, A. Semb, F. Stordal, and O. Hov (1996). Boundary layer ozone depletion as seen in the Norwegian Arctic. *J. Atmos. Chem. 23*, 301–332.

Spivakovsky, C. M., J. A. Logan, S. A. Montzka, Y. J. Balkanski, M. Foreman-Fowler, D. B. A. Jones, L. W. Horowitz, A. C. Fusco, C. A. M. Brenninkmeijer, M. J. Prather, S. C. Wofsy, and M. B. McElroy (2000). Three-dimensional climatological distribution of tropospheric OH: Update and evaluation. *J. Geophys. Res. 105*(D7), 8931–8980.

Stutz, J. (1991). *Charakterisierung von Photodiodenzeilen zur Messung stratosphärischer Spurenstoffe*. Diploma thesis, Universität Heidelberg.

Stutz, J. (1996). *Messung der Konzentration troposhärischer Spurenstoffe mittels Differentieller-Optischer-AbsorptionsSpektroskopie: Eine neue Generation von Geräten und Algorithmen.(D455)*. Ph. d. thesis, Ruprecht-Karls-Universität Heidelberg.

Stutz, J., R. Ackermann, J. Fast, and L. Barrie (2002). Atmospheric reactive chlorine and bromine at the Great Salt Lake, Utah. *Geophys. Res. Lett. 29*(10), 1380–1384.

Stutz, J., K. Hebestreit, B. Alicke, and U. Platt (1999). Chemistry of halogen oxides in the troposphere: Comparison of model calculations with recent field data. *J. Atmos. Chem. 34*(1), 65–85.

Stutz, J. and U. Platt (1992). Problems in Using Diode Arrays for Open Path DOAS Measurements of Atmospheric Species. In: *EOS/SPIE Symp. Berlin, Optical Methods in the Atmospheric Chemistry*, Band 1715, Berlin, S. 329–340.

Takegawa, N., Y. Kondo, M. Ko, M. Koike, K. Kita, D. R. Blake, W. Hu, C. Scott, S. Kawakami, Y. Miyazaki, J. Russell-Smith, and T. Ogawa (2003). Photochemical production of O3 in biomass burning plumes in the boundary layer over northern Australia. *Geophys. Res. Lett. 30*(10), 7–1 to 7–4.

Tang, T. and J. C. McConnell (1996). Autocatalytic release of bromine from Arctic snowpack during polar sunrise. *Geophys. Res. Lett. 23*(18), 2633–2636.

Tellinghuisen, J. (1973). Resolution of the visible-infrared absorption spectrum on I_2 into three contributing transitions. *J. Chem. Phys. 58*, 2821–2834.

Thomas, K., A. Volz-Thomas, D. Mihelcic, H. Smit, and D. Kley (1998). On the Exchange of NO3 Radicals with Aqueous Solutions: Solubility and Sticking Coefficient. *Journal of Atmospheric Chemistry 29*, 17 – 43.

Tokarczyk, R. and R. M. Moore (1994). Production of volatile organohalogens by phytoplankton cultures. *Geophys. Res. Lett. 21*(4), 285–288.

Toumi, R. (1994). BrO as a sink for dimethylsulphide in the marine atmosphere. *Geophys. Res. Lett. 21*(2), 117–120.

Trainer, M., Y. Hsie, S. McKeen, R. Tallamraju, D. Parrish, F. Fehsenfeld, and S. Liu (1987). Impact of natural hydrocarbons on hydroxyl and peroxy radicals at a remote site. *J. Geophys. Res. 92*(D10), 11.879–11.894.

Tuckermann, M., R. Ackermann, C. Goelz, H. Lorenzen-Schmidt, T. Senne, J. Stutz, B. Trost, W. Unold, and U. Platt (1997). DOAS-observation of halogen radical-catalysed arctic boundary layer ozone destruction during the ARCTOC-campaigns 1995 and 1996 in Ny-Alesund, Spitsbergen. *Tellus B 49*(5), 533–555.

Turnipseed, A., S. Barone, and A. Ravishankara (1993). Reactions of CH_3S and CH_3SOO with O_3, NO_2 and NO. *J. Phys. Chem. 97*, 5926–5934.

Ulshofer, V., O. Flock, G. Uher, and M. Andreae (1996). Photochemical production and air-sea exchange of OCS in the eastern Mediterranean Sea. *Marine Chemistry 53*, 25–39.

Van Doren, J. M., L. R. Watson, P. Davidovits, D. R. Worsnop, M. Zahniser, and C. E. Kolb (1990). Temperature Dependence of the Uptake Coefficients of HNO_3, HCl, and N_2O_5 by Water Droplets. *J. Phys. Chem. 94*, 3.265–3.269.

van Duyl, F., W. Gieskes, A. Kop, and W. Lewis (1998). Biological control of short-term variations in the concentration of DMSP and DMS during a Phaeocystis spring bloom. *J Sea Res 40*, 221231.

Vogt, R., P. J. Crutzen, and R. Sander (1996). A mechanism for halogen release from sea-salt aerosol in the remote marine boundary layer. *Nature 383*(6598), 327–330.

Vogt, R., C. Elliott, H. Allen, J. Laux, J. Hemminger, and B. Finlayson-Pitts (1996). Some new labarotory approaches to studying tropospheric heterogeneous reactions. *Atmos. Environ. 30*(10 - 11), 1729–1737.

Vogt, R., R. Sander, R. von Glasow, and P. J. Crutzen (1999). Iodine chemistry and its role in halogen activation and ozone loss in the marine boundary layer: a model study. *J. Atmos. Chem. 32*, 375–395.

von Glasow, R. and P. J. Crutzen (2003). Model study of multiphase DMS oxidation with a focus on halogens. *Atmos. Chem. Phys. Discuss. 3*, 145.

von Glasow, R., R. Sander, A. Bott, and P. J. Crutzen (2002). Modeling halogen chemistry in the marine boundary layer 2. Interactions with sulfur and the cloud-covered MBL. *J. Geophys. Res. 107*(D17), ACH 2–1 to ACH 2–12. 2001JD000943.

von Kuhlmann, R. (2001). *Tropospheric Photochemistry of Ozone, its Precursors and the Hydroxyl Radical: A 3D-Modeling Study Considering Non-Methane Hydrocarbons*. Ph. D. thesis, Johannes Gutenberg Universität Mainz.

Vrekoussis, M., M. Kanakidou, N. Mihalopoulos, P. J. Crutzen, J. Lelieveld, D. Perner, H. Berresheim, and E. Baboukas (2003). Role of NO3 radical in oxidation processes in the eastern Mediterranean troposphere during the MINOS campaign. *Atmos. Chem. Phys. Discuss. 3*(3135), 3135–3169.

Wagner, T., C. Leue, M. Wenig, K. Pfeilsticker, and U. Platt (2001). Spatial and temporal distribution of enhanced boundary layer BrO concentrations measured by the GOME instrument aboard ERS-2. *J. Geophys. Res. 106*(D20), 24,225–24,236.

Wagner, T. and U. Platt (1998). Satellite mapping of enhanced BrO concentrations in the troposphere. *Nature 395*(6701), 486–490.

Wahner, A., T. F. Mentel, and M. Sohn (1998). Gas-phase reaction of N_2O_5 with water vapor: Importance of heterogeneous hydrolysis of N_2O_5 and surface desorption of HNO_3 in a large Teflon chamber. *Geophys. Res. Lett. 25*(12), 2169–2172.

Wahner, A., T. F. Mentel, M. Sohn, and J. Stier (1998). Heterogeneous reaction of N_2O_5 on sodium nitrate aerosol. *J. Geophys. Res. 103*(D23), 31,103–31,112.

Wang, Y., B. Ridley, A. Fried, C. Cantrell, D. Davis, G. Chen, J. Snow, B. Heikes, R. Talbot, J. Dibb, F. Flocke, A. Weinheimer, N. Blake, D. Blake, R. Shetter, B. Lefer, E. Atlas, M. Coffey, J. Walega, and B. Wert (2003). Springtime photochemistry at northern mid and high latitudes. *J. Geophys. Res. 108*(D4), TOP 6–1 to TOP 6–32.

Wängberg, I., T. Etzkorn, I. Barnes, U. Platt, and K. Becker (1997). Absolute determination of the temperature behaviour of the $NO_2 + NO_3(+M) < -> N_2O_5(+M)$ equilibrium. *J. Phys. Chem. A 101*(50), 9694–9698.

Watts, S. (2000). The mass budgets of carbonyl sulfide, dimethyl sulfide, carbon disulfide and hydrogen sulfide. *Atmos. Environ. 34*(5), 761–779.

Wayne, R., I. Barnes, P. Biggs, J. Burrows, C. Canosa-Mas, J. Hjorth, G. Le Bras, G. Moortgat, D. Perner, G. Poulet, G. Restelli, and H. Sidebottom (1991). The nitrate radical: physics, chemistry, and the atmosphere. *Atmos. Environ. 25A*(1), 1–203.

Wayne, R., G. Poulet, P. Biggs, J. Burrows, R. Cox, P. Crutzen, G. Haymann, M. Jenkin, G. Le Bras, G. Moortgat, U. Platt, and R. Schindler (1995). Halogen oxides: radicals, sources and reservoirs in the laboratory and in the atmosphere. *Atmos. Environ. 29*(Special Issue), 2675–2884.

Weiss, P. S., J. E. Johnson, R. H. Gammon, and T. S. Bates (1995). Reevaluation of the open ocean source of carbonyl sulfide to the atmosphere. *J. Geophys. Res. 100*(D11), 23,083–23,092.

Wennberg, P. (1999). Bromine explosion. *Nature 397*(6717), 299–300.

Wever, R., M. Tromp, B. Krenn, A. Marjani, and M. Vantol (1991). Brominating activity of the seaweed Ascophyllum nodosum: impact on the biosphere. *Environ. Sci. Technol. 25*(3), 446–449.

Winer, A. M., R. Atkinson, and J. N. Pitts (1984). Gaseous nitrate radical: possible nightime atmospheric sink for biogenic organic compounds. *Science 224*, 156–159.

Winer, A. M. and H. W. Biermann (1994). Long path differential optical absorption spectroscopy (DOAS) measurements of gaseous nitrous acid, NO2, and HCHO in the California South Coast air basin. *Res. Chem. Intermed. 20*, 423–445.

Wittrock, F., R. Müller, A. Richter, H. Bovensmann, and J. P. Burrows (2000). Measurements of Iodine monoxide (IO) above Spitsbergen. *Geophys. Res. Lett. 27*(10), 1471–1474.

Wolfe, G. V. and M. Steinke (1996). Grazing-activated production of dimethyl sulfide (DMS) by two clones of Emiliania huxleyi. *Limnol. Oceanogr. 41*, 1151–1160.

Wuosmaa, A. and L. Hager (1990). *Science 249*, 160.

Xie, H., R. M. Moore, and W. L. Miller (1998). Photochemical production of carbon disulphide in seawater. *J. Geophys. Res. 103*(CC3), 5635–5644.

Yin, F., D. Grosjean, and J. H. Seinfeld (1990). Photoxidation of Dimethyl Sulfide and Dimethyl Disulfide. I: Mechanism Development. *J. Atmos. Chem. 11*, 309–364.

Yoch, D., J. Ansede, and K. Rabinowitz (1997). Evidence for intracellular and extracellular dimethylsulfoniopropionate (DMSP) lyases and DMSP uptake sites in two species of marine bacteria. *Appl Environ Microbiol 63*, 3182–3188.

Yokouchi, Y., L. A. Barrie, D. Toom, and H. Akimoto (1996). The seasonal variation of selected natural and anthropogenic halocarbons in the arctic troposphere. *Atmos. Environ. 30*(10–11), 1723–1727.

Yokouchi, Y., H. Mukai, H. Yamamoto, A. Otsuki, C. Saitoh, and Y. Nojiri (1997). Distribution of methyl iodide, ethyl iodide, bromoform, and dibromomethane over the ocean (east and southeast Asian seas and the western Pacific). *J. Geophys. Res. 102*(DD7), 8805–8810.

Yvon, S., J. Plane, C.-F. Nien, D. Cooper, and E. Saltzman (1996). Interaction between nitrogen and sulfur cycles in the polluted marine boundary-layer. *J. Geophys. Res. 101*(D1), 1379–1386.

Zhou, X., H. J. Beine, R. E. Honrath, J. D. Fuentes, W. Simpson, P. B. Shepson, and J. W. Bottenheim (2001). Snowpack Photochemical Production of HONO: a Major Source of OH in the Arctic Boundary Layer in Springtime. *Geophys. Res. Lett. 28*(21), 4087–4090.

Zhou, X., K. Civerolo, H. Dai, G. Huang, J. Schwab, and K. Demerjian (2002). Summertime nitrous acid chemistry in the atmospheric boundary layer at a rural site in New York State. *J. Geophys. Res. 107*(D21), ACH 13–1 to ACH 13–11. 2001JD001539.

Zingler, J. and U. Platt (2004). Inorganic sources of boundary layer iodine oxide. unpublished paper.

Acknowledgements–Danksagung

Herrn Prof. Dr. Ulrich Platt, danke ich für die Ermöglichung dieser Arbeit, für seine Vorschläge und Anregungen sowie diverse Korrekturlesungen. Ihm und natürlich den Geldgebern der Europäischen Union danke ich für die Bereitstellung der finanziellen Mittel für die drei Messkampagnen in Creta, Kuujjuarapik und Kerguelen, sowie den Sondereinsatz am toten Meer. Ein besonders großes Dankeschön auch im Namen meines Sohnes Luca und der Mama (Sandra), die ich durch die unproblematische Verlängerung meines Vertrages weiterhin durchfüttern konnte ;-).
Herrn Prof. Dr Schurath danke ich für die freundliche Übernahme der Begutachtung dieser Arbeit, flexible Termingestaltung, Korrekturen und Geduld.

Dank an Gerd Hoenninger für Organisation, Teilnahme, Auswertung der Kampagnen in Kreta und Hudson Bay. Für viele lustige Stunden nicht nur bei Ice-Beer und Raki und die vielen Abenteuer in engen Kurven auf Kreta oder auf dem knirschendem Eis der Hudson Bay. Besonderer Dank auch an Andy Geyer für die Einführung in die Analyse, die DOAS-Urlaubswochen in Kreta und Korrektur meiner wissenschaftlichen Werke. Dank an Hans für die ausgiebigen DOAS-Justagesessions, Ausdauer und die vielen Dinge die für gute Stimmung sorgten. Dank an Jutta für die Hilfe bei der Pinguinzucht in Kerguelen, den Plausch in stillen Stunden, Schlüssel, Auto u.v.m. Dank an Roland für die Hilfe in den letzten Wochen meiner Arbeit, für Papers, Tips und die Fhrung durch den Einheitendschungel.

Dank für lustige Stunden, den Plausch mal zwischendurch, diverse Schleppaktionen für meine Kampagnen und und und ... auch an die restlichen Kollegen aus dem IUP, den Tropis, Satellitis, Balloneuren, Wolkis, Maxis und Minis: Andreas(Lotti), Bärbel, Barbara, Frank, Jens, Lena, Nicole, Roman, Steffen, Thierry, Tina,... und die "ehemaligen" Hartmuth, Richie, Kai, Falko... und wen auch immer ich zu später Stunde jetzt vergessen habe.

Dank für die gute Atmosphäre und den alltäglichen Pausentratsch an meine "former and actual" Zimmerkollegen: Dirk, Andreas, Rainer, Simon, Jörg, Achim und Christian sowie der unendlichen Zahl von Irenes Schergen die den Tisch in meinem Büro für wenige Stunden ergattern konnten.

Merci beaucoup a tout le monde qui nos a aidé en la rèalisation des manipes a Kuujjuarapik et dans les terres australes (TAAF). A Claude Tremblay pour le immesurable et aimable soutien pendant le stage a Kuujjuarapik, pour le arrangement du emplacement pour le DOAS et la prise en charge des problemes qui sortent. A Jean Sciare et la 51ème mission

de Kerguelen pour la organisation du "Tour de Kerguelen" et le boulot sur place. Encore a Jean et a Haido, Constantina, Bernard et Nikos pour nos offrir les donns du DMS et ses produits, la mteo et tout ça qu'on peut trouver dans les pages de cette thèse.

Danke für die Hilfe bei der Diplomandenwerkstatt an Herrn Spiegel vom Kirchhoff Institut, Günther Balschbach, Herrn Fledderer und seinem Team aus der Werkstatt, Reinhold Bayer und an die "Elefanten" für die großzügige Bereitstellung finanzieller Mittel. Dank an alle Kollegen die zur/von der Werkstatt (bei)getragen haben, allen voran der Scholli mit seiner Heldenhaften Streichaktion. Dank auch an Inge Clos und Karoline Thomas, für die Übernahme des Schlüssels und dem alltäglichen Papierkram der einem das Leben so schwer macht. Speziell für Karoline hoffe ich, daßnun keine weitere Rechungen aus Kreta kommen ;-)

Unendlich grosser Dank a mis "papis", Irmhild und José–Miguel, sowie an meine queridas hermanas Verena und Katja ohne dessen Unterstützung die Fertigstellung dieser Arbeit nicht möglich gewesen wäre. Por creer en mi cuando yo ya no lo hacia, por vuestra infinita confianza, etliche Finanzspritzen, Luca's Intensivtraining in Sant Just Desvern und die Verwöhneinheiten bei Heimatbesuchen. Un gran besote a tothom ! Dank auch an Sandra und meinen Sohn Luca (alias Lucky, Quietschie, bum-bum), die für das notwendige Chaos in der letzten Phase dieser Arbeit gesorgt haben aber auch unendlich viele Mühen des Alltags von mir fernhielten ;-)

Widmen möchte ich diese Arbeit meiner Oma, Olly Müller de Vries und meinen spanischen Großeltern (el abuelo y la iaia), die nach einem langen Leben den Abschluss dieser Arbeit nicht mehr abwarten konnten. So gerne hätte ich diesen Moment noch mit Euch erleben wollen.